An experimental study of the spread of buoyant water into a rotating environment

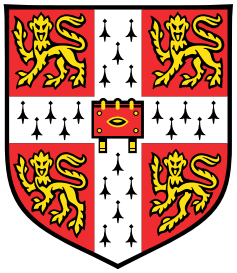

Thomas Joseph Crawford

Department of Applied Mathematics and Theoretical Physics
University of Cambridge

This dissertation is submitted for the degree of
Doctor of Philosophy

Queens' College May 2017

I would like to dedicate this thesis to my loving parents without whose unwavering support it would not have been possible. I hope that I have done you proud.

Declaration

This dissertation is the result of my own work and includes nothing which is the outcome of work done in collaboration except where specifically indicated in the text. No parts of this dissertation have been submitted for any other qualification.

Thomas Joseph Crawford
May 2017

Acknowledgements

I cannot begin to express my gratitude towards my PhD supervisor, Professor Paul Linden. From providing me with this opportunity, to supporting me throughout the past four years and allowing me to make the most of my time in Cambridge, I will always be grateful. There are numerous other members of the department who have helped me from the team of lab technicians of David Page-Croft, Colin Hitch, John Milton and Paul Mitton, to Dr Stuart Dalziel and his never-ending knowledge of all things Digiflow. A special mention to Dr Jamie Partridge and Dr Scott Bachman for answering my many questions and Dr Dan Whitt for some very fruitful discussions.

I must also thank my friends and family for supporting me throughout this endeavour. My brother George for always being willing to talk about football, my friends Jon and Nick for never failing to provide me with a source of entertainment and Camilla for always being there. Finally, I have made many good friends in the department who have helped to make this experience one which I have throughly enjoyed. A massive thank you to everyone mentioned above and all of the GK Batchelor Laboratory team, it really has been great fun.

My work was financially supported by the Natural Environment Research Council.

Abstract

This thesis examines previously unresolved issues regarding the fluid dynamics of the spread of buoyant water into a rotating environment. We focus in particular on the role that finite potential vorticity and background turbulence play in determining the flow properties.

When water of an anomalous density enters into an oceanic basin, gravity-driven surface flows can be established as a result of the density difference. These flows are often of a sufficiently large scale that the dynamics are affected by the Coriolis force arising from the rotation of the earth. This causes the formation of a large outflow gyre near to the source which feeds into a propagating gravity current that is confined to the coast. Previous experimental work in this field has sought to simplify the problem through the use of a point source and a quiescent ambient. We extend this work to provide a better representation of the real-world flow by introducing a source of finite depth and background turbulence to the rotating ambient.

This study seeks to answer three key questions that are critical to the understanding of the flow behaviour in this scenario. First, what is the effect of the finite potential vorticity of the outflow on the properties of the outflow vortex and the boundary current? Second, what role does the presence of the outflow vortex play in determining the behaviour of the current? Third, what is the effect of background turbulence on the flow properties? To carry out the investigation, experiments were conducted in the laboratory and compared with a theoretical description of the flow. The currents are generated inside a rotating tank filled with saltwater by the continuous release of buoyant freshwater from a source structure located at the fluid surface. A horizontal source of finite depth is used to introduce finite potential vorticity into the outflow. The impact of background turbulence is examined by introducing an oscillating grid into the rotating tank.

We find that the finite potential vorticity of the outflow plays an important role in determining the flow properties for sufficiently low Rossby and Froude number. As the value

of these parameters is increased a zero potential vorticity model is able to capture the key elements of the flow behaviour. The outflow vortex is found to act as a time-varying source to the boundary current, with the current velocity fixed by the vortex velocity field. The vortex vorticity is seen to decrease with time, while the vortex radius continues to increase at late times despite the vortex having reached a limiting depth, which enables potential vorticity to be conserved and the current to be supplied with a non-zero velocity. Finally, the structure of the background turbulence is found to be key in determining the effect that it has on the flow properties, with different behaviours observed for three-dimensional and quasi-two-dimensional turbulence.

Table of contents

Chapter 1

Introduction

Outflows of buoyant water entering into the ocean are a major source of nutrients, pollutants and sediments to coastal regions. The movement of this water and its constituents has a major effect on the water quality of these regions and understanding where it is transported and how it affects the physical processes at work in the ocean is an invaluable tool for future environmental planning. The quality status report on the North Sea (OSPAR, 2010), for example, identified nutrient inputs from sources on land as an issue of high importance that needs to be addressed to achieve their goal of a clean, healthy and biologically diverse sea. The source of the outflows may be a discharging river (eg. the Rhine or the Hudson), a narrow connecting channel between an ocean and a marginal sea (eg. the Yucatan Channel or the Strait of Gibraltar), or meltwater from the polar regions (eg. East Greenland Current). Investigating the features of these outflows has been the focus of numerous past studies, ranging from fieldwork, to numerical simulations, to laboratory experiments, all with the aim of furthering the understanding of the complex fluid dynamical systems present.

The most local example to the UK is the North Sea, with various rivers, such as the Rhine, Elbe and Thames, and the Baltic Sea providing a steady supply of buoyant water into the region. The North Sea project (1987) collected data across the North Sea in a series of 39 cruises between August 1988 and October 1990. Measurements were made of the physical, chemical, biological and sedimentological properties in the plume areas at the outflows of the Humber, Wash, Thames and Rhine. The outflow from the Rhine, for example, produces a coastal current extending $>$ 200km along the coast which demonstrates Nitrogen levels more than an order of magnitude greater than those found elsewhere in the North Sea (Simpson and Sharples, 2012). Research by van der Voet et al. (1996) found that in the North Sea, riverine inflow contributes the largest anthropogenic input of nitrogen compounds, with

food production and consumption the major source via the import of fertiliser. The main environmental problem related to nitrogen compounds is the eutrophication of coastal seas as the increased nutrient availability leads to toxic algae blooms resulting in mass fish mortality. Eutrophication can also lead to hypoxia and the effects of this in the Baltic Sea have been studied, for example by Conley et al. (2009) and Conley et al. (2011).

Alongside those found in the North Sea, there are many other examples of coastal currents that have been studied in the literature. Typical ones being the Delaware coastal current (Münchow and Garvine, 1993), the Hudson river plume (Bowman and Iversen, 1978), the Chesapeake Bay outflow (Rennie, Largier and Lentz, 1999), the Tsugaru (Kawasaki and Sugimoto 1984) and the Leeuwin current (Chabert D'Hieres, Didelle and Obaton, 1991).

Buoyant outflows into shallow shelf seas in particular have been examined in great detail due to their ability to dominate the dynamics in coastal regions. The major physical processes at work in a shallow shelf sea can be described by the basic competition between buoyancy and stirring. Stirring occurs mainly in the form of wind and tidal motions, while buoyancy input has two main sources: solar heating at the surface and freshwater outflows from rivers and fjords. The solar heating dominates over the majority of a shelf sea, but freshwater discharge can make a significant contribution to buoyancy input in areas of shelf seas adjacent to estuaries, known as regions of freshwater influence or ROFIs (Simpson and Sharples, 2012). A ROFI is defined as the region between the shelf sea regime and the estuary where the local input of freshwater buoyancy from the coastal source is comparable with, or exceeds, the seasonal input of buoyancy as heat which occurs all over the shelf (Simpson, 1997). As an example, for the North Sea the input of freshwater from the two largest rivers, the Rhine and Elbe, totals ~ 2700 m^3 s^{-1}, which over the surface area of the North Sea equates to solar heating at a rate of ~ 77 W m^{-2}, approximately one third of the peak summer heat input. The input of buoyancy from coastal sources of freshwater is very localised in space and as a result strong horizontal gradients in salinity are seen in ROFIs. This is in contrast to the buoyancy input from heat, which is relatively uniform in space and therefore the process is well understood; in shallow areas where tidal effects are strongest, the heat is well-mixed throughout the water column, whereas in deeper areas where the tides have less of an impact, the heat accumulates in the surface layer creating stratification. In a ROFI the competition between buoyancy and stirring is similar to that between surface heating and stirring but with one key difference: the freshwater outflow enters from a lateral boundary. This induces a density-driven circulation with the freshwater at the surface moving offshore and the denser

saltwater at the bottom moving onshore. The horizontal density gradient also interacts with the vertical shear in tidal currents via the process of tidal straining. When the tidal flow is offshore, the shear in the tidal current structure interacts with the offshore salinity gradient to induce stratification, whilst when the flow is onshore the shear acts to destabilise the water column causing overturning (Simpson, 1997). Experiments by Linden and Simpson (1988) showed that longer periods between overturning events allow the flow to become re-established for long enough to restore stratification. The addition of tidal stirring to the tidal straining model leads to the formation of a bottom mixed layer, while introducing wind stirring at the surface induces a surface mixed layer (Simpson et al. 1991).

Numerical modelling of ROFIs has been successful in reproducing the main qualitative features of the region being studied. Modelling of the Rhine ROFI shows that when the water column is stratified the tidal currents exhibit a marked cross-shore structure with cross-shore currents showing a 180° phase difference between the surface and the bed, in agreement with observations (de Boer et al., 2008). Further studies show that water from the Rhine spreads a considerable distance southward from the estuary mouth reaching the French-Belgian coastal border where more than 1% of the water originates from the Rhine estuary (Lacroix et al., 2004). This horizontal dispersion of the freshwater is in the opposite direction to that expected due to the Coriolis force and emphasises the role that other flow dynamics play in this complex and highly variable system.

Buoyant outflows have also been studied in a wider context with particular interest paid to the fluid dynamical phenomena that are present. When buoyant water is discharged from a narrow channel into a large ocean basin, it results in the formation of gravity-driven surface flows. When the scale of these flows is sufficiently large the flow is affected by the rotation of the earth via Coriolis forces which confine the flow to the coastal region. In the northern hemisphere the effect of the Coriolis force is to turn the freshwater to the right of the outflow. Two key dynamical features result: an anticyclonic bulge close to the source and a propagating coastal current. These features have been studied in the literature via a theoretical approach (e.g. Hacker and Linden 2002, Martin and Lane-Serff 2005, Martin, Smeed and Lane-Serff 2005), numerical simulations (e.g. Fong and Geyer, 2002) and laboratory experiments (e.g. Griffiths 1986, Thomas and Linden 1998, Avicola and Huq 2003). A comprehensive review of coastal river plumes is provided by Horner-Devine et al. (2015).

Davies et al. (1993) and Lentz and Helfrich (2002) use a scaling analysis to determine the properties of a coastal current. The current width, depth and velocity are given as a function of the independent parameters in the problem with the constants of proportionality having to be inferred from the experimental data (Lentz and Helfrich, 2002). Avicola and Huq (2002) assume that the frontal dynamics are the same as those of a Margules front and derive relations for the current depth and the Rossby deformation radius. The scalings derived in these studies are seen to reoccur in many of the theoretical models of a coastal current.

A number of laboratory studies have examined the behaviour of buoyant gravity currents under the effects of rotation. Those of particular interest to the present work investigated the currents formed downstream of a buoyant outflow (e.g. Stern, Whitehead and Hua 1982, Griffiths and Hopfinger 1983, Whitehead and Chapman 1986). In these studies the buoyant water is discharged parallel to the boundary wall via a constant flux source or a 'dam break' mechanism. The dynamics of a parallel outflow have been shown by e.g. Horner et al. (2000), Horner-Devine (2003), Avicola and Huq (2003b), to be fundamentally different to those of an outflow where the water is discharged perpendicular to the boundary. In the natural environment freshwater outflows generally enter into the ocean laterally and therefore the results of these studies may not accurately represent the real-world scenario. Horner-Devine et al. (2006) sought to address this issue by performing laboratory experiments where the inflowing water was discharged perpendicular to the tank wall from a rectangular source. The growth of an anticyclonic bulge occured near to the source and a coastal current formed downstream of the bulge. Measurements of the velocity and buoyancy fields in the outflow plume showed the bulge to be in a gradient-wind balance and the coastal current to be geostrophic. The bulge centre, defined by the point of zero velocity on the across-bulge velocity profile, was found to migrate offshore at a constant rate proportional to the inertial radius $L_i = V/f$, for V the inflow velocity and f the rotation rate. For experiments with high inflow discharge or low density anomaly the bulge was found to go unstable. The depth of the bulge h was found to increase slightly during the experiments with an exponential fit giving $h \sim t^n$ for $n < 0.16$, while the bulge radius was found to grow as $t^{0.25}$ during the first five rotation periods and $t^{0.39}$ at later times. Similar growth rates were also observed by Avicola and Huq (2003) who found the bulge depth increased as $t^{1/5}$ and the radius as $t^{2/5}$.

Another experimental study, on which the experimental setup used in the present work is based, is that of Thomas and Linden (2007), hereafter TL, who investigated the formation of a rotating gravity current similar to that observed in nature with a discharging river. A circular

rotating tank was filled with saltwater and then freshwater released from a source at the fluid surface. The fluid was discharged vertically upwards to reduce momentum-flux effects and mixing near to the source, which consisted of a small foam ball positioned on the end of a circular pipe of diameter 1 cm. In each of the experiments the formation of an anticyclonic gyre next to the source was observed, rotating in the opposite direction to the tank, as well as a propagating boundary current that moved with the boundary of the tank to the right of the flow direction as expected due to the Coriolis effect. Alongside the experiments, TL also formulated a geostrophic model to describe the dynamics of the coastal current. The model uses the shallow water equations which are derived from the Navier-Stokes equations in a rotating frame. The momentum equation in a rotating frame is given by

$$\rho\left(\frac{D\mathbf{u}}{Dt}+2\Omega\times\mathbf{u}\right)=-\nabla p-\rho\nabla(\Phi)+\rho\mathbf{F}, \tag{1.1}$$

where $\mathbf{u}$ is the velocity, Ω the rotation vector about a vertical axis, p the pressure, ρ the density, Φ the gravitational potential modified to include the centrifugal force $\frac{1}{2}|\Omega\times\mathbf{x}|^2$ introduced by the rotating frame and $\mathbf{F}$ a frictional force. For an incompressible fluid, $\nabla\cdot\mathbf{u}=0$, which gives via a scaling argument $W\sim HU/L$, for a typical vertical velocity W, typical horizontal velocity U, typical vertical lengthscale H and typical horizontal lengthscale L. Under the shallow water assumption, the vertical lengthscale $H<<L$ and thus $W<<U$. The rotation vector is simplified under the f-plane approximation, which assumes that the motion does not extend over significant changes in latitude and gives

$$2\Omega\times\mathbf{u}\sim(-fv,fu,0), \tag{1.2}$$

for $f=2\Omega\sin\theta$ where θ is the latitude. In the laboratory, when in solid body rotation the free-surface of the fluid is a geopotential surface which allows the further approximation $f\sim 2\Omega$, where Ω is the constant rotation rate. Applying a scaling argument to the z-momentum equation, the pressure is given by the hydrostatic relation

$$\frac{\partial p}{\partial z}=-g\rho, \tag{1.3}$$

where the correction term is $O(H/L)^2$. Assuming that $p=0$ on the free surface $z=\eta$, we have $p=g\rho(\eta-z)$. This implies that accelerations are independent of z and therefore if the flow starts from rest, velocities are independent of z also. This means that shallow water theory assumes that velocities are independent of z which is consistent with the Taylor-Proudman theorem (Gill, 1982). The resulting shallow water momentum equations are given

by

$$u_t + uu_x + vu_y - fv = -g\eta_x, \tag{1.4}$$

$$v_t + uv_x + vv_y + fu = -g\eta_y, \tag{1.5}$$

where u_t represents the derivative of u with respect to t. Mass conservation is derived from a kinematic boundary condition $w = D\eta/Dt$ (where w is fixed by a zero normal velocity at the bottom boundary), applied at the free surface $z = \eta$ to give

$$H_t + (uH)_x + (vH)_y = 0, \tag{1.6}$$

for H the total depth of water. The conservation of potential vorticity is another key result used in the model of TL and as such we derive it here in the case of shallow water theory. The absolute vorticity of the flow is given by the local vorticity $\nabla \times \mathbf{u}$ plus the background vorticity f. In the case of shallow water theory we are only concerned with the vertical component of the relative vorticity $\zeta = v_x - u_y$. Taking the partial x-derivative of (1.5) minus the partial y-derivative of (1.4) and substituting from (1.6) gives the result

$$\frac{D}{Dt}\Big(\frac{\zeta + f}{H}\Big) = 0, \tag{1.7}$$

where we define the shallow water potential vorticity (PV) by $q = (\zeta + f)/H$. The model of TL also assumes geostrophic balance, which means that the Coriolis force balances the pressure gradient. This assumes weak time-dependence, small Ekman number $Ek = \nu/fL^2 << 1$ for ν the kinematic viscosity and small Rossby number $Ro = U/fL << 1$. This gives

$$\rho fu = -\frac{\partial p}{\partial y}, \tag{1.8}$$

$$\rho fv = \frac{\partial p}{\partial x}. \tag{1.9}$$

The geostrophic model derived by TL predicts the height, width and propagation velocity of the current as a function of the background rotation rate, volumetric discharge rate and density difference at the source. Since the source in their experiments was small the discharging fluid was assumed to have zero potential vorticity as a first approximation. Their experimental results showed that the current velocity decreased with time and was not constant as predicted by the model. Furthermore, they found that there is a transition between currents that initially increase in velocity before slowing down and those which decrease in velocity throughout the

experiment, though they were unable to conclusively define the parameter regime at which the transition occurs. The experimental data also gave a larger current width than predicted by the theory and they discussed two possible reasons for this disagreement in the form of shear instabilities along the boundary between the current and the ambient and viscous effects meaning that the fluid is no longer governed by geostrophy. Finally, the current height was shown to decrease linearly over a large interval of the current with the maximum current depth occurring just downstream of the source.

When conducting experimental studies in the laboratory it is important that they can be related to the conditions seen in real-world flows. For the study of buoyant outflows entering into a rotating environment, the Rossby deformation radius is a key parameter as it gives the lengthscale at which rotational effects become as important as buoyancy effects in the evolution of the flow. We define a source deformation radius $R_d = \sqrt{g'H_0}/f$ for f the Coriolis parameter, $g' = g(\rho_s - \rho_f)/\rho_f$ the reduced gravity representing the density difference between the outflow density ρ_f and the ocean density ρ_s, and H_0 the source depth. By scaling the source deformation radius with the source width D we form a dimensionless parameter given by

$$\frac{R_d}{D} = \frac{\sqrt{g'H_0}}{fD}, \tag{1.10}$$

which characterises the balance between the effects of buoyancy and rotation for an outflow. The value of R_d/D varies considerably in the natural environment depending on the characteristics of the outflow. For a freshwater outflow near to the equator, such as the Amazon, where rotational effects are weak, $R_d/D \sim 100$, whereas for a wide mid-latitude outflow, such as the Yangtze, where rotational effects play a more dominant role, $R_d/D \sim 1$. For the North Sea the Rhine gives a value of $R_d/D \sim 5$ and for the Elbe $R_d/D \sim 2$. The experimental setup used for the present work (described in chapter 2) is designed to simulate outflows such as the Rhine and Elbe, with the parameter range $0.2 \leq R_d/D \leq 4.8$.

Alongside the formation of coastal currents, which is the focus of many of the studies discussed above, there are many situations where water of one density enters into an oceanic basin with a different density and a large outflow gyre is seen to form near to the source of the outflow. One of the largest ($20-30$ Sv) is the Yucatan Strait where warm Caribbean water enters the cooler Gulf of Mexico, with the formation of a gyre $3-4$ times the width of the downstream current (Sturges 1994). Smaller scale flows through the Tsugaru and the Gibraltar straits (~ 1 Sv) form gyres that are larger than their respective downstream

currents by up to a factor of ten (Nof and Pichevin, 1999). River outflows are typically smaller (< 1 Sv) and smaller, modest-sized gyres are seen which are at most twice the size of the downstream current (Nof and Pichevin, 2001).

The occurrence of an outflow bulge near to the source of a buoyant outflow can be seen in field studies of the Columbia river plume (Hickey et al. 1998) and numerical simulations of the Rhine outflow (Jacobs, 2004). Pichevin and Nof (1997) show that the formation of the bulge is due to an imbalance in the momentum of the system. They find that a steady alongshore current cannot be established due to the impossiblity of balancing the alongshore momentum-flux. To offset the momentum-flux leaving in the current, the outflow forms a large anticyclonic bulge next to the source which slowly migrates offshore. They also construct an analytical model for the system where they use a Bernoulli condition to fix the velocity of the coastal current alongside the boundary. Bernoulli's principle is applied along a streamline, defined by a curve that is instantaneusly tangent to the velocity vector of the flow, and says

$$\frac{1}{2}u^2 + \frac{p}{\rho} + gz = constant, \tag{1.11}$$

along the streamline on which it is applied, where u is the velocity, p the pressure and ρ the density (Batchelor, 2000). The outflow may be modelled as a two-layer fluid due to the much deeper lower layer and relatively small density difference between the two fluids. This allows the use of the Boussinesq approximation where density differences are negligible except when multiplied by gravity. They are represented by the reduced gravity $g' = g\Delta\rho/\rho$ for a density difference of $\Delta\rho$ between the layers. Under the hydrostatic approximation (1.3) for a two-layer fluid the Bernoulli condition reduces to $\frac{1}{2}u^2 + g'h = constant$ where h is the depth of the upper layer.

Nof and Pichevin (2001) presented a nonlinear analytical solution for the growth of an outflow bulge on an f-plane and conducted numerical simulations to validate the analytical calculations. The analytical model is based on the inviscid shallow water equations and an integrated balance of forces along the boundary wall. They find that the growth of the outflow vortex corresponds to a balance between the along-wall momentum flux of the downstream current and the compensating Coriolis force associated with the migration of the vortex centre away from the wall. The growth of the bulge contains two timescales: the fast timescale, $O(f^{-1})$, given by the time required for a particle to complete a single revolution within the gyre and the slow timescale which is associated with the slow offshore migration of the bulge.

In the model it is assumed that the bulge diameter is much greater than the downstream current width to allow for the separation of the timescales and a perturbation scheme is used to find the leading order solution for the growth of a circular vortex. They find that an intense anticyclonic vorticity (zero PV) outflow produces a steep gyre with a radius that increases quickly with time. The majority of the mass flux from the outflow (66%) enters into the bulge with the remaining 33% entering into the alongshore current. For an outflow with a weakly anticyclonic vorticity ($-\alpha f$ where α is analogous to the Rossby number) most of the water enters into the downstream current ($Q/(1+2\alpha)$ where Q is the outflow discharge) rather than the bulge. Despite the smaller mass flux for a weak vorticity outflow, the bulge is found to grow at a faster rate due to its relatively flat shape meaning that the radius increases rather than the depth. They compared the results of the analytical model with numerical simulations which showed that even though small frictional effects accumulate over time to alter the PV, the inviscid solution is valid at each moment. The analytical model requires the PV to be conserved on the short timescale of order $1/f$ which is much less than the timescale over which the decrease in the mean bulge vorticity occurs.

Nof et al. (2004) investigate the effect that the direction of an outflow has on the formation of the outflow bulge. They show that a southward outflow leads to the formation of a steady and almost stagnant region with the current broadening itself until the forces in the system balance. In the Northward outflow case (Pichevin and Nof, 1997), for example Loop Current eddies in the Gulf of Mexico, a chain of westward-propagating eddies and an eastward current are produced. For the Eastward outflow case (Nof and Pichevin 1999), for example the Tsugaru and Alboran gyres, a steady gyre is generated. Finally for a westward outflow (Nof et al. 2002), for example Teddies and the Leeuwin current, a chain of westward-propagating eddies and northward current are produced.

The outflow bulge occurring near to the source may also be modelled from a theoretical viewpoint as a vortex. Griffiths and Linden (1981) conducted an experimental study investigating the growth of a vortex formed by releasing a constant flux of freshwater into a rotating saltwater environment. Fluid was released from a confined source at the free surface of the saltwater ambient which was initially in solid body rotation. The source consisted of a small sphere of foam rubber (1 cm in diameter) attached to the end of a vertical pipe (0.3 cm in diameter). The formation of an anticyclonic vortex was observed with the source at the centre. The vortex depth and radius increased with time and the vortex was shown to always go unstable to baroclinic instability if allowed to grow for a long enough time. An

inviscid flow model based on the principle of the conservation of PV was also constructed and used to model the growth of a zero PV vortex, based on the small size of the source. Their experimental results showed that the vortex radius and depth increase at the time-dependent rates predicted by the model, but the radius is seen to be $50-100\%$ greater and the depth $30-70\%$ smaller than predicted.

An important factor in the natural environment that will affect the dynamics of a buoyant outflow and the resulting fluid dynamical features, is the action of the wind and tides which lead to the generation of turbulent mixing in the ocean. The flow of a freshwater current over the ocean bathymetry will also generate a turbulent friction that will act on the current from beneath. This is particularly prominent in a shallow sea environment such as the North Sea, which despite its relatively small size, is responsible for $3-4\%$ of the global tidal dissipation of energy (Otto et al., 1990). The Rhine and Elbe enter the Southern region of the North Sea with an approximately uniform depth of $10-20$ m and the shallowness of the southern North Sea means that turbulence due to bottom friction plays an important role (Jacobs, 2004). Fisher et al. (2002) analysed this role via measurements of the turbulent kinetic energy dissipation in the Rhine ROFI which demonstrated a strong peak near to the seabed. Similar observations were observed in the Liverpool Bay system by Simpson et al. (1996).

In the laboratory, the effects of turbulence on a density interface have been studied extensively in the past, with detailed reviews provided by Linden (1979) and Fernando (1991). Turner (1968) investigated the role of mixing across a density interface for turbulence produced by an oscillating grid. The experimental setup used has become the norm for this area of study. Turner provided a model for the rate of turbulent entrainment across a density interface as a function of the Richardson number, defined by the turbulent velocity and turbulent lengthscale. Hopfinger and Toly (1976) related the turbulent properties in the case of grid-generated turbulence to the experimental parameters of the grid mesh size, the grid stroke frequency and the grid stroke amplitude. The turbulent velocity was found to decay with increasing distance z from the grid as $1/z$, while the turbulent lengthscale increased linearly with z. Thompson and Turner (1975) and Nokes (1988) also carried out similar studies of grid-generated turbulence, with the dependence of the turbulent velocity on the distance from the grid found to be sensitive to the choice of virtual origin from which the distance z is measured. McDougall (1979) showed that the turbulence in a mixed layer is not

significantly affected by the entrainment of fluid across the density interface.

The rotation of the earth acts to alter the structure of the turbulence seen in the oceans with a transition to quasi-two-dimensional turbulence in deeper water. The previously three-dimensional turbulent structure seen close to the source of the turbulence, transitions to become non-isotropic with the integral length scale in the vertical direction parallel to the rotation axis, much larger than the integral lengthscale in a direction perpendicular to the axis. Examples of the large eddies formed can be seen along the California coast (Brink et al., 1991) and in the Norwegian coastal current (Mork 1981, Johannessen et al. 1989). Oey and Cheng (1992) conducted numerical simulations of the Norwegian coastal current which showed good agreement with observational data. The velocity field at the surface was shown to extend to depths upwards of 50 m with little change in the magnitude of the velocity and the scale of the eddies.

The effects of rotation on turbulent mixing across a density interface have been studied in the laboratory by Hopfinger et al. (1983) and Fleury et al. (1991) via an oscillating grid. Hopfinger et al. investigated the height above the grid at which the transition to non-isotropic turbulence occurs and found it to occur at a critical Rossby number. Fleury et al. studied the qualitative change in the turbulent behaviour across the three regimes of three-dimensional turbulence close to the grid, quasi-two-dimensional turblence far from the grid and a short transition regime inbetween.

Having studied the wealth of literature available on the dynamics of a buoyant outflow entering into a rotating environment, we have identified three key questions that remain unanswered, but are critical to understanding the flow behaviour. These questions provide the motivation for the work conducted in this thesis.

First, what is the effect of the finite potential vorticity of the outflow on the properties of the outflow vortex and the boundary current? Many previous studies have sought to simplify the problem through the use of a point source with the freshwater being discharged vertically. This is not the case in the natural environment as can be attested to by Horner-Devine et al. (2015) who describe the distinguishing feature of a river plume to be ‘the horizontal advection of freshwater from a river mouth that defines the shape and character of the plume’. We conduct laboratory experiments where the buoyant freshwater is discharged from a horizontal source of finite depth. The finite depth of the source introduces a finite value of potential

vorticity (PV) to the flow and we extend the steady-state current model of Thomas and Linden (2007) to account for the new source conditions. The new finite PV model is compared with the experimental measurements of the current depth, width and velocity to determine the effect of finite PV on the steady-state current properties. We also extend the vortex growth model of Griffiths and Linden (1981) to the case of finite PV and investigate the effect of finite PV on the vortex properties. We compare experimental measurements of the vortex depth and radius with the new finite PV vortex growth model and the model of Nof and Pichevin (2001).

Second, what role does the presence of the outflow vortex play in determining the behaviour of the current? In previous models of the boundary current the presence of the outflow vortex is often neglected or the vortex modelled as a separate entity to the current. We investigate the role that the vortex plays by introducing a time-dependent vorticity model that links the flow conditions in the vortex to those of the current. The need for a time-dependent vorticity parameter arises from experimental measurements of the vortex velocity profile and we see that is essential for PV to be conserved. The model is compared with time-dependent experimental data for the vortex depth, vortex radius, current velocity and current width.

Third, what is the effect of background turbulence on the flow properties? The impact of background turbulence is examined by introducing an oscillating grid into the rotating tank to provide a more realistic simulation of the natural environment in the laboratory. The properties of the grid-generated turbulence are analysed in comparison to similar studies both without rotation (eg. Hopfinger and Toly 1976) and with rotation (eg. Hopfinger et al. 1983) to verify their robustness. The structure of the turbulence is varied from isotropic, such as that seen in shallow seas with a bottom-generated turbulent friction, to quasi-two-dimensional with surface gyres as seen in the California and Norwegian coastal currents. The effects of the turbulent ambient on the properties of the outflow vortex and the boundary current are investigated for both regimes across a range of Richardson numbers.

The structure of this thesis is as follows. In chapter 2 we describe the experimental setup and the methods used to obtain the data, alongside an analysis of the source conditions and a classification of the experiments based on their qualitative features. We then introduce a finite potential vorticity model for the boundary current in a steady state in chapter 3 which is compared with experimental observations of the current in chapter 4. In chapter 5 we also derive a finite potential vorticity model for the growth of the outflow vortex which is

compared with experimental observations of the vortex in chapter 6. The second key question of this thesis is addressed in chapters 7 and 8 with the introduction of a time-dependent vorticity model that provides a coupling between the flow in the vortex and that of the boundary current. The properties of the grid-generated turbulence in the experimental setup are analysed in chapter 9 in comparison to the results seen in the literature both with and without rotation. Finally, in chapter 10 the effects of a non-quiescent ambient on the outflow are investigated in the two cases of three-dimensional and quasi-two dimensional turbulence. Overall conclusions are presented in chapter 11.

Chapter 2

Experiments

2.1 Introduction

The experiments were designed to simulate the discharge of buoyant freshwater from a source such as a river estuary into the more dense, salty ocean. The work of Thomas and Linden (2007) provided the foundation upon which this work was built. In their experimental setup a vertical source with low momentum-flux was used which allowed them to model the source as a zero potential vorticity (PV) outflow. The experimental setup used in the present work was designed to better represent the natural environment of a discharging outflow into the ocean through the use of a specially designed source structure. The freshwater is discharged horizontally and the finite depth of the source introduces a finite potential vorticity to the flow. A horizontal source structure was also used by Horner-Devine et al. (2006) though it was not discussed in terms of potential vorticity. Furthermore, the design of the source structure used in the present work allows for much larger discharge rates to be considered than those used by Horner-Devine et al. which varied from $2.9 \leq Q \leq 16.7$ cm^3 s^{-1}.

The experimental setup is related to real-world outflows via the dimensionless parameter R_d/D, for R_d the source deformation radius and D the source width, which represents the balance between the effects of buoyancy and rotation for an outflow. In the experiments the values range from $0.2 \leq R_d/D \leq 4.8$, with the Rhine and Elbe having the values $R_d/D \sim 5$ and $R_d/D \sim 2$ respectively.

In this chapter we describe the experimental setup and the methods used to collect the data. We also present an analysis of the source conditions and a classification of the experiments

based on the key qualitative features seen in the flow.

2.2 Experimental setup

The same basic experimental setup is used throughout the study and is shown in a diagram in figure 2.1. The experiments were conducted in a transparent rectangular acrylic tank with sides of length 99 cm and 79 cm and depth 51 cm. For an average experiment length of 120 seconds with an incoming volume flux of 50 cm^3s^{-1} this equates to a depth increase of ~ 8 mm. Rounded corner pieces were inserted at each corner of the tank to minimise the impact of the rectangular shape on the current progression. For the preliminary experiments when the rounded corners were not present, a decrease in the current speed and an increase in the current depth was seen as the current impacted with the tank wall at a corner. The use of the rounded corner pieces greatly reduced these effects. The tank was placed on a rotating turntable to simulate the rotation of the Earth and introduce Coriolis effects. We define the rotation rate by the Coriolis frequency $f = 4\pi/T_\Omega$, where T_Ω is the table rotation period, following the standard definition used by Horner-Devine et al. (2006). The rotation rate remains constant for the duration of an experiment and lies in the range $0 \leq f \leq 2$ s^{-1}. The upper limit of the rotation speed was limited for safety reasons due to the size of the tank. The tank was filled to a depth of $32-34$ cm with saltwater of density ρ_s to represent the ocean. The depth was adjusted so that in all experiments the source opening remained fully submerged throughout an experiment. A separate smaller tank (width $\times$ depth $\times$ height = 40 cm $\times$ 25 cm $\times$ 30 cm) was attached to the top of the turntable superstructure to act as a reservoir of freshwater of density ρ_f supplying the outflow source. The density difference between the freshwater and the saltwater is represented by the reduced gravity $g' = g(\rho_s - \rho_f)/\rho_f$, where we take $g = 981$ cm s^{-2}. The values used in the experiments range from $0 \leq g' \leq 72.6$ cm s^{-2}.

Fluid was released continuously from the freshwater reservoir with a constant volume flux Q, which was maintained via a motor that ensured a constant head of water above the outflow valve. A schematic of the setup within the freshwater reservoir is shown in figure 2.2. The tank was divided into two sections, with a pump acting to maintain the level in the right-hand section that fed into the outflow pipe. An overflow menchanism between the two sections ensured a contant height of water and thus a constant head of pressure which provided a constant volume flux Q. The volume flux in the experiments varied from $42-100$ cm^3 s^{-1}. The freshwater flows down a pipe of diameter 2 cm and length ~ 160 cm before

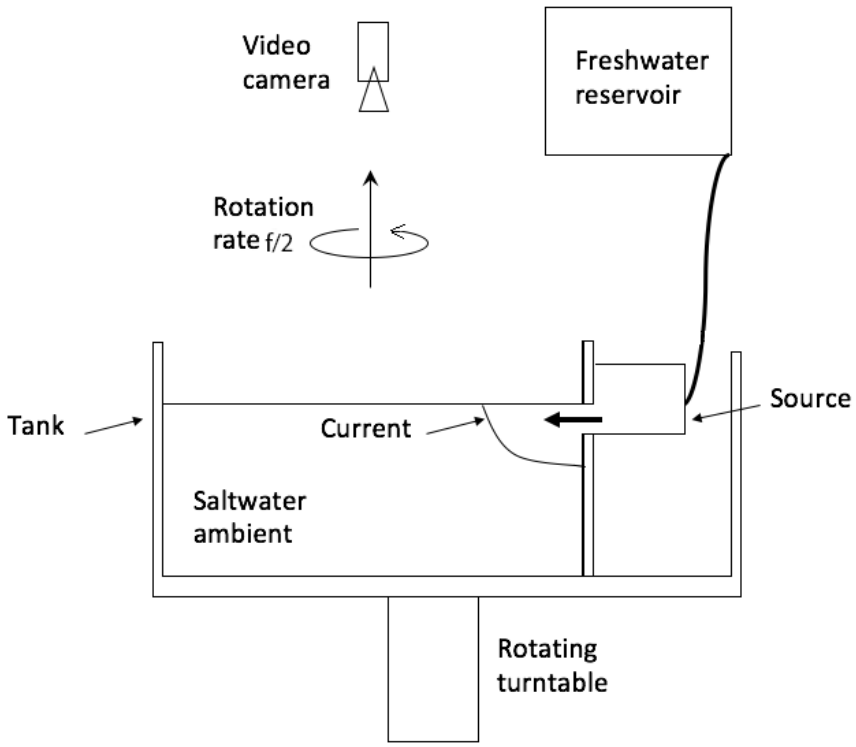

Figure 2.1 Schematic of the experimental setup.

reaching the source structure and entering into the saltwater ambient.

Calibration experiments were carried out to ensure that the volume flux Q remained constant throughout an experiment. The change in the depth of the ambient was measured at the end of an experiment and converted into an estimate of the volume flux. The amount of freshwater entering into the tank during an experiment was also estimated using depth measurements obtained via the dye attenuation technique (discussed in section 2.3.1). The ratio of the two values lies between $0.89 - 1.10$ giving an error of $\pm 10\%$. Figure 2.3 plots the estimated freshwater volume in the tank versus time for a typical experiment. The data show that the volume flux into the tank remains constant for the duration of an experiment with a linear fit to the data showing very good agreement. The estimated value of Q from the dye attenuation data is slightly lower ($\sim 4\%$) than the value measured via the change in the depth of the ambient, but is within the experimental error.

The source structure used in the experiments consists of an L-shaped acrylic box, which is filled with 60 PPI foam to help to reduce the momentum-flux of the incoming freshwater

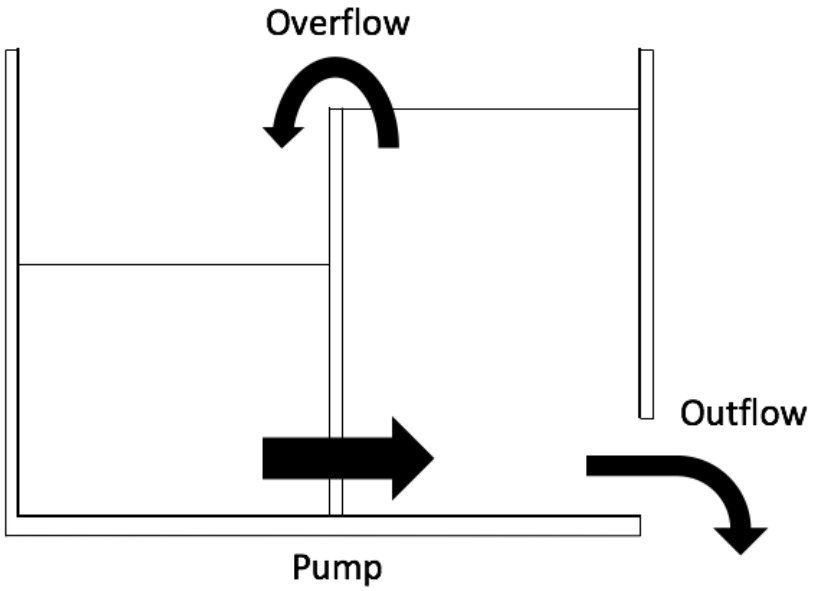

Figure 2.2 Schematic of the setup within the freshwater resevoir explaining how a constant head was maintained.

from the hosepipe. The dimensions of the source structure and its orientation can be seen in figure 2.4. A photograph showing the source from above is also included for clarity. The design of the source structure means that the freshwater is discharged into the tank horizontally, as is the case for a freshwater outflow such as a river, in the natural environment. Several designs of varying shapes and sizes were tested and the data obtained used to inform the construction of the final source shown in figure 2.4. The outflow conditions at the source are discussed in more detail in section 2.5. The endplate fixed to the front face of the source structure is visible in the photograph in figure 2.5 which views the source from the front. The endplate is interchangeable and a total of three were used, each with a different source opening. The one shown in figure 2.5 has a rectangular opening with a width of $D = 5$ cm and a depth of $H_0 = 2$ cm, giving a fixed area $A = 10$ cm^2. The parameters for all three endplates are shown in figure 2.6.

Before the freshwater was released from the upper reservoir the turntable was started at the chosen rotation rate and the saltwater in the bottom tank allowed to reach solid-body rotation. We estimate the spin-up time to be given by $\tau_s \sim H_a/\sqrt{f\nu}$, where H_a is the ambient depth and $\nu = 0.01$ cm^2 s^{-1} is the kinematic viscosity of water. The release of the freshwater was controlled via a valve fixed to the inflow pipe at the top of the source structure and an

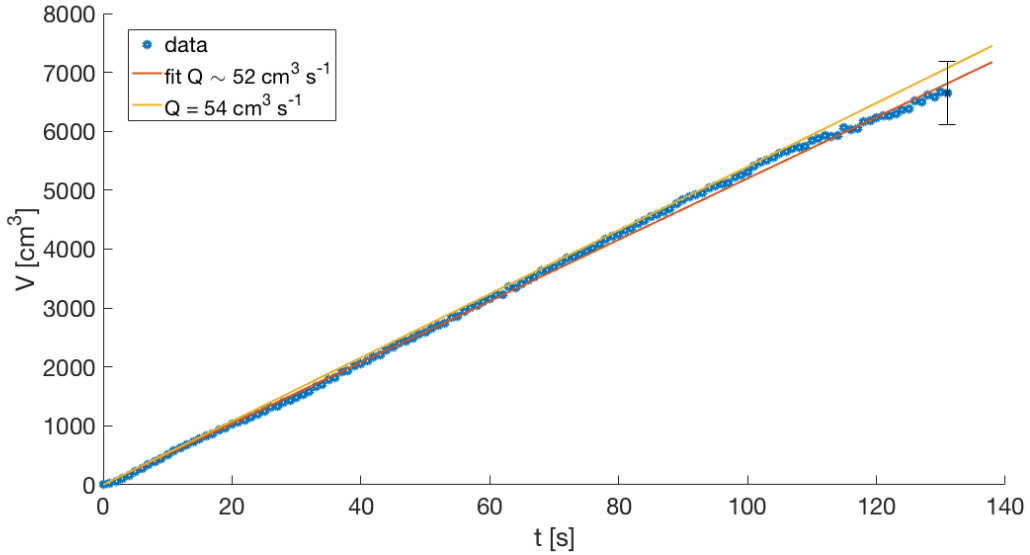

Figure 2.3 Estimated freshwater volume in the tank over time for a typical experiment. A linear fit to the data is shown alongside the value of Q obtained by measuring the change in the depth of the ambient. Typical error bars are also displayed.

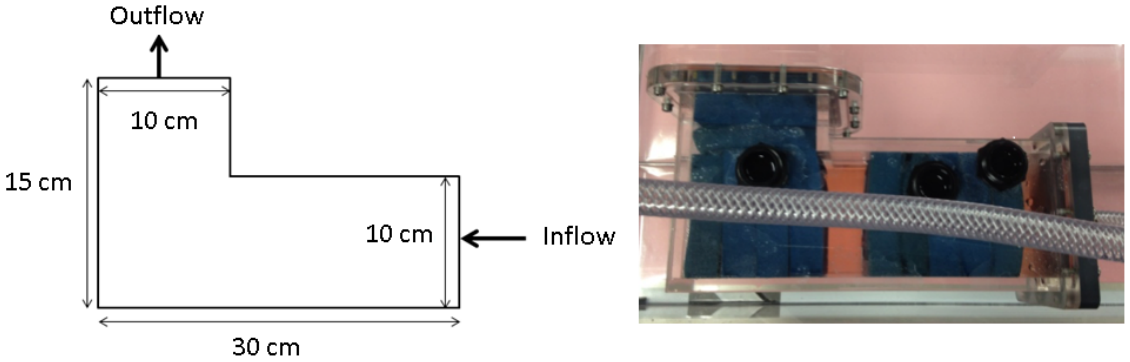

Figure 2.4 The dimensions of the source structure viewed from above and a plan-view photograph of the source in situ.

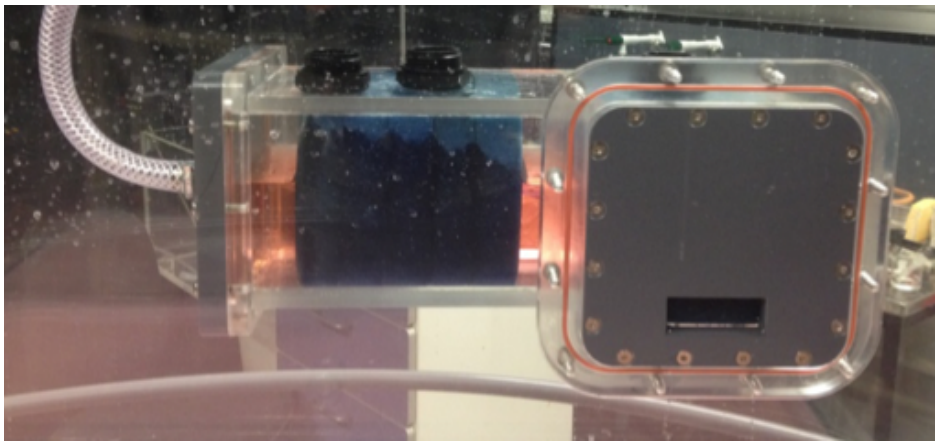

Figure 2.5 A photograph of the front of the source showing an example of one of the source openings used in the experiments. The dimensions of the opening shown are $D = 5$ cm and $H_0 = 2$ cm.

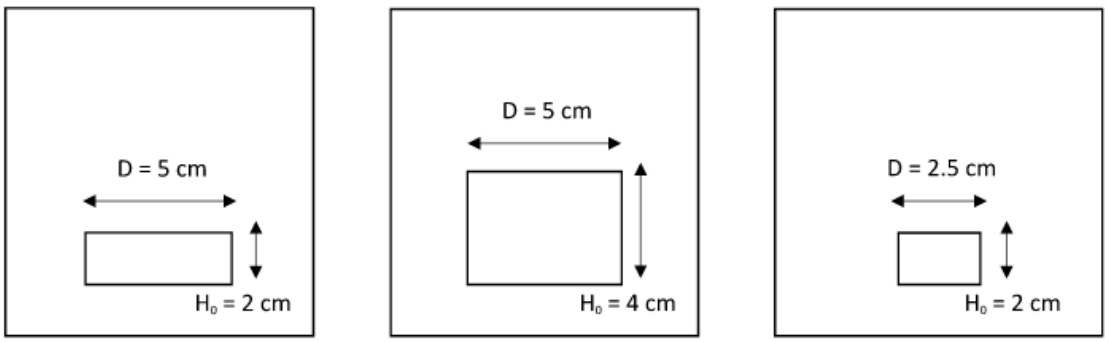

Figure 2.6 The dimensions of the three endplates used in the experiments.

electronic switch. For visualisation purposes the freshwater is dyed with red fiesta food colouring while the ambient saltwater remains clear. The use of the food dye allowed for the depth of the freshwater to be calculated via the technique of dye attenuation. The full details of this process are described in section 2.3.1. An experiment began when the freshwater was released and ended once the boundary current has propagated around the full perimeter of the tank. This was to ensure that the propagation of the current did not interfere with the conditions at the source. The experiments were filmed with a single video camera rigidly mounted on the superstructure of the turntable which filmed the current from above. The videos were recorded at 30 frames per second and were processed using an original script written in Digiflow (Dalziel, 2006). A green filter was attached to the camera to enhance the flow visualisation when analysing the data and a fluorescent light sheet was fitted beneath the bottom surface of the tank to illuminate the flow. The uniformity of the light sheet was ensured by measuring the light intensity over a period of time and averaging across the series to correct for any slight fluctuations that may have occurred.

2.2.1 Turbulent ambient

The experimental setup was modified for a subset of the experiments to introduce turbulence into the saltwater ambient. This was achieved via the addition of an oscillating grid into the main tank. The mixing grid was switched on once solid body rotation had been reached and the freshwater released after a further five rotation periods. Calibration experiments verified that this allowed enough time for the turbulent flow to become established. A diagram of the grid is shown in figure 2.7. The grid is rectangular with dimensions 982 mm $\times$768 mm and a mesh size $M = 5$ cm. The bars are square of size 10 mm and are made from aluminium to ensure rigidity during oscillation. The grid was held in position by a solid 20 mm diameter rod which was slightly offset from the centre of the grid to enable the experiments to be filmed from above. The oscillation of the grid was controlled via a motor with a range of oscillation frequencies $0 \leq n \leq 2$ Hz. The frequencies were calibrated using a movie of the oscillating grid at a known frame rate and were found to be within an error of $\sim 5\%$. The stroke height s of the grid could also be varied, though it remained fixed for this study at $s = 3$ cm. This value was chosen to reduce the effect of the interaction with the boundaries of the tank. The height of the grid in the tank could be adjusted and we use three different heights corresponding to distances from the surface of $z = 4, 8$ and 16 cm (recall that the fluid depth is fixed at 32 cm). This meant that for most experiments the grid

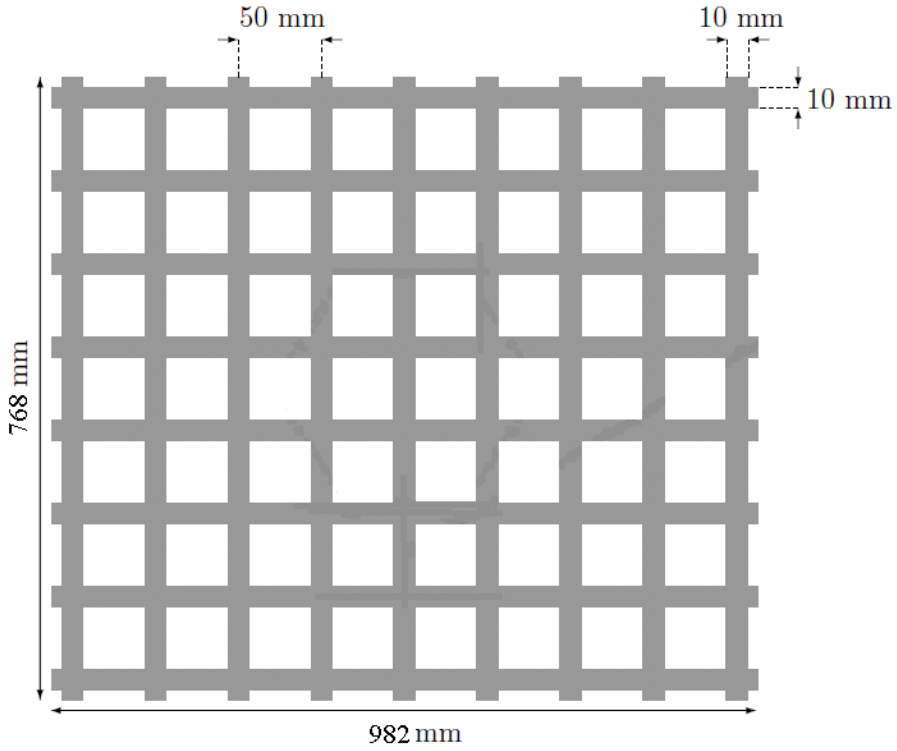

Figure 2.7 A diagram of the mixing grid used in the experiments.

oscillated beneath the current, though in some cases interference with the current propagation occurred. The experiments conducted with the mixing grid are discussed in chapters 9 and 10.

2.3 Experimental methods

Several methods were employed to obtain data in the experiments. The use of dye in the freshwater current allowed it to be distinguished from the saltwater ambient so that measurements of depth, width and current length could be made. Particle Image Velocimetry (PIV) was also used to give more details of the velocity field in the flow as well as vorticity and turbulence measurements. Figure 2.8 indicates the locations in the tank at which each set of measurements of the flow properties were made. We will refer back to this figure throughout this section as we outline the details of the methods employed to measure each of the flow properties. When measuring a property of the flow at a fixed location, the start time was taken to be the point at which the current reached that location. This allows the experiments to be compared across different parameter sets without the need to adjust for the difference

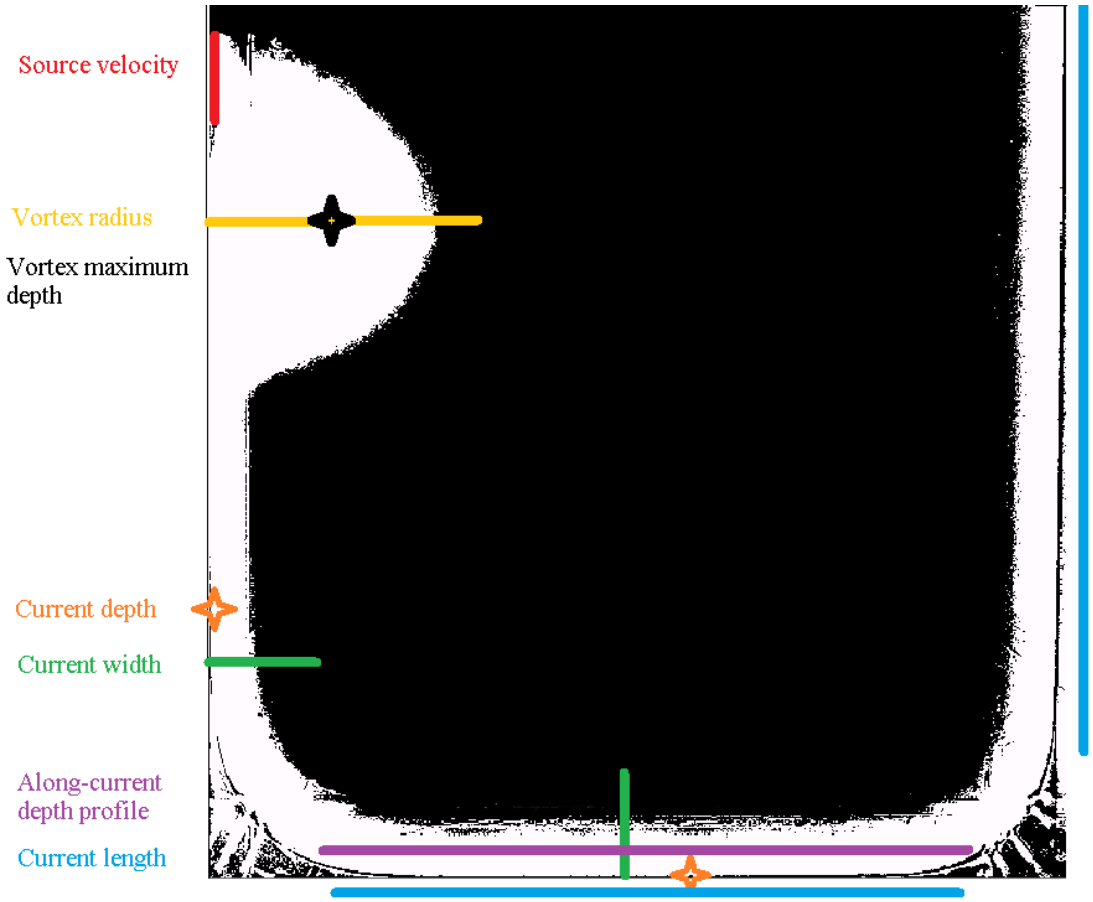

Figure 2.8 A plan view of the locations at which the flow properties indicated were measured during an experiment. The freshwater is white and the saltwater ambient black.

in the propagation velocities and thus the time taken to reach the point of measurement.

2.3.1 Dye attenuation

The technique of dye attenuation was used to provide measurements of the depth of the freshwater outflow. The freshwater was dyed with red fiesta food colouring and the density ρ_f was measured after the dye had been added, though since we used only small amounts ~ 0.05ml/L the change in density is negligible. The strength of the dye solution used varied depending on the expected depth of the current, with a higher concentration of dye required to visualise shallower currents. The depth of the current was approximated via the maximum depth scaling of TL, given by $h_{0z} = (2fQ/g')^{1/2}$. For shallow currents $h_0 \lesssim 2$cm, the dye concentration 0.05 ml/L was used. For intermediate depth currents $2 \lesssim h_0 \lesssim 4$cm a dye

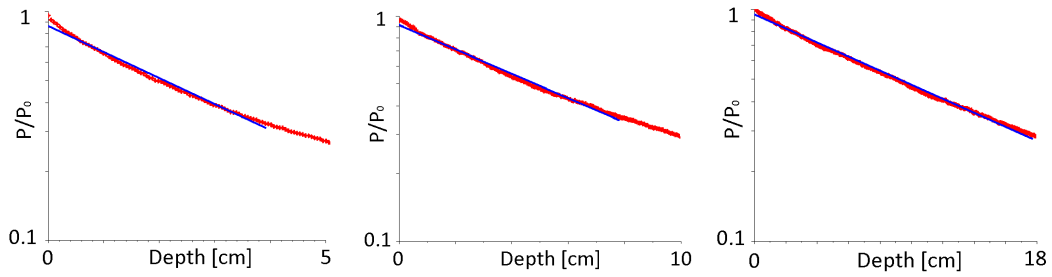

(a) $h_0 \lesssim 2$cm. **(b)** $2 \lesssim h_0 \lesssim 4$cm. **(c)** $h_0 \gtrsim 4$cm.

Figure 2.9 Calibration curves used in the dye attenuation method. The linear fit used for the conversion to depth measurements is also shown.

concentration of 0.02 ml/L was used and for deep currents $h_0 \gtrsim 4$cm the dye concentration was 0.01 ml/lL. These concentration values were chosen to ensure that the relationship between the current depth and the light intensity was approximately linear to allow for a simple conversion (Cenedese and Dalziel, 1998). Figure 2.9 plots the calibration curves for the three dye concentrations. The linear fit used for the conversion to depth measurements is also shown. Whilst the calibration curves give a small error in the conversion from light intensity to depth, larger errors occur from the experimental procedures when measuring the volumes of dye and freshwater. Estimates of experimental error were calculated in two ways: by assessing the repeatability of measurements and by calculating the level of uncertainty in the data. Several experiments were repeated across the full range of the experimental parameters and the error found to be $\pm 8\%$. For the dye attenuation technique the level of uncertainty in the measurements is small at $\sim 5\%$. Individual error bars for each experiment are given when presenting the data in later chapters.

2.3.1.1 Current depth

The current depth was measured experimentally at a fixed point at one second intervals for the duration of an experiment. Two positions were used for the the point of measurement, both of which are indicated in figure 2.8. The locations were chosen such that they remained as close to the source as possible, without interference from the outflow vortex. This was to maximise the time over which measurements could be made. The location closest to the vortex was used unless the vortex became so large that it extended beyond this point. In such an instance the second location was used. In both cases, the point of measurement is located at a distance $\sim 0.1 - 0.2$ cm from the wall of the tank. With the addition of the mixing grid

to the tank, the fixed point depth measurements were taken at position two. The distance from the tank wall at which the measurements were made varied from $0.1 - 1$ cm. They were taken as close to the wall as possible such that the motion of the mixing grid did not block the light source beneath the tank needed for the measurements. When comparing measurements between experiments the same position was used.

2.3.1.2 Current width

The current width was measured via the method of front-tracking. A cross-section was taken across the current and the dye concentration measured beginning at the wall of the tank and moving outwards until it fell below a threshold value. A polynomial curve was then fitted to the depth measurements along the cross-section and the distance from the wall at which it crossed zero taken as the current width. A twelfth order polynomial curve was used to provide sufficient accuracy for the width measurements, whilst also allowing for the process to be automated within Digiflow. This was the highest order polynomial fit available within Digiflow and was chosen to ensure that the fluctuations in the data were not over-simplified. The fitted polynomial was only used for the width measurements, as it led to the exaggeration of many features close to the boundary wall. For this reason the raw experimental data was used for any measurements of depth.

The location of the across current cross-sections used to estimate the current width are shown in figure 2.8. We use the same procedure as for the current depth: two locations, with the one nearest to the vortex being used whenever possible. We used two threshold values corresponding to a current depth of ~ 0.25 cm for intermediate and deep currents, and a depth of ~ 0.1 cm for a shallow current. The use of a fitted curve helped to remove fluctuations in the data. An example of the depth measurements along a cross-section and the corresponding fitted curve is shown in figure 2.10 for a typical experiment with a shallow current. The uncertainty in the width measurement differs depending on the experimental parameters (individual errors are given in later chapters) but we estimate it to be on the order of $\pm 10\%$ based on repetition of experiments.

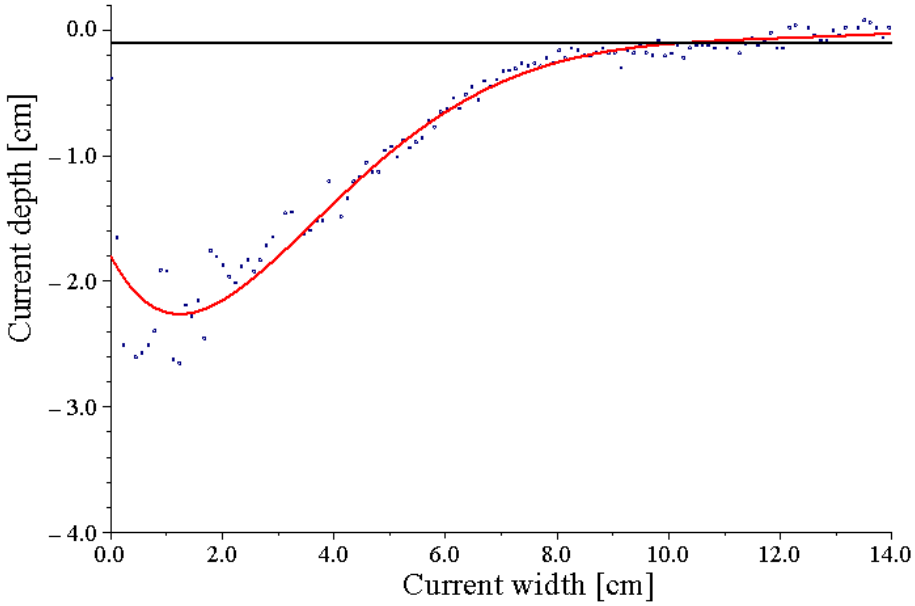

Figure 2.10 Depth measurements along a cross-section across the current and the fitted polynomial curve used to estimate the current width only. The horizontal line gives the threshold value with the crossing point used to estimate the width. The data shown is for a typical experiment with a shallow current.

2.3.1.3 Vortex radius and depth

The vortex radius was measured using the same method as the current width. The diameter of the vortex was measured in the direction perpendicular to the boundary wall, which provided a definitive boundary at which to begin the method of front-tracking. The location is shown in figure 2.8. The same threshold depths were used as for the current width and the errors were found to be of the same order at $\pm 10\%$. The location of the cross-section taken across the vortex is aligned with the point of maximum vortex depth, corresponding to the vortex centre. The point of maximum depth in the vortex is tracked in time throughout an experiment and the measurements of the vortex maximum depth made at this point via dye attenuation.

2.3.1.4 Current length measurements

The current length was measured along two edges of the tank as shown in figure 2.8. The current front was tracked as it progressed along the perimeter of the tank using the method of front-tracking described in section 2.3.1.2. Along current cross-sections were taken along the bottom and right-hand edges of the tank and the location of the current front identified by

the depth measurements falling below a threshold value. The same thresholds were used as for the current width and the errors were again found to be of the same order or magnitude at $\pm 10\%$. The round corners of the tank prevent measurements from being made and as a result there is a gap in the data. Analysis of the experimental videos indicates no major changes in the velocity as the current rounds the corner and thus we have no reason to expect any change in the trend identified before and after the corner.

2.3.1.5 Cross-sections

Depth cross-sections were taken through the flow at three key locations: along the current, across the current and across the vortex. The location of the along current cross-sections is displayed in figure 2.8. The vortex depth cross-sections were taken along the same path as the vortex radius measurements, while the across current cross-sections are taken at the same position as the second current width measurement, both of which are indicated in figure 2.8. For the along current cross-sections the depth profiles were measured at short intervals initially as the current rounded the corner of the tank to track the front progression. The vortex depth profiles were taken through the centre of the vortex defined by the point of maximum depth (see section 2.3.1.3). For each cross-section a twelfth-order polynomial curve was fitted to the data to provide a smooth profile and an estimate of its shape for comparison with the theory. This led to some exaggeration of features, in particular close to the tank boundary, which are discussed for individual profiles when presenting the data in later chapters.

2.3.2 Particle image velocimetry

The method of particle image velocimetry (PIV) was employed to provide a detailed analysis of the velocity field within the flow. Both the freshwater outflow and the saltwater ambient were seeded with Dantec PSP-50 polyamid seeding particles of diameter 50μm. The particles are neutrally buoyant in water of density $\rho_n = 1.03$ g cm^{-3}. When analysing the properties of the turbulence generated by the mixing grid (see chapter 9) the ambient fluid was of density $\rho_s = \rho_n$. For the experiments conducted with a freshwater outflow entering into a turbulent ambient (see chapter 10) the density varied from $0.99 \leq \rho_s \leq 1.07$. To ensure that the particles were evenly distributed in the flow the fluid in the freshwater reservoir and the saltwater ambient was vigorously stirred before beginning each experiment. The particles

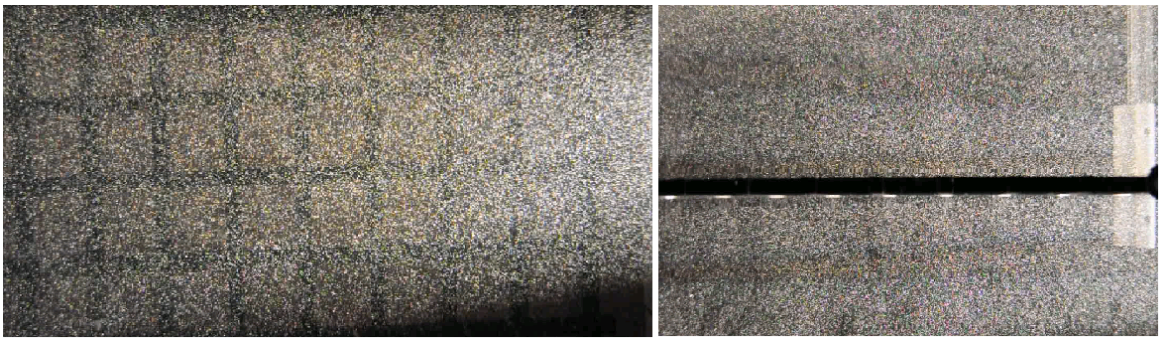

Figure 2.11 Images of the light-planes used to visualise the turbulent flow generated by the oscillating grid. In the left-hand image (horizontal plane) the grid is ~ 7 cm below the light plane, while it is visible in the right-hand image (vertical plane). For scale, the mesh size of the grid in the left-hand image is 5cm and the grid has a thickness of 1cm in the right-hand image.

were illuminated using an arc lamp which provided a thin sheet of light approximately 1 cm in thickness. The light source could be moved to provide illumination in the vertical (plane of grid oscillation) and horizontal (parallel to the grid and fluid surface) planes. The height of the horizontal plane could be adjusted across the full depth of the ambient fluid. Images from each plane with the particles and grid visible are shown in figure 2.11. The images are recorded at a rate of 24 fps and the motion of the particles is tracked between frames using the inbuilt Digiflow PIV algorithm (Dalziel, 2006) producing a velocity and vorticity field.

2.3.2.1 Turbulence

The properties of the turbulence were measured using PIV. The mixing grid was turned on and allowed to oscillate for ~ 300 seconds to allow the turbulence to become fully established. The images were then recorded at a rate of 24 fps for 60 seconds giving a sample size of 1440 images. The standard deviation of the velocity across all of the images was computed and the mean value of the resulting field used to give the turbulent velocity u^*. For $\mathbf{u_k}$ the velocity field of the k^{th} image, m the number of horizontal pixels in the measurement window and n the number of vertical pixels in the measurement window, the explicit formula for u^* is given by

$$\frac{1}{mn}\Sigma_{i=1,j=1}^{m,n}\left(\frac{1}{1440}\Sigma_{k=1}^{1440}\mathbf{u_k^2}-\left(\frac{1}{1440}\Sigma_{k=1}^{1440}\mathbf{u_k}\right)^2\right)_{i,j}^{1/2}. \tag{2.1}$$

The turbulent lengthscale was computed using the in-built Digiflow auto-correlation funtion (Dalziel, 2006). The auto-correlation of the velocity field, minus the mean field, was computed for each image. The arithmetic mean was then taken over all of the images and

normalised to produce an auto-correlation curve with a peak at 1. We then integrated the curve between the limits of $1/e$ and 1 to give the turbulent integral lengthscale l.

Measurements of the properties of the turbulence were made in both the horizontal and vertical planes. In the vertical plane the properties were averaged in the horizontal direction x at each height z above the grid. This provided measurements at small vertical resolution. In the horizontal plane the turbulent properties were averaged over both the x and y directions and the autocorrelation function computed radially. This provided more detailed measurements at a fixed height. We conducted several calibration experiments at intervals of $\sim$ 1cm across heights $2.75 \leq z \leq 15$ cm above the mid-point of the grid oscillation. The data from both the vertical and horizontal planes was used in the experimental results discussed in chapter 9.

2.3.2.2 Current velocity profiles

The method of PIV was also used to provide across-current velocity profiles. The cross-sections run from the tank wall outwards across the current and were measured at the same location as the current width measurements shown in figure 2.8. The horizontal light plane was used to illuminate the current at a depth of $0.5 - 1.5$ cm, which was seeded with particles. The velocity field was measured every 0.2 seconds and averaged over 5 measurements to give the velocity profiles. The current width was also estimated from the current velocity profiles. The distance was measured from the tank wall (where the profile begins) to the point at which the current velocity falls below 0.1 cm s^{-1}. A non-zero value was used to allow for the effect of entrainment from the stationary ambient. In the presence of turbulence, the turbulent rms velocity u^* was used as the threshold velocity to define the current width. The estimates of the current width obtained in this way were used to determine the effects of turbulence on the flow properties in chapter 10. The current width measurements obtained via front-tracking (as described in section 2.3.1.2) were used to provide measurements of the current width that are compared with the theory in chapters 4 and 8.

2.3.2.3 Source vorticity

Measurements of the velocity field close to the source were made using PIV. Cross-sections were taken across the width of the source opening at a depth of $0.5 - 1.5$ cm. The location of

the measurement field is shown in figure 2.8. The measurements were made as close to the source as possible at a distance of $\sim 0.1-0.2$ cm in front of the source opening. The velocity field was measured every 0.2 seconds and averaged over 5 measurements. The vorticity field was calculated as $\zeta = \partial v/\partial x - \partial u/\partial y$.

2.3.2.4 Vortex velocity field

Velocity profiles were measured across the outflow vortex in two directions: parallel to the boundary wall and perpendicular to the boundary wall. An example image of the velocity and vorticity field in the vortex is shown in figure 2.12 and the locations of the cross-sections indicated. In both cases, the profiles were taken through the vortex centre, which is identified by a region of approximately zero velocity. PIV measurements were taken every 0.2 seconds and averaged over five images. The light sheet was located close to the surface of the flow at a depth of $\sim 0.5-1.5$ cm. Using the vortex velocity profiles the vortex radius was estimated using a similar method to the current width in section 2.3.2.2. The distance from the peak velocity closest to the boundary wall (positive or negative depending on whether the parallel or perpendicular profiles were used) to the point at which the velocity reaches zero was used to provide an estimate of the vortex radius. The measurements obtained in this way are used in chapter 10 when investigating the effects of turbulence on the vortex properties. The radius measurements obtained via the method of front-tracking (discussed in section 2.3.1.3) are used for the comparison with the theory in chapters 6 and 8.

The velocity profiles across the vortex are found to be approximately linear (see chapter 6) and therefore the gradient of the profiles was used as an estimate for the vorticity ratio in chapters 6 and 8. A linear curve was fitted to the experimental profiles at each timestep between the points of maximum positive and maximum negative velocity. The gradient of the curve was used to provide an estimate of the time-development of the vorticity ratio. The velocity field was also measured across the entire area of the vortex at a depth of $\sim 0.5-1.5$ cm, which allowed measurements of the mean vorticity in the vortex to be made. The velocity profiles measured across the vortex were used to establish the edge of the vortex at the points of maximum positive and maximum negative velocity. A rectangular box was then created around the centre of the vortex and the mean vorticity defined by $\zeta = \partial v/\partial x - \partial u/\partial y$ measured within the box. An example of such a box is shown in figure 2.12. The measurements were made every 0.2 seconds and averaged over five measurements.

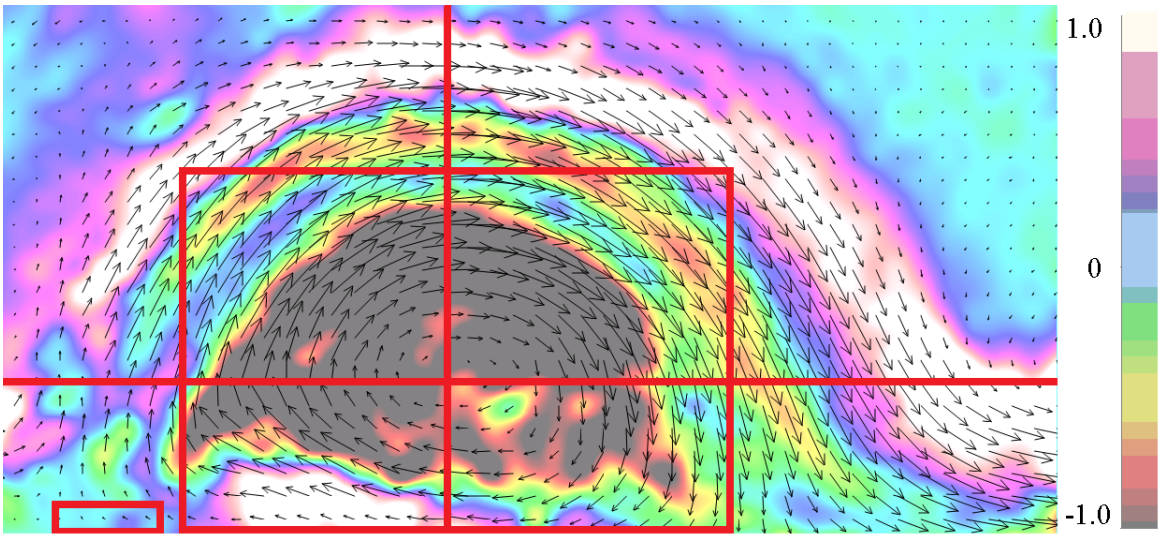

Figure 2.12 An example of the vortex velocity and vorticity field with the locations of the cross-sections and the area where the mean vorticity measurements were made indicated in the image. The location of the source is also shown which has a width of 5cm for scale. The vorticity is in rad s^{-1} and a scale bar is shown. The arrows indicate the direction of the velocity field with their size proportional to the magnitude of the velocity. The velocity scale is arbritrary.

2.3.2.5 Vortex depth

Vertical velocity profiles were also measured through the centre of the vortex. The vortex was illuminated in the vertical plane at a distance $2-4$ cm downstream of the source opening. PIV measurements were made every 0.2 seconds and averaged over five values. The velocity profiles were measured passing through the approximate centre of the vortex, defined as the point of maximum vortex depth. The profiles show the horizontal velocity in the y-direction moving away form the source for the upper 16 cm of the fluid. The vortex depth was estimated from the vertical velocity profiles as the point at which the velocity decreased below a threshold value. This value was taken to be 0.1 cm s^{-1} for the experiments with a quiescent ambient and u^* for the experiments with a turbulent ambient. The estimates of the vortex depth obtained in this way were used to determine the effects of the turbulent ambient on the vortex properties in chapter 10. The vortex maximum depth measurements obtained via the dye attenuation technique (see section 2.3.1.3) are used in the comparison with the theory in chapters 6 and 8.

Rotation rate f *[*s^{-1}*]*	$0 \leq f \leq 2$
Volume flux Q *[*$cm^3\ s^{-1}$*]*	$42 \leq Q \leq 100$
Reduced gravity g' *[*$cm\ s^{-2}$*]*	$0 \leq g' \leq 72.6$
Source depth H_0 *[cm]*	$2 \leq H_0 \leq 4$
Source width D *[cm]*	$2.5 \leq D \leq 5$

Table 2.1 Summary of the ranges of the independent parameters in the group (1) experiments.

Rotation rate f *[*s^{-1}*]*	$0.25 \leq f \leq 1.5$
Volume flux Q *[*$cm^3\ s^{-1}$*]*	$16.5 \leq Q \leq 40$
Reduced gravity g' *[*$cm\ s^{-2}$*]*	$1.5 \leq g' \leq 64.6$
Grid depth z *[cm]*	$4 \leq z \leq 16$

Table 2.2 Summary of the ranges of the independent parameters in the group (2) experiments.

2.4 Parameter ranges

The experiments conducted can be divided into four groups: (1) dye attenuation for a quiescent ambient, (2) dye attenuation for a turbulent ambient, (3) PIV for turbulent properties and (4) PIV with an outflow. We summarise the experimental parameters and the ranges considered for each group of experiments below.

For group (1) a total of 52 experiments were conducted across a full range of the five experimental parameters: reduced gravity g', rotation rate f, source volume flux Q, source depth H_0 and source width D. The values of the parameters are displayed in table 2.1. Measurements of the current depth, current width, current length, vortex maximum depth and vortex radius in a quiescent ambient were obtained from this group of experiments.

For group (2) a total of 32 experiments were conducted across a range of the four experimental parameters: reduced gravity g', rotation rate f, source volume flux Q and grid depth z. The values of the parameters are displayed in table 2.2. Measurements of the current depth in a turbulent ambient were obtained from this group of experiments. They were also used to analyse the ability of the turbulence to halt the progression of the current.

For group (3) a total of 78 experiments were conducted, 46 for non-rotating turbulence and 32 with rotation. The experimental parameters are: rotation rate f, distance from the grid z and stroke frequency n. The values of the parameters are displayed in table 2.3. Mea-

Rotation rate f [s^{-1}]	$0 \leq f \leq 2$
Distance from grid z [cm]	$2.75 \leq z \leq 15$
Stroke frequency n [Hz]	$0.5 \leq n \leq 2$

Table 2.3 Summary of the ranges of the independent parameters in the group (3) experiments.

Rotation rate f [s^{-1}]	$0.5 \leq f \leq 1$
Volume flux Q [$cm^3\ s^{-1}$]	$48 \leq Q \leq 75$
Reduced gravity g' [$cm\ s^{-2}$]	$1.6 \leq g' \leq 16.5$
Grid depth z [cm]	$4 \leq z \leq 16$
Stroke frequency n [Hz]	$0 \leq n \leq 1$

Table 2.4 Summary of the ranges of the independent parameters in the group (4) experiments.

surements of the turbulent rms velocity and the turbulent integral lengthscale were obtained from this group of experiments.

Finally, for group (4) a total of 60 experiments were conducted across a large range of the five experimental parameters: reduced gravity g', rotation rate f, source volume flux Q, stroke frequency n and grid depth z. The values of the parameters are displayed in table 2.4. Measurements of the source velocity field, current velocity field and vortex velocity field in a quiescent ambient were obtained from these experiments. They were also used to obtain measurements of the current velocity field, current width, vortex velocity field, vortex radius and vortex depth in a turbulent ambient.

2.5 Source conditions

The design of the source structure is critical to our aim of creating a better representation of a freshwater outflow entering into the ocean in the laboratory. We have already discussed the parameter R_d/D, for $R_d = \sqrt{g'H_0}/f$ the source deformation radius and D the source width, in chapter 1 with the experimental setup giving values in the range $0.2 \leq R_d/D \leq 4.8$, which compare favourably with those of the Rhine $R_d/D \sim 5$ and the Elbe $R_d/D \sim 2$. Here we present further analysis of the source conditions seen in the experiments and how they compare to the natural environment.

The source was designed to discharge the fluid horizontally as is seen in nature, whilst also minimising momentum-flux effects to prevent the occurrence of a jet and reduce mixing. For a large source momentum-flux there will be significant mixing between the freshwater outflow and the saltwater ambient near to the source. Since we model the flow as a two-layer fluid with zero mixing between the layers in the theory (see e.g. chapter 3), we sought to reduce the occurrence of mixing by reducing the source momentum-flux. We define the source momentum flux by Q^2/A where Q is the volume flux of the freshwater and A the area of the source opening. The balance between momentum and rotation is represented by the lengthscale $L_B = (Q^2/Af^2)^{1/4}$. We also define a source buoyancy flux $g'Q$ where g' is the reduced gravity and a lengthscale $L_M = (g'Q/f^3)^{1/4}$, which represents a balance between buoyancy and rotation. The ratio of the two lengthscales L_M/L_B gives the balance between buoyancy and momentum at a given rotation rate. The values achieved in our experiments range from $0.34 \leq L_B/L_M \leq 1.91$, while for real rivers we see values of ~ 0.1 for the Amazon to ~ 1 for the Nile and Yellow River. The values for the Rhine and Elbe are ~ 0.6 and ~ 0.3 respectively. The conditions at the source therefore provide a good representation of the natural environment across several parameters.

Horner-Devine et al. (2006) define an inertial radius $L_i = V_s/f$ where $V_s = Q/A$ is the velocity of the fluid released from the source. They find that the inflow momentum determines the offshore migration of the outflow bulge with the location of the vortex centre proportional to L_i. The inertial radius also characterises the distance at which the outflow from the source is turned to the right by Coriolis forces. Figure 2.13 displays plan-view images of the initial release of the freshwater from the source for two different values of L_i. The images in figure 2.13 show the initial effect of the Coriolis force to turn the current to the right of the outflow. For the smallest value of $L_i = 3.8$ cm the current turns to the right shortly after leaving the source. We estimate the turning radius by the distance from the boundary to the centre of the current once it is parallel to the wall, which gives a distance of $\sim 4 \pm 2$ cm in this instance. For the larger value of $L_i = 14.8$ cm the current is also turned to the right of the source, but over a larger distance of $\sim 12 \pm 2$cm. In both cases, the current is turned by the Coriolis parameter at a distance approximately equal to the inertial radius L_i. The same behaviour is seen across the full experimental parameter range with $1.8 \leq L_i \leq 20$ cm.

We conclude our analysis of the source conditions by considering the velocity of the discharging freshwater. The velocity field at the source following the initial release of the freshwater was measured using the method of PIV. The measurements are made at a distance

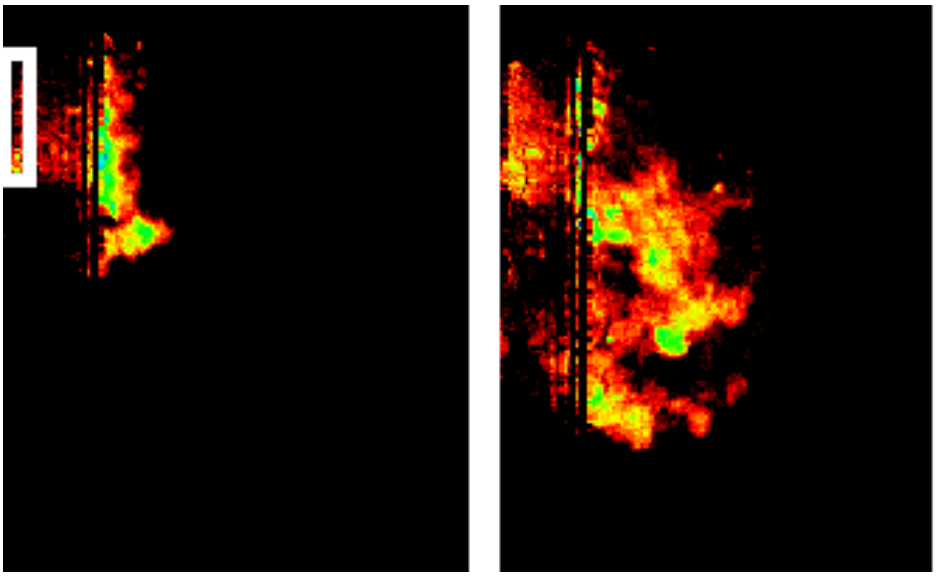

(a) $L_i = 3.8$ cm. The images are taken at 1 second (left-hand image) and 2 seconds (right-hand image) after the release of the freshwater. The source width is $D = 5$cm.

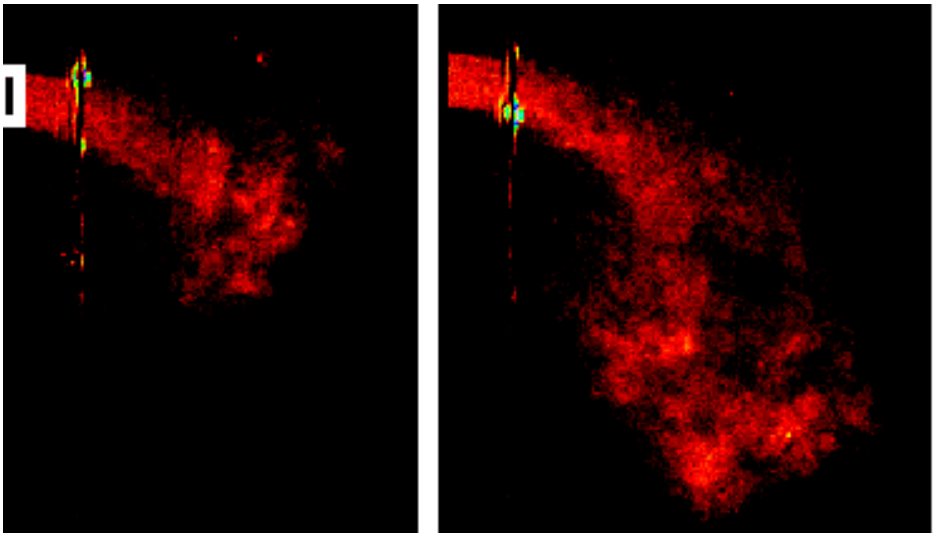

(b) $L_i = 14.8$ cm. The images are taken at 2 second (left-hand image) and 4 seconds (right-hand image) after the release of the freshwater. The source width is $D = 2.5$cm.

Figure 2.13 Plan-view images of the initial release of the freshwater from the source for two different values of the inertial radius L_i. The location of the source is indicated by the white box and its size given for each image to provide scale.

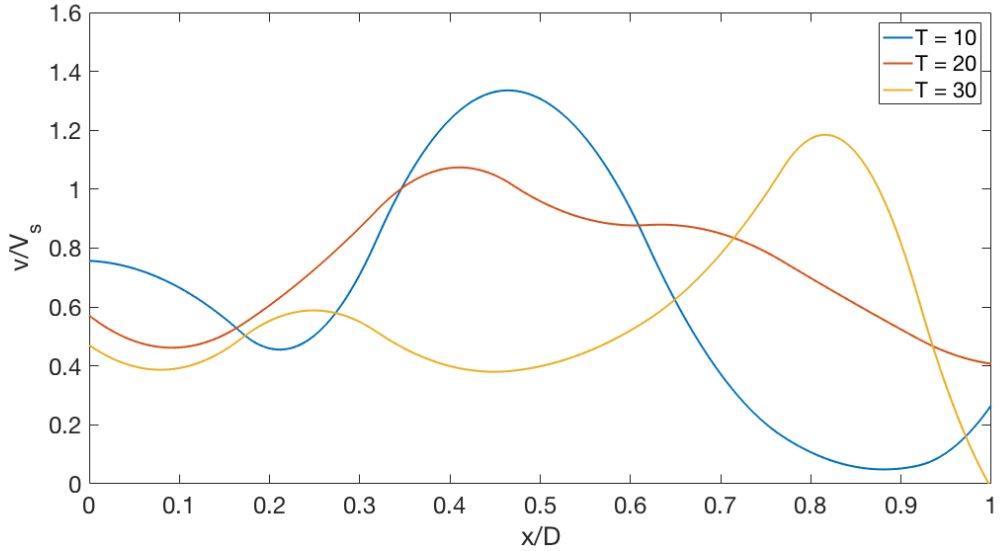

Figure 2.14 Across-source velocity profiles for the velocity in the direction perpendicular to the source. The distance across the source is non-dimensionalised by the source width D, time is non-dimensionalised by the rotation rate f and the velocity is scaled with the expected source velocity $V_s = Q/A$.

$\sim 0.1 - 0.2$ cm in front of the source opening across its full width. Figure 2.14 displays the source velocity profiles for v (the velocity in the direction perpendicular to the source opening) for a typical experiment at three different times. The distance across the source is non-dimensionalised by the source width D, time is non-dimensionalised by the rotation rate f and the velocity is scaled with the expected source velocity $V_s = Q/A$. The profiles show a peak velocity towards the centre of the source opening which is of the same magnitude as the expected source velocity V_s. The velocity decreases towards the edges of the opening due to the effect of shear between the freshwater and the stationary ambient. The variations over time are caused by interference from the outflow vortex which is a constraint of measuring the velocity field outside of the source, rather than at the source opening and is discussed in more detail in chapter 4. There is reasonable agreement between the peak source velocity and V_s across three different times which shows that the source conditions are as expected and that they remain relatively consistent during an experiment.

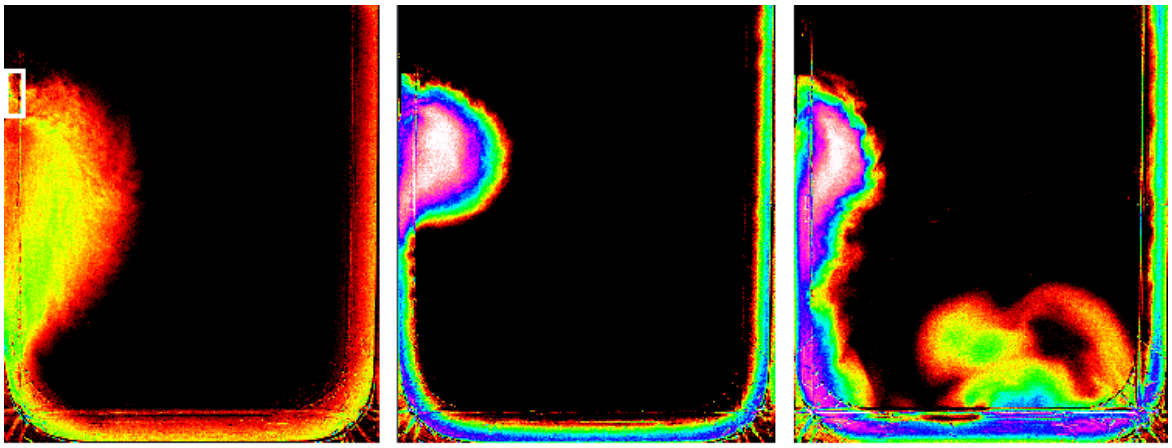

Figure 2.15 Aerial snapshots of three experiments at low ($I^* = 0.33$), intermediate ($I^* = 1.23$) and high ($I^* = 4.08$) values of I^*. The images were taken at the end of the experiment once the current had propagated around the full perimeter of the tank. The location of the source is indicated by a white box and is the same for each image. The ambient is represented by black and the freshwater by the arbritrary colour scale, with white the deepest and red the shallowest.

2.6 Flow classification

In each experiment it is possible to identify two persistent features present in the flow: an anticyclonic vortex generated next to the source and a current propagating around the boundary of the tank. The vortex rotates anticyclonically to oppose the cyclonic rotation of the tank and thus conserve the angular momentum. Three different regimes are present in the experiments which can be classified according to the dimensionless parameter I^*, defined as the ratio of the current aspect ratio (depth divided by width) and the source aspect ratio. It is given by

$$I^* = \frac{fQ^{1/5}D^{4/5}}{2^{1/5}g'^{3/5}H_0^{4/5}}. \tag{2.2}$$

Figure 2.15 shows a plan view of the flow taken at the end of three different experiments. The images are representative of the typical flow behaviour at low ($I^* = 0.33$), intermediate ($I^* = 1.23$) and high ($I^* = 4.08$) values of I^*. The coloured area represents the freshwater (arbritrary scale) and the black area represents the saltwater ambient. The experimental parameters for the three runs are given in table 2.5.

The visualisations in figure 2.15 show that the flow is qualitatively different for different values of I^*. For low values of I^*, the outflow vortex is very large and elongated towards the bottom edge of the tank. The circulation within the vortex is also relatively weak compared to the other regimes and the vortex almost acts as an extension of the boundary current.

I^*	Q [cm^3 s^{-1}]	f [s^{-1}]	g' [cm s^{-2}]	H_0 [cm]	D [cm]
0.33	75	1	70.9	2	5
1.23	62	1.5	14.9	2	5
4.08	97	1.5	2.3	2	5

Table 2.5 Experimental parameters for the experiments shown in figure 2.15.

For intermediate values of I^*, the vortex has a smaller surface area, but has a shape that more closely resembles a circle. The circulation within the vortex is much stronger and the vortex is in general much larger than the width of the current. Finally, for high values of I^*, the vortex becomes unstable as it sheds smaller vortices that are then carried along with the propagating boundary current. The large disturbance to the boundary current along the bottom edge of the tank in the third image of figure 2.15 is an example of a smaller vortex that has been shed from the main outflow bulge. The vortex can become indistinguishable from the boundary current for the highest values of I^*.

The parameter I^* is similar to the one used in the work of TL, $I = \frac{fQ^{1/5}}{2g'^{3/5}}$, which was defined as the aspect ratio of the current (depth divided by width). With the introduction of changing source conditions in our experiments, the source aspect ratio $A_s = H_0/D$ represents a second dimensionless parameter that we may expect to play a role in determining the flow dynamics. The parameter I^*, as defined above, combines both dimensionless parameters with a specific choice of curve in the two-dimensional parameter space. The reasoning behind this choice of curve is based on the work of TL. They found three distinct flow regimes which occurred at low ($I \sim 0.05$), intermediate ($I \sim 0.30$) and high ($I \sim 2.76$) values of I. Their classification was based on the relative size of the outflow vortex and the boundary current. Using the scalings for the current depth h_{0z} and the current width w_{0z} used by TL the parameters I and I^* are related by

$$I^* = I(\frac{2D}{H_0})^{4/5} = (\frac{h_0 D}{w_0 H_0})^{4/5} = (\frac{A_c}{A_s})^{4/5}, \tag{2.3}$$

where $A_c = h_{0z}/w_{0z}$ is the current aspect ratio. Therefore, the parameter I is related to the current aspect ratio by $I = (A_c/2)^{4/5}$ and thus we have chosen the same scaling for the souce aspect ratio of $(A_s/2)^{4/5}$ when defining I^*.

For the three source openings used in the experiments, the source aspect ratio takes only two values at $A_s = 0.4$ and $A_s = 0.8$ (see figure 2.6). Therefore, since the value only

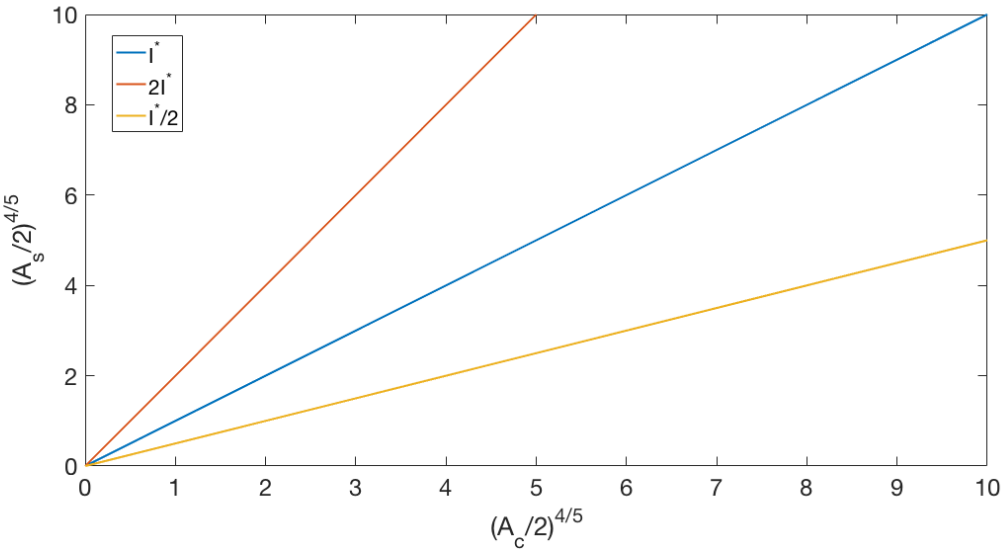

Figure 2.16 Example curves in the two-dimensional paramter space defined by the current aspect ratio A_c and the source aspect ratio A_s.

varies by a factor of two the choice of a specific curve when defining I^* is not unreasonable. Were the source aspect ratio allowed to vary over a larger range in future experiments, the relationship between the two aspect ratios of the current and the source would need to be investigated further. Figure 2.16 plots the specific curve used when defining I^* alongside possible alternatives based on the source aspect ratio changing by a factor of two.

The parameter I^* is effectively telling us how the flow changes from the initial conditions at the source. Initially the flow knows the fixed source conditions with depth H_0 and width D, but will quickly adjust to the geostrophic depth h_{0z} shortly after leaving the source and will no longer be constrained by the source conditions. In general, for a small value of I^* we expect a shallow and wide current and for large values of I^* the current will be much deeper and narrower.

A qualitative analysis of all of the experiments reveals the approximate boundaries of the values of I^* between each regime. For those experiments in the regime of low I^* the values range from $0.15 \leq I^* \leq 0.50$. Those in the second regime of intermediate I^* have values in the range $0.39 \leq I^* \leq 1.73$. Finally, the experiments in the third regime of high I^* have values in the range $1.48 \leq I^* \leq 5.61$. There is a slight degree of overlap between the values seen in the three regimes which is due to the qualitative nature of their description. We estimate the transition from an elongated to a contracted vortex for $0.39 \leq I^* \leq 0.50$

and the transition to instability for $1.37 \leq I^* \leq 1.73$. The value of the parameter I^* will be used throughout this thesis to refer to the experiments being considered. The experimental data are grouped into low, intermediate and high I^* regimes and the properties of the flow investigated for each of the regimes.

Chapter 3

Steady state model for rotating gravity currents

3.1 Problem description

When estuarine water is discharged into the coastal zone, gravity-driven surface flows can be established as a result of the density difference between the river water and the ocean. These flows are often of a sufficiently large scale that the current dynamics are affected by the Coriolis force arising from the rotation of the earth. This causes the discharged freshwater to be confined near to the coast, where it will propagate as a coastal gravity current. In this chapter we introduce a theoretical model to describe the properties of a rotating gravity current in a steady state.

We have previously discussed experiments by TL, which examined rotating gravity currents in the laboratory. Here we present the key results of their geostrophic model for a steady state current under the assumption of zero PV. They find scalings for the maximum current depth h_{0z}, maximum current width w_{0z}, and constant current velocity u_{0z} in terms of the experimental parameters, which are

$$h_{0z} = (\frac{2fQ}{g'})^{1/2}, \tag{3.1}$$

$$w_{0z} = (\frac{8g'Q}{f^3})^{1/4}, \tag{3.2}$$

$$u_{0z} = \frac{3}{2^{9/4}}(fg'Q)^{1/4}. \tag{3.3}$$

They also obtain an equation for the current profile, $h_z(y)$ where y is the across-current coordinate, given by

$$h_z = h_{0z} - \frac{f^2}{2g'}y^2. \tag{3.4}$$

We seek to build on the work of TL by constructing a steady state model for the boundary current in the case of a finite potential vorticity source. The motivation for the introduction of a finite potential vorticity source arises from the fact that real outflows, such as rivers, have a finite value of PV. As discussed in chapter 2, the experimental setup is based on that of TL, but with a modified source structure that better represents the natural environment. The freshwater is injected horizontally in the experiments, as seen in nature, in contrast to the vertical source used by TL. The introduction of a horizontal source of finite depth introduces a finite potential vorticity into the flow and the effects of this will be the focus of our investigation as we seek to answer the first key question of this thesis: what is the effect of finite PV on the flow?

An alternative approach to modelling a buoyant outflow in a rotating environment is presented by Pichevin and Nof (1997), hereafter PN. The main focus of their work was to show that the growth of the bulge next to the source is a result of the imbalance of momentum in the system and the slow offshore migration of the bulge is required to balance the momentum-flux lost in the current downstream. The key part of the work of PN which we are interested in here is the use of an upstream Bernoulli condition to fix the constant velocity of the boundary current along the wall. Their model relies on knowing the value of the upstream Bernoulli $B^*_{PN} = 1 + Fr_{up}/2$, for Fr_{up} the upstream Froude number, and they carry out numerical simulations of the flow for different values of this parameter.

Alongside our extension of the TL model to incorporate a finite PV source, we also present an alternative steady state model for the current that allows for a finite current velocity along the boundary wall. The use of a Bernoulli condition, as in the work of PN, is one way in which this velocity can be fixed. The motivation for the inclusion of this second model can be seen in the experimental results in chapter 4 where the PIV data show that the velocity close to the wall, ~ 0.1 cm, is non-zero and can be as large as the peak velocity in the current in some instances. We first introduce a steady state model for a finite PV source with a general wall velocity, before then considering the specific cases of a zero and a finite value fixed by an upstream Bernoulli condition at the source. The models will then be compared with one another and their zero PV counterparts to determine the effect that finite

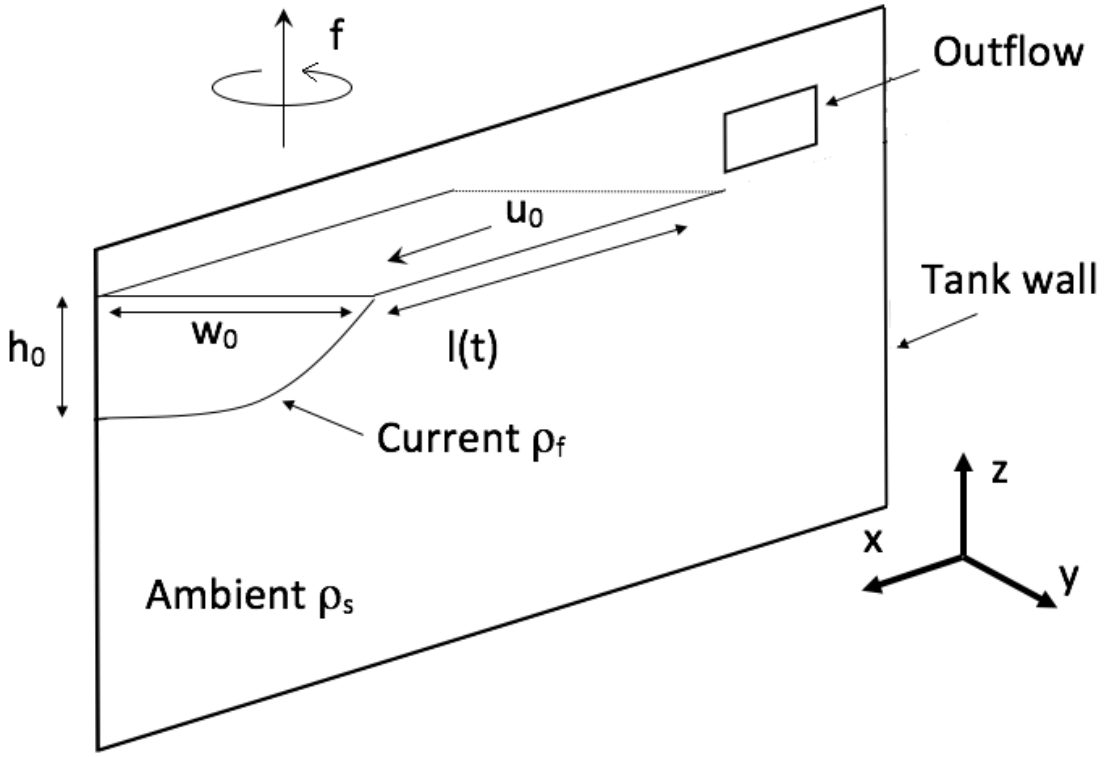

Figure 3.1 The nomenclature employed to develop the theoretical model for the current.

PV has on the properties of the steady state current.

3.2 Theoretical model

We consider the steady state of a buoyancy-driven surface current alongside a vertical solid boundary. In this instance we are concentrating on the motion of the current along the wall of the tank, rather than the outflow vortex occuring at the source. Separate theoretical models for the outflow vortex will be presented in chapters 5 and 7. The geometry and coordinate system used to describe the problem is shown in figure 3.1. The rectangular nature of the tank is neglected and instead we model the boundary as a single straight wall with a Cartesian coordinate system as indicated in the figure.

The new and critical aspect of this problem is the modification of the source structure from which the freshwater is discharged. In previous work, such as that of TL, the source is

modelled as a zero potential vorticity outflow, which is an assumption based on the small size of the source allowing it to be modelled as a delta function (Gill et al. 1979). In our experiments, the source is of finite depth, ranging from 2 cm $\leq H_0 \leq$ 4 cm, meaning that the assumption of zero PV is invalid and we must instead model a finite PV source.

3.2.1 Finite PV general model

We begin in the same way as the zero PV model of TL. The freshwater current and the saltwater ambient are modelled as a two-layer fluid with zero mixing between the layers. This allows the use of the shallow water equations discussed in chapter 1, modified for a two-layer flow. We assume that the velocity components in the y- and z-directions are negligible in comparison to the velocity u in the x-direction. We also neglect all variations in the x-direction so that the velocity has the form $\mathbf{u} = (u(y), 0, 0)$. This also means that for now we are neglecting the head of the current. The pressure p is given by the hydrostatic relation

$$p = \begin{cases} g\rho_f(\eta - z), & -h < z < \eta \\ g\rho_f(h+\eta) - g\rho_s(z+h), & z < -h \end{cases} \tag{3.5}$$

where $\eta = \eta(y)$ represents the free-surface elevation above $z = 0$, h is the depth of the current, ρ_f is the current density for $z > -h$, ρ_s is the ambient fluid density for $z < -h$ and the pressure is taken to be zero at the free surface. We assume that the saltwater ambient is infinitely deep so that there is no interaction between the current and the bottom of the tank. We also assume that the current is in geostrophic balance on an f-plane (see chapter 1), giving the following relation:

$$f\rho_f u = -\frac{\partial p}{\partial y}, \tag{3.6}$$

where f is the Coriolis parameter. This assumption relies on a small Rossby number, where $Ro = U/Lf$ for a typical length scale L and velocity scale U, and that the motion does not extend over significant changes in latitude. Both assumptions are valid for an outflow such as the Rhine or Elbe which match the parameter regimes seen in our experiments. In the ambient fluid, which we have taken as infinitely deep, there will be no flow and therefore the pressure gradient is zero for $z < -h$. Using (3.5) the pressure gradient in the current, for $-h < z < \eta$, is given by

$$\frac{\partial p}{\partial y} = (\rho_s - \rho_f) g \frac{\partial h}{\partial y}. \tag{3.7}$$

Finally, we obtain the current velocity from (3.6),

$$u = -\frac{g'}{f}\frac{\partial h}{\partial y}, \tag{3.8}$$

where $g' = g(\rho_s - \rho_f)/\rho_f$ is the reduced gravity. Under the shallow water approximation the potential vorticity in the current is defined by

$$q = \frac{\zeta + f}{h}, \tag{3.9}$$

where $\zeta = -\partial u/\partial y$ is the local vorticity. Conservation of potential vorticity says that the value of q must remain fixed at its initial uniform and constant value q_0. Replacing q by q_0 in (3.9) and substituting from (3.8) for u, we obtain a differential equation for the current depth:

$$\frac{\partial^2 h}{\partial y^2} - (\frac{q_0 f}{g'})h = -\frac{f^2}{g'}. \tag{3.10}$$

The initial PV q_0 will be fixed by the source conditions. In the model of TL the source used in their experiments is so small that they approximate the intial PV by $q_0 = 0$. Here, we wish to investigate the effect that a finite value of PV has on the flow and therefore take $q_0 \neq 0$. Integrating (3.10) with respect to y we obtain the general solution

$$h = \frac{f}{q_0} + A\cosh(y(\frac{q_0 f}{g'})^{1/2}) + B\sinh(y(\frac{q_0 f}{g'})^{1/2}), \tag{3.11}$$

where A and B are constants to be determined by the boundary conditions. The first boundary condition imposed is that the maximum depth h_0 is obtained alongside the boundary at $y = 0$. This is the same as used by TL and fixes the constant A. The second boundary condition arises by considering the velocity alongside the boundary wall at $y = 0$. The assumption of geostrophy provides a relationship between the current depth and the velocity as given in (3.6), and therefore for a general wall velocity u_l we are able to solve for B. Since we are using an inviscid model for the flow, viscosity is neglected and thus we do not necessarily require the wall velocity to be zero. We will see in our analysis later that u_l must be constant according to the x-momentum equation and depending on our interpretation of the initial conditions of the current, it can be both zero or finite. We therefore continue with u_l as a free parameter at this point. Imposing both of the boundary conditions gives the solution

$$h = \frac{f}{q_0} + (h_0 - \frac{f}{q_0})\cosh(y(\frac{q_0 f}{g'})^{1/2}) - u_l(\frac{f}{q_0 g'})^{1/2}\sinh(y(\frac{q_0 f}{g'})^{1/2}). \tag{3.12}$$

3.2.1.1 Current depth profile

The steady state current depth profile for a source of finite PV, q_0, is given by (3.12). We next determine the maximum current depth h_0. Assuming that the width and depth of the current at any downstream location remain constant in time, continuity requires that the volume flux from the source must be equal to the volume flux across any cross-section of the current. Expressed mathematically, this means

$$Q = \int_0^{w_0} h(y)u(y)dy \tag{3.13}$$

where w_0 is the maximum current width which is given by the point at which the interface intersects the fluid surface, i.e. when $h(y = w_0) = 0$. Using the geostrophic relation (3.8) and substituting into (3.13) we have

$$Q = \int_0^{w_0} h(y)u(y)dy = \int_0^{w_0} -\frac{g'}{f}\frac{\partial h}{\partial y}hdy = [-\frac{g'}{2f}h^2]_0^{w_0} = \frac{g'}{2f}h_0^2, \tag{3.14}$$

which gives the maximum current depth

$$h_0 = (\frac{2fQ}{g'})^{1/2}. \tag{3.15}$$

We can see from (3.14) that for any depth profile h that obtains a maximum value of h_0 along the boundary at $y = 0$, we will always obtain the same value for the maximum current depth under the asumption that the current is in geostrophic balance. It is therefore no suprise that our result here agrees with previous models (eg. TL, Avicola and Huq 2002, Lentz and Helfrich 2002, Horner-Devine et al. 2006). The result also shows that the maximum current depth is unaffected by the initial PV at the source. Now that since h_0 is known we non-dimensionalise the current depth profile in (3.12) by h_0 to give

$$\frac{h}{h_0} = \frac{1}{Q^*} + (1 - \frac{1}{Q^*})\cosh(\sqrt{Q^*}\frac{y}{R_{dc}}) - U_l\frac{1}{\sqrt{Q^*}}\sinh(\sqrt{Q^*}\frac{y}{R_{dc}}) \tag{3.16}$$

where $Q^* = q_0/(f/h_0)$ is the dimensionless initial PV, $U_l = u_l/\sqrt{g'h_0}$ is the dimensionless wall velocity and $R_{dc} = \sqrt{g'h_0}/f$ is the current deformation radius. We analyse the effect of the initial PV on the shape of the current depth profile given in (3.16) by plotting profiles at different values of Q^*. Figure 3.2 displays depth profiles for three such values of Q^* where the wall velocity is fixed at an arbitrary non-zero value $U_l = 0.5$. Similar profiles are seen

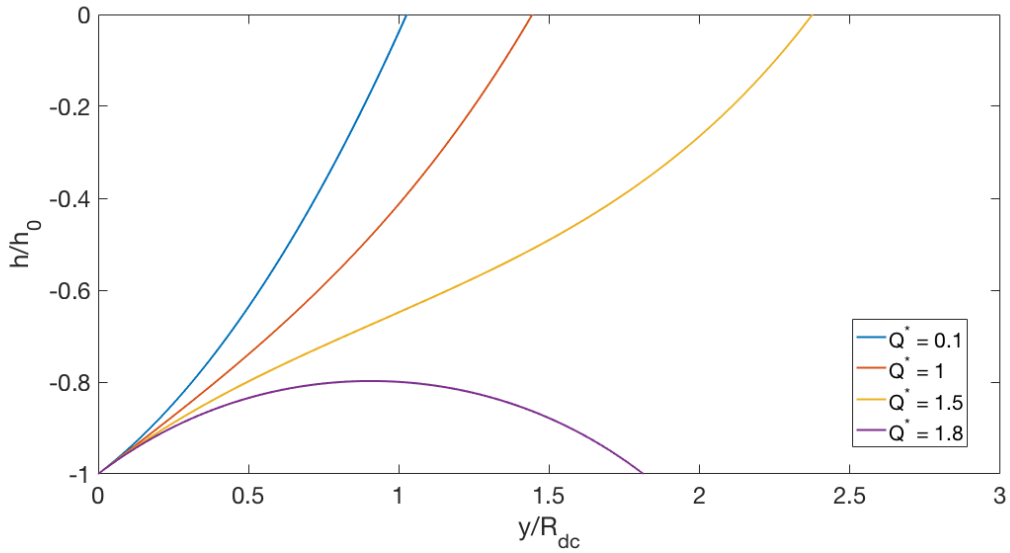

Figure 3.2 The dimensionless current depth profile for four different values of the dimensionless initial PV Q^*. The wall velocity $U_l = 0.5$ is held constant.

whilst varying Q^* for different fixed values of U_l.

As the value of the initial PV increases we see an increase in the maximum current width. The maximum current depth remains the same as we have shown above that it is independent of the initial PV. Furthemore, there is a shift in the shape of the current profile at the value of $Q^* = 1.5$ switching from a convex profile to one which is 's-shaped'. We also note that if the value of Q^* becomes too large in comparison to U_l the depth profile becomes non-physical as seen for $Q^* = 1.8$ where the profile never intersects the fluid surface. This is a result of the continued increase in the current width as Q^* increases, with the width reaching infinity at a finite limiting value of Q^*. As the current width tends to infinity, the depth profile no longer intersects the surface at $h = 0$ and therefore a physical solution for the depth profile no longer exists. Physically, the increase in the initial PV leads to an increase in the current width, whilst the current depth remains fixed. Since there is only a finite volume of freshwater in the system, the depth profile shape must tend towards a right-angle shape to allow for the increase in the width towards infinity. Eventually, a critical point is reached where the depth-profile switches direction (as for $Q^* = 1.8$ in figure 3.2) and becomes non-physical.

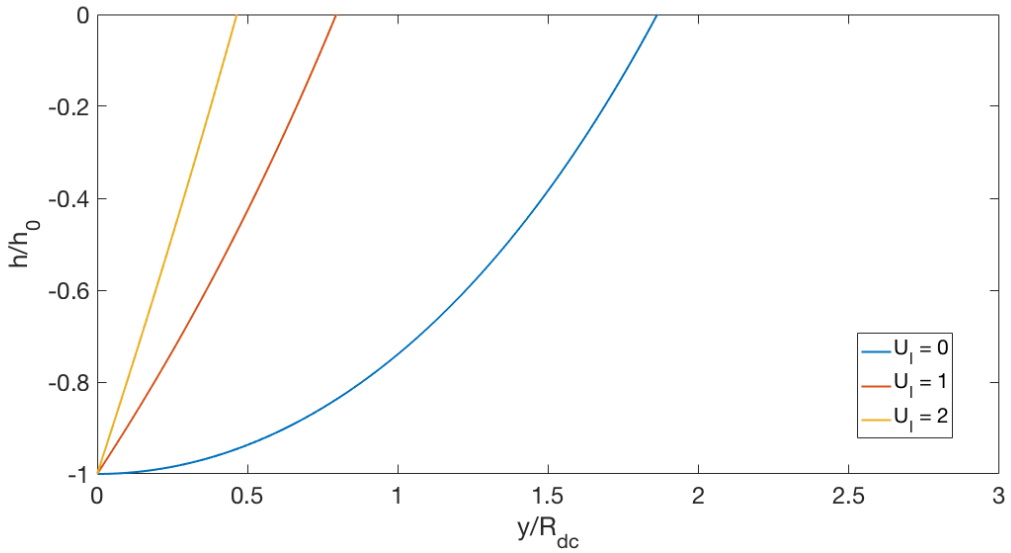

Figure 3.3 The dimensionless current depth profile for three different values of the dimensionless wall velocity U_l. The initial PV $Q^* = 0.5$ is held constant.

The critical value of Q^* can be expressed in terms of the wall velocity U_l. Using the fact that $\tanh(x) < 1$ for all x, we find that we must have

$$\sqrt{Q^*} - \frac{1}{\sqrt{Q^*}} < U_l, \tag{3.17}$$

for a physical current depth profile to exist. In the case of a zero wall velocity this reduces to $Q^* < 1$. As the value of U_l increases, the range of allowed Q^* values increases also. For $Q^* < 1$ the model is valid for any specified wall velocity U_l. For $Q^* > 1$ we are able to rearrange (3.17) to find the upper limit of Q^* values for which the model is valid which is given by

$$0 < Q^* < \frac{2 + U_l^2 + \sqrt{4U_l^2 + U_l^4}}{2}. \tag{3.18}$$

We also investigate the effect of the wall velocity on the depth profile by fixing Q^* and allowing U_l to vary. Figure 3.3 shows three depth profiles for different values of U_l with the initial PV Q^* fixed. As the value of the wall velocity increases we see a decrease in the current width. The current depth profiles also increase in gradient and become more triangular in shape as U_l is increased. The decrease in the width is expected as the depth profile equation in (3.16) is linear in U_l.

The analysis of the current depth profiles has shown that the maximum current depth is unaffected by the value of the source PV and also that the current width increases with increasing PV. We investigate this second point in more detail in the next section with the derivation of the explicit form for the current width.

3.2.1.2 Current width

The maximum current width w_0 occurs when $h = 0$ at the edge of the current. Setting (3.16) equal to zero and using the hyperbolic identity $\sinh(x) = \sqrt{\cosh^2(x) - 1}$ we obtain a quadratic for the $\cosh(\sqrt{Q^*}\frac{w_0}{R_{dc}})$ term. This is solved via the quadratic formula and then the inverse cosh function applied to give the maximum current width as

$$\frac{w_0}{R_{dc}} = \frac{1}{\sqrt{Q^*}} \operatorname{acosh}\Big(\frac{1 - Q^* - Q^* U_l \sqrt{2 + U_l^2 - Q^*}}{(Q^* - 1)^2 - Q^* U_l^2}\Big), \tag{3.19}$$

where we have non-dimensionalised by the current deformation radius R_{dc}. When applying the quadratic formula we have taken the minus root to give a physically valid solution. The positive root gives an increasing current width with increasing U_l which is the opposite of the behaviour seen in the current depth profiles in figure 3.3.

The application of the quadratic formula and acosh function to obtain the current width solution in (3.19) lead to various mathematical solvability conditions. When applying the quadratic formula we must have $a \neq 0$ and $b^2 - 4ac \geq 0$ and the inverse cosh function requires an argument greater than or equal to one. Analysis of these conditions reveals that the limits on the initial PV for a solution for the current width to exist are the same as the limits found above in (3.18) when considering the physics of the problem. This makes sense since the depth profile becomes non-physical due to the current width tending to infinity.

We now investigate the effect that the initial PV has on the current width in more detail. Figure 3.4 plots the dimensionless current width as a function of Q^* for three different values of the wall velocity U_l. For all three values of U_l the model breaks down once the value of Q^* reaches its upper limit given in (3.18), with the limiting value increasing as the value of U_l is increased. The plot shows that the current width increases with increasing PV, as seen in the current depth profiles. We also see that for a fixed value of Q^* a larger wall velocity leads to an decreased current width, which is again the same behaviour as seen in the depth

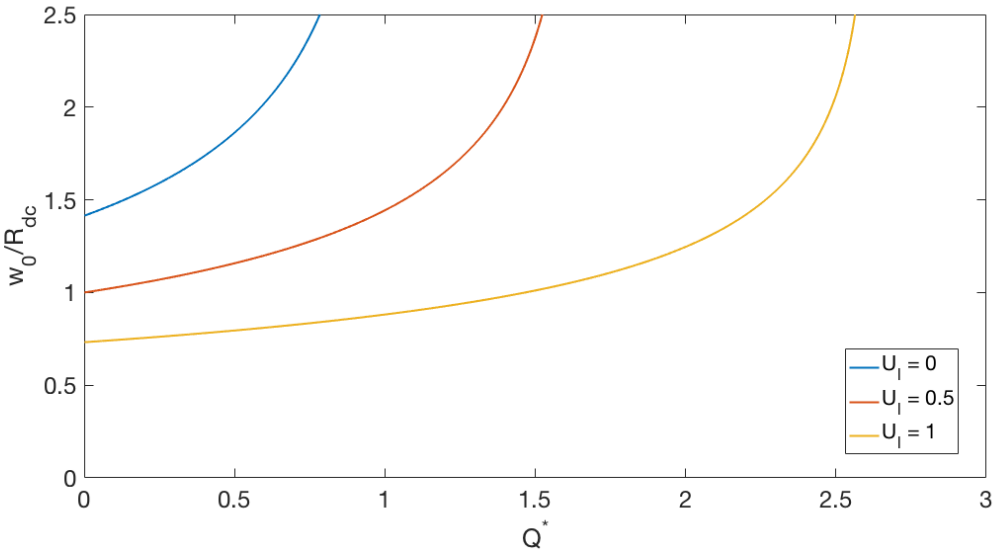

Figure 3.4 The dimensionless current width as a function of the initial PV Q^*. Three curves are shown, each with a different value of the wall velocity U_l.

profiles in figure 3.3.

In summary, we have derived a steady state model for an inviscid boundary current originating from a source with finite PV. The maximum current depth is independent of the source PV, while the current width is seen to increase with increasing PV. The model requires a choice of wall velocity U_l and in the next section we present two possible choices.

3.2.2 Wall velocity

We begin with the zero wall velocity model of TL and extend it to the finite PV case derived above. We then use the Bernoulli condition of the PN model to prescribe the wall velocity and investigate the effect of finite PV on the solutions.

3.2.2.1 Zero wall velocity

The use of a zero wall velocity follows the model of TL, but with an extension to a finite PV source. We begin by considering the shallow water x-momentum equation (see chapter 1), given by

$$u_t - fv = -g'\eta_x. \tag{3.20}$$

In the coordinate system of the model given in figure 3.1, the velocity parallel to the boundary is given by u and the velocity perpendicular to the boundary is given by v. This means that at the wall both v and η_x are zero. The value of u is therefore constant in time by (3.20) and must be equal to its initial value. Since the freshwater current is discharged from the source perpendicular to the boundary, it has velocity only in the y-direction and thus $u = 0$ initially at the boundary. In terms of our nomenclature this means that $u_l = 0$ and hence the current depth profile in (3.16) simplifies to give

$$\frac{h}{h_0} = \frac{1}{Q^*} + (1 - \frac{1}{Q^*}) \cosh(\sqrt{Q^*} \frac{y}{R_{dc}}). \tag{3.21}$$

The solvability condition in (3.18) for a physical depth profile is simply $Q^* < 1$. The significance of this will be discussed in section 3.3 when modelling the initial value for the PV. Figure 3.5 plots the current depth profile for three different values of the initial PV. We see the same general behaviour as in figure 3.2 (where U_l is fixed but non-zero) with an increase in the current width with increasing Q^*. We do not, however, see the change in the shape of the current profile that occurs at large Q^* for a finite value of U_l. The profile shape is consistently convex with the widening of the current as Q^* is increased leading to a more gently sloping profile. This suggests that it is the effect of the non-zero wall velocity that is acting to change the shape of the current at high Q^* in figure 3.2, rather than the increase in the initial PV.

The maximum current width is found by substituing $U_l = 0$ into (3.19) to obtain

$$\frac{w_0}{R_{dc}} = \frac{1}{\sqrt{Q^*}} \operatorname{acosh}\Big(\frac{1}{1 - Q^*}\Big). \tag{3.22}$$

The same validity condition of $Q^* < 1$ applies. The current width as a function of Q^* for a zero wall velocity has already been plotted in figure 3.4. The width increases with increasing Q^* until the model breaks down at $Q^* = 1$. There is a rapid increase in the width as Q^* increases close to 1.

In the limit as $Q^* \to 0$ we expect to be able to recover the zero PV solutions of the TL model. Taking the limit in (3.21) we expand the cosh term as a Taylor series, $\cosh x \sim 1 + x^2/2 + ...$ for $x << 1$, which gives

$$\frac{h}{h_0} \sim 1 - \frac{y^2}{2R_{dc}^2}. \tag{3.23}$$

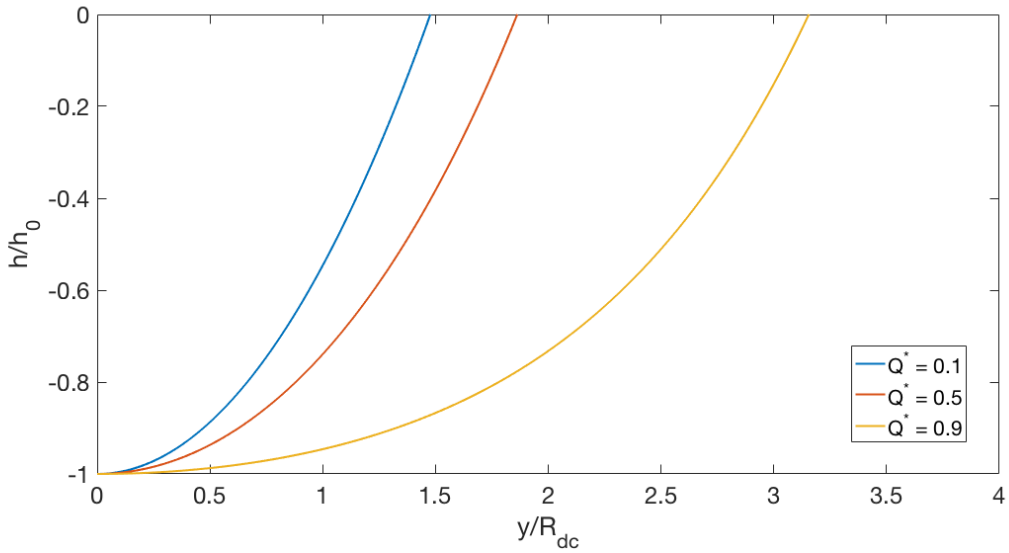

Figure 3.5 The current depth profile using a zero wall velocity for three different values of the initial PV Q^*.

This is the same parabolic depth profile that was obtained by TL in (3.4) with zero potential vorticity. Taking the zero PV limit for the current width we first apply the cosh function to both sides of (3.22) and expand the left-hand side using the Taylor series for cosh. With the right-hand side we use the binomial expansion $(1-\varepsilon)^{-1} \sim 1+\varepsilon+\ldots$ to get at leading order

$$1+\frac{Q^*}{2}\left(\frac{w_0}{R_{dc}}\right)^2 \sim 1+Q^*, \tag{3.24}$$

which gives the current width scaling found by TL in (3.2) upon rearranging.

So far when considering the case of a zero wall velocity we have used the results of section 3.2.1 for the general finite PV current model with wall velocity U_l. For a finite value of U_l we expect the current velocity to have the same constant value, however, by fixing $U_l = 0$ we have to determine the current velocity via a different method. We follow the method of TL and appeal to volume conservation. The total current volume is given by

$$V = Qt = l\int_0^{w_0} h(y)dy, \tag{3.25}$$

where l represents the length of the current. Integrating and non-dimensionalising gives

$$\frac{Qt}{lh_0R_{dc}} = \frac{1}{Q^*}\frac{w_0}{R_{dc}} + \frac{1}{\sqrt{Q^*}}\left(1-\frac{1}{Q^*}\right)\sinh\left(\sqrt{Q^*}\frac{w_0}{R_{dc}}\right). \tag{3.26}$$

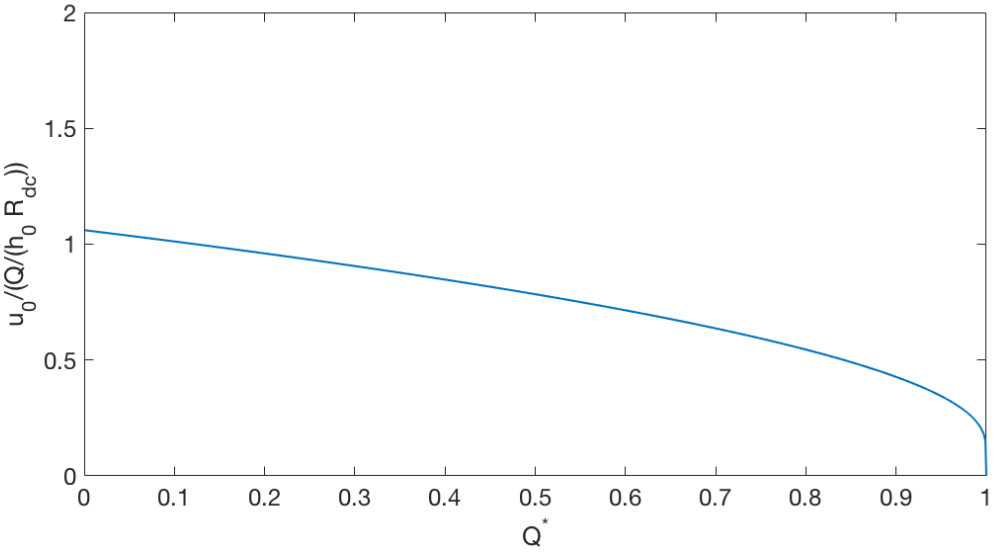

Figure 3.6 The dimensionless current velocity for the zero wall velocity model as a function of the initial PV Q^*.

Substituting for the current width in (3.22) we obtain the following expression for the constant current velocity $u_0 = l/t$,

$$\frac{u_0}{Q/(h_0 R_{dc})} = \Big(\frac{1}{Q^{*3/2}}\,\mathrm{acosh}\,\big(\frac{1}{1-Q^*}\big)\frac{1}{\sqrt{Q^*}}(1-\frac{1}{Q^*})\sinh(\sqrt{Q^*}\frac{w_0}{R_{dc}})\Big)^{-1}. \tag{3.27}$$

Figure 3.6 plots the dimensionless current velocity as a function of Q^*. We see a decrease in the current velocity as the initial PV is increased up to $Q^* = 1$ where the model breaks down. The decrease in the current velocity is to be expected as the current width increases with increasing PV, but the volume flux from the source remains constant and therefore the current must slow down to conserve the volume passing through a given cross-section.

As with the current width and depth profile we are able to recover the zero PV solution obtained by TL by taking the limit as $Q^* \to 0$. We return to (3.26) and use the Taylor expanison $\sinh(x) \sim x + x^3/6 + \ldots$ as well as the approximation for the current width in (3.24) to recover the TL zero PV result in (3.3).

In summary, for the zero wall velocity model, the current velocity remains constant as in the case of the zero PV model of TL and its value decreases as the initial PV is increased. The current width is seen to increase as the PV is increased.

3.2.2.2 Finite wall velocity

Having analysed a model with a zero wall velocity we now consider an alternate case where the wall velocity U_l is finite and is specified by a Bernoulli condition. The use of such a condition follows from the work of PN. Physically the velocity of the current must be zero at the wall with a thin boundary layer existing close to the wall, beyond which the velocity reaches a constant finite value. In the finite wall velocity model we are considering the current velocity at the edge of this boundary layer, which allows for a non-zero value. Since we are modelling the flow as non-viscous, the dynamics within the boundary layer may be neglected at first order.

In section 3.2.2.1 the use of a zero wall velocity came from the shallow water equations. The value of u at the wall was found to be constant in time and therefore must be equal to its initial value. For the zero wall velocity model we take this constant value to be zero based on the fact that the freshwater is discharged from the source perpendicular to the boundary. Here we choose to neglect the flow at the source and instead define the initial conditions for the boundary current to be given at the point at which the flow is parallel to the boundary. The turning of the flow to the right under the Coriolis force is seen as a transition phase and we define the boundary current to begin once this turning has occurred. In some sense we can think of this as an adjustment period during which the current changes between the prescribed source depth H_0 and the geostrophic current depth h_0, in such a way as to satisfy a Bernoulli condition. This means that we take the initial value of u to be given by the constant current velocity U_l, which is fixed according to an upstream Bernoulli condition (see chapter 1). We choose to use the known conditions at the source to fix the upstream Bernoulli, which gives two possible streamlines that we may use: one following the boundary wall and the other the outer edge of the vortex and the current (see figure 3.7). Since we are concentrating only on the boundary current in this model and have so far neglected the presence of the outflow vortex, we use the streamline following the flow along the boundary wall. This is also in agreement with the work of PN who use a similar Bernoulli condition along the boundary wall. In chapter 7 we incorporate the outflow vortex into the model and the choice of streamline is different to the one used here.

We begin with the previous results for the current depth profile in (3.16) and the maximum current width in (3.19) and substitute in the 'new' value for U_l. The use of the Bernoulli condition relies only on the assumption of a two-layer hydrostatic fluid, which is the same as used above. Figure 3.7 shows the setup of the model, with the streamline along which the

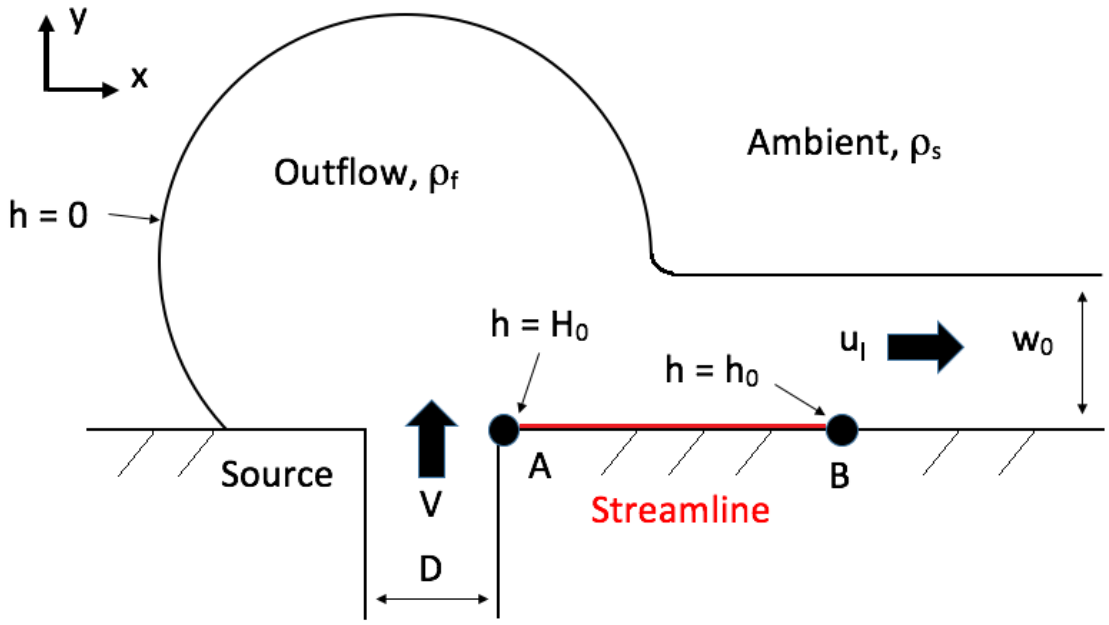

Figure 3.7 The idealised setup used to describe the problem. The Bernoulli condition is valid along the streamline from A at the corner of the source to B along the boundary wall further downstream.

Bernoulli condition is applied extending from the downstream corner of the source opening at A to a point B along the wall further downstream in the current. Applying the Bernoulli condition along the chosen streamline gives

$$\frac{1}{2}V^2 + g'H_0 = \frac{1}{2}u_l^2 + g'h_0 \tag{3.28}$$

where V is the velocity of the freshwater as it leaves the source in the direction perpendicular to the boundary and H_0 is the source depth. This can be non-dimensionalised and rearranged to give

$$U_l^2 = \frac{(Fr^2+2)}{H^*} - 2, \tag{3.29}$$

where we have defined a source Froude number $Fr = V/\sqrt{g'H_0}$ and a depth ratio $H^* = h_0/H_0$. Figure 3.8 plots the Bernoulli wall velocity U_l as a function of H^* for three different values of the source Froude number. For all values of Fr we see a sharp decrease in the value of U_l as H^* is increased until the model breaks down at the maximum limiting value of H^*. As the source Froude number is increased, the range of validity of the model increases and for a fixed value of H^* the wall velocity increases also.

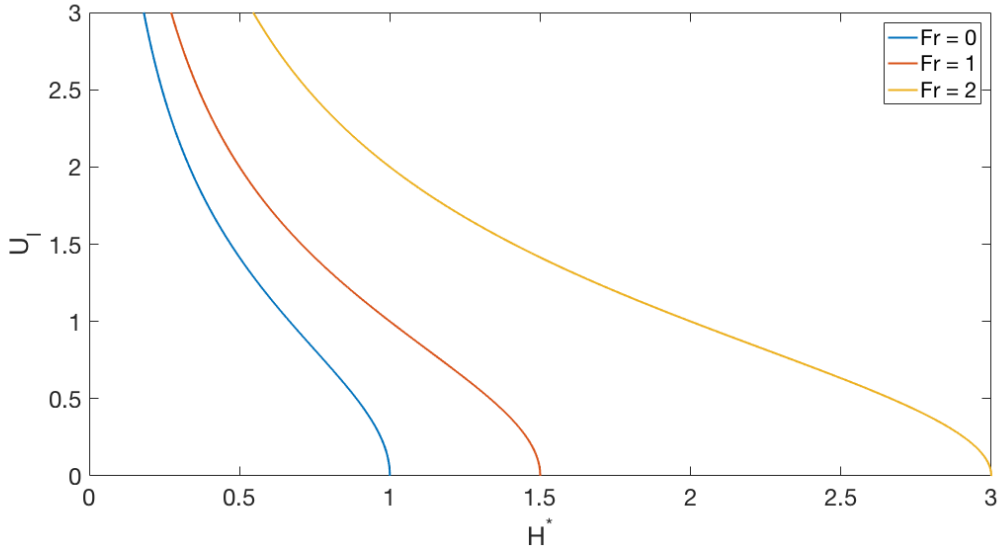

Figure 3.8 The Bernoulli wall velocity as a function of the depth ratio $H^* = h_0/H_0$ for three different values of the source Froude number $Fr = V/\sqrt{g'H_0}$.

Increasing the value of the depth ratio H^* is equivalent to reducing the source depth whilst holding the maximum current depth fixed. For the Froude number to remain constant, a decrease in the source depth must be offset by a reduction in the source velocity V. Therefore, since the current depth is fixed, we must have a decrease in the wall velocity U_l according to (3.28), which is the behaviour seen in figure 3.8. The limiting value of H^* at which the model breaks down occurs when taking the square root in (3.29). This gives rise to the first solvability condition for the finite wall velocity model, namely that

$$B^* = \frac{(Fr^2+2)}{H^*} > 2, \tag{3.30}$$

where B^* is given by the source conditions. From (3.29) we see that $U_l = \sqrt{B^*-2}$ and therefore as B^* is increased the wall velocity increases also.

Now that we have the value of the wall velocity we can substitute from (3.29) into (3.16) to give the current depth profile

$$\frac{h}{h_0} = \frac{1}{Q^*} + (1-\frac{1}{Q^*})\cosh(\sqrt{Q^*}\frac{y}{R_{dc}}) - \sqrt{\frac{B^*-2}{Q^*}}\sinh(\sqrt{Q^*}\frac{y}{R_{dc}}). \tag{3.31}$$

The exact form of the depth profile will depend on the value of $U_l = \sqrt{B^* - 2}$, which is fixed by the source conditions. The depth profile has already been plotted in figure 3.3 for different values of the wall velocity at a fixed value of Q^*. Increasing the value of the wall velocity U_l (and therefore the source Bernoulli B^*) leads to a decrease in the current width and a steepening of the current depth profile towards a more triangular shape. The effect of finite PV on the finite wall velocity current depth profile has also already been shown in figure 3.2 where the current depth profiles are plotted for a fixed non-zero wall velocity at different values of Q^*. We see an increase in the current width and a change in the profile shape from concave to 's-shaped' as the initial PV is increased.

The maximum current width is obtained by substituting for U_l from (3.29) into (3.19) to give

$$\frac{w_0}{R_{dc}} = \frac{1}{\sqrt{Q^*}} \operatorname{acosh}\Big(\frac{1 - Q^* - Q^*\sqrt{(B^* - 2)(B^* - Q^*)}}{Q^{*2} - Q^* B^* + 1}\Big). \tag{3.32}$$

The solvability conditions established in section 3.2.1, require that (3.18) is satisifed for the model to remain valid. In terms of the source Bernoulli this becomes

$$0 < Q^* < \frac{B^* + \sqrt{B^{*2} - 4}}{2}. \tag{3.33}$$

As for the current depth profile, the behaviour of the current width with varying initial PV is analysed for a general fixed non-zero value of the wall velocity in figure 3.4 in section 3.2.1.2. The width increases with increasing Q^* up to the point of model breakdown given in (3.33). We see a decrease in the current width at a fixed value of Q^* and an increasing value of U_l. This matches the behaviour seen in the current depth profiles in figure 3.2.

Taking the limit as $Q^* \to 0$ in (3.31) we are able obtain the depth profile in the case of a zero PV source. We expand the hyperbolic terms as a Taylor series, $\cosh(x) \sim 1 + x^2/2 + ...$ and $\sinh(x) \sim x + ...$ to give at leading order

$$\frac{h}{h_0} \sim 1 - \frac{y}{R_{dc}}\Big(\sqrt{B^* - 2} + \frac{y}{2R_{dc}}\Big). \tag{3.34}$$

The current width is found by solving for $h = 0$ at $y = w_0$ and gives for a zero PV source

$$\frac{w_0}{R_{dc}} \sim -\sqrt{B^* - 2} + \sqrt{B^*}, \tag{3.35}$$

where we have taken the positive square root to ensure a positive value for the current width. We are also able to recover the TL zero PV solution for the depth profile with a zero velocity boundary condition given in (3.4) by taking the limit as $U_l \to 0$. This is equivalent to substituing $B^* = 2$ into (3.34). Making the same substitution in (3.35) also recovers the width scaling obtained by TL. If we return to (3.32) and substitute in $B^* = 2$ we recover the zero wall velocity finite PV solution for the current width in (3.22). We are also able to make the same substitution in the current depth profile given in (3.31) to recover the depth profile in the case of finite PV and $U_l = 0$.

Finally, taking the limit as $Q^* \to 0$ in (3.32) will enable us to recover the zero PV Bernoulli solution for the current width in (3.35). We first rearrange the equation so that we have a cosh term on the left-hand side allowing us to use the Taylor series $\cosh(x) \sim 1 + x^2/2 + ...$, while on the right-hand side we neglect $O(Q^{*2})$ terms in the denominator and use the binomial expansion $(1-\varepsilon) \sim 1 + \varepsilon + ...$ to obtain

$$1 + \frac{Q^*}{2}(\frac{w_0}{R_{dc}})^2 \sim (1 - Q^* - Q^*\sqrt{(B^*-2)(B^*-Q^*)})(1+Q^*B^*). \tag{3.36}$$

We now multiply out the brackets, again neglecting terms $O(Q^{*2})$ and higher, to give the result

$$(\frac{w_0}{R_{dc}})^2 \sim 2B^* - 2 - 2\sqrt{B^*(B^*-2)}, \tag{3.37}$$

which is the square of the zero PV Bernoulli current width given in (3.35).

In summary, the finite wall velocity model shows the same qualitative behaviour as the zero wall velocity model with an increase in the current width with increasing PV. The current velocity is dependent on the source Bernoulli B^* which is a function of the source Froude number Fr and the depth ratio H^*.

3.3 Initial PV

In our analysis so far, we have derived a theoretical model for the steady state boundary current produced by a finite PV source of buoyant freshwater for both the cases of a zero wall velocity and a finite wall velocity. The next step in our analysis is to parameterise the

initial PV.

3.3.1 Vorticity parameterisation model

Conservation of PV means that the initial value at the source must be conserved throughout the flow. For a source depth of H_0 and an initial local vorticity $\zeta_i = -\alpha_i f$, the PV conservation equation (3.9) gives the PV at the source as

$$q_0 = \frac{f(1-\alpha_i)}{H_0}. \tag{3.38}$$

With this definition we note that $\alpha_i = -\zeta_i/f$ must be positive due to the anticyclonic circulation seen in the outflow vortex. If we look back at our general model the dimensionless initial PV is given by $Q^* = q_0/(f/h_0)$, which now becomes

$$Q^* = (1-\alpha_i)H^*, \tag{3.39}$$

where we recall the depth ratio $H^* = h_0/H_0$. This means that the local vorticity ratio at the source α_i plays a key role in determining the properties of the current. The case of $\alpha_i = 1$ corresponds to a zero PV source as used in the model of TL. The linear relationship between Q^* and α_i means that when varying α_i we will see the same behaviour as found when varying Q^*, but in the opposite direction. Varying the value of the depth ratio H^* will cause the same change in the value of Q^* and thus the same behaviour will be seen.

One important property of the vorticity parameterisation model is that we are now able to describe the effect of finite PV on the current velocity for the finite wall velocity model in section 3.2.2.2. The current velocity was seen to decrease as the value of H^* was increased, which corresponds to an increase in the PV. The current velocity therefore decreases as the initial PV is increased for both the zero and finite wall velocity models.

Turning our attention to the solvability conditions for the models, we are able to reformulate the validity condition for the zero wall velocity model of $Q^* < 1$ as

$$\alpha_i > 1 - \frac{1}{H^*}. \tag{3.40}$$

This gives a minimum value for the source local vorticity ratio determined by the depth ratio H^*. For $H^* > 1$, which corresponds to a current depth greater than that of the source, α_i must increase towards the zero PV limit of $\alpha_i = 1$. For $H^* < 1$, corresponding to a source depth greater than that of the current, the source vorticity ratio may extend across the full range $0 \leq \alpha_i \leq 1$. For the Bernoulli finite wall velocity model we found a solvability condition in (3.33) that gives a limiting value of Q^* in terms of the source Bernoulli $B^* = (Fr^2+2)/H^*$. Using the form of Q^* in (3.39) the solvability condition gives

$$\alpha_i > 1 - \frac{(Fr^2+2) + \sqrt{(Fr^2+2)^2 - 4H^{*2}}}{2H^{*2}}. \tag{3.41}$$

We find that a solution will always exist in the range $0 \leq \alpha_i \leq 1$, provided $B^* = (Fr^2 + 2)/H^* > 2$.

3.3.2 Estimation of source vorticity

The vorticity parameterisation model introduced above requires that the local vorticity of the source $\zeta_i = -\alpha_i f$ is known. In practice this is difficult to obtain, though we will present some experimental measurements in chapter 4. In terms of specifying the value of the parameter in our model, we use an observation from the work of Nof and Pichevin (2001), that for an outflow with a weakly anticyclonic vorticity the local vorticity is given by $-\alpha f$, where α is analogous to the Rossby number (and defines the vorticity ratio in the same way as our parameter α_i). We define the Rossby number as

$$Ro = \frac{u_0}{f w_0}, \tag{3.42}$$

where u_0 is the constant current velocity and w_0 the steady state current width. This can be calculated by using the theoretical predictions for the current width and current velocity for each model. Since $Q^* = H^*(1-\alpha_i)$ we obtain an implicit equation to solve for $\alpha_i = Ro$ which depends on the depth ratio H^*. For a general wall velocity U_l, the implicit equation for $\alpha_i \sim Ro$ is

$$\alpha_i = \frac{U_l}{\frac{1}{\sqrt{H^*(1-\alpha_i)}} \operatorname{acosh}\left(\frac{1-H^*(1-\alpha_i)-H^*(1-\alpha_i)U_l\sqrt{2+U_l^2-H^*(1-\alpha_i)}}{(H^*(1-\alpha_i)-1)^2-H^*(1-\alpha_i)U_l^2}\right)}. \tag{3.43}$$

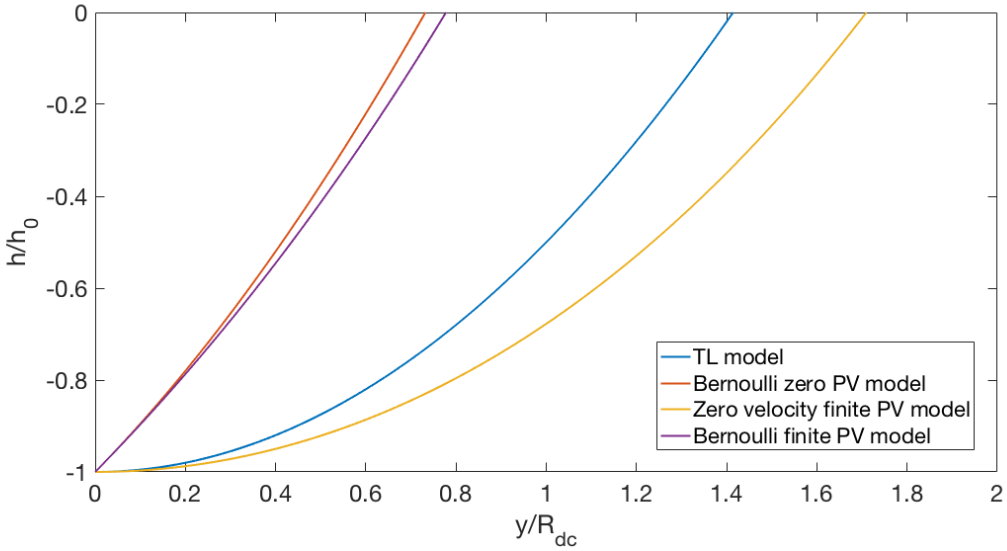

Figure 3.9 Current profiles for the four different models which have varying source and boundary wall conditions.

The specific forms for the zero wall velocity and source Bernoulli models are obtained by substituting in the required value of U_l. Analysis of (3.43) reveals that solutions only exist for a narrow range of the experimental parameters. For example, for a zero wall velocity the approximation $\alpha_i \sim Ro$ is only valid for $H^* \lesssim 1$. For the case of a finite wall velocity fixed by the source Bernoulli, for each value of Fr solutions for α_i only exist for a narrow range of H^* values. In practice when comparing the theoretical models with the experimental data, we expect that the best approximation for α_i will be given by the experimentally measured Rossby number $Ro_{exp} = u_{exp}/(fw_{exp})$. We use a combination of both Ro and Ro_{exp} to provide an estimation of the value of α_i when comparing the experimental data with the theory in chapter 4.

3.4 Model comparison

We now have a total of four models for the steady state boundary current and we conclude our analysis by comparing their main features. There are two types of model: the zero wall velocity model based on the work of TL and the finite wall velocity model using an upstream Bernoulli condition as used in the work of PN. For each model we will look at the case of zero and finite PV.

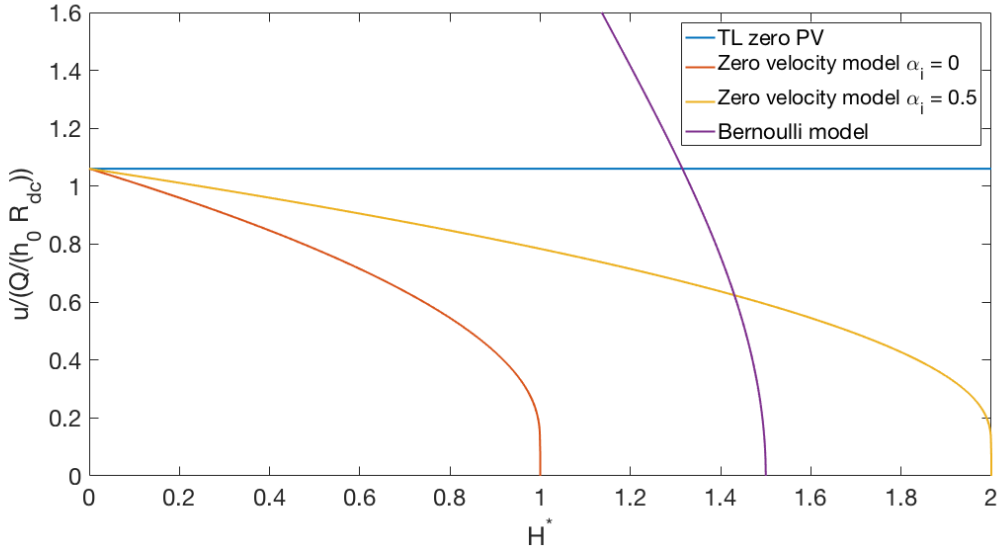

Figure 3.10 A plot of the current velocity predicted by the different theoretical models as a function of the depth ratio H^*.

We begin with a comparison of the current depth profiles. Figure 3.9 displays the profile for each model for a fixed set of parameters. We fix the initial PV $Q^* = 0.375$, the depth ratio $H^* = 0.75$ and the source Froude number $Fr = 0.5$. Comparing the four profiles in figure 3.9 we see large differences in the current width and slight differences in the current shape. The maximum current depth remains the same for each model since it is independent of the PV and is fixed by the assumption of geostrophic balance. For both models, the introduction of finite PV leads to an increase in the current width. The profile shape remains consistent, though it is slightly less steep for finite PV. In terms of the two different models, the zero wall velocity models give a wider current with a more convex profile in comparison to the almost triangular shape of the Bernoulli finite wall velocity model profiles. The change in the value of the PV to be non-zero has little effect in the case of the Bernoulli model, with only a slight increase in width, whereas for the zero wall velocity models the increase in the current width is much larger.

We next compare the current velocity profiles as a function of the initial PV for both the zero wall velocity and the Bernoulli finite wall velocity models. The finite wall velocity model predicts a current velocity that depends on the source Bernoulli $B^* = (Fr^2 + 2)/H^*$. Therefore, to capture the dependence on the initial PV, we must consider the current velocity as a function of H^*. Using the vorticity parameterisation model the initial PV $Q^* = H^*(1 - \alpha_i)$ and thus by fixing α_i and allowing H^* to vary we are able to compare the effect of finite

PV on all of the models on the same plot shown in figure 3.10. For the zero wall velocity model three curves are shown at different values of α_i. The case of $\alpha_i = 1$ corresponds to the zero PV model of TL. For low values of H^*, the Bernoulli model predicts a much higher current velocity than the zero wall velocity model. For the zero wall velocity model the maximum current velocity is achieved for zero PV and decreases as the initial PV is increased. We also see a higher velocity as the value of α_i is increased, which corresponds to smaller PV. The Bernoulli model continues to predict a larger current velocity until $H^* \sim 1.4$ when it decreases below the zero PV model and at $H^* \sim 1.45$ when it falls below the zero wall velocity model with $\alpha_i = 0.5$.

3.5 Discussion

We have presented a collection of theoretical models that aim to describe the steady state properties of a propagating boundary current formed when a freshwater outflow enters into a rotating saltwater environment. Ultimately, the choice of model will depend on the setup for which it is being used to describe, with the choice of the value of the wall velocity U_l playing a key role in the theory. In chapter 4 we present experimental measurements of the wall velocity with values ranging from $0 - 1/2$ times the peak current velocity across different parameter regimes. The range of values suggests that the consideration of both a zero and a finite value for the wall velocity is required.

For each model we have derived expressions for the current steady state depth, width and velocity. The zero wall velocity model extends the theory of TL, while the finite wall velocity makes use of an upstream Bernoulli condition as used in the work of PN. The theory shows that for both models a finite value of PV will lead to significant changes in the steady state current properties compared to the case of zero PV. The current width and current velocity decrease as the value of the PV is increased, while the current maximum depth remains constant. The same results are seen for both models.

In chapter 4 we present experimental measurements of the current properties and compare them with the theoretical models presented here to see if the changes predicted by the finite PV models are realised in practice.

Chapter 4

Experimental observations of rotating gravity currents

4.1 Introduction

The previous chapter presented a steady state theoretical model for the boundary current produced when a freshwater outflow enters into a rotating saltwater environment. Here we present experimental observations from such a scenario which were obtained in the experiments described in chapter 2. We begin with a look at the qualitative features of the boundary current observed in the experiments with along current and across current depth profiles. We then examine PIV measurements of the current wall velocity and the source vorticity to help to determine the model parameters. Finally, we present an analysis of the effect of finite PV on the current properties in comparison with the steady state theoretical model.

4.2 Current features

In chapter 2 the experiments were classified according to the dimensionless parameter I^*, which is equal to the aspect ratio of the current divided by the aspect ratio of the source. Three different flow regimes were found at low, intermediate and high values of I^*. At low values, the outflow vortex is elongated with a weak circulation and is comparable in size with the current. At intermediate values, the circulation within the outflow vortex is much stronger and the vortex grows much larger than the current. Finally, at the highest values of

I^*	Q [cm^3 s^{-1}]	f [s^{-1}]	g' [cm s^{-2}]	H_0 [cm]	D [cm]
0.36	100	1	69.8	2	5
1.23	62	1.5	14.9	2	5
4.08	97	1.5	2.3	2	5

Table 4.1 Experimental parameters for the experiments discussed in this section.

I^* the vortex is seen to go unstable and sheds smaller eddies that are carried along by the current. Images of the flow from each of the regimes are displayed in figure 2.15 in chapter 2. We investigate the general shape of the boundary current in each of the three regimes with an analysis of the current depth profiles in both the along current and across current directions. The along current cross-sections provide a profile along the length of the current as it traverses the perimeter of the tank, while the across current profiles provide insight into the current depth and the current width. We have taken profiles at different times during an experiment, thus creating a full picture of the current shape. We consider each set of profiles in turn for experiments across the three regimes of low, intermediate and high values of I^*. The methodology used to obtain the profiles is given in chapter 2. The experimental parameter values are given in table 4.1.

4.2.1 Along current profiles

Figures 4.1 - 4.3 display along current profiles for three experiments at low ($I^* = 0.36$), intermediate ($I^* = 1.23$) and high ($I^* = 4.08$) values of I^*. The profiles shown are characteristic for the different values of I^*. The current depth h is non-dimensionalised by the maximum depth scaling $h_0 = (2fQ/g')^{1/2}$ and plotted against the current length l, which is non-dimensionalised by the current deformation radius $R_{dc} = \sqrt{g'h_0}/f$. Each plot shows a cross section along the current at ten different times, which have been non-dimensionalised by the rotation rate f. The start time at $T = 0$ is defined to be when the current reaches the first corner of the tank and begins to propagate along the edge of the tank where the measurements are taken. This is to ensure consistency across the different experiments as for each different parameter set the current velocity and thus the time taken to reach the point of measurement will vary. The final time is at the end of the experiment. The data have been fitted with a polynomial curve which results in a slight exaggeration of some features, in particular leading to the apparent positive depth values which are not present in reality. See

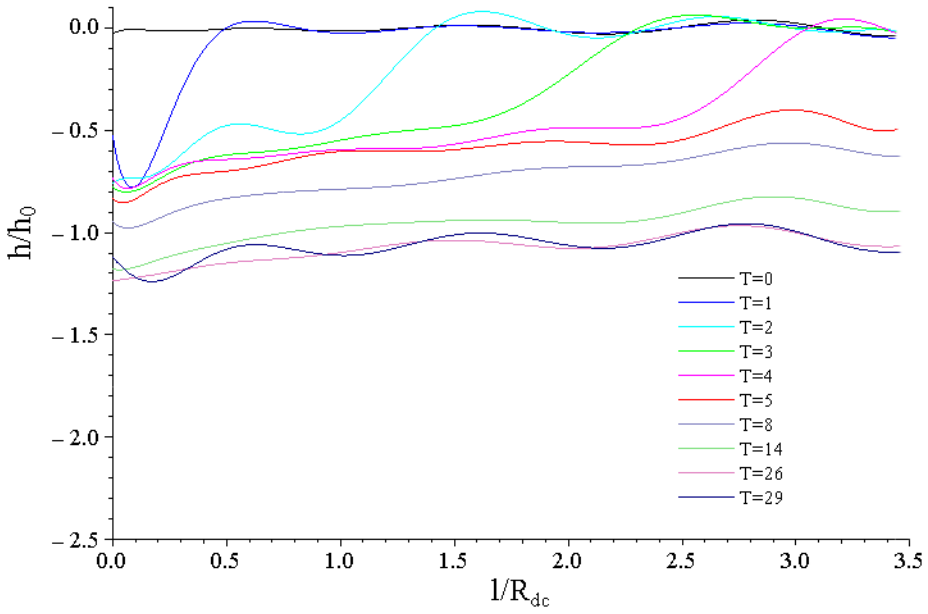

Figure 4.1 Along current cross-section from a typical experiment with a low value of I^*. The profile is taken from an experimental run with $I^* = 0.36$. The values of $T = tf$ for each profile are shown in the legend.

chapter 2 for more details.

There are several general trends that can be seen across the three cross-sections in figures 4.1 - 4.3. Firstly, as the value of I^* increases we see a decrease in the dimensionless current depth at late times from $h/h_0 \sim 1.2$ to $h/h_0 \sim 1$ to $h/h_0 \sim 0.5$. This demonstrates a tendency for the current to overshoot the maximum geostrophic depth h_0 at lower values of I^*. We also see that in the cases of low and intermediate I^* the depth profiles become increasingly clustered together as time increases, suggesting the existence of a limiting steady state depth. This feature is particularly clear in figures 4.1 and 4.2 when considering the latest times. Secondly, we note that across all values of I^* the current maintains a constant shape once the initial front has passed. This suggests that the shape of the current (away from the current head) is self-similar and again supports the hypothesis of the existence of a steady state, should the experiment be allowed to run long enough for it to be reached. This is in contrast to the observations of TL where the along current depth profile was found to reach a maximum shortly after leaving the source and then decrease moving towards the current head. Near to the current head, which corresponds to the early times in figures 4.1 - 4.3, the current depth decreases towards zero, but the current front is much sharper than seen in the work of TL and the current maintains a relatively consistent depth along its remaining

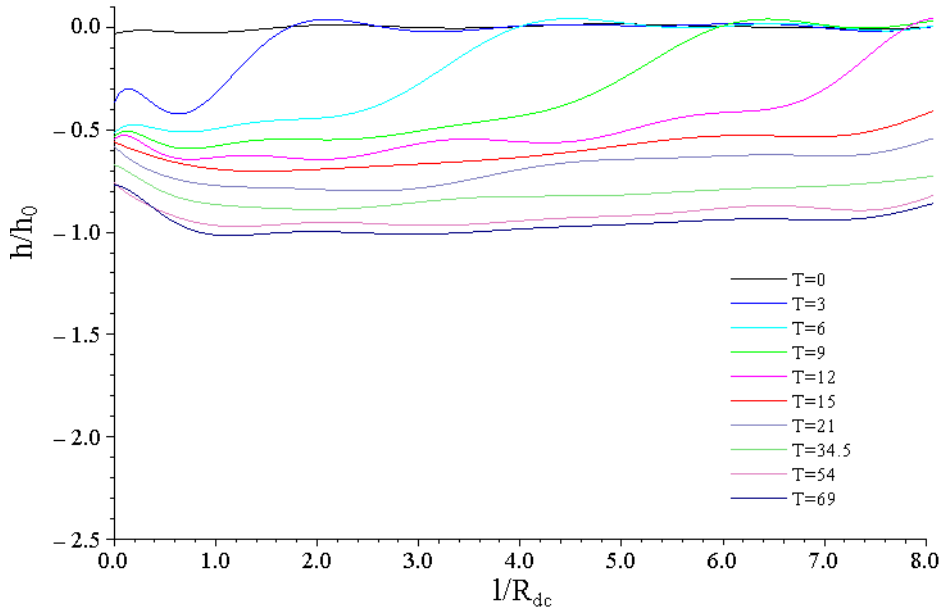

Figure 4.2 Along current cross-section from a typical experiment with an intermediate value of I^*. The profile is taken from an experimental run with $I^* = 1.23$. The values of $T = tf$ for each profile are shown in the legend.

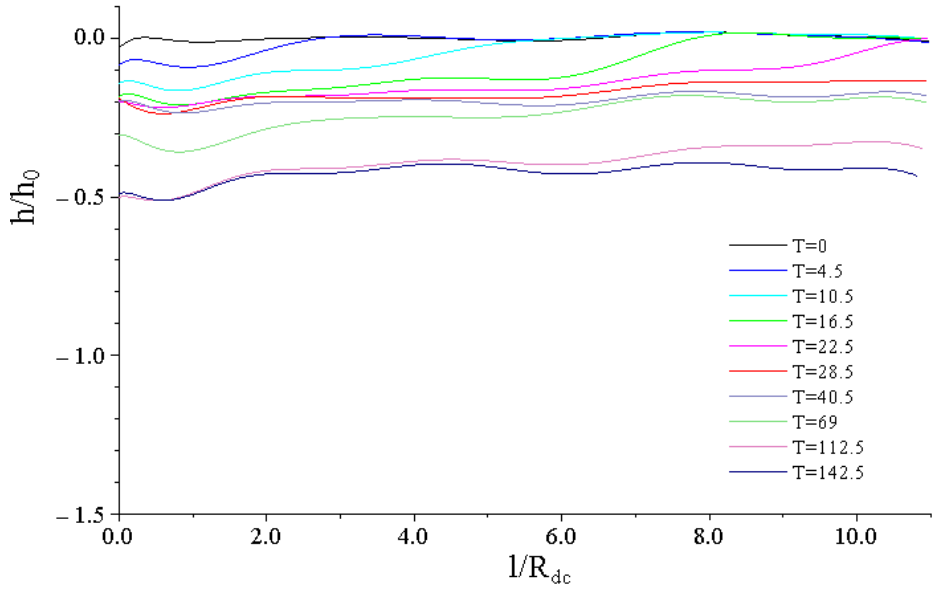

Figure 4.3 Along current cross-section from a typical experiment with a high value of I^*. The profile is taken from an experimental run with $I^* = 4.08$. The values of $T = tf$ for each profile are shown in the legend.

length, with no obvious maximum. This change in behaviour may be a result of the change in the source structure, where our experiments use a horizontal outflow that discharges the freshwater with a finite value of PV. This differs greatly from the small vertical source used in the work of TL.

For each value of I^* we are able to identify the propagation of the current front at early times. In each case the front seems to propagate at an approximately constant dimensionless speed, which can be estimated by the distance between the fronts at successive timesteps. For low I^* in figure 4.1 we estimate the dimensionless speed as 0.83 ± 0.07, for intermediate I^* in figure 4.2 we estimate the dimensionless speed as 2 ± 0.1 and finally for high I^* in figure 4.3 we obtain the estimated dimensionless speed 2.7 ± 0.3. We will present more detailed measurements of the current velocity in section 4.3.1. The shape of the current front changes across the different values of I^* and in general is sharper for lower values. We measure the front length as the distance from the leading edge of the current to the point where the gradient of the current slope decreases to less than $1/4$ of the initial front gradient. For example, if we consider the profile at $T = 4$ in figure 4.1, the leading edge of the current is at $l/R_{dc} \sim 3.1$ and the gradient becomes sufficiently flat at $l/R_{dc} \sim 2.4$, giving a dimensionless current front length of 0.7. Similar calculations for the profiles at intermediate and high I^* in figures 4.2 and 4.3 give the estmated current front length as 1 and 1.6 respectively. The increase in the length of the current front means that the front is becoming more gently sloping as I^* increases.

4.2.2 Across current profiles

Figures 4.4 - 4.6 display across current profiles for three experiments that are characteristic of the flow behaviour seen at different values of I^*. The experimental runs are the same as those used in the previous section with low ($I^* = 0.36$), intermediate ($I^* = 1.23$) and high ($I^* = 4.08$) values of I^*. The cross-sections are taken at the same times as the along current cross-sections above and the dimensionless times are given in each figure.

The general behaviour of the across current profiles seen in figures 4.4 - 4.6 is an increase in width with time and an increase in depth with time. At low and intermediate I^* the current depth profile is almost triangular in shape, with a slight concavity, and decreases from a maximum value at (or very close to) the boundary wall. The apparent occurrence of the

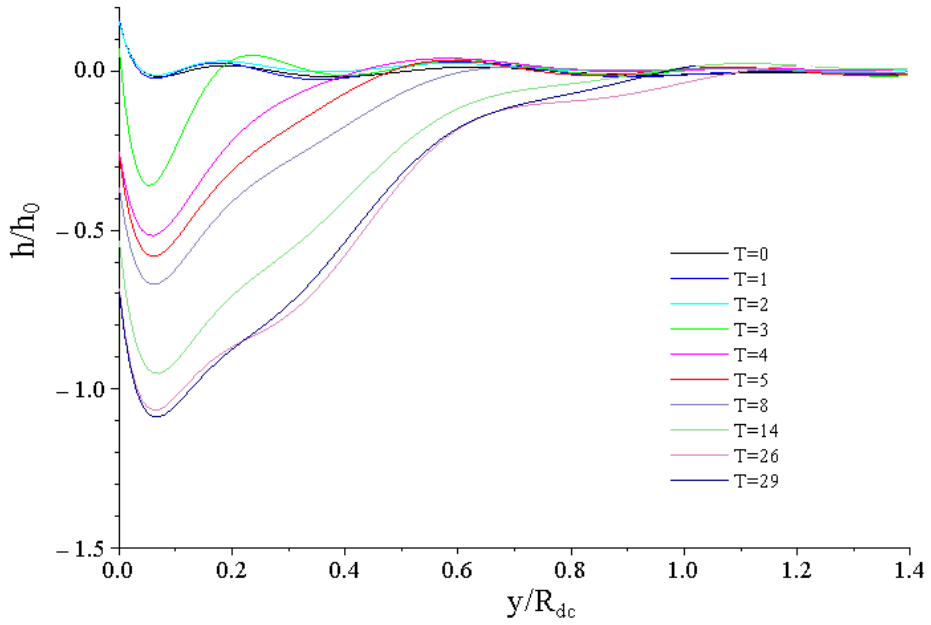

Figure 4.4 Across current cross-section from a typical experiment with a low value of I^*. The profile is taken from an experiment with $I^* = 0.36$. The values of $T = tf$ for each profile are shown in the legend.

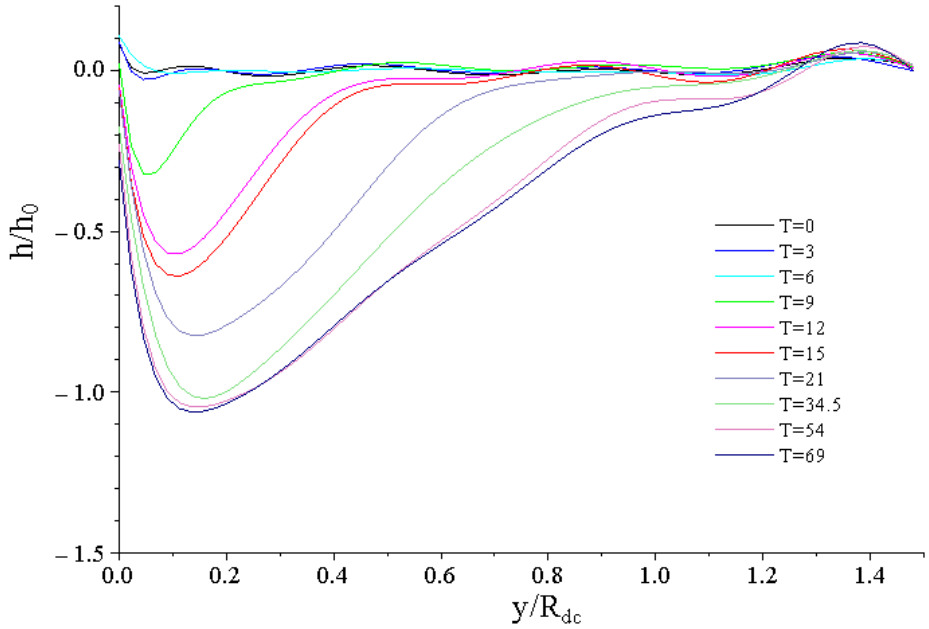

Figure 4.5 Across current cross-section from a typical experiment with an intermediate value of I^*. The profile is taken from an experiment with $I^* = 1.23$. The values of $T = tf$ for each profile are shown in the legend.

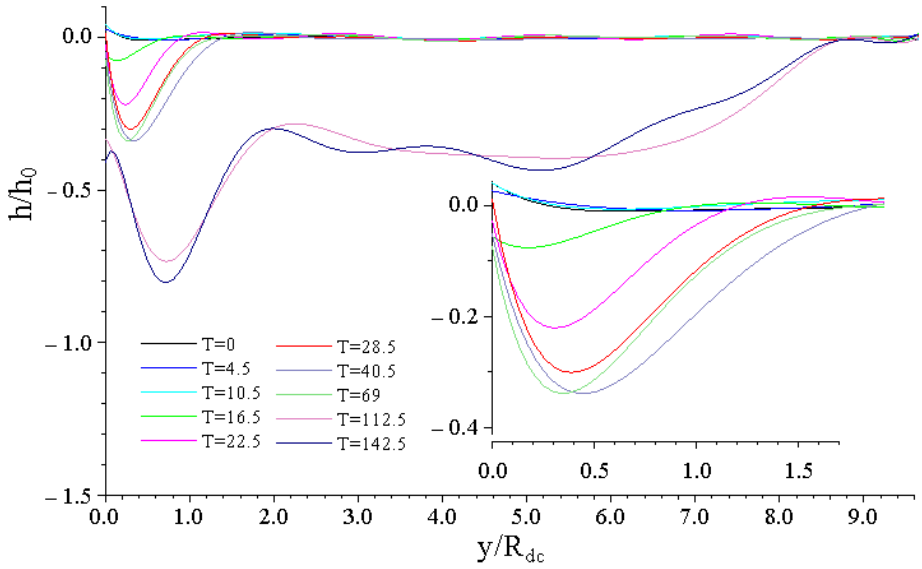

Figure 4.6 Across current cross-section from a typical experiment with a high value of I^*. The profile is taken from an experiment with $I^* = 4.08$. The values of $T = tf$ for each profile are shown in the legend. A close-up view of the current depth profile at early times is also shown.

maximum current depth at a location away from the boundary wall is exaggerated by the curve-fitting process used to obtain the profiles. The raw data points show the maximum depth occurs close to the boundary wall, at a distance $y/R_{dc} < 0.1$, with a slight decrease in depth at the wall itself of $h/h_0 < 0.2$. We also note that the profiles in figures 4.4 and 4.5 are self similar in shape. The width and depth of the profiles increases over time, but the underlying profile shape remains consistent. This seems to suggest the existence of a steady state current depth profile at long times. For high I^* the depth profile behaves in a similar manner to the profiles at low and intermediate I^* at early times, but changes dramatically for $T > 69$. The profiles at $T = 112.5$ and $T = 142.5$ differ greatly from those at earlier times as a result of a vortex that has been shed from the main outflow bulge which is now propagating along with the current. This feature was observed in all of the high I^* experiments. An example image of a vortex being carried along by the boundary current can be seen in figure 2.15. A close-up view of the depth profiles at early times, $T < 69$, is also shown in figure 4.6. The similarity in the current profile shape with the low and intermediate I^* experiments is easier to identify.

As the value of I^* is increased, we see a general increase in the current width. In figure 4.4 the point at which the current depth at the largest time reaches a value of zero is at $y/R_{dc} \sim 0.9$. For intermediate I^* in figure 4.5 this value increases to $y/R_{dc} \sim 1.3$ and for

I^*	Q [cm^3 s^{-1}]	f [s^{-1}]	g' [cm s^{-2}]	H_0 [cm]	D [cm]
0.39	74	2	68.0	2	2.5
1.23	62	1.5	14.9	2	5

Table 4.2 Experimental parameters for the experiments compared with the theory.

high I^* at $T < 69$ in figure 4.6 we estimate the current width to be $y/R_{dc} \sim 1.5$. The current profile at the largest value of T is used for the measurements as it will provide the best approximation to the final steady state value. We present detailed measurements of the current width in section 4.4.2. Restricting our analysis to low and intermediate I^* where the current remains stable and unaffected by the outflow vortex, we see that the current profiles become closer together for successive timesteps at larger T. In particular for the last two timesteps $T = 54$ and $T = 69$ in figure 4.5 the current profiles are almost identical. This again suggests that the flow will reach a steady state provided the experiment is allowed to continue to run at long times.

Overall, both the along current and across current profiles suggest the existence of a steady state current shape towards which the current tends to at late times for the low and intermediate I^* regimes. For the high I^* regime the instability of the outflow vortex distorts the measurements of the current. We next compare the across current depth profiles with the steady state theoretical model.

4.2.2.1 Current depth profiles

The theoretical current depth profiles obtained from both the zero and finite wall velocity models are compared with the across current depth profiles for two experiments at low and intermediate I^* in figures 4.7 and 4.8. The fitted values of α_i obtained in section 4.4.4 are used in the theory giving a non-zero value for the potential vorticity. The TL zero PV model curves are also shown for completeness. The full experimental parameters are given in table 4.2.

Figure 4.7 displays the data alongside the theoretical profiles from the three models for $I^* = 0.39$. The agreement between the finite wall velocity model and the data is quite good and in particular the model shows a capability to capture the current shape. The zero wall velocity profile shows an overestimation of the current width, but we again see quite

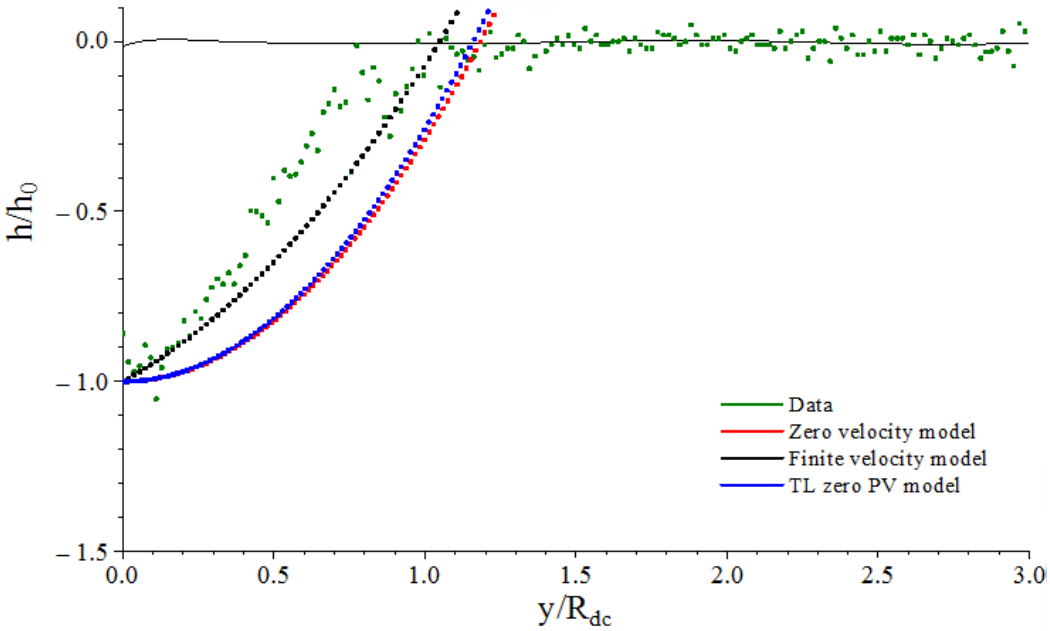

Figure 4.7 Across current depth profile for a low value of $I^* = 0.39$. The data are measured at the end of the experiment to give the best comparison with the steady state models. Theoretical depth profiles for the zero velocity model, TL zero PV model and finite velocity model are also shown.

good agreement with the current shape. Both models show agreement with the maximum current depth at the boundary wall. The overestimation of the current width by the zero wall velocity model seems to have been caused by the fluctuations in the depth measurements at the surface between $1.0 \lesssim y/R_{dc} \lesssim 1.2$. The TL zero PV model gives a very similar profile to the zero velocity model, but gives a slightly smaller current width which is better aligned with the data. The finite velocity model gives the best agreement with the data overall.

Figure 4.8 displays the current depth profile data measured experimentally alongside the theoretical profiles for an experiment with $I^* = 1.23$. The zero wall velocity model shows good agreement with the data, though it perhaps slightly underestimates the current width. The TL zero PV model profile gives a similarly curved profile shape but the underestimation of the current width is even greater. In comparison, the finite wall velocity model predicts the current width well, but is unable to capture the shape of the depth profile. The increased curvature of the zero velocity model profile with a slowly decreasing depth close to the boundary, means that overall it perhaps gives the best representation of the data. The finite wall velocity model predicts a sharp decrease in the current depth moving away form the boundary wall at $y/R_{dc} = 0$ which is not seen in the experimental measurements.

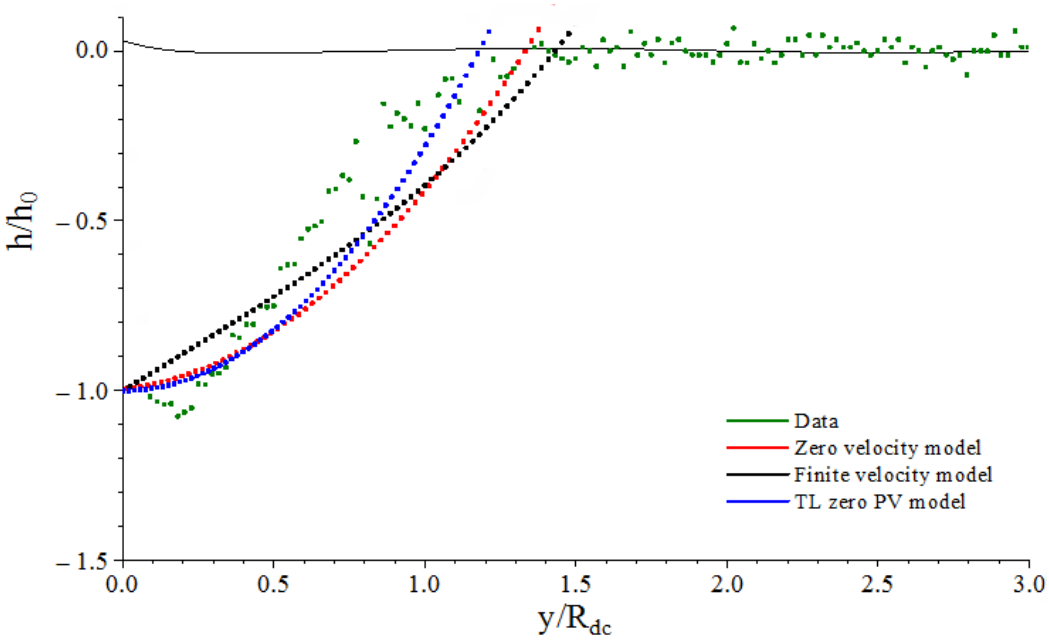

Figure 4.8 Across current depth profile for an intermediate value of $I^* = 1.23$. The data are measured at the end of the experiment to give the best comparison with the steady state models. Theoretical depth profiles for the zero velocity model, TL zero PV model and finite velocity model are also shown.

Analysis of the current depth profiles for other experiments at steady state reveal there to be no obvious trend in the data regarding the performance of the zero and finite wall velocity models across the range of I^* values. In some instances the zero wall velocity model provides a better representation of the data and in others the current depth profile is better approximated by the finite wall velocity model. In all cases, however, one of the two new finite PV models provides better agreement with the data than the TL zero PV model which suggests that the finite PV modification is able to better capture the flow dynamics. Since we are unable to conclusively distinguish between the performance of the two finite PV models, both will be compared with experimental measurements throughout this chapter.

4.3 Model parameters

The theoretical model for the steady state current introduced in chapter 4 requires a choice of two model parameters: the wall velocity U_l and the source vorticity ratio α_i. In this section we present experimental measurements obtained using the method of PIV of both the current

Experiment	Q [cm^3 s^{-1}]	f [s^{-1}]	g' [cm s^{-2}]	H_0 [cm]	D [cm]	I^*
PIV 1	48	0.5	13.3	2	5	0.42
PIV 2	48	1	13.8	2	5	0.81
PIV 3	48	1	3.7	2	5	1.80
PIV 4	48	0.5	4.4	2	5	0.81

Table 4.3 Experimental parameters for the four experiments where PIV measurements of the boundary current were taken.

wall velocity and the estimated source vorticity.

4.3.1 Across current velocity profiles

A total of four PIV experiments focusing on the boundary current were carried out. The PIV data are measured close to the surface of the flow at a depth of $\sim 0.5-1.5$ cm. The parameter values were chosen to provide as good a representation as possible of the different behaviours seen across the full parameter range at low, intermediate and high values of I^*. For the high I^* regime the parameters were chosen such that the vortex only goes unstable at the very end of the experiment to allow measurements of the current properties to be made for the majority of the experiment before the current is distorted by the shedding of vortices from the outflow vortex. The experimental parameters used are displayed in table 4.3. Full details of the methodology of the PIV measurements are given in chapter 2.

Across current velocity profiles for the three regimes of low, intermediate and high values of I^* are displayed in figures 4.9 - 4.11 for six different timesteps. The profiles are taken across the current at approximately one-fifth of the distance around the perimeter of the tank. The boundary wall is located at $y/R_{dc} = 0$.

The data in figure 4.9 show the current velocity increasing away from the boundary wall, reaching a maximum value at $y/R_{dc} \sim 0.2-0.4$, before then decreasing to zero at the far-edge of the current. For early times, $T \leq 40$ there is a general increase in the current velocity as the current is established and tends towards a quasi-steady state. The maximum velocity remains approximately constant for $T = 40-60$ until the experiment ends. The profile retains a reasonably consistent shape throughout the experiment, with a narrow region of peak velocity in the centre of the current and the velocity decreasing towards the edges

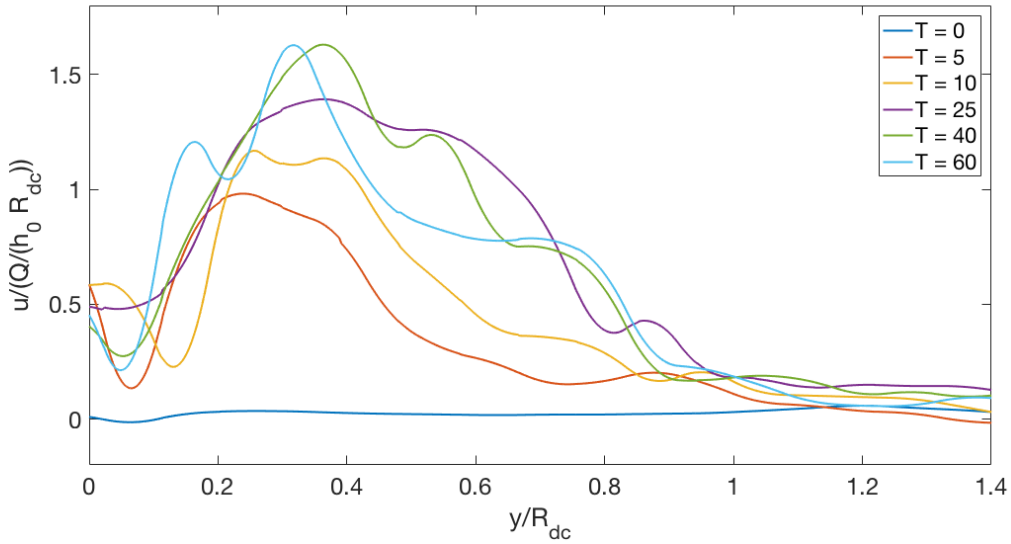

Figure 4.9 Across current velocity profiles for the low $I^* = 0.42$ regime.

of the current. Alongside the wall at $y/R_{dc} = 0$ the value of the dimensionless velocity remains reasonably consistent at ~ 0.5. This is equal to approximately $1/3 - 1/2$ of the maximum velocity reached at the centre of the current depending on the time of measurement. The experimental velocity at the wall must be zero in reality, but due to limitations in the measurement techniques (see chapter 2) we were unable to resolve the full velocity profile in the narrow region at the wall. The closest measurements were made approximately $0.1 - 0.2$ cm from the boundary.

Figure 4.10 displays the across current velocity profiles for an intermediate value of $I^* = 0.81$. The current velocity increases at early times up to $T = 10$ and then we see a decrease at $T = 30$ before it remains reasonably constant for the remainder of the experiment. The profiles show a decrease in the current velocity away from the maximum value that is achieved at the centre of the current as seen in figure 4.9 for low I^*. The velocity close to the wall is in general quite large ranging from $1/3 - 1$ times the maximum current velocity.

For the velocity profiles for the high I^* regime in figure 4.11 we see an increase in the velocity for $T \leq 30$, where it then remains approximately constant until very late times at $T = 110$ when it increases again. This late increase is a result of the outflow vortex going unstable, with vortices shed from the main bulge being carried along by the current. The shape of the profiles in figure 4.11 is different to those seen above for PIV runs 1 and 2, as

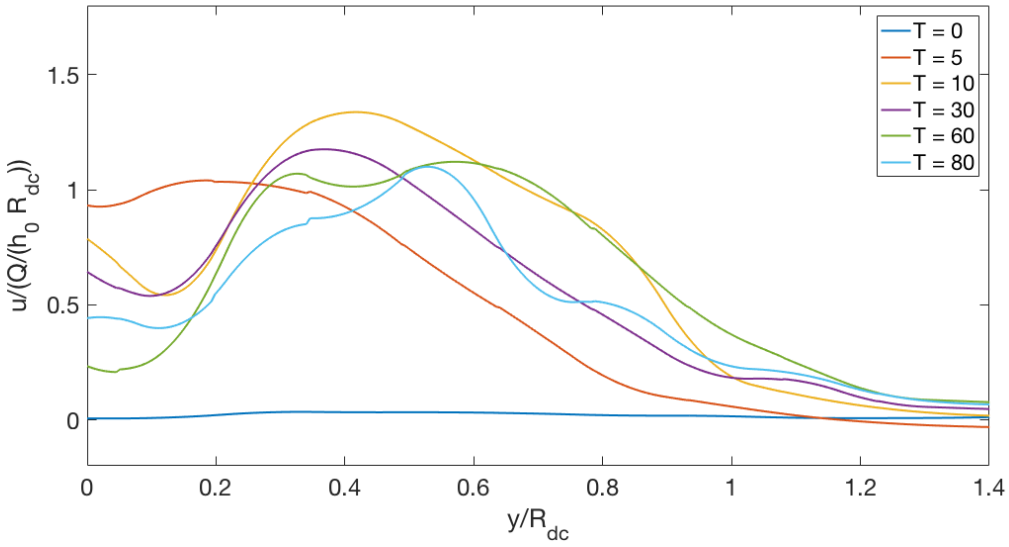

Figure 4.10 Across current velocity profiles for the intermediate I^* regime with $I^* = 0.81$.

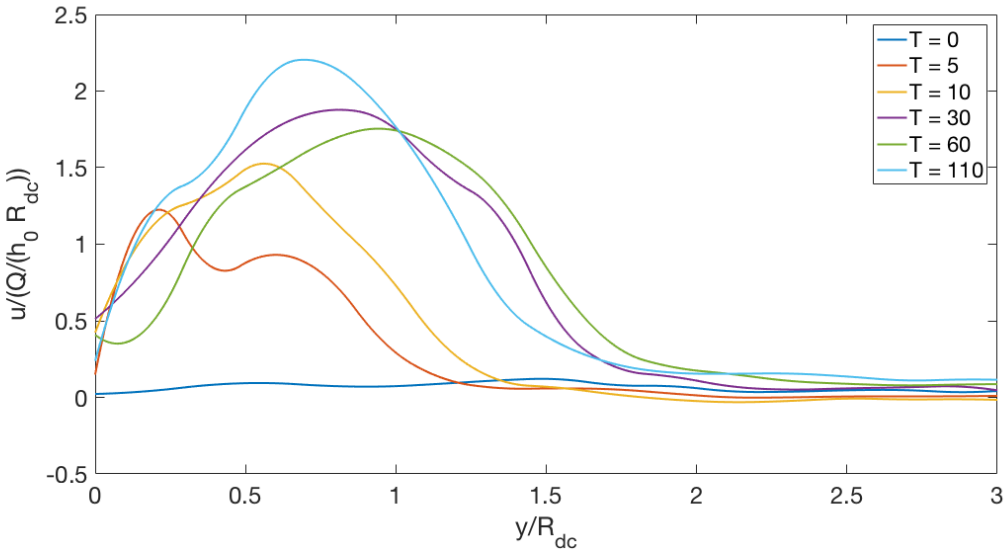

Figure 4.11 Across current velocity profile from an experiment in the high I^* regime with $I^* = 1.80$.

here the velocity decreases to a much lower value at the wall. It generally remains non-zero, however, it is much smaller than the maximum velocity seen in the current at $\sim 1/4$ of the peak value. The velocity also demonstrates a consistent decrease near to the boundary, which is in contrast to the profiles in figures 4.9 and 4.10 where the velocity remains approximately constant or increases as it approaches the wall.

In summary, the across current velocity profiles show that the peak current velocity remains reasonably constant for the duration of an experiment following an initial increase. The largest velocity is achieved across the central part of the current and it decreases towards zero as we move away from the peak value. Close to the boundary wall there is a decrease to a lower speed, which in general remains non-zero. The closest measurements are made ~ 0.1 cm from the wall and therefore the velocity does not necessarily have to zero, but the magnitude of the values seen suggests that the flow behaviour may not be adequately captured by a zero wall velocity model for certain parameter regimes. The wall velocity ranges from approximately $0-1/2$ times the peak current velocity across the different values of I^*. This large range of values means that we cannot really draw a firm conclusion and as such both a zero value and a finite value for the wall velocity are used in the theory.

4.3.2 Source vorticity

The theoretical work in chapter 3 showed that the properties of the steady state current vary depending on the initial PV of the source. We presented a vorticity parameterisation model where the steady state current properties are a function of the vorticity ratio at the source $\alpha_i = -\zeta_i/f$. Using the method of PIV we were able to measure the velocity field very close to the source, at a distance of $y \sim 0.1-0.2$ cm, for subset of the experimental parameter range. These data will be presented below and used to formulate an accurate method of estimation of the value of α_i across the full range of experiments. PIV measurements at the source are available for experiments covering the three regimes of low, intermediate and high values of I^*. The data are presented for early times only as the measurements at late times are distorted by the presence of the outflow vortex, which is a constraint of measuring the source properties outside of the source. Full details of the methodology are given in chapter 2. The experimental parameters are given in table 4.4.

Experiment	Q [cm^3 s^{-1}]	f [s^{-1}]	g' [cm s^{-2}]	H_0 [cm]	D [cm]	I^*
PIV 5	48	1	12.9	2	5	0.85
PIV 6	48	0.5	12.9	2	5	0.42
PIV 7	48	0.5	3.2	2	5	0.97
PIV 8	48	1	3.6	2	5	1.83

Table 4.4 Experimental parameters for the four experiments where PIV measurements of the source conditions were made.

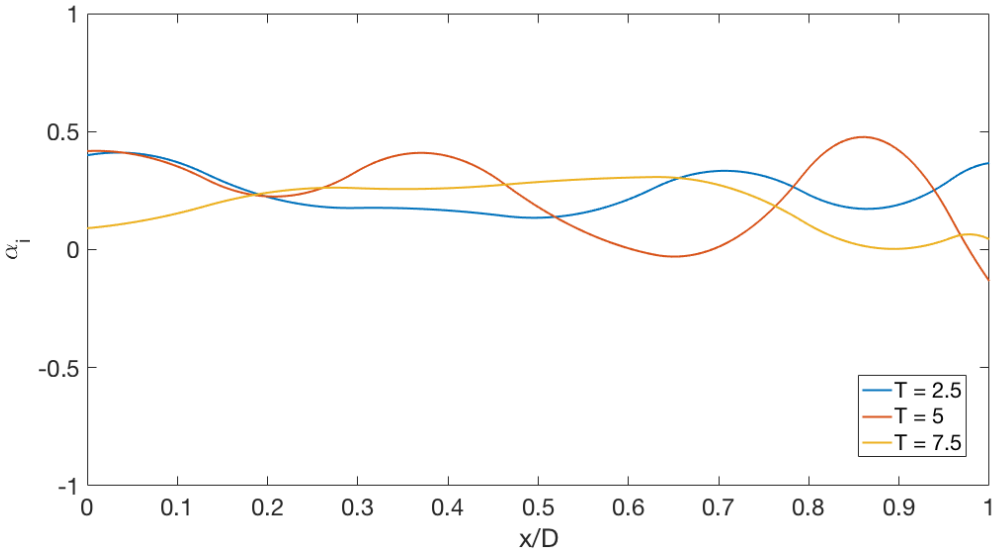

Figure 4.12 PIV measurements of the source vorticity ratio $\alpha_i = -\zeta_i/f$ for a low value of $I^* = 0.42$.

Figure 4.12 plots the value of the source vorticity ratio $\alpha_i = -\zeta_i/f$ across the source width D for the low I^* regime at early times. When viewed looking out of the source, the left-hand or upstream edge of the source is at $x/D = 0$, with the right-hand edge at $x/D = 1$. The measurements give a vorticity ratio that remains small and positive in general, though we see fluctuations across the source width and over time. The variability in the data is an unfortunate consequence of the limitations of the experimental setup, with actual measurements inside the source required for improved accuracy. The measurements of the vorticity were taken as close to the source as possible, but were still susceptible to interference from the ambient and the flow within the vortex. We expect this interference to cause a decrease in the vorticity and thus we estimate the value of α_i at the source to be the maximum value measured across the source width.

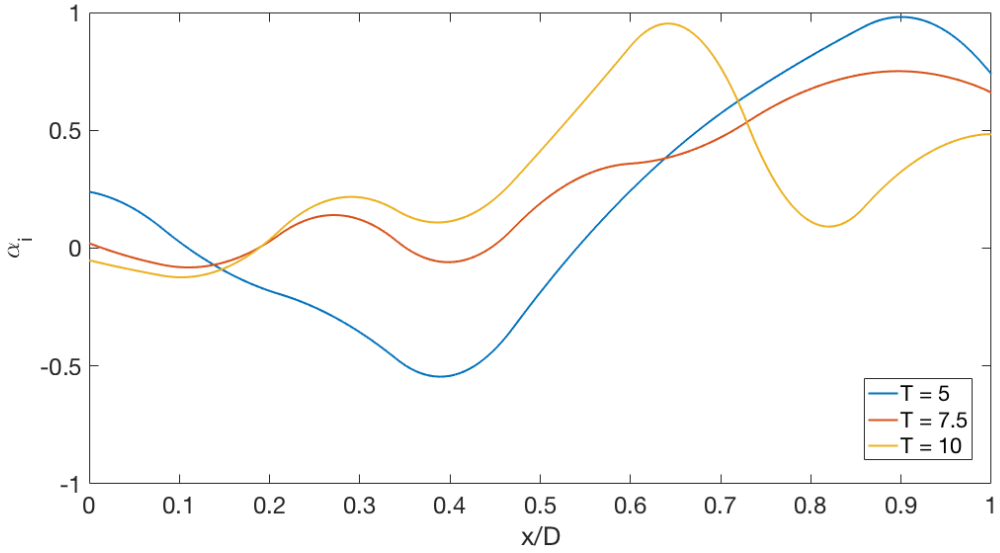

Figure 4.13 PIV measurements of the source vorticity ratio $\alpha_i = -\zeta_i/f$ for an intermediate value of $I^* = 0.97$.

Figure 4.13 shows the value of the source vorticity ratio $\alpha_i = -\zeta_i/f$ across the source width for an intermediate value of $I^* = 0.97$. Again we see fluctuations across the source width and over time. The value of α_i is much larger however, with the maximum at $T = 5$ reaching the zero PV limit of $\alpha_i = 1$.

The source vorticity ratio measurements for the high I^* regime are displayed in figure 4.14 at early times. The value again fluctuates across the source width and over time, but the profile shape remains relatively consistent, with the maximum value being reached at the right-hand edge of the source.

Figure 4.15 plots the estimated value of α_i from the four PIV experiments as a function of time. We estimate the value at the source by the maximum value seen in the profiles in figures 4.12 - 4.14. The mean values for each experiment at early times $T < 20$ are shown as solid lines and the estimated values from the theory are shown as dotted lines. For the data in figure 4.15 we see quite good agreement between the time-averaged mean value and the estimates from the theory, suggesting that the experimental values provide a reasonable estimate of the actual source conditions. Ultimately, measurements are needed inside the source opening just before the freshwater enters into the ambient to accurately quantify the source conditions, however, the measurements obtained here provide some insight into the initial PV at the source. There does not appear to be any trend between the source vorticity

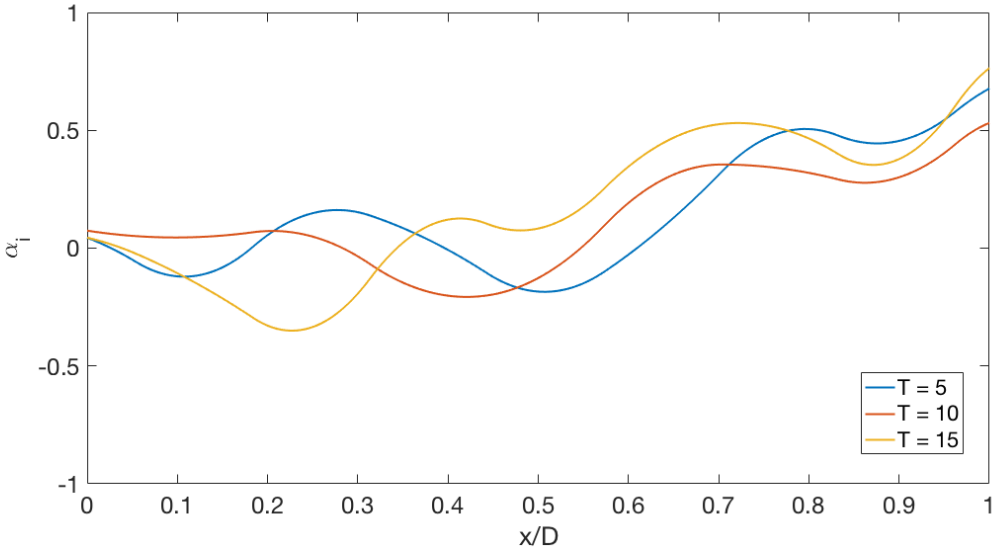

Figure 4.14 PIV measurements of the source vorticity ratio $\alpha_i = -\zeta_i/f$ for a high value of $I^* = 1.83$.

ratio and the value of I^*. For example, for the two experiments at intermediate values of $I^* = 0.85$ and $I^* = 0.97$ we see both the smallest and largest estimated values of α_i. The theoretical estimates for α_i are calculated by taking the maximum of the experimentally measured Rossby number and the theoretical Rossby number. The theoretical estimates for α_i will be discussed in more detail in section 4.4.4. Another important feature of the data in figure 4.15 is that for three out of the four experiments at low, intermediate and high values of I^*, the estimated value of α_i is smaller than 1. This means that the source has a non-zero value of potential vorticity for these experiments. We will investigate whether or not the finite PV of the source has an effect on the steady state current properties in the next section.

Whilst the data presented in this section provides some insight into the source conditions, ultimately more accurate measurements are required, in particular for the source vorticity. The measurements were made as close to the source as possible at $\sim 0.1 - 0.2$ cm in front of the source opening. As a result the values are distorted by the presence of the outflow vortex and by the shear generated at the boundary between the moving freshwater current and the stationary ambient. In future work, measurements are needed inside the source structure to provide a more accurate representation of the vorticity field at the source which can then be used in the theoretical models. We will outline one possible modification to the experimental setup that could be used to achieve the required measurements in future studies.

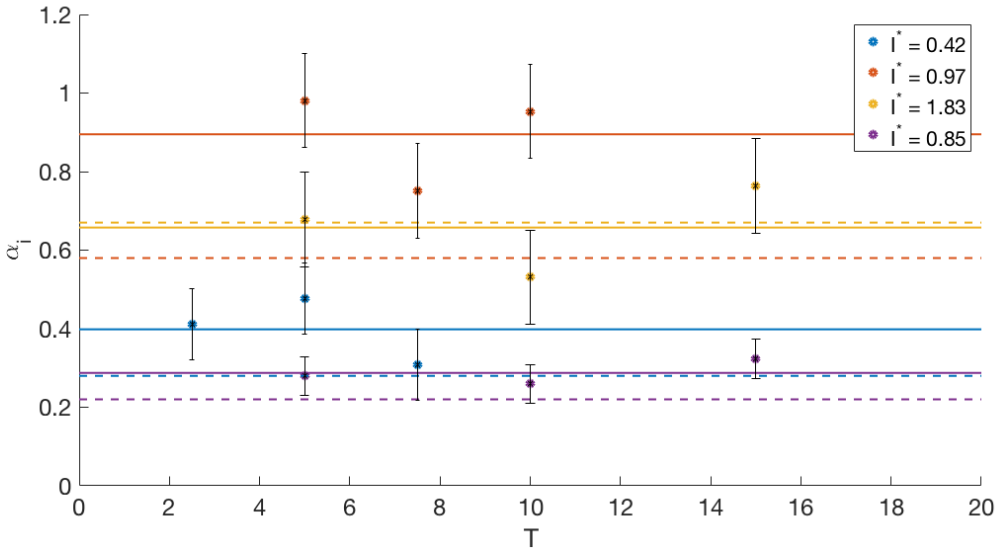

Figure 4.15 The estimated value of the source vorticity ratio α_i versus dimensionless time T.

Currently, the source opening is aligned with the boundary wall which prevents an aerial view of the flow within the source. By offsetting the source opening to be behind the boundary wall and creating a gap in the wall at the source, the flow can be viewed from above. Using similar PIV techniques to those used in the experiments described in this thesis, a light sheet may be used to illuminate the flow at the source which can be seeded with particles and recorded, thus enabling PIV measurements to be made using Digiflow. A diagram of the possible setup is shown in figure 4.16.

4.4 Current measurements

Having analysed the qualitative features of the boundary current via the current profiles and investigated the choice of model parameters for the wall velocity and source vorticity ratio, we now proceed to examine the effect of finite PV on the current properties. Experimental measurements of the key current properties of depth, width and velocity are presented and then compared with the steady state theoretical model.

Due to the unstable nature of the experiments in the high I^* regime, many of the measurements of the current properties are distorted by the propagation of vortices that have been shed by the main outflow bulge. Since we are concentrating on a comparison of the current

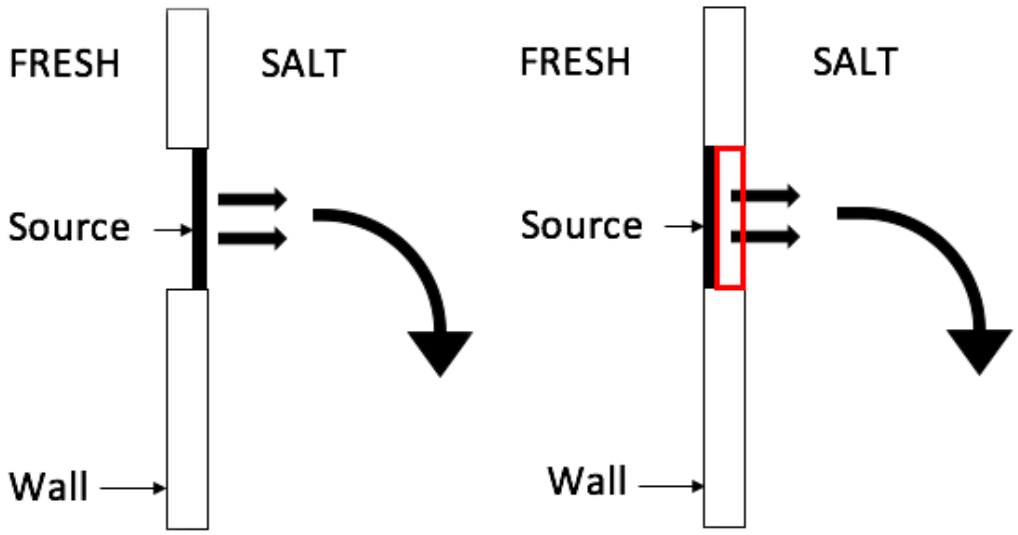

(a) Current experimental setup showing alignment of source and boundary wall.

(b) New experimental setup with source opening offset behind boundary wall.

Figure 4.16 Modified experimental setup near to the source to allow accurate measurements of the source vorticity field in future work. The red box indicates the area that can be viewed from above to allow PIV measurements to be made.

properties with the finite PV theoretical model of chapter 3, we only include measurements from the experiments that remain stable, i.e. at low and intermediate values of I^*. We also exclude three experiments where the outflow vortex grows so large that it collides with the far wall of the tank, interfering with the boundary current propagation. These experiments have the lowest values of I^* and the vortex is able to grow so large due to the low rotation rate and large density difference in these experiments. The full parameter ranges of the experiments considered in this section are: $0.5 \leq f \leq 2$ s^{-1}, $42 \leq Q \leq 100$ cm^3 s^{-1}, $2.1 \leq g' \leq 71.6$ cm s^{-2}, $2 \leq H_0 \leq 4$ cm and $2.5 \leq D \leq 5$ cm, giving the range $0.19 \leq I^* \leq 1.73$.

4.4.1 Current depth

The current depth was measured during each experiment at a fixed point alongside the wall of the tank. The point at which the depth measurements are made is taken as close to the source as possible, without interference from the outflow vortex, to allow maximum time between the first depth measurement and the end of the experiment. Full details of the methodology

I^*	Q [cm^3 s^{-1}]	f [s^{-1}]	g' [cm s^{-2}]	H_0 [cm]	D [cm]
0.19	74	1	69.1	2	2.5
0.60	42	2	70.3	2	5
0.75	47.5	1	15.8	2	5
0.95	72	2	15.4	4	5
1.15	42	0.5	2.3	2	5
1.55	45	2	14.7	2	5
1.73	62	2	13.5	2	5

Table 4.5 Experimental parameters for the experiments shown in figure 4.17.

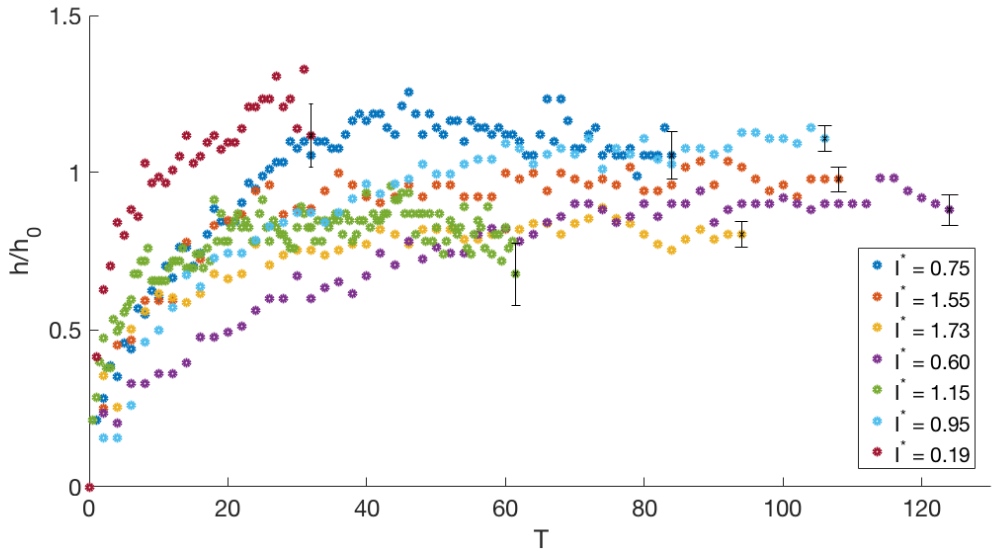

Figure 4.17 The fixed point current depth scaled with the maximum current depth, h_0, for a subset of the experiments. The legend gives the I^* values for the data shown.

are given in chapter 2 and the experimental parameters are shown in table 4.5.

Figure 4.17 plots the measured current depth over time for a subset of the experiments. The data from seven experiments are shown which are representative of the different behaviour seen across all of the stable experiments. The aspect ratio ratio has a range $0.19 \leq I^* \leq 1.73$. The current depth is scaled with the maximum geostrophic current depth value $h_0 = (2fQ/g')^{1/2}$ and time with the rotation rate f. The general pattern across all of the data is the same. The fastest increase in depth is seen initially, with the rate of increase gradually slowing down over time. For around $2/3$ of the experiments the current depth reaches an approximately constant value at long times. This can be seen in figure 4.17 for

the experiment with $I^* = 0.60$ which reaches an approximately constant value at $T \sim 80$ that is maintained until the end of the experiment at $T = 125$. In the remaining cases the depth is still increasing at the end of the experiment. An example of this behaviour is seen in figure 4.17 for $I^* = 0.19$. The fact that some of the experiments are stopped before a constant current depth has been reached is a constraint of the experimental setup. Each experimental run has to be stopped once the boundary has propagated around the full perimeter of the tank and returned back to the source. If we were to allow the experiment to continue beyond this point the current would interfere with the freshwater being released from the source and alter the initial conditions. This means that the experiments with the largest current velocity, which in general corresponds to low I^*, are less likely to reach a steady state and a constant current depth. Some of the experiments also show fluctuations in the measured values for the current depth, for example the runs with I^* values of $1.55, 1.73$ and 0.60 in figure 4.17. These fluctuations are possibly the result of waves along the density interface.

4.4.1.1 Theoretical comparison

In chapter 3 we saw that the theoretically predicted maximum current depth is the same across all models, regardless of the initial PV or the choice of wall velocity. The value of $h_0 = (2fQ/g')^{1/2}$ is the same as that in previous models of TL, Avicola and Huq (2002), Lentz and Helfrich (2002) and Horner-Devine et al. (2006) and is in fact fixed under the assumption of geostrophic balance in the current. The theory predicts that the maximum current depth will be achieved at the boundary wall and that it is independent of the x-coordinate meaning it will be the same along the length of the current. We saw in figures 4.1 - 4.3 that the depth is approximately constant in the x-direction once the initial current front has passed. The depth is also seen to increase with time as the flow tends towards a steady state and a final constant depth value. Since the theoretical model of chapter 3 assumes that a steady state has been reached, we will concentrate only on those experiments which demonstrate such behaviour, i.e. where the value of the current depth remains approximately constant at late times.

Figure 4.18 plots the ratio of the experimentally measured steady state current depth h_{ss} and the theoretically predicted maximum current depth h_0 versus the experimental Rossby number $Ro_{exp} = u_{exp}/(fw_{exp})$, where u_{exp} and w_{exp} are the experimentally measured current velocity and width respectively. The agreement between the theoretical model and the experimental data is on the whole quite good across a wide range of experimental parameters. The final values for h/h_0 lie in the approximate range $0.7 \leq h_{ss}/h_0 \leq 1.2$. In general the

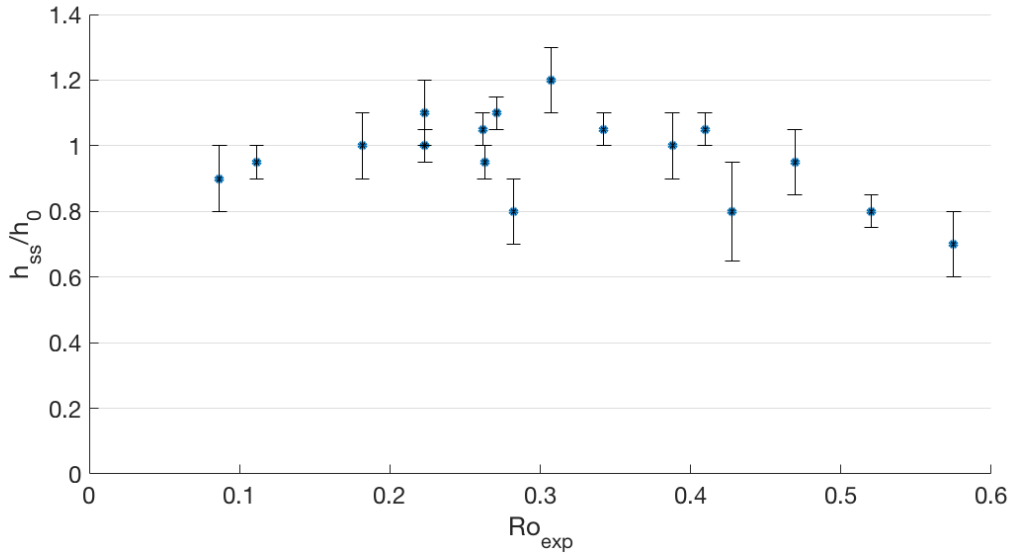

Figure 4.18 The ratio of the maximum experimentally measured steady state current depth h_{ss} and the theoretically predicted current depth h_0, versus the experimental Rossby number Ro_{exp}. Only the data from the experiments deemed to have reached a steady state before the end of the experiment are included.

experiments with the lowest Rossby number show the best agreement with the theory. For the lowest values of the Rossby number, $Ro < 0.3$, the agreement is good with $0.8 \leq h_{ss}/h_0 \leq 1.1$. As the value of Ro is increased further, the level of agreement decreases as we see the theory begins to over-estimate the experimentally measured values. The steady state theoretical model relies on the assumption that the flow is in geostrophic balance and the depth scaling h_0 is a direct consequence of this assumption. The assumption of geostrophy is valid for small Rossby number and the data in figure 4.18 suggest that the overestimation of the current depth for some of the experiments may be caused by the large value of the Rossby number.

4.4.2 Current width

The maximum width of the boundary current is measured for the duration of each experiment. The measurements are taken at a fixed location along the boundary of the tank which is chosen to be as close to the source as possible, but such that the current is unaffected by the presence of the outflow vortex. This is to allow the maximum amount of time between the first measurement and the end of the experiment. The full details of the method used for the measurements are given in chapter 2 and the experimental parameters are shown in table 4.6.

I^*	Q [cm^3 s^{-1}]	f [s^{-1}]	g' [cm s^{-2}]	H_0 [cm]	D [cm]
0.19	74	1	69.1	2	2.5
0.30	42	1	71.5	2	5
0.40	47.5	0.5	14.3	2	5
0.60	42	2	70.3	2	5
1.14	45	1.5	15.1	2	5
1.31	61	0.5	2.1	2	5
1.73	62	2	13.5	2	5

Table 4.6 Experimental parameters for the experiments shown in figure 4.19.

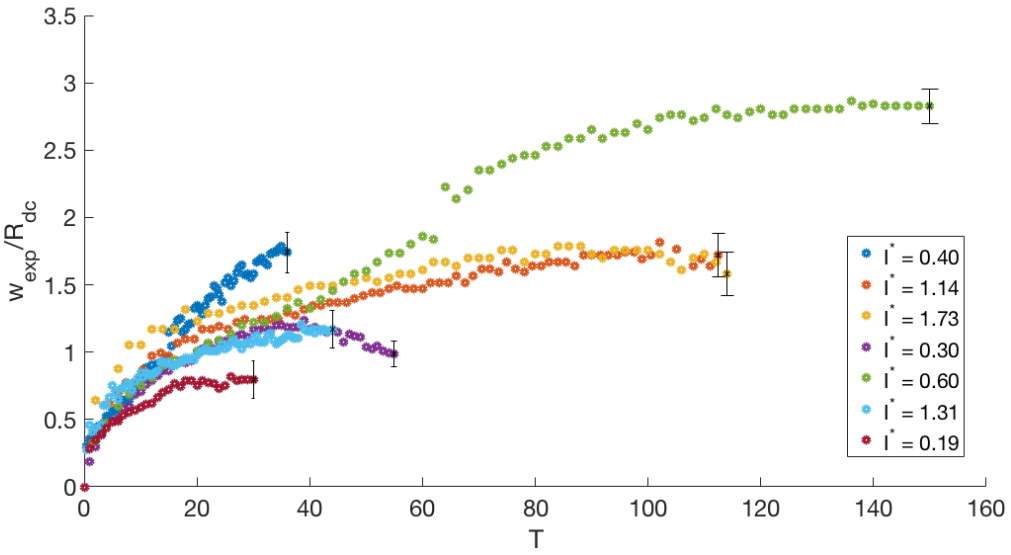

Figure 4.19 The experimentally measured current width, scaled with the current deformation radius $R_{dc} = \sqrt{g'h_0}/f$, versus time for a subset of the experiments.

The data from a subset of the experiments are shown in figure 4.19. The current width is scaled with the current deformation radius $R_{dc} = \sqrt{g'h_0}/f$ and time is non-dimensionalised by the rotation rate f. The experiments shown provide a good representation of the different behaviours seen across the experimental parameter range. The I^* values for the experiments from which the data are taken are given in the legend and have a range $0.19 \leq I^* \leq 1.73$. Typical error bars for each experiment are also shown. Overall, the data show the same trend across all of the experiments, with an increase in the current width over time at a rate which decreases with time. Around two-thirds of the experiments show a clear plateau in the value of w/R_{dc} suggesting that a steady state limit exists and is reached before the end of the experiment. The experiments with I^* values $1.14, 1.73$ and 0.19 in figure 4.19 are good examples of this type of behaviour. On the other hand, there are other experiments that are yet to reach a steady state before the end of the experiment. The current width for the run at $I^* = 0.40$ for example, looks to be still increasing at the end of the experiment and were the experiment allowed to run longer we would expect it to increase further. There are two further features in the data shown in figure 4.19 that require comment. Firstly, for the run at $I^* = 0.30$ we see an apparent decrease in the current width for $T > 40$ and for the run with $I^* = 0.60$ there is an apparent jump in the width at $T \sim 60$. Analysis of the experimental videos reveals both of these features to be incorrect, suggesting that they are in fact a result of the curve fitting process used to estimate the current width (see chapter 2). The data from these experiments have been included to provide examples of some of the possible pitfalls when using the curve fitting process.

We compare the finite PV theoretical model introduced in chapter 3 with the current width data in section 4.4.4. The model requires a choice of wall velocity U_l and source vorticity ratio α_i in order to fix all of the model parameters. Therefore, we first consider the current velocity data to aid our parameter choice.

4.4.3 Current length and velocity

Measurements of the current length were made using the technique of front-tracking as given in chapter 2. Figure 4.20 plots the experimentally measured current length versus dimensionless time $T = tf$. The current length is non-dimensionalised by $Q/(h_0 R_{dc} f)$, where $R_{dc} = \sqrt{g'h_0}/f$ is the current deformation radius. The start time for each set of measurements is taken as the time at which the current rounds the first corner of the tank. We see good

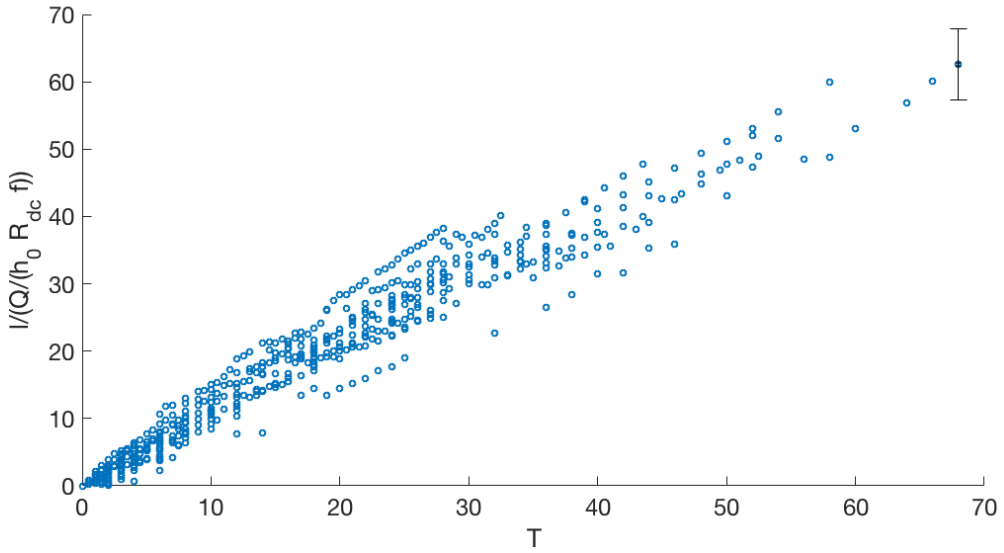

Figure 4.20 The non-dimensionalised current length versus dimensionless time $T = tf$.

collapse in the data across the full range of experimental parameters with $0.19 \leq I^* \leq 1.73$. The gradient of the curve is approximately constant for each of the experiments, implying a constant current speed. Estimates of the current speed are acquired by fitting a linear curve to the current length data for each experiment and this method is used to obtain the experimentally measured current speed u_{exp}. In each instance the linear regression curve gives a R^2-value greater than 0.96. The values of u_{exp} are used for comparison with the theory in section 4.4.4.

The measurements of the current length also enable estimates of the current velocity to be made at each timestep by considering the mean velocity l/t. It is important to emphasise that this is the mean velocity and not the instantaneous velocity dl/dt. The curves for dl/dt are very sensitive to measurement errors and can fluctuate substantially (as noted by TL). The mean velocity curves provide an estimate of the initial acceleration of the current for early times and then settle to an approximately constant value at later times. This value is equal to the gradient of the current length curves u_{exp}. Figure 4.21 displays the experimentally measured mean velocity versus dimensionless time $T = tf$ for a subset of the experiments that provide a good representation of the general behaviour seen in the data. The mean velocity is non-dimensionalised by $Q/(h_0 R_{dc})$. The experimental parameters are given in table 4.7.

I^*	Q [cm^3 s^{-1}]	f [s^{-1}]	g' [cm s^{-2}]	H_0 [cm]	D [cm]
0.19	74	1	69.1	2	2.5
0.40	47.5	0.5	14.3	2	5
0.43	100	0.5	15.8	2	5
1.14	45	1.5	15.1	2	5
1.15	42	0.5	2.3	2	5
1.31	61	0.5	2.1	2	5
1.73	62	2	13.5	2	5

Table 4.7 Experimental parameters for the experiments shown in figure 4.21.

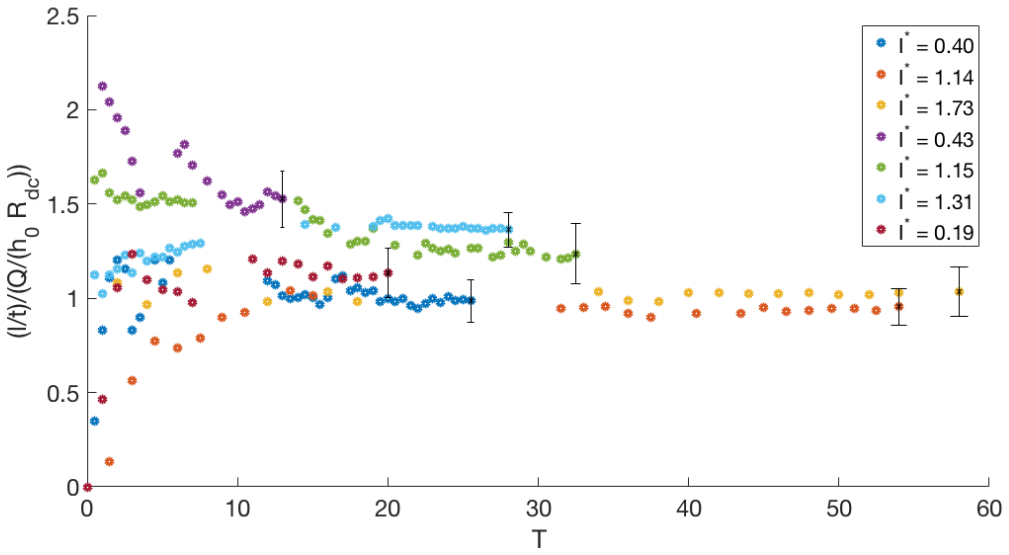

Figure 4.21 The experimentally measured mean current velocity l/t versus dimensionless time $T = tf$ for a subset of the experiments.

The data in figure 4.21 show two different qualitative behaviours. For the majority of the experiments the values of the mean velocity show an initial sharp increase, followed by a slight decrease, before settling to an approximately constant value at late times. However, for some of the experiments, such as for $I^* = 0.43$ and $I^* = 1.15$, the final constant value for the mean velocity is approached from above throughout. The mean velocity reaches its largest value initially and then decreases towards its long time limit. TL identified similar behaviour in their experimental data and found the transition to occur above a critical volume flux. The reduced gravity and rotation rate remained fixed across their experiments and thus they were unable to draw any concrete conclusions about the change in behaviour. The time-dependent theoretical model presented in chapter 7 reveals that the change in behaviour is the result of a change in the source vorticity ratio α_i. For low values of $\alpha_i \lesssim 0.6$ the current velocity approaches an approximately constant value from above, while for higher values of α_i the velocity increases initially before tending towards an approximately constant value. The data in figure 4.21 also show a slight decrease in the current velocity for some experiments at long times. It does not seem to be a major effect, but does demonstrate the possible effect of friction acting to slow down the current. The duration of our experiments is limited by the time taken for the current to propagate around the perimeter of the tank and therefore in general there is little time for the frictional effects to accumulate. We estimate this timescale as $h_0 w_0/\nu \sim O(100)$ seconds, where $\nu = 0.01\text{cm}^2\text{s}^{-1}$ is the kinematic viscosity of water. The longest experiment has a run time of 141 seconds. Were the experiments able to be run for a longer time we might expect the current velocity to continue to decrease at late times due to the accumulation of frictional effects.

4.4.4 Theoretical comparison

We compare the experimental data for the current width and current velocity with the theoretical model introduced in chapter 3. Since the theoretical modelling of the flow assumes that a steady state has been reached, we only consider those experiments that reach a steady state before the end of the experiment. For the current width data, we proceed as with the current depth data in section 4.4.1, by considering only the experiments for which the current width reaches an approximately constant value at long times. This constant long-time value is used as an estimate of the steady state value in the comparison with the theory. For the current velocity, it is more difficult to determine whether or not a steady state has been reached and as such we initially consider all of the data in the comparison. The theoretical

model requires a choice of wall velocity U_l and source vorticity ratio α_i in order to fix all of the model parameters. In the theoretical model of chapter 3 we approximated α_i by the theoretical Rossby number $Ro = u_0/(fw_0)$, but found that we were only able to obtain a solution for a limited range of values of the depth ratio H^*. We may also estimate α_i by the experimentally measured Rossby number $Ro_{exp} = u_{exp}/(fw_{exp})$ where a theoretical solution is unavailable. In section 4.3.2 measurements of the vorticity ratio close to the source were presented and compared with theoretical estimates for the source vorticity ratio α_i. The theoretical values of $\alpha_i = Ro_{max}$ were calculated from the maximum of the theoretical and experimental Rossby numbers and showed relatively good agreement with the data. We therefore use the same method here to derive the values of α_i to use in the model.

4.4.4.1 Zero wall velocity

We begin with a comparison of the experimental data with the zero wall velocity model corresponding to the choice $U_l = 0$. Figure 4.22 displays the ratio of the experimentally measured current width and the theoretically predicted value as a function of I^* for $\alpha_i = Ro_{max}$ and $\alpha_i = 1$ which corresponds to the case of zero PV. For the $\alpha_i = Ro_{max}$ data we see that the theory is overestimating the current width for the vast majority of the experiments. For the zero PV case, the theory tends to overestimate the current width at low values of I^* and underestimate the width at larger I^* values. In general, the agreement between the theory and the width data is poor for both $\alpha_i = Ro_{max}$ and $\alpha_i = 1$, with the zero PV model perhaps performing slightly better overall.

Figure 4.23 displays the ratio of the experimentally measured current velocity and the theoretically predicted value as a function of I^* for $\alpha_i = Ro_{max}$ and $\alpha_i = 1$. Estimated error bars are also shown. For $\alpha_i = Ro_{max}$ the model in general seems to underestimate the current velocity, particularly at larger values of I^*. The agreement is much better for a value of $\alpha_i = 1$ corresponding to the case of zero PV. In fact, the zero PV model is very robust across all values of I^* and shows good agreement with the data with $0.7 \lesssim u_{exp}/u_0 \lesssim 1.3$. This seems to suggest that the finite PV of the source does not play a dominant role in determining the current velocity in the case of a steady state model.

For both the current width and the current velocity the value of $\alpha_i = 1$ corresponding to the zero PV model of TL shows the best agreement with the data overall. The difficulty in estimating the value of the source vorticity ratio α_i hinders the application of the finite

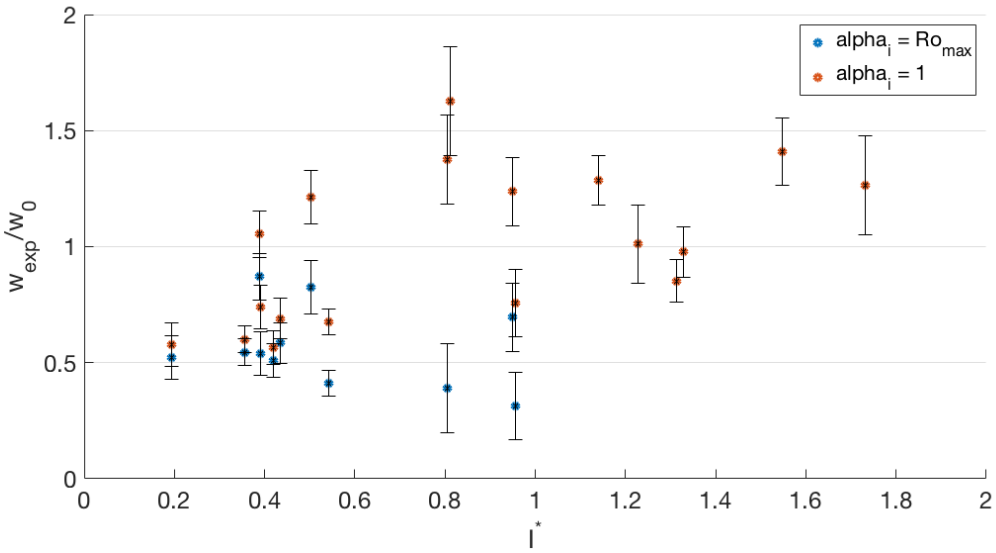

Figure 4.22 The experimentally measured current width scaled with the theoretical predictions using the estimated α_i values in the zero wall velocity model, versus the aspect ratio ratio I^*.

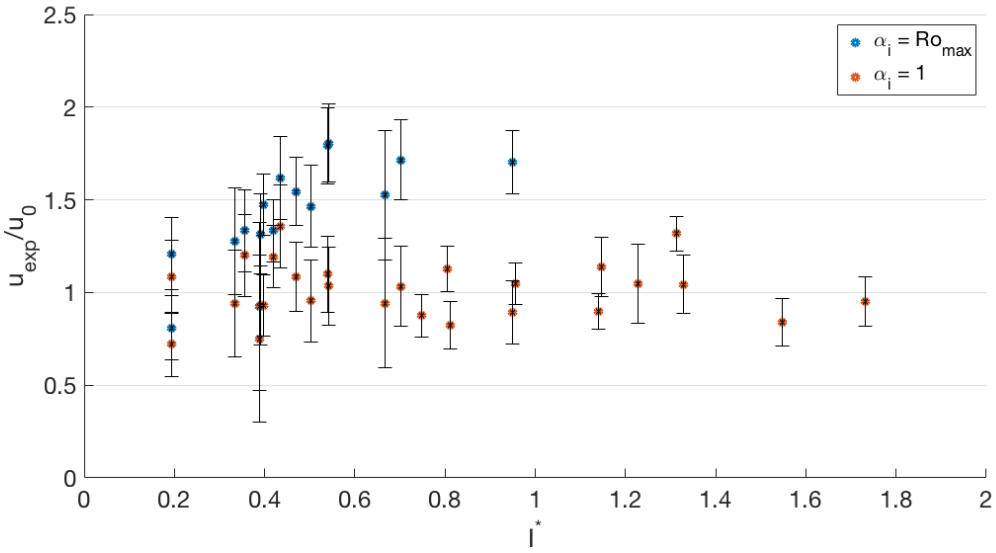

Figure 4.23 The ratio of the experimentally measured current velocity and the value predicted by the zero wall velocity model with the estimated α_i values.

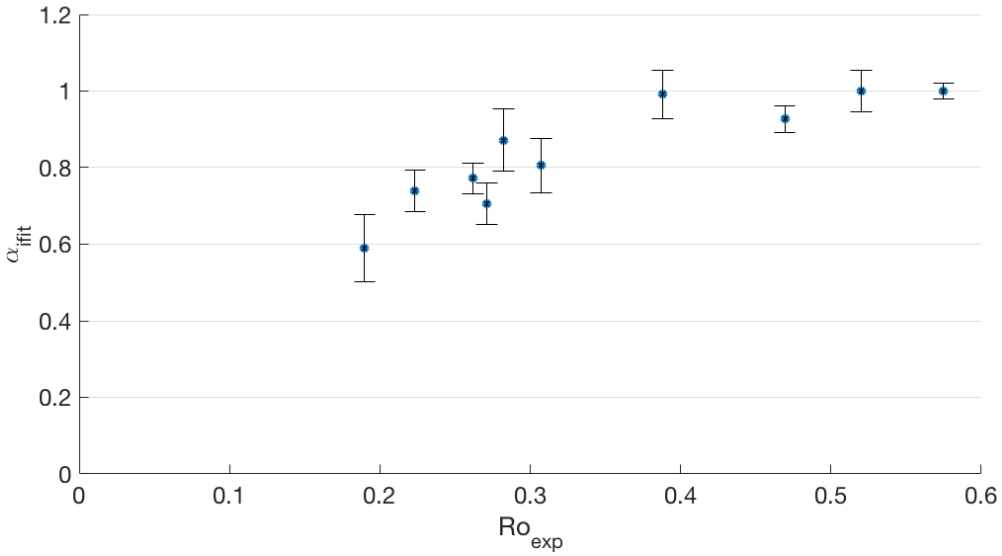

Figure 4.24 The value of α_i that provides the best fit between the experimental data and the zero wall velocity model versus the experimental Rossby number Ro_{exp}.

PV model, which is a possible reason for the poor agreement seen in figures 4.22 and 4.23. To investigate this further we present an alternative method of evaluating the performance of the model where we fit the experimental data to the model to determine the value of α_i that provides the best fit for each individual experiment. Such an approach is only possible a posteriori, but without accurate measurements of the source local vorticity available we hope that it will enable us to identify trends across the data and improve our understanding of the role that finite PV plays in the flow dynamics. To ensure that the estimated values of α_i obtained by fitting the data to the model are as accurate as possible, we will use both the width and velocity data together. Furthermore, only the experiments that are deemed to have reached a steady state for all current properties will be considered. The fitted values of α_i are calculated separately for both the current width and current velocity data and then the average value used in the model comparison. The ratio of the fitted values obtained from the two sets of data lies in the range $0.8 \leq \alpha_{iv}/\alpha_{iw} \leq 1.3$ which suggests that the mean value is an appropriate choice. The fitted values are plotted as a function of the experimental Rossby number in figure 4.24.

The fitted values lie in the range $0.6 \leq \alpha_i \leq 1$ and increase in value as Ro_{exp} increases. The values are in general larger than the estimates for $\alpha_i \sim Ro_{max}$ which explains the poor agreement seen in figures 4.22 and 4.23. The fitted values are close to 1 for many of the experiments which also explains why the zero PV model appears to provide the best agree-

ment with the data. The increase in the value of α_i with Rossby number suggests that the role of finite PV in governing the flow behaviour changes depending on the experimental parameter regime. For lower values of the Rossby number the finite PV of the source plays a more important role in the flow behaviour, but as the value of Ro_{exp} is increased its effect is reduced and a zero PV model is able to successfully capture the key flow dynamics. If we return to the zero PV model of TL and consider the Rossby number $Ro_z = u_{0z}/(fw_{0z})$ we obtain a constant value of 0.375. The data in figure 4.24 give a value of $\alpha_i \sim 1$ corresponding to a zero PV model for $Ro_{exp} > Ro_z$ and a decreasing value of α_i as Ro_{exp} decreases below Ro_z. This suggests that the critical value of the Rossby number, above which finite PV no longer plays a leading order role in the flow, is given by Ro_z.

Figure 4.25 plots the fitted values of α_i versus the experimentally measured current Froude number $Fr_c = u_{exp}/\sqrt{g'h_{ss}}$. We see similar behaviour to that in figure 4.24, with the finite PV of the source playing a more important role in governing the flow behaviour for small values of Fr_c and its effect diminishing as Fr_c increases. The critical value for this change in behaviour is $Fr_c \sim 0.5 - 0.6$ with a zero PV model able to capture the flow dynamics beyond this point. The zero PV model of TL gives a constant Froude number $Fr_z = u_{0z}/\sqrt{g'h_{0z}} = 0.5303$. The data in figure 4.25 show a transition to the zero PV model for $Fr_c > Fr_z$ with $\alpha_i = 1$ above this critical value. This suggests that there also exists a critical Froude number given by Fr_z, above which the finite PV of the source is no longer important in determining the flow behaviour.

Finally, figure 4.26 plots the fitted α_i values versus the ratio of the Rossby and Froude numbers Ro_{exp}/Fr_c. This number expresses the ratio of body forces to Coriolis forces present in the flow. The data reiterates the argument above regarding the existence of a critical value of the flow parameters, which according to the zero PV TL model is given by $Ro_z/Fr_z = 1/\sqrt{2}$. The data again support the use of this value. As well as the existence of a critical parameter value above which finite PV is no longer important, the data present evidence of a transition regime during which its importance diminishes. For small values of Ro/Fr the Coriolis forces dominate the flow behaviour. This means that in the initial PV of the source, $q_0 = (f + \zeta_i)/H_0$, the local vorticity term ζ_i is negligible compared to the Coriolis force f and can be neglected. This gives an initial PV of $q_0 \sim f/H_0$ which corresponds to $\alpha_i = 0$. As the value of Ro/Fr increases the body forces begin to play a role in the dynamics of the flow and correspondingly the initial local vorticity of the source is no longer negligible relative to f. This sees an increase in the value of $\alpha_i = -\zeta_i/f$, where

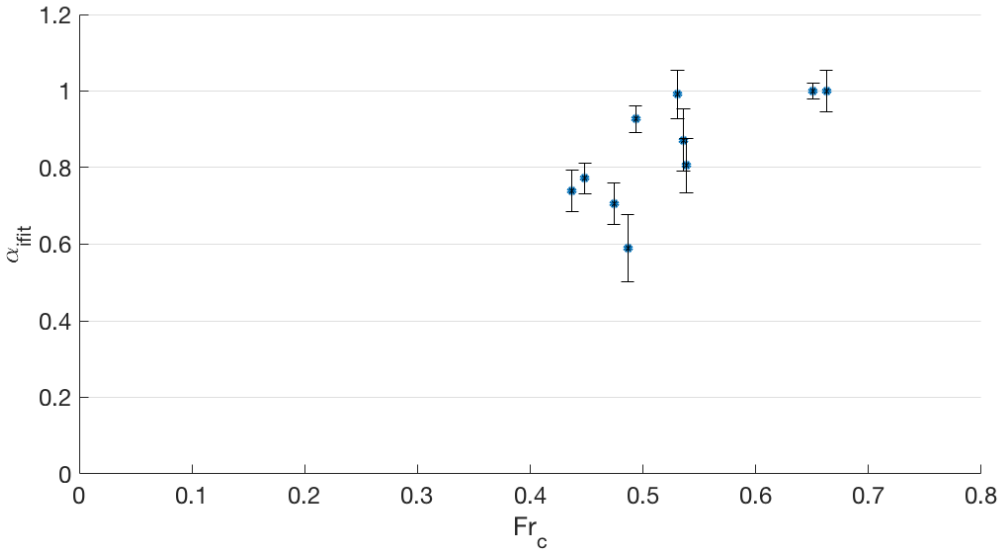

Figure 4.25 The value of α_i that provides the best fit between the experimental data and the zero wall velocity model versus the current Froude number Fr_c.

the vorticity is anticyclonic and thus negative. Once the value of Ro/Fr increases to the critical value of $1/\sqrt{2}$, the local vorticity and Coriolis terms are now of approximately equal magnitude and thus act to cancel each other out, reducing the source PV to zero. This corresponds to the increase in α_i to a value of 1 as seen in figure 4.26.

In summary, a comparison of the experimental data with the theory shows that the finite PV of the source is only important in determining the properties of the steady state boundary current below a critical parameter value. We find the critical value for the Rossby number and Froude number is given by the zero PV model values from the work of TL. Above this critical value, a zero PV model is able to capture the key current dynamics at steady state.

4.4.4.2 Finite wall velocity

We now use the same approach for the finite wall velocity model based on the use of a source Bernoulli condition. Figure 4.27 plots the ratio of the experimentally measured current width and the theoretical predictions from the Bernoulli source model with $\alpha_i = Ro_{max}$ and $\alpha_i = 1$, versus the aspect ratio ratio I^*. For $\alpha_i = Ro_{max}$ the theory underestimates the current width in general, particularly at lower values of I^*. The agreement improves as the value of I^* increases and we enter into the intermediate I^* regime. For the zero PV model the level of

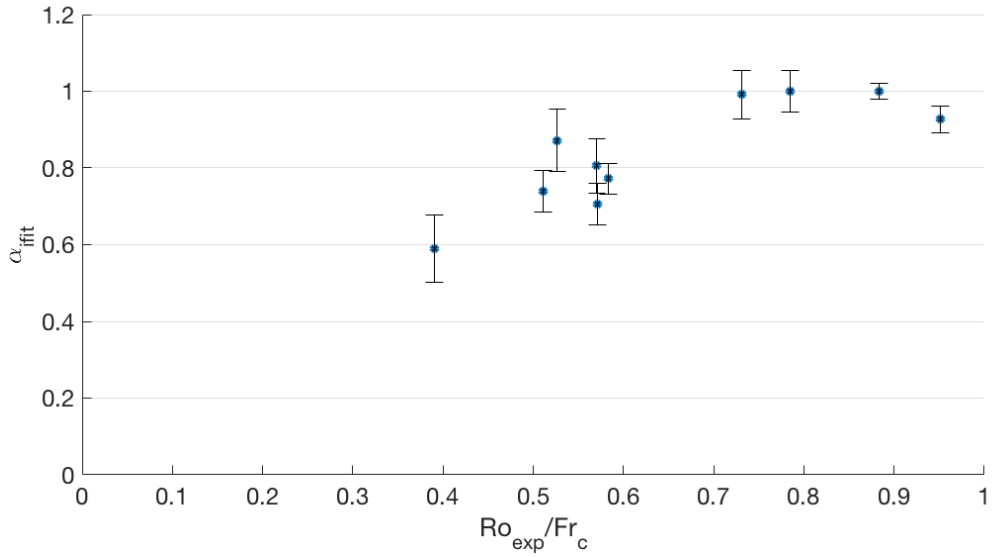

Figure 4.26 The value of α_i that provides the best fit between the experimental data and the zero wall velocity model versus the ratio of the experimental Rossby number and the current Froude number Ro_{exp}/Fr_c.

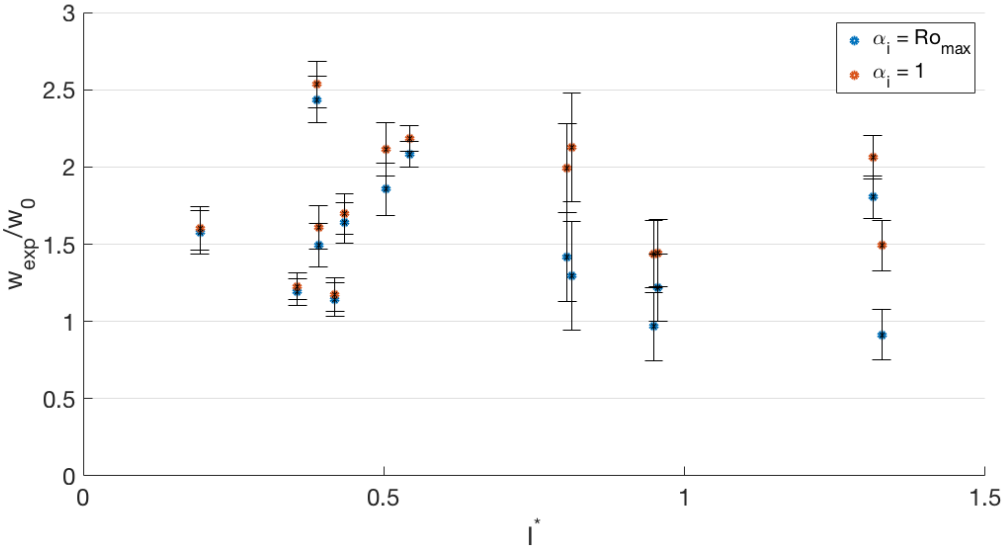

Figure 4.27 The experimentally measured current width scaled with the theoretical predictions using two estimates for α_i in the Bernoulli source model, versus the aspect ratio ratio l^*.

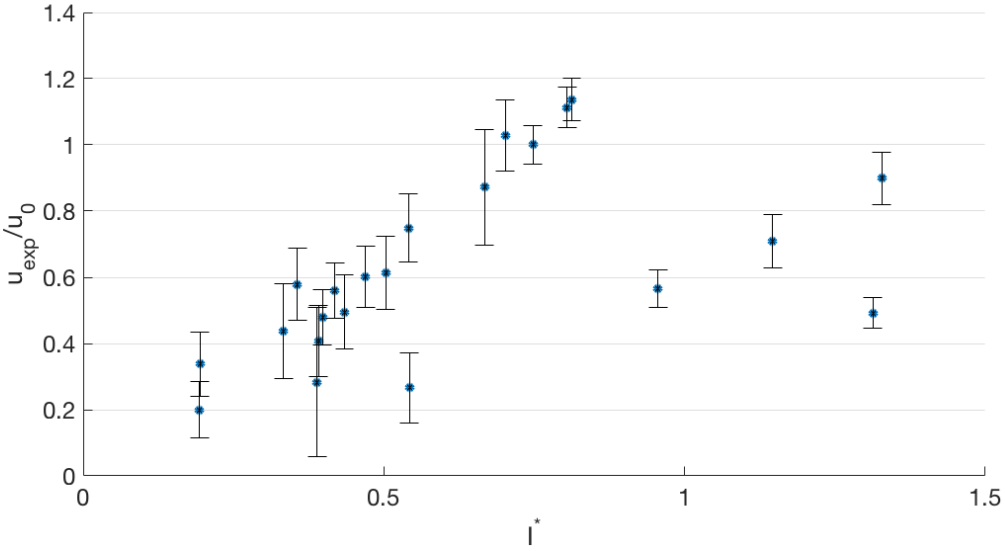

Figure 4.28 The experimentally measured current velocity scaled with the theoretical predictions for the Bernoulli source model, versus the aspect ratio ratio I^*.

agreement is also quite poor, with the theory tending to underestimate the current width. The data for the two models are very similar, despite the changing value of α_i. This suggests that the cause of the disagreement between the theory and the data is not due to the choice of source PV in the model, but is a result of the choice of the upstream Bernoulli based on the source conditions. To investigate this further we consider the ratio of the experimentally measured current velocity and the theoretical prediction from the source Bernoulli model as a function of I^* in figure 4.28. The value of U_l is fixed according to the source Bernoulli $B^* = (Fr^2 + 2)/H^*$ (see section 3.2.2.2) where all of the parameters are known and thus has no dependence on the unknown initial source vorticity ratio α_i.

The model in general over-estimates the current velocity for the majority of the experimental runs, suggesting that the use of the source conditions for the upstream Bernoulli B^* is an incorrect assumption in our model. This is in agreement with the current width data in figure 4.27. In chapter 7 we present a time-dependent model for the boundary current that incorporates the presence of the outflow vortex. For this model the conditions in the vortex are used to fix the upstream Bernoulli and therefore U_l. For the steady state current model being considered here, we investigate the suitability of a finite wall velocity model by using the experimentally measured current velocity u_{exp} to fix the value of U_l. This will be used to fit the current width data to the theory to determine the best choice for the value of α_i as we

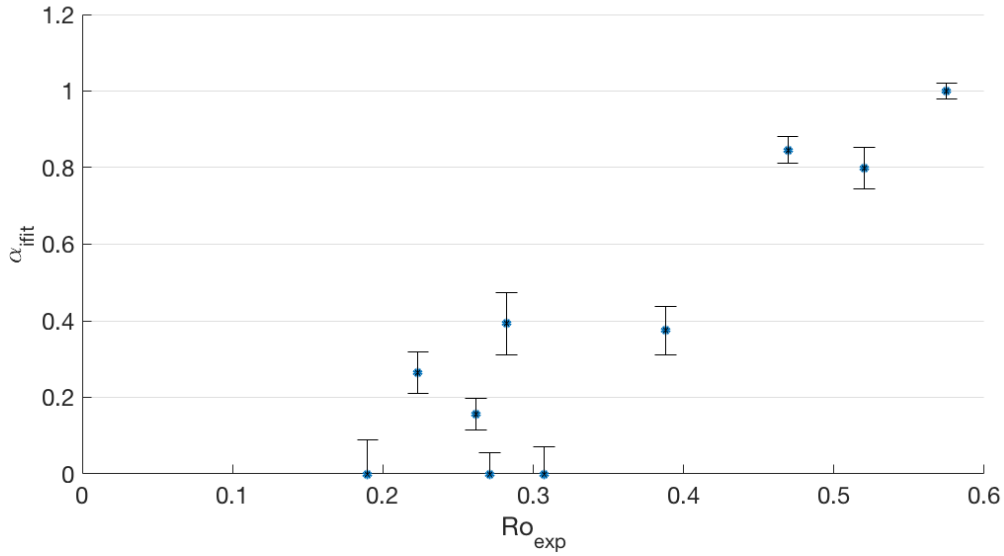

Figure 4.29 A plot of the value of α_i that provides the best fit between the experimental data and the finite wall velocity model for the current width data versus Ro_{exp}.

have done previously for the zero wall velocity model.

The fitted values of α_i for the finite wall velocity model with $U_l = u_{exp}$ are displayed in figure 4.29 versus the experimental Rossby number. We only consider the experiments that appear to have reached a steady state for both the current width and the current depth. We see a larger range of values for α_i for the finite wall velocity model than for the zero wall velocity model (see figure 4.24) with $0 \leq \alpha_i \leq 1$. The value of α_i increases with increasing Ro_{exp}, which is the same behaviour as seen for the zero wall velocity model. Analysis of the dependence on the Froude number also reveals an increase in α_i with increasing Fr_c. Figure 4.30 plots the fitted values of α_i from the Bernoulli model versus Ro_{exp}/Fr_c. Again we see an increase in the value of α_i with increasing Ro_{exp}/Fr_c. As with the zero wall velocity model, the data for the finite wall velocity model also suggest a transition to a zero PV model beyond a critical parameter value. For the zero wall velocity model the value of the critical parameter could be determined from the zero PV model of TL which gives a constant value for the Rossby and Froude numbers. In the case of the finite wall velocity model, there is no such constant and therefore we rely on the data to determine the critical parameter values. The data suggest critical values of $Ro_{exp} \sim 0.5-0.6, Fr_c \sim 0.6-0.7$ and $Ro/Fr_c \sim 0.9-1$.

In summary, we once again see that the finite PV of the source is only important in determining the steady state current properties below a critical parameter value. The transition

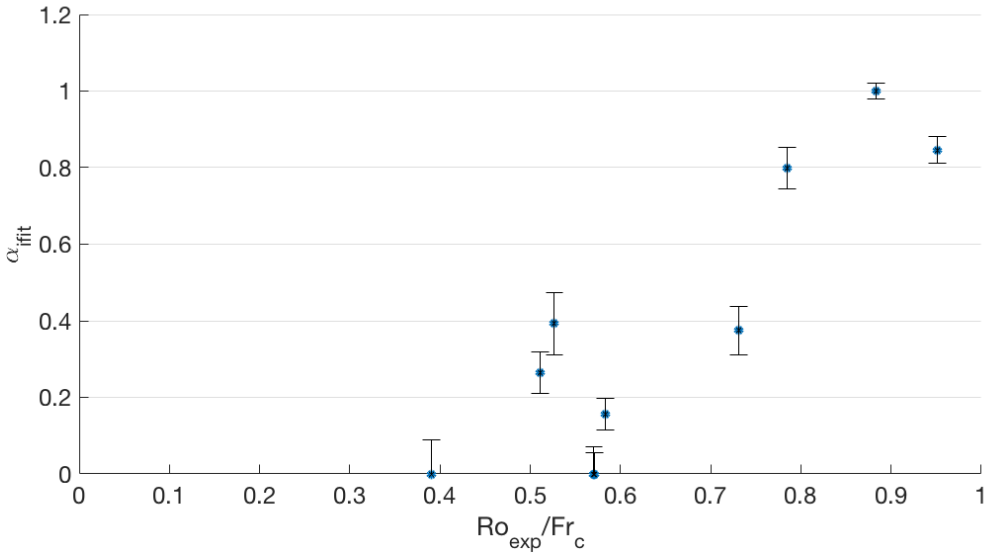

Figure 4.30 The fitted α_i values from the finite wall velocity Bernoulli model versus Ro_{exp}/Fr_c for the subset of the experiments that best represent a steady state.

from a finite PV model to a zero PV model is less clear than for the zero wall velocity model, but the critical values of the Rossby and Froude numbers can be estimated from the data, giving larger values than for the zero wall velocity model.

4.5 Discussion

Experiments were conducted in the laboratory to simulate the real-world scenario of a buoyant outflow discharging into the ocean. The introduction of a horizontal source of finite depth to provide more realistic outflow conditions led to the need for a finite PV theoretical model for the steady state current which was introduced in chapter 3. In this chapter we have compared the experimental observations with the theory.

The theoretical model was presented with a choice for the value of the wall velocity. Velocity profiles were measured experimentally across the current and the wall velocity was found to range from $0-1/2$ times the peak current velocity. The range of values seen makes it difficult to draw any firm conclusions and thus the use of either of the zero or finite wall velocity models may be appropriate depending on the parameter range. The model also requires parameterisation of the source vorticity ratio α_i. The value was estimated using experimental measurements close to the source and the use of the approximation of $\alpha_i \sim Ro_{max}$ was

seen to perform reasonably well, though ultimately more accurate measurements are required.

Measurements of the maximum current depth showed that once the current has reached a steady state the theory gives good agreement with the data, particularly at low values of Ro_{exp}. A finite value of PV did not affect the maximum current depth, as predicted by the theory. Measurements of the current width and velocity were used to fit the experimental data to the theoretical model to derive estimates for the value of the source vorticity ratio for the experiments that were deemed to have reached a steady state. The value of α_i was seen to increase with Rossby number, current Froude number and the ratio Ro/Fr_c for both the zero wall velocity and finite wall velocity models. For both models, a zero PV approximation was able to capture the key flow dynamics beyond a critical parameter value. For the zero wall velocity model the critical values of Ro, Fr_c and Ro/Fr_c are given by the zero PV TL model values. For the finite wall velocity model, the critical values are estimated from the data.

Ultimately, we believe that the use of a steady state model for the boundary current limits the ability of the theory to fully capture the flow behaviour. Whilst we see reasonable agreement for the quantitative features of the current, such as the maximum depth, width and velocity, the model is unable to accurately predict many of the qualitiative features seen in the experiments, such as the current depth profile shape and the across current velocity profile. To really understand these features a time-dependent theoretical model is required, which will be derived in chapter 7.

Chapter 5

Theoretical model for the outflow vortex

5.1 Problem description

In chapters 3 and 4 we investigated the properties of the coastal gravity currents that form when a buoyant outflow enters into a rotating environment. There is a second important feature present for these outflows that takes the form of a large vortex located next to the freshwater source. The growth of this outflow vortex will be discussed in this chapter.

The work of Nof and Pichevin (2001), hereafter NP, modelled the growth of an outflow bulge formed when water of anomalous density empties into an ocean. They presented a nonlinear analytical solution for the growth of a bulge on a f-plane under the assumption that the problem was slowly-varying in time and the vortex was approximately circular. They found for an outflow with weakly anticyclonic relative vorticity equal to $-\alpha f$, where α is analogous to the Rossby number, the vortex radius grows according to

$$R_{NP} = \left(R_i^4 + \frac{32 g' Q (t - t_i)}{\pi f^2 (1 + 2\alpha)(2 - \alpha)} \right)^{1/4}, \tag{5.1}$$

whilst the maximum vortex depth grows as

$$H_{NP} = \left(H_i^2 + \frac{f^2 \alpha^2 (2 - \alpha) Q (t - t_i)}{(1 + 2\alpha) 2\pi g'} \right)^{1/2}. \tag{5.2}$$

The initial state denoted with the subscript i refers to an arbitrary time at which the bulge is already much larger than the downstream current. These results combine to give the vortex

depth profile as

$$h_{NP} = H_{NP} + \frac{\alpha f^2 r^2 (\alpha - 2)}{8g'}. \tag{5.3}$$

In the analytical model, α is assumed to be constant on the fast timescale associated with geostrophic adjustment, $O(1/f)$, which enables the solutions for the vortex growth to be obtained. In the numerical simulations the PV is seen to decrease over a longer timescale due to the accumulation of small frictional effects.

Griffiths and Linden (1981), hereafter GL, investigated the growth of a vortex formed by releasing a constant flux of freshwater into a rotating saltwater environment. They constructed an inviscid flow model based on the principle of conservation of potential vorticity which was used to model the growth of a zero potential vorticity vortex. The volume of the vortex at time t is given by

$$Qt = \frac{1}{2}\pi R^2 H_a \Big(1 - \frac{2R_{da} I_1(R/R_{da})}{R I_0(R/R_{da})}\Big), \tag{5.4}$$

where H_a is the ambient depth, $R_{da} = \sqrt{g'H_a}/f$ is the Rossby radius of deformation for the ambient, R is the vortex radius at time t and I_0 and I_1 are modified Bessel functions of the first kind. The depth profile of the vortex is given by

$$h_{GL} = H_{GL} - \frac{H_a(I_0(r/R_{da}) - 1)}{2I_0(R/R_{da})}, \tag{5.5}$$

where the maximum vortex depth is

$$H_{GL} = \frac{H_a(I_0(R/R_{da}) - 1)}{2I_0(R/R_{da})}. \tag{5.6}$$

In the limit of a shallow vortex, $H/H_a << 1$ the series expansions of I_0 and I_1 give the explicit behaviour of the vortex radius and maximum depth with time as

$$\hat{R_{GL}} \sim (\frac{16\hat{t}}{\pi})^{1/4}, \tag{5.7}$$

$$\hat{H_{GL}} \sim (\frac{\hat{t}}{4\pi})^{1/2}, \tag{5.8}$$

where the depth and radius are non-dimensionalised by g'/f^2 and dimensionless time is $\hat{t} = Qf^6 t/g'^3$.

The experiments of Horner-Devine et al. (2006) and Avicola and Huq (2003) also investigated the time-dependent growth of the outflow bulge. They both found the depth of the bulge to increase slowly over time with an exponential fit of t^n giving $n < 0.16$ and $n = 0.2$, while for the growth of the radius they found $n = 0.25 - 0.39$ and $n = 0.4$ respectively.

We saw in chapter 2 that for our experiments with a finite PV source, an anticyclonic vortex forms next to the source which feeds into the propagating boundary current. Our analysis in chapters 3 and 4 has neglected the presence of the outflow vortex and considered the properties of the boundary current in a steady state. We will now consider the effect of a finite PV source on the growth of the outflow vortex. In this chapter we extend the model of GL to the case of a finite PV source and look to compare the new model with that of NP. Both models will then be compared with experimental data in chapter 6. Here we are continuing our investigation into the effect of finite PV on the flow dynamics, as well as beginning to address the second key question of this thesis: what is the role of the presence of the outflow vortex?

5.2 Theoretical model

The GL model assumes that once the outflow has spread radially over an area much greater than that of the source, the source may be regarded as a delta function at the origin (Gill et al. 1979). This assumption led to the construction of a zero PV model for the growth of the vortex. In our experiments the source of freshwater is of a finite size and supplies the flow with a source of non-zero potential vorticity. We present a modified version of the GL model to include the effects of finite PV on the growth of the vortex produced from a constant flux source.

5.2.1 Shallow vortex model

We consider an inviscid model for the growth of an anticyclonic vortex formed by the release of a constant flux of freshwater into a rotating saltwater environment. Initially the saltwater ambient is in solid body rotation and the presence of the boundary wall is neglected. The effect of this assumption will be discussed in more detail in section 5.4. The model is constructed following the same methods as those used by GL, but with the important modification to include the effects of a finite PV source. This is done by introducing the

vorticity ratio parameter $\alpha = -\zeta/f$ as used in the model of NP. The value $\alpha = 1$ corresponds to a zero PV outflow and substituting this into the new model will recover the original model of GL.

We begin by appealing to the principle of conservation of potential vorticity in the inviscid flow both inside and outside of the vortex. Working in polar coordinates, the local vorticity in the vortex ζ_v is given by

$$\zeta_v = \frac{1}{r}\left(\frac{\partial}{\partial r}(rv_\theta) - \frac{\partial v_r}{\partial \theta}\right), \tag{5.9}$$

where v_θ and v_r are the tangential and radial velocity components respectively. Assuming that $v_r = 0$, which will be the case for a rigid-body-like vortex, we substitute for $\zeta_v = -\alpha f$, rearrange and integrate to obtain the vortex tangential velocity

$$v_\theta = -\frac{\alpha}{2} f r, \tag{5.10}$$

where we have assumed a zero velocity at the vortex centre. The assumptions relating to the vortex velocity field are verified with analysis of the experimental data in section 6.2.4. For a constant value of α this gives a linear velocity profile outwards from the centre of the vortex. As with the NP model, we assume that the value of the vorticity ratio α remains approximately constant in time. This assumption is discussed in much greater detail in section 6.2.4 and chapter 7. In the saltwater ambient of depth H_a, the initial PV is f/H_a. Since PV is conserved we have

$$\frac{f + \zeta_a}{H_a - h_v} = \frac{f}{H_a}, \tag{5.11}$$

where ζ_a is the relative vorticity in the ambient and h_v the vortex depth. Changing to polar coordinates such that $\zeta_a = dv_a/dr + v_a/r$ and rearranging, we find that the ambient tangential velocity v_a is given by

$$\frac{dv_a}{dr} + \frac{v_a}{r} = -f\frac{h_v}{H_a}. \tag{5.12}$$

Proceeding in the same manner as GL we assume that the incoming volume flux is small, meaning that the radial pressure gradient due to buoyancy forces must be balanced by the coriolis and centrifugal forces. This assumption is valid for the volume flux Q much less than the vortex volume and is verified by experimental data for the vortex depth and radius in section 6.3. For a Boussinesq fluid under the hydrostatic approximation (see chapter 1) this means

$$f(v_\theta - v_a) + \frac{v_\theta^2}{r} - \frac{v_a^2}{r} = g'\frac{dh_v}{dr}. \tag{5.13}$$

Here we make the important assumption that the vortex is much shallower than the ambient, $H/H_a << 1$, where H is the vortex maximum depth at the centre. This means that $v_a^2 << v_\theta^2$ and thus we can neglect the centrifugal force in the ambient. The conditions for this assumption are discussed in more detail in section 5.3 and the experiments used for comparison with the model in section 6.3.3 are chosen to satisfy these conditions. Differentiating (5.12) and substituting for dh_v/dr in (5.13) gives a second order differential equation for the ambient velocity v_a

$$r^2\frac{d^2v_a}{dr^2}+r\frac{dv_a}{dr}-\big(1+\frac{r^2f^2}{g'H_a}\big)v_a=\frac{f^3r^3}{4g'H_a}\alpha(2-\alpha). \tag{5.14}$$

With a change of variables to r/R_{da}, where $R_{da}=\sqrt{g'H_a}/f$ is the Rossby deformation radius for the ambient, (5.14) has the form of a modified Bessel's equation. The solution regular at the origin is given by the modified Bessel function of the first kind I_1. The full solution is

$$v_a=AI_1(r/R_{da})-\frac{fr}{4}\alpha(2-\alpha). \tag{5.15}$$

The constant A is to determined by a boundary condition at $r=R$, where R is the vortex radius at the surface. The analysis here is identical to that of GL since we are working in the ambient. Appealing to mass conservation we must have that the flux across any cylindrical surface of radius $r\geq R$ in the ambient is equal to the volume flux Q into the vortex. Expressed mathematically this means

$$Q=2\pi rH_au_r, \tag{5.16}$$

where $u_r=dr/dt$ is the radial velocity component. We may integrate to obtain the initial radial displacement of fluid at $r=r_0$ as

$$r^2-r_0^2=\frac{Qt}{\pi H_a}. \tag{5.17}$$

We next appeal to the conservation of angular momentum which gives

$$v_Lr=\frac{1}{2}fr_0^2, \tag{5.18}$$

where v_L is the tangential velocity measured in the laboratory frame. We substitute for r_0^2 in (5.17) and convert back to the rotating frame by subtracting the velocity $fr^2/2$ to obtain

$$v_a=-\frac{fQt}{2\pi H_ar}, \tag{5.19}$$

for $r \geq R$. Substituting for our solution for v_a in (5.15) the boundary condition at $r = R$ becomes

$$-\frac{fQt}{2\pi H_a R} = AI_1(R/R_{da}) - \frac{fR}{4}\alpha(2-\alpha). \tag{5.20}$$

To apply the boundary condition in (5.20) we first need to calculate the vortex volume Qt. Returning to (5.13) and substituting in our solutions for v_a in (5.15) and for v_θ in (5.10), we obtain

$$g'\frac{dh_v}{dr} = -fAI_1(r/R_{da}). \tag{5.21}$$

Using the relation $I_1(z) = \frac{d}{dz}I_0(z)$ we are able to integrate (5.21) to give

$$g'h_v = C - fR_{da}AI_0(r/R_{da}), \tag{5.22}$$

where $C = fR_{da}AI_0(R/R_{da})$ is fixed by the condition that $h_v = 0$ at $r = R$. To find the volume we integrate the depth profile h_v over the vortex:

$$Qt = \frac{R_{da}2\pi fA}{g'}\int_0^R I_0(R/R_{da})r - rI_0(r/R_{da})dr. \tag{5.23}$$

where we use the identity $\int xI_0(x)dx = xI_1(x)$ to integrate the Bessel funtion $I_0(r/R_{da})$. The final result is given by

$$Qt = \frac{R_{da}2\pi fA}{g'}\big(I_0(R/R_{da})\frac{R^2}{2} - R_{da}RI_1(r/R_{da})\big). \tag{5.24}$$

Substituting for Qt from (5.24) into (5.20) allows us to solve for the constant $A = \frac{R_{da}f\alpha(2-\alpha)}{2I_0(R/R_{da})}$. Returning to (5.24) and substituting in for A gives the vortex volume at time t as

$$Qt = \frac{\pi R^2 H_a\alpha(2-\alpha)}{2}\Big(1 - \frac{2R_{da}I_1(R/R_{da})}{RI_0(R/R_{da})}\Big). \tag{5.25}$$

The depth of the vortex at time t is therefore given by

$$h_v(r,t) = H(t) - \alpha(2-\alpha)\frac{H_a(I_0(r/R_{da})-1)}{2I_0(R/R_{da})}, \tag{5.26}$$

where $H(t)$ is the maximum vortex depth at $r = 0$ and is given by

$$H(t) = \alpha(2-\alpha)\frac{H_a}{2}\Big(\frac{I_0(R/R_{da})-1}{I_0(R/R_{da})}\Big). \tag{5.27}$$

Comparing these results with those of the original GL model we see that they are identical except for the $\alpha(2-\alpha)$ factor that appears here in all of (5.25), (5.26) and (5.27). These expressions give the exact shallow vortex model solution.

Again following the methods of GL we seek to obtain more information about the explicit time-dependent behaviour of the vortex radius R and maximum depth H by using the shallow vortex approximation. Recall that we used the approximation $H/H_a << 1$ above to simplify (5.13) and we shall use it here again to enable us to use the series expansions of $I_0(z) \sim 1+z^2/4+...$ and $I_1(z) \sim z/2+z^3/16+...$ in (5.25) and (5.27). Expanding first in (5.25) we obtain at leading order

$$Qt \sim \frac{\pi H_a R^4}{16 R_{da}^2}\alpha(2-\alpha), \tag{5.28}$$

which can be rearranged to give R as a function of t. We non-dimensionalise the variables with $\hat{R} = f^2 R/g'$ and $\hat{t} = Qf^6 t/g'^3$ to give the result

$$\hat{R} \sim \Big(\frac{16\hat{t}}{\pi\alpha(2-\alpha)}\Big)^{1/4}. \tag{5.29}$$

Finally using the series expansion in (5.27) and substituting for $\hat{R}$ we have

$$\hat{H} \sim \Big(\frac{\alpha(2-\alpha)\hat{t}}{4\pi}\Big)^{1/2}, \tag{5.30}$$

where the dimensionless depth $\hat{H} = f^2 H/g'$. We see that $\hat{R} \sim \hat{t}^{1/4}$ and $\hat{H} \sim \hat{t}^{1/2}$ in the same way as the NP model expressions in (5.1) and (5.2), though the dependence on the vorticity ratio α is different. The expressions in (5.29) and (5.30) give the approximated shallow vortex model solution which has the advantage over the exact solution of giving the explicit time dependent growth of both the vortex radius and depth. We will compare the two shallow vortex models with the NP model in the next section.

5.3 Model comparison

We begin our comparison of the shallow vortex and NP models with an analysis of the depth profiles given in (5.26) and (5.3). The shallow vortex model depth profile is displayed in figure 5.1 at four different times for $\alpha = 0.5$. The form of the equation in (5.26) suggests a

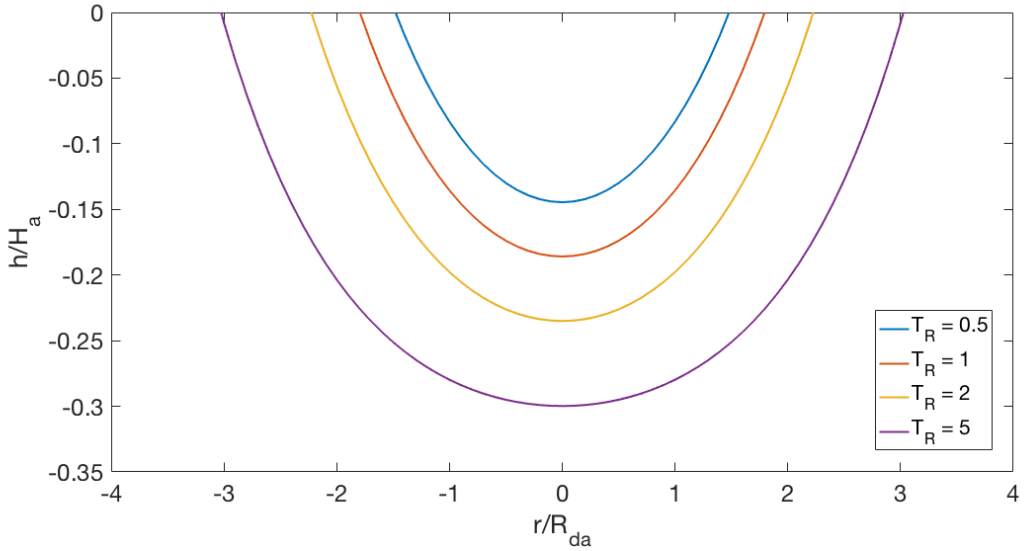

Figure 5.1 Vortex depth profiles at five different times for the shallow vortex model. The source vorticity ratio is fixed at $\alpha = 0.5$

non-dimensionalisation by the ambient depth H_a and the ambient deformation radius R_{da}. We define a dimensionless time by $T_R = tQ/(H_a R_{da}^2)$. The solution gives a symmetric vortex depth profile with depth and radius increasing over time. The shape of the vortex is a parabola with a flat bottom and gently sloping sides. The same depth profiles for the NP model are shown in figure 5.2. Since we are concentrating on the growth rate we take the initial values R_i and H_i for the NP model to be zero. We again see a symmetric vortex that increases in both depth and radius over time. The shape also represents a parabola but with steeper sides and a more pointed bottom than the shallow vortex model profile.

As well as the time-development of the vortex depth profile, we are particularly interested in the effect of the finite PV source on the vortex. We recall that the PV in the vortex is given by

$$q_v = \frac{f(1-\alpha)}{H}, \tag{5.31}$$

for α the vorticity ratio and H the vortex depth. The vortex depth profiles for the shallow vortex model are shown in figure 5.3 for five different values of α at a fixed time $T_R = 0.5$. As the value of α is increased we see a significant change in the vortex shape from a wide shallow vortex to a deep and narrow vortex. The introduction of finite PV therefore leads to a shallower and wider vortex. The same depth profiles are shown in figure 5.4 for the NP model. The vortex deepens with increasing α and therefore once again the effect of finite

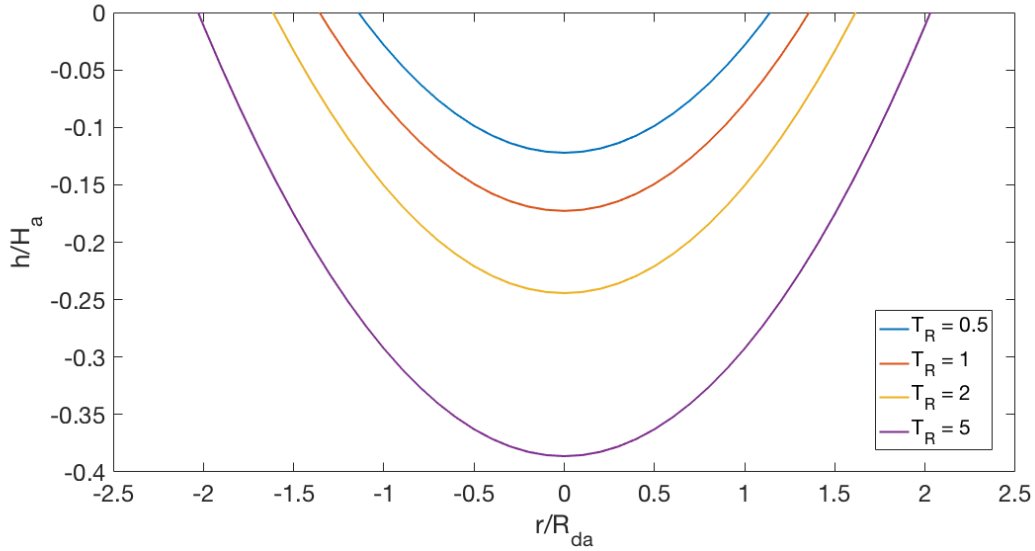

Figure 5.2 Vortex depth profiles for the NP01 model at four different times. The source vorticity ratio is fixed at $\alpha = 0.5$

PV is to produce a shallower vortex. There is little change in the vortex radius, with a slight decrease as the value of α increases, corresponding to smaller PV.

To gain further insight into the vortex growth we compare the model predictions for the maximum vortex depth and vortex radius as functions of time and of the source vorticity ratio α. In our analysis of the vortex depth profiles we have considered the exact solution of the shallow vortex model. We will now also consider the approximated solutions for the depth and radius given in (5.30) and (5.29) which are valid for a vortex depth much less than that of the ambient $H << H_a$. The time-development of the vortex maximum depth is plotted in figure 5.5 for the three theoretical models with $\alpha = 0.5$. The vortex depth increases with time for both the shallow vortex and the NP models, with the shallow vortex model initially giving a larger depth. At late times, $T_R \gtrsim 2$, the NP model gives a larger vortex depth as the depth increase according to the shallow vortex model exact solution slows down considerably. The shallow vortex model approximation diverges from the exact solution for $T_R \sim 0.5$, giving a larger depth which continues to increase with time at a rate similar to that of the NP model.

We also consider the time-development of the vortex radius in figure 5.6. The three theoretical curves are shown for a fixed value of $\alpha = 0.5$. The radius increases over time for both the shallow vortex and NP models with the shallow vortex model giving a larger value both with and without the approximation. The exact shallow vortex solution increases at the

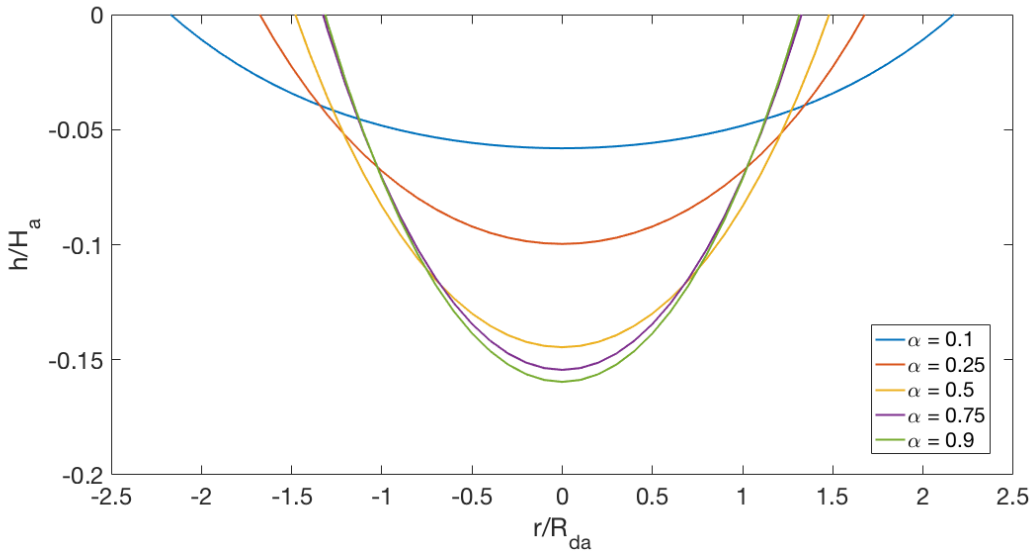

Figure 5.3 Vortex depth profiles at five different values of α for the shallow vortex model. Time is fixed at $T_R = 0.5$.

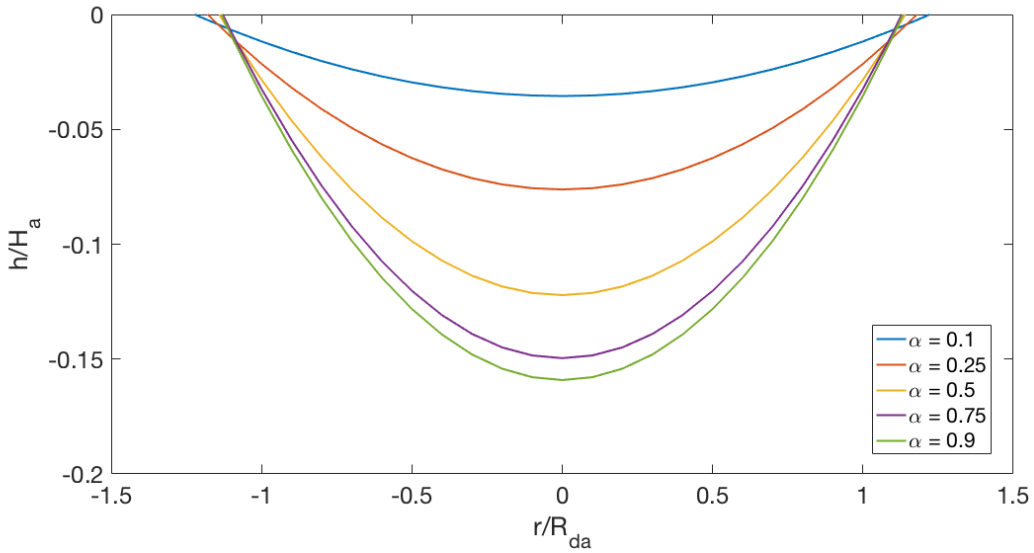

Figure 5.4 Vortex depth profiles at five different values of α for the NP01 model. Time is fixed at $T_R = 0.5$.

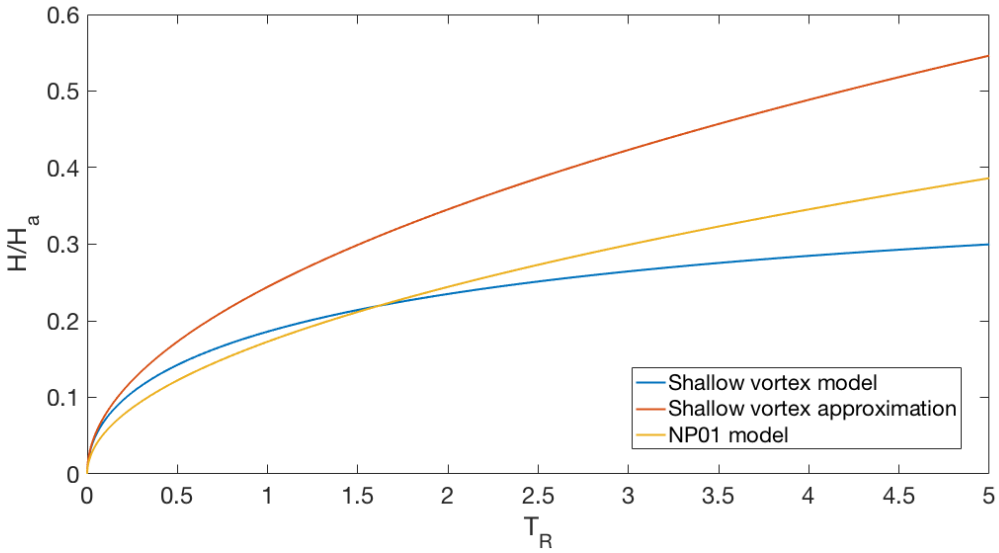

Figure 5.5 Dimensionless vortex maximum depth H/H_a plotted as a function of dimensionless time T_R. The vorticity ratio $\alpha = 0.5$ is fixed.

fastest rate and is slightly larger than the approximated solution. Considering both the vortex maximum depth and radius in figure 5.5 and 5.6, we would expect the shallow vortex model approximation to only remain valid for $T_R \lesssim 1$. The shallow vortex model approximation gives a larger vortex depth and smaller vortex radius than the exact solution, and both are larger than those predicted by the NP model.

We also analyse the dependence of the vortex radius and vortex depth on the vorticity ratio α for each of the models. The vortex maximum depth is plotted in figure 5.7 for both of the shallow vortex and NP models as a function of the vorticity ratio α at fixed time $T_R = 0.5$. The approximated shallow vortex solution is also shown. We see an increase in the vortex maximum depth as α is increased for both models, with the steepest increase occurring at low values of α. The shallow vortex model gives a larger depth across all values of α, with the approximated solution larger than the exact one, and both larger than the NP model solution. The introduction of a finite value of PV leads to a shallower vortex.

Figure 5.8 plots the radius as a function of α at fixed time $T_R = 0.5$. As the value of α is increased we see a general decrease in the vortex radius for both models which slows down as α is increased further. The decrease is much steeper for the shallow vortex model at low α due to the discontinuity as $\alpha \to 0$. We recall that $\alpha = -\zeta/f$ where ζ is the anticyclonic vorticity in the flow. The rapid increase in the vortex radius accounts for the decrease in the

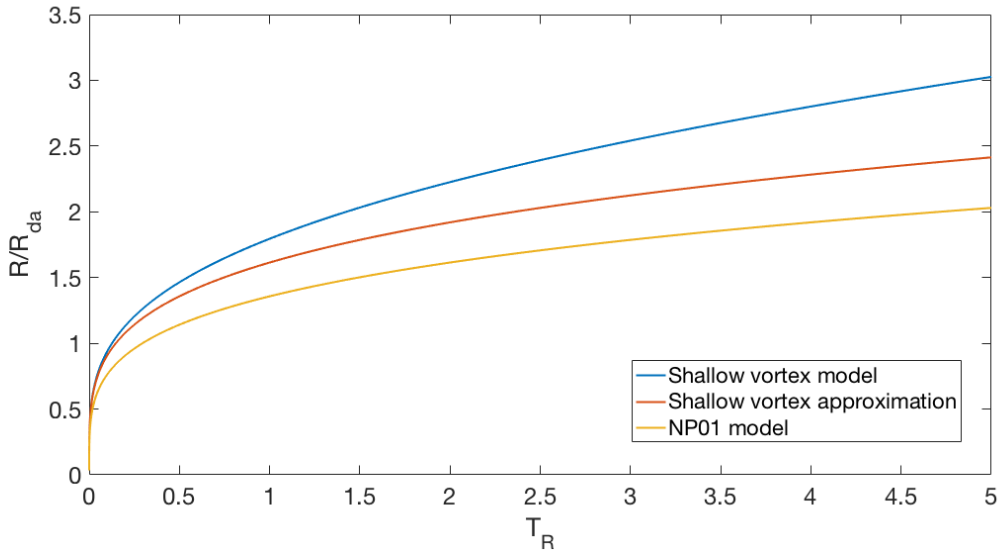

Figure 5.6 Dimensionless vortex radius R/R_{da} plotted as a function of dimensionless time T_R. The vorticity ratio $\alpha = 0.5$ is fixed.

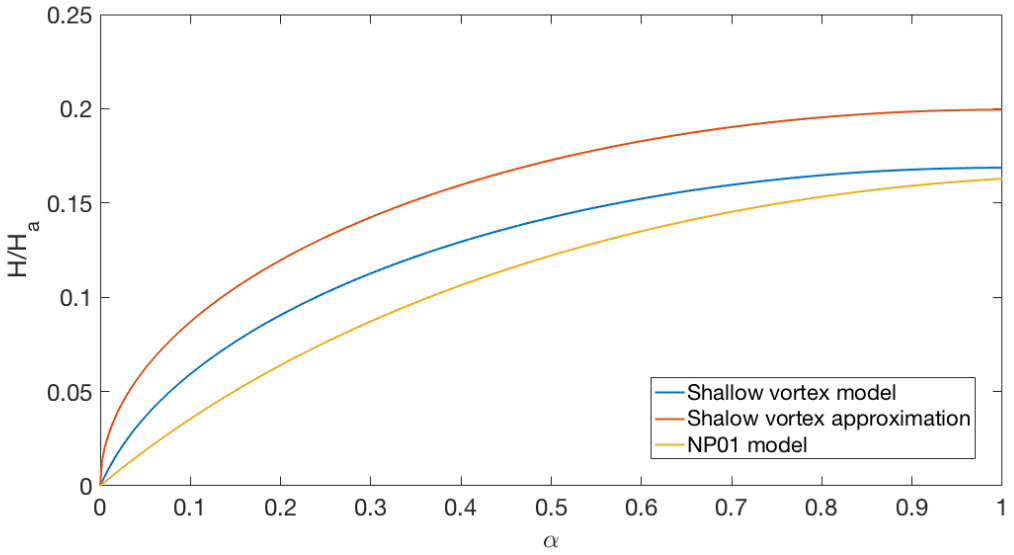

Figure 5.7 Dimensionless vortex maximum depth H/H_a plotted as a function of the vorticity ratio α at fixed time $T_R = 0.5$.

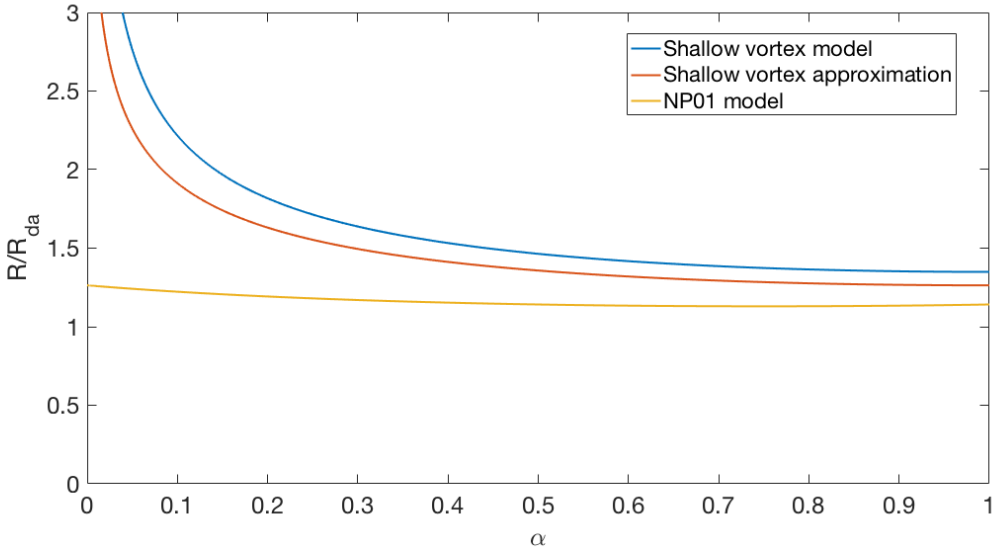

Figure 5.8 Dimensionless vortex radius R/R_{da} plotted as a function of the vorticity ratio α at a fixed time $T_R = 0.5$.

vortex maximum depth to zero as $\alpha \to 0$ and maintains the constant mass flux into the vortex from the source. The NP model attains a minimum radius at the value $\alpha_i = 0.75$ with a slight increase in the radius for larger α values and as $\alpha \to 0$. The NP model gives a reasonably constant radius across all α values which is smaller than that predicted by the shallow vortex model. The shallow vortex approximation and the exact solution are very similar across all α values. Overall, the introduction of finite PV ($\alpha < 1$) leads to an increase in the vortex radius in general for both models.

We continue our analysis with a comparison of the vortex depth profile for the models at a fixed time and fixed source vorticity. Figure 5.9 displays the profiles for $T_R = 0.5$ and $\alpha = 0.5$. For the NP model we see a shallower vortex with a smaller radius compared to the deeper and wider profiles of the shallow vortex model. We compare the experimentally measured vortex depth profiles with the two theoretical models in chapter 6.

As a final remark we compare the vortex maximum depth predicted by both the shallow vortex and NP01 models with the maximum geostrophic current depth h_0. Figure 5.10 displays the vortex depth scaled with h_0 as a funtion of dimensionless time $T = ft$ for the two models at two different values of the source vorticity ratio α, where $\alpha = 1$ represents zero initial PV. The time-development is shown over a period representative for a typical set of experimental parameters. For both the shallow vortex and NP01 models the vortex

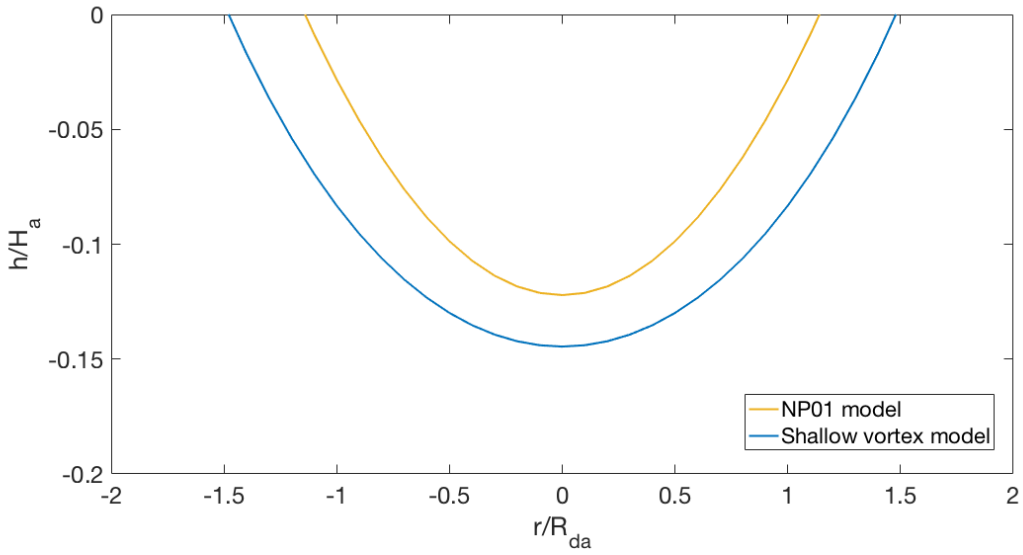

Figure 5.9 A comparison of the vortex depth profiles for the shallow vortex and NP models. Time is fixed at $T_R = 0.5$ and the vorticity ratio $\alpha = 0.5$.

maximum depth increases beyond the geostrophic current depth for $T \geq 70$. The shallow vortex model gives a vortex depth that increases over a shorter timescale and we see a faster increase for both models at larger α corresponding to smaller initial PV. For experiments with small f or short run-times the vortex depth may not reach the geostrophic depth before the end of the experiment, though were the experiment able to continue the theory predicts an increase beyond h_0 at later times.

5.4 Boundary wall

In deriving the shallow vortex model for the growth of the outflow vortex we have assumed that the vortex is able to grow unimpeded, as in the experiments of GL. In our experiments the vortex growth is restricted by the presence of a boundary wall which will play an important role in the vortex formation. The presence of the wall leads to a change in the shape of the vortex such that it no longer forms a circle at the surface, whilst a a boundary current flowing parallel to the wall also forms to the right of the source (in the northern hemisphere) as seen in our experiments. To account for this the shallow vortex model must be adapted to incorporate the new physics present in the system and we will use the results of the NP model to help to provide the appropriate modifications.

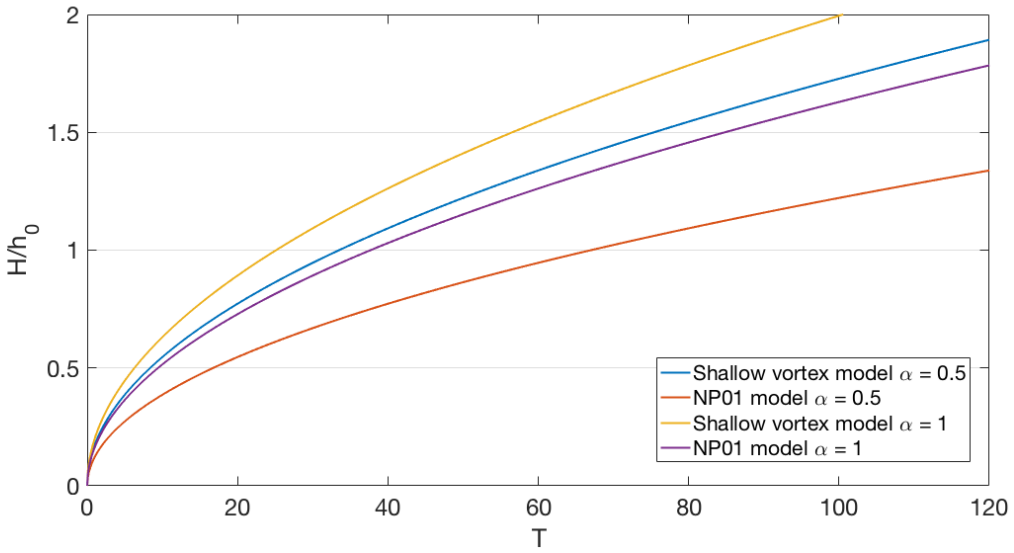

Figure 5.10 A comparison of the vortex maximum depth with the geostrophic current depth h_0 for two different models at two different values of α over time.

In the NP model the equations for the vortex growth are derived from a momentum balance between the offshore migration of the vortex centre and the momentum-flux leaving in the downstream current. Therefore, the boundary wall and the associated impact it has on the flow is inherently present in the dynamics of the system. In comparison, the shallow vortex model is derived via PV conservation without any consideration of the effect that the boundary wall will have on the physics of the problem. This provides a stand-alone model for pure vortex growth which can be used alongside the experimental results to measure the level of deviation from pure growth and thus what effect the current has on the vortex.

We present two possible modifications to the shallow vortex model to account for the presence of the boundary wall. First, we consider the mass-loss to the boundary current in the presence of the boundary wall. The shallow vortex model assumes that the vortex is able to grow unimpeded and thus all of the mass from the source accumulates in the vortex, which is not the case in our experiments. The mass-loss to the boundary current can be estimated using the results of NP who found that for a vortex with tangential velocity $v_\theta = -\alpha f r/2$ the instantaneous volume is given by $V = \alpha(2-\alpha)\pi f R^4/16g'$. Using their solution for the vortex radius in (5.1) and differentiating with respect to time gives

$$\frac{dV/dt}{Q} = \frac{2\alpha}{1+2\alpha}. \tag{5.32}$$

This means that with the formation of a boundary current the amount of volume flux entering into the vortex is a function of the vorticity ratio α and is given by $Q_v = 2\alpha Q/(1+2\alpha)$. With the addition of the boundary wall to our model, we may approximate the loss of mass to the current by a reduction in the volume flux entering into the vortex. Replacing Q in (5.25) by Q_v, the vortex volume at time t is now given by

$$Qt = \frac{\pi R^2 H_a \alpha(2-\alpha)(1+2\alpha)}{4\alpha}\Big(1 - \frac{2R_{da}I_1(R/R_{da})}{RI_0(R/R_{da})}\Big). \tag{5.33}$$

The vortex depth profile and the maximum vortex depth $H(t)$ will also be modified, though the change is incorporated into the value of R and thus is not explicitly seen in the formulae in (5.26) and (5.27). In order to see the effect of the modified volume flux, we must consider the limit of a shallow vortex, $H/H_a << 1$. Using the series expansions for I_0 and I_1 (as above) we obtain

$$\hat{R} \sim \Big(\frac{32\hat{t}}{\pi(1+2\alpha)(2-\alpha)}\Big)^{1/4}, \tag{5.34}$$

$$\hat{H} \sim \Big(\frac{\alpha^2(2-\alpha)\hat{t}}{2\pi(1+2\alpha)}\Big)^{1/2}. \tag{5.35}$$

These results are in fact identical to those of the NP model in (5.1) and (5.2), despite having been derived via a different approach.

The second option for incorporating the boundary wall into the shallow vortex model is to consider the effect that its presence will have on the shape of the vortex. In the model of GL the vortex is assumed to be circular, which is verified by their experimental results. In their experiments, the source is located at the surface in the centre of the growing vortex. The use of a horizontal source in our experiments adds horizontal momentum to the system and we might expect the vortex centre to be located slightly downstream of the source and close to the boundary wall. To some degree, the wall can be thought of as acting to split the vortex in half producing a shape resembling a semi-circle. In practice, this will not be exactly the case as the recirculation within the vortex will force the centre to move away from the wall, but we would certainly expect a degree of asymmetry in the vortex shape. We will consider experimental data in chapter 6 to gain a better understanding of the vortex shape seen in practice, but in terms of modifying our model the assumption of a semi-circular shaped vortex is a reasonable approximation. This means that the vortex radius in the direction parallel to the boundary wall will grow according to the shallow vortex model in (5.25), while the vortex radius in the direction perpendicular to the boundary wall will grow at half

of that rate. The decrease in the volume of the vortex which will occur when modelling it with a semi-circular shape will account for the loss of volume flux into the boundary current.

The two modifications to the shallow vortex model will be compared with the experimental data in chapter 6. The volume flux modification will be referred to as the NP model, since we recover the solution of NP when using the value Q_v for the volume flux.

5.5 Discussion

In this chapter we have presented a theoretical model for the growth of a vortex from a constant flux source of finite potential vorticity. This model is based on the work of GL and extends their zero PV model to the case of finite PV. The increase in the PV to a finite value leads to an increase in the vortex radius and a decrease in the vortex maximum depth. The vortex radius is seen to increase significantly at large values of PV.

Under the assumption of a shallow vortex depth relative to the depth of the ambient, $H/H_a << 1$, we are able to expand the Bessel function solutions of the model to obtain the explicit time dependence for the growth of the vortex maximum depth and the vortex radius. The approximation is found to remain valid for $T_R \lesssim 1$. The shallow vortex model was then compared with the finite PV vortex growth model of NP. The two models are derived using different physical considerations and therefore account for the presence of the boundary wall in different ways. The NP model is derived by consideration of the momentum balance in the system and the boundary wall is inherently present throughout in the physical description of the problem. The shallow vortex model is derived via PV conservation and the resultant solutions must be modified to account for the presence of the boundary wall.

It was found that by incorporating the smaller mass flux into the vortex caused by the presence of the boundary current, the shallow vortex model was in fact equivalent to the NP model. An alternative modification to the shallow vortex model was also considered, which assumes a semi-circular vortex shape. In this instance the vortex radius perpendicular to the boundary wall will be equal to approximately half of the radius in the direction parallel to the wall. This reduction in the vortex volume accounts for the mass flux lost to the boundary current.

The results of the shallow vortex model and the NP model will be compared with experimental data in chapter 6.

Chapter 6

Experimental observations of the outflow vortex

6.1 Introduction

In this chapter we analyse the experimental results for the outflow vortex, much in the same way that we investigated the features of the boundary current in chapter 4. In chapter 5 we introduced a theoretical model to describe the growth of an outflow vortex from a constant flux source of finite potential vorticity. The model was modified to include the presence of a boundary wall next to the source, similar to the coastline alongside a river outflow. This model and the model of NP will be compared with the experimental observations of the vortex shape and the vortex depth profiles across the three regimes of low, intermediate and high I^*. The instability of the vortex at high I^* is also briefly discussed in terms of a baroclinic instability and the work of GL.

An analysis of the vortex velocity profiles reveals the need for a time-dependent vorticity model which will be introduced in chapter 7. The time-dependent model incorporates the vortex growth models discussed in chapter 5 and therefore in the second part of this chapter we assess the ability of the shallow vortex and NP models to adequately capture the time-dependent growth of the vortex. A summary of the experimental measurements for the vortex maximum depth and radius is presented and then the time-dependent growth of these properties analysed in comparison with the theory.

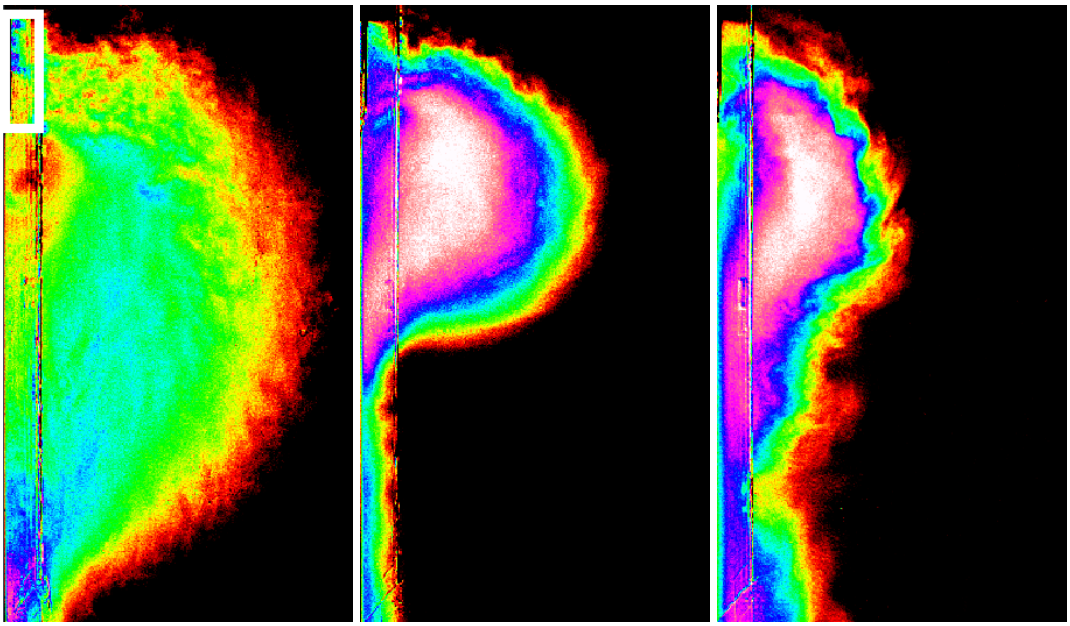

(a) $I^* = 0.36$. **(b)** $I^* = 1.23$. **(c)** $I^* = 4.08$.

Figure 6.1 Plan views of the outflow vortex taken at the end of experiments with low (a), intermediate (b) and high (c) values of I^*. The colour scale (arbitrary) represents the depth of the freshwater with white the deepest and red the shallowest. The location of the source is indicated by the white rectangle in the first image and is the same for each experiment. The scale of the images is the same.

6.2 Vortex features

In chapter 2 the experiments were classified according to the dimensionless parameter I^*, which is defined as the ratio of the source aspect ratio H_0/D with the current aspect ratio h_0/w_0. The experimental observations reveal that the vortex is qualitatively different in each regime. For low values of I^* the vortex is elongated in the direction along the boundary with a weak anticyclonic circulation, for intermediate values it is more circular in shape with a stronger circulation and for high values of I^* the vortex becomes unstable and sheds smaller vortices that are propagated along with the boundary current. We will analyse the features of the vortex in each regime, including the vortex shape and the vortex depth profile. We will also briefly anlayse the instability of the vortex for high values of I^* in terms of a baroclinic instability.

I^*	Q [cm^3 s^{-1}]	f [s^{-1}]	g' [cm s^{-2}]	H_0 [cm]	D [cm]
0.36	100	1	69.8	2	5
1.23	62	1.5	14.9	2	5
4.08	97	1.5	2.3	2	5

Table 6.1 Experimental parameters for the experiments shown in figure 6.1.

I^*	Q [cm^3 s^{-1}]	f [s^{-1}]	g' [cm s^{-2}]	H_0 [cm]	D [cm]
0.36	100	1	69.8	2	5
0.50	75	1.5	70.2	2	5
0.54	74	1	12.4	2	2.5
0.67	75	2	70.8	2	5
0.75	47.5	1	15.8	2	5
0.81	47.5	1	13.8	2	5
1.31	61	0.5	2.1	2	5

Table 6.2 Experimental parameters for the experiments shown in figure 6.2.

6.2.1 Vortex shape

Typical vortices from experiments at low, intermediate and high values of I^* are displayed in figure 6.1, with the exact parameter values displayed in table 6.1. The vortex is elongated along the boundary at low I^* and goes unstable at high I^*. For both low and intermediate I^* the vortex shape is closer to that of a semi-circle than a circle. To investigate this feature further we consider the ratio of the vortex diameter in each direction, defined by the parameter

$$D^* = \frac{D_{perp}}{D_{par}}, \tag{6.1}$$

where D_{perp} is the vortex diameter in the direction perpendicular to the boundary wall and D_{par} is the diameter parallel to the wall. Figure 6.2 plots the values of the diameter ratio over time for seven experiments across the full range of experimental parameters in the low and intermediate I^* regimes, with $0.36 \leq I^* \leq 1.31$. The instability of the vortex in the high I^* regime prevents consistent measurements from being made. The exact experimental parameters are given in table 6.2.

The data show that in general the value of D^* remains reasonably constant throughout an experiment across a large range of values of I^*. Figure 6.3 plots the mean diameter ratio D^* versus the aspect ratio ratio I^* for all of the experiments where the outflow vortex

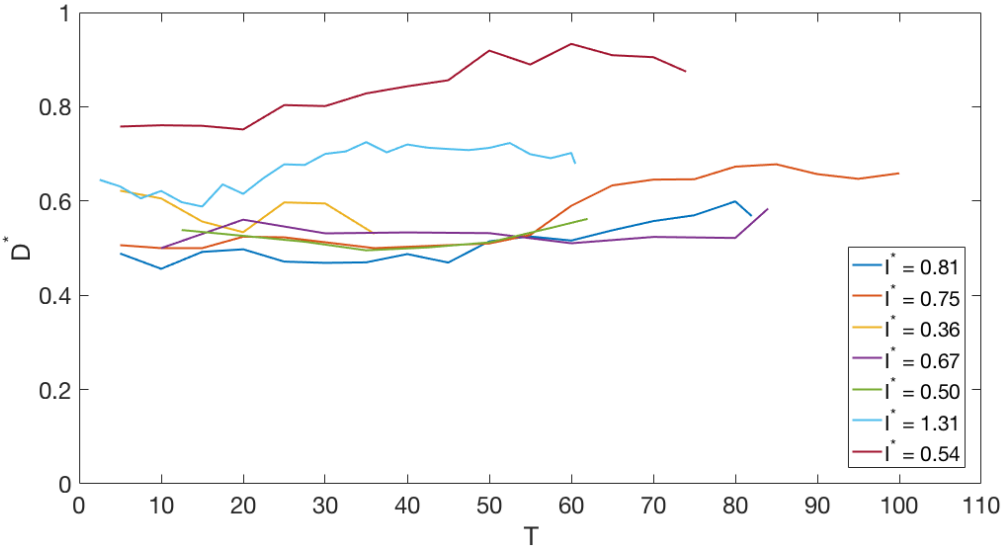

Figure 6.2 A plot of the vortex diameter ratio $D^* = D_{perp}/D_{par}$ versus dimensionless time $T = tf$ for a subset of the experiments in the low and intermediate I^* regime.

demonstrates self similar growth. There does not appear to be a trend in the value of D^* as I^* varies, however, the data show that the vortex is in general not circular. In many instances $0.4 \lesssim D^* \lesssim 0.6$ with a mean value of $D^* = 0.63$ suggesting that the vortex is more similar to a semi-circle. Using a value of $D^* = 3/5$ for the reduction in the perpendicular radius we may formulate an equation to describe the approximate shape of the vortex as a half-ellipse, given by

$$x^2 + \frac{25y^2}{9} = 1, \tag{6.2}$$

where x is the direction parallel to the boundary and y the perpendicular direction. In the derivation of the shallow vortex model in chapter 5, a modification was made to account for the presence of the boundary wall. We assumed that the presence of the wall will act to approximately split the vortex in half and thus the radius in the direction perpendicular to the wall will be smaller than the radius parallel to the wall by a factor of $1/2$. The data in figure 6.3 show that the radius is indeed smaller in the perpendicular direction, but by a slightly larger factor of $\sim 3/5$. The vortex radius is analysed in more detail in chapter 8 in comparison with the time-dependent vorticity model.

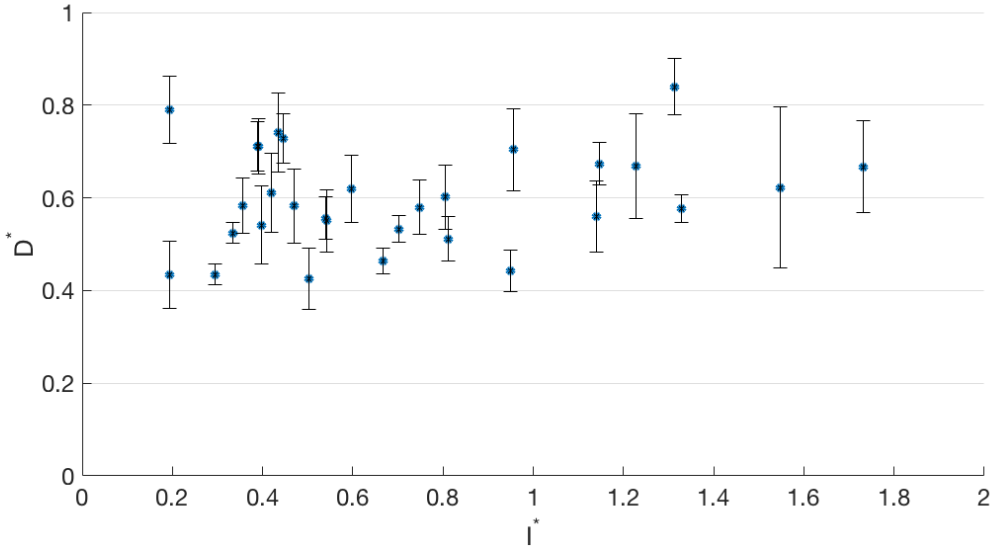

Figure 6.3 A plot of the vortex diameter ratio $D^* = D_{perp}/D_{par}$ versus I^*.

I^*	Q [cm^3 s^{-1}]	f [s^{-1}]	g' [cm s^{-2}]	H_0 [cm]	D [cm]
0.50	75	1.5	70.2	2	5
1.23	62	1.5	14.9	2	5
4.08	97	1.5	2.3	2	5

Table 6.3 Experimental parameters for the experiments considered in this section.

6.2.2 Vortex depth profile

The vortex depth profile was obtained experimentally by measuring the depth for a cross-section through the vortex. The cross-section was taken in the direction perpendicular to the boundary wall along the central axis of the vortex. We choose the centre of the vortex to be defined by the point of maximum depth, which means that it changes over time as the vortex grows. The experimental parameters for the runs considered in this section are given in table 6.3.

Figure 6.4 displays the vortex depth profile for an experiment at a low value of $I^* = 0.50$. The vortex depth is scaled with the source depth H_0 and the vortex radius with the source deformation radius $R_d = \sqrt{g'H_0}/f$. The maximum depth and radius of the vortex both increase for the duration of the experiment. We see several changes in the vortex shape. Initially, for $T < 25.5$ the vortex reaches its maximum depth at or very close to the boundary wall, which appears to split the vortex in half compared to the expected growth without the presence of

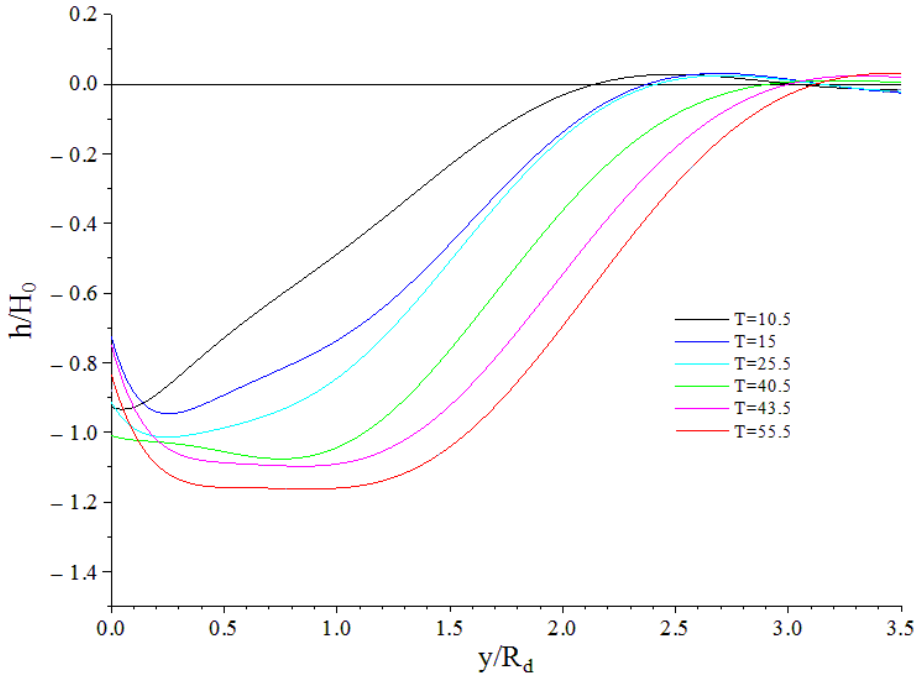

Figure 6.4 Vortex depth profile at different times for an experiment with a low value of $I^* = 0.50$. The depth is scaled with the source depth H_0 and the vortex radius with the source deformation radius $R_d = \sqrt{g'H_0}/f$.

a boundary wall seen by GL. The initial behaviour ($T < 25.5$) gives a semi-circular vortex shape viewed from above as seen in figure 6.1 for the low I^* regime. For $25.5 \leq T$ the vortex centre, defined by the point of maximum depth, moves further away from the wall and we see a flat-bottom that persists for a considerable distance of $y/R_d \sim 1$ at $T = 55.5$ for example. The semi-circular shape persists with the location of the vortex centre suggesting a D^* value of ~ 0.6.

Figure 6.5 displays the vortex depth profile for an experiment with an intermediate value of $I^* = 1.23$. The vortex maximum depth and radius increase over time while the vortex shape remains consistent. We see a migration of the vortex centre further away from the boundary wall as the experiment progresses. For early times the depth profile is highly asymmetrical and gradually becomes more symmetrical around the point of maximum depth as time increases. At the end of the experiment a degree of asymmetry still remains, however, resulting in a diameter ratio $D^* < 1$ due to the vortex being squashed against the boundary wall.

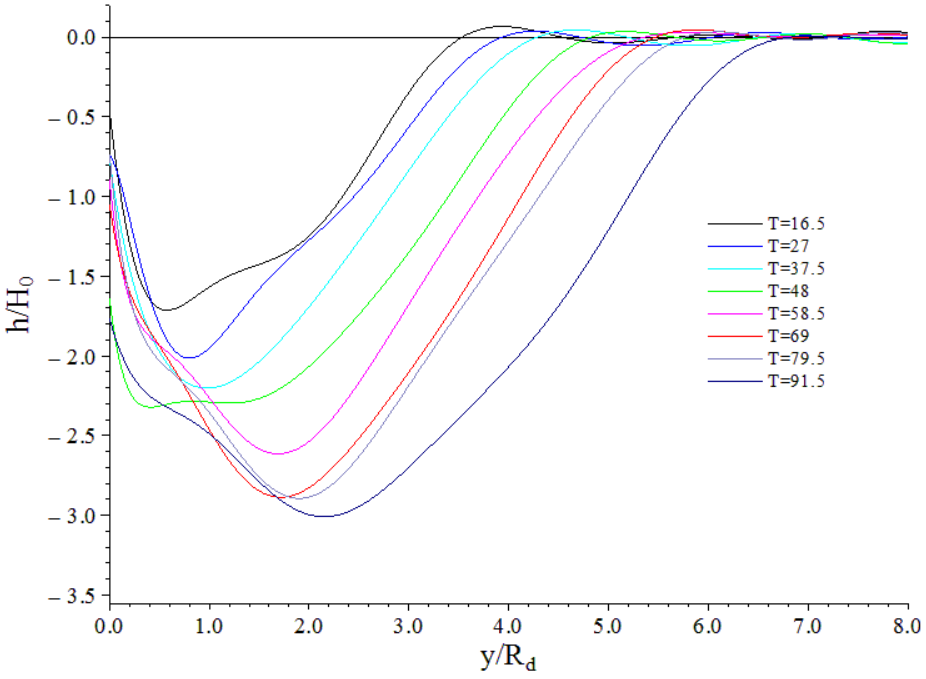

Figure 6.5 Vortex depth profile at different times for an experiment with an intermediate value of $I^* = 1.23$. The depth is scaled with the source depth H_0 and the vortex radius with the source deformation radius $R_d = \sqrt{g'H_0}/f$.

Finally, figure 6.6 displays the vortex depth profile for an experiment with a high value of I^*. For early times $T < 75$ we see an increase in the vortex depth and radius and a migration of the vortex centre away from the boundary wall, however, at later times the changes in the depth profile become erratic. For example, the radius decreases between $T = 75 - 97.5$ and then increases at $T = 120$ before decreasing again at $T = 163.5$. These changes are due to the vortex becoming unstable and starting to shed smaller cyclonic vortices which are carried away with the propagating boundary current. The stability of the vortex will be discussed in more detail in section 6.2.3.

In the cases of low and intermediate I^* the vortex depth profiles show an increasing vortex depth and radius over time. This follows the expected pattern of vortex growth predicted by the theory in chapter 5. The vortex shape in figures 6.4 and 6.5 shows evidence of self-similarity, particularly for intermediate I^*. We will investigate this further by comparing the experimentally measured vortex depth profiles with the theoretical models introduced in chapter 5. Guided by our observations above, we will consider a depth profile from an experiment with an intermediate value of I^*. Figure 6.7 plots the experimentally measured vortex depth profile for an experiment with $I^* = 1.23$ at time $T = 27$. The theoretical profiles

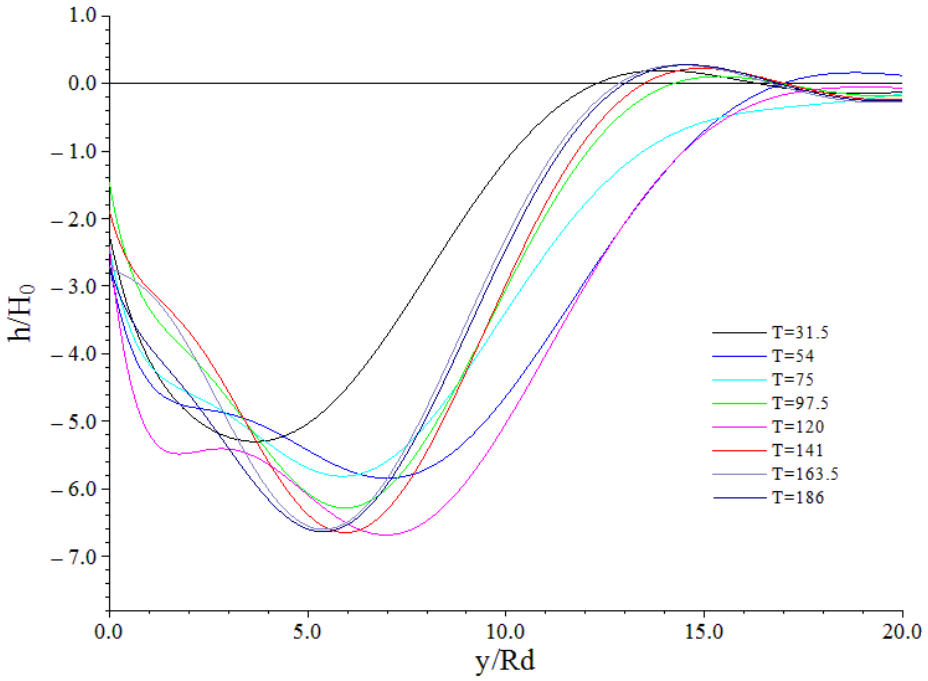

Figure 6.6 Vortex depth profile at different times for an experiment with a high value of $I^* = 4.08$. The depth is scaled with the source depth H_0 and the vortex radius with the source deformation radius $R_d = \sqrt{g'H_0}/f$.

from the shallow vortex and the NP models are also shown where we have used the fitted values of α derived in chapter 8. The experimental data are shifted so that the point of maximum depth is located at $r = 0$. The models appear to underestimate the vortex depth and overestimate the vortex radius during the early part of the experiment. The NP model shows the best agreement, though the data gives a more pointed profile than is predicted by the theory. Figure 6.8 displays the depth profile measurements for the same experiment at a later time of $T = 58.5$. Here we see better agreement between the data and the theory, in particular for the shape of the depth profile. The shallow vortex model provides the best fit to the vortex depth, but overestimates the vortex radius. The NP model provides a good approximation of the vortex radius, but underestimates the depth. Finally, the depth profile measurements taken at the end of the experiment at $T = 91.5$ are shown in figure 6.9. We see the best agreement between the theory and the data at later times. The NP model shows good agreement with the data and is able to capture the vortex shape, depth and radius well. The shallow vortex model predicts more of a flat-bottomed vortex than is seen experimentally, but provides a better fit to the maximum vortex depth and the vortex radius.

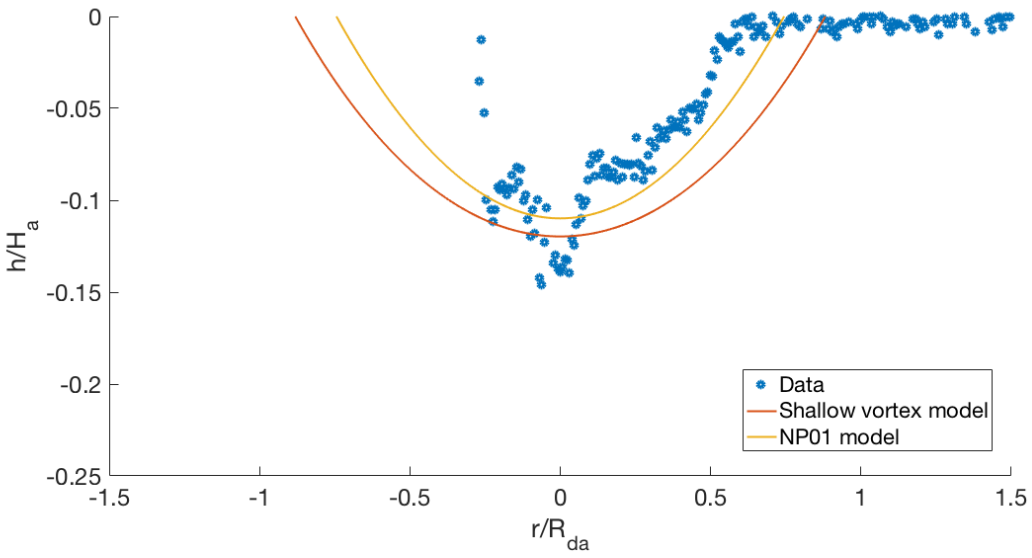

Figure 6.7 The experimentally measured vortex depth profile for an experiment with $I^* = 1.23$ which is taken at $T = 27$. The theoretical profiles from the shallow vortex and the NP models are also shown. The depth is scaled with the ambient depth H_a and the vortex radius with the ambient deformation radius $R_{da} = \sqrt{g'H_a}/f$.

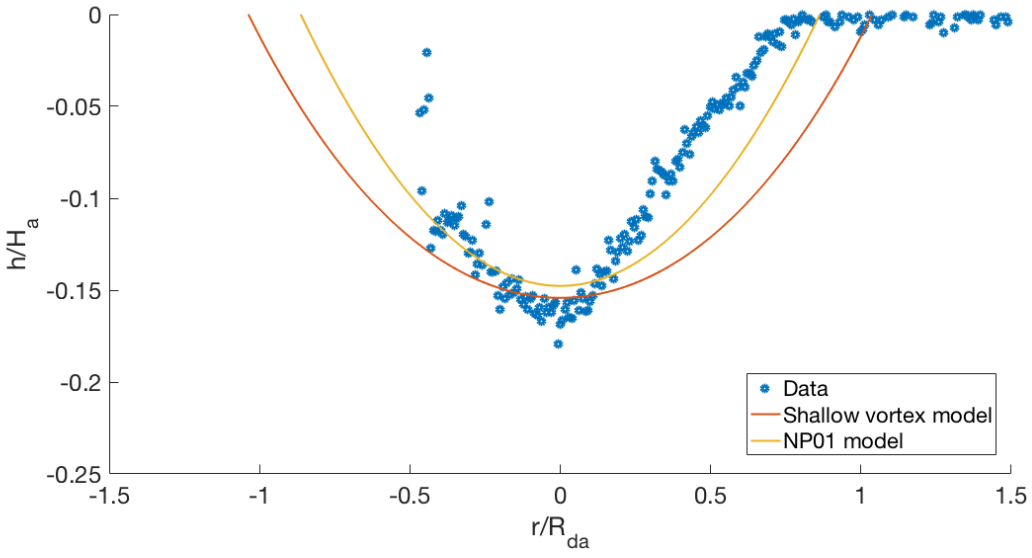

Figure 6.8 The experimentally measured vortex depth profile for an experiment with $I^* = 1.23$ which is taken at $T = 58.5$. The theoretical profiles from the shallow vortex and the NP models are also shown. The depth is scaled with the ambient depth H_a and the vortex radius with the ambient deformation radius $R_{da} = \sqrt{g'H_a}/f$.

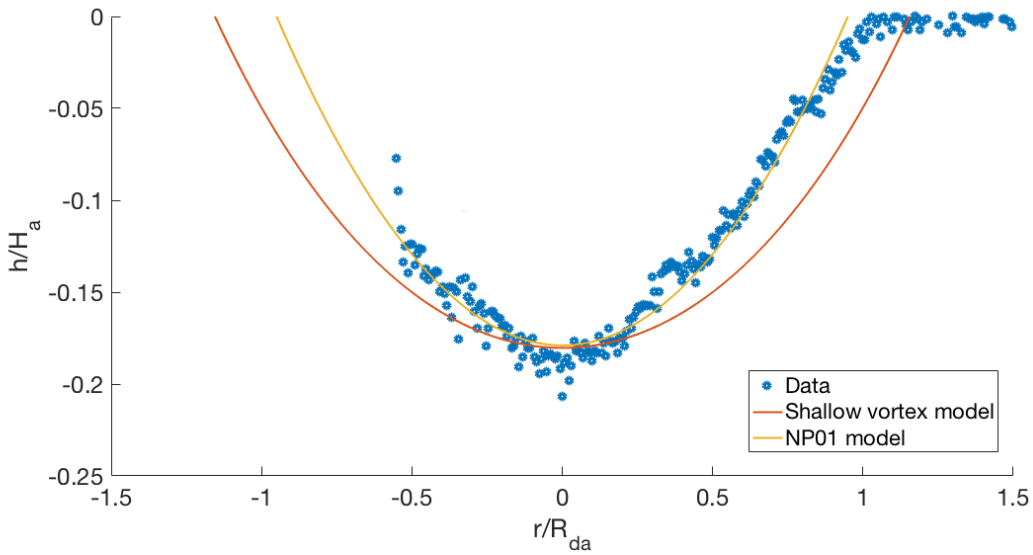

Figure 6.9 The experimentally measured vortex depth profile for an experiment with $I^* = 1.23$ which is taken at $T = 91.5$. The theoretical profiles from the shallow vortex and the NP models are also shown. The depth is scaled with the ambient depth H_a and the vortex radius with the ambient deformation radius $R_{da} = \sqrt{g' H_a}/f$.

Overall, the agreement between the theoretical models and the data is reasonable and shows that the theory is able to capture the key features of the flow in the vortex. The model performance improves as the experiment progresses, suggesting that the theory is best suited to modelling the long-time growth of the vortex. The NP model accounts for this with the terms H_i and R_i in the formulae for the maximum depth and radius, which represent the vortex depth and radius at a time when the vortex is already larger in size than the boundary current. The values of H_i and R_i will be explored in more detail in chapter 7 with a time-dependent model.

6.2.3 Vortex stability

For experiments with a high value of I^* the outflow vortex becomes unstable and begins to shed smaller cyclonic vortices which are then carried along with the boundary current. The work of GL showed that the vortex produced from a constant flux source will always go unstable if left for a long enough time. The vortex radius increases according to $t^{1/2}$ in both of the theoretical models introduced in chapter 5 and therefore their observation suggests the existence of a critical vortex size beyond which the vortex becomes unstable. GL analysed the vortex stability in terms of baroclinic instability and we shall do the same here, albeit

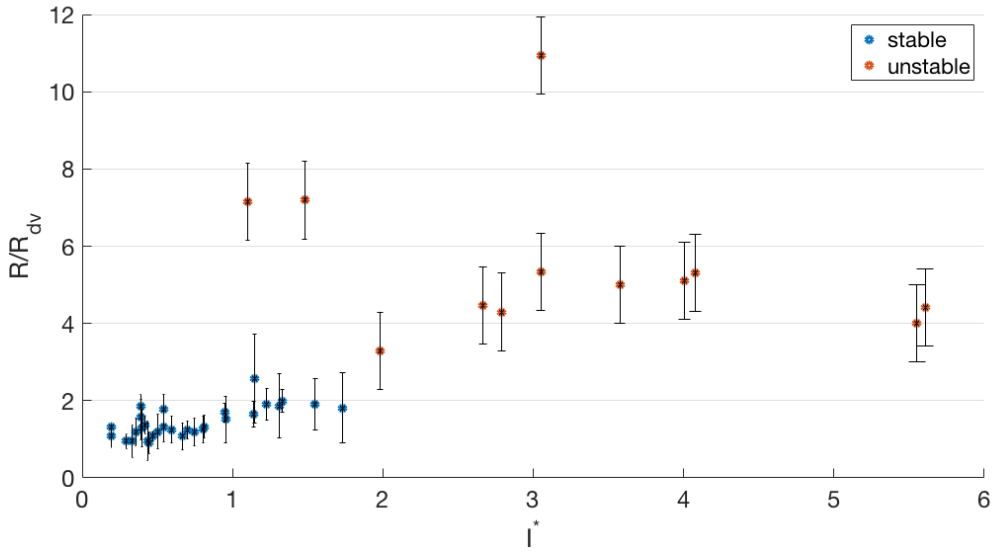

Figure 6.10 A plot of the maximum vortex radius measured experimentally in the direction perpendicular to the boundary, scaled with the vortex deformation radius $R_{dv} = \sqrt{g'H}/f$, versus the aspect ratio ratio I^*.

briefly. We present data that show the instability is most likely baroclinic as seen by GL, but leave a full analysis of the features of the instability for a future study.

Figure 6.10 plots the experimentally measured vortex radius, scaled with the deformation radius based on the vortex maximum depth H, $R_{dv} = \sqrt{g'H}/f$, versus I^*. For the experiments that remain stable the maximum vortex perpendicular radius is shown, while for the experiments that go unstable we use the radius and vortex depth at the time of the onset of instability. As the value of I^* increases we see an increase in the value of the radius as well as a transition to an unstable vortex. This suggests that the vortex reaches a critical size relative to the Rossby radius of deformation, beyond which it goes unstable. The data in figure 6.10 gives a value of $R/R_{dv} \sim 2$ beyond which the instability occurs. This can be related to a internal Richardson number for the vortex defined by

$$\theta = \frac{g'H}{f^2R^2}, \tag{6.3}$$

as in the work of GL. The value $R/R_{dv} = 2$ gives a critical Richardson number of $\theta = 1/4$ below which the vortex goes unstable to baroclinic instability. The values of θ are plotted in figure 6.11 versus I^*. The data show that for small Richardson number the vortex does indeed go unstable. The critical value of $\theta = 1/4$ provides a good estimate for the transition

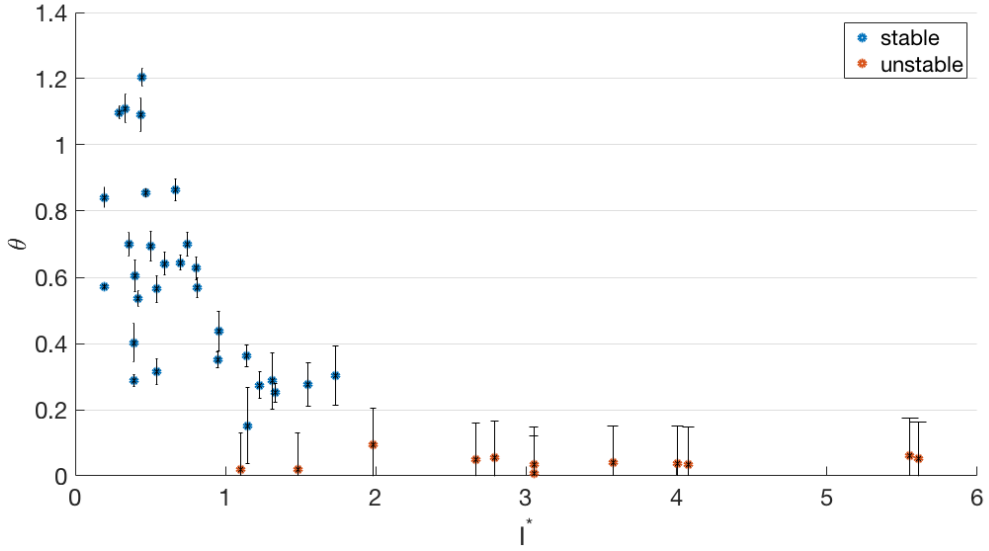

Figure 6.11 The internal vortex Richardson number θ versus I^* for the stable and unstable experiments.

to instability. Following the analysis of GL we define a depth ratio $\delta = H/H_a$ where H_a is the depth of the ambient and we define the function

$$f(\delta) = \left(\frac{\delta}{1-\delta}\right)^{-1/2}, \tag{6.4}$$

used in the work of Phillips (1954). GL showed that without the presence of a boundary wall the vortex goes unstable below a critical value of $\theta f(\delta) \sim 0.02$. In figure 6.12 the value of $\theta f(\delta)$ is plotted against I^*. The data suggests a critical value of $\theta f(\delta) \sim 0.06 \pm 0.06$, which is of the same order of magnitude found by GL. The difficulty in identifying the onset of instability in the vortex combined with the rapid increase in the vortex depth initially at low values of g' (where the majority of the instabilities occur) makes it difficult to estimate a critical parameter value with the required level of accuracy.

As mentioned above, the issue of vortex stability is an interesting one, but is not something that we wish to pursue in great detail in this study. The experimental observations and measurements suggest that the instability is indeed baroclinic in nature, which is in agreement with the results of GL.

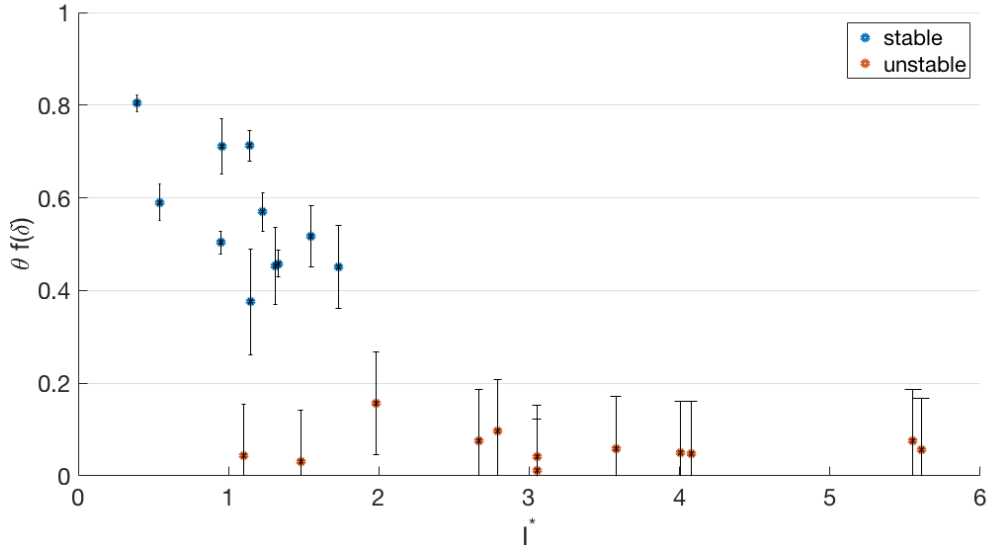

Figure 6.12 The value of $\theta f(\delta)$ measured experimentally versus I^*.

Experiment	Q [cm^3 s^{-1}]	f [s^{-1}]	g' [cm s^{-2}]	H_0 [cm]	D [cm]	I^*
PIV 9	48	0.5	13.2	2	5	0.42
PIV 10	48	1	13.1	2	5	0.84
PIV 11	48	1	3.4	2	5	1.90
PIV 12	48	0.5	2.5	2	5	1.12

Table 6.4 Experimental parameters for the four experiments where PIV measurements were made at the surface of the vortex.

6.2.4 Vortex velocity profile

Measurements of the velocity field at the surface of the vortex were obtained for a subset of the experimental parameters using the method of PIV. Four PIV experiments were conducted that focused on the centre of the outflow vortex across the three regimes of low, intermediate and high I^*. Cross-sections were taken through the centre of the vortex in the directions perpendicular to the boundary wall and parallel to the boundary wall at a depth of $\sim 0.5-1.5$ cm and the velocity profile in each direction measured every 10 seconds for the duration of an experiment. The experimental parameters used in the vortex PIV experiments are shown in table 6.4.

To demonstrate the general features of the flow at the surface of the vortex a streak image is shown in figure 6.13 identifying the paths of particles in the vortex. The loca-

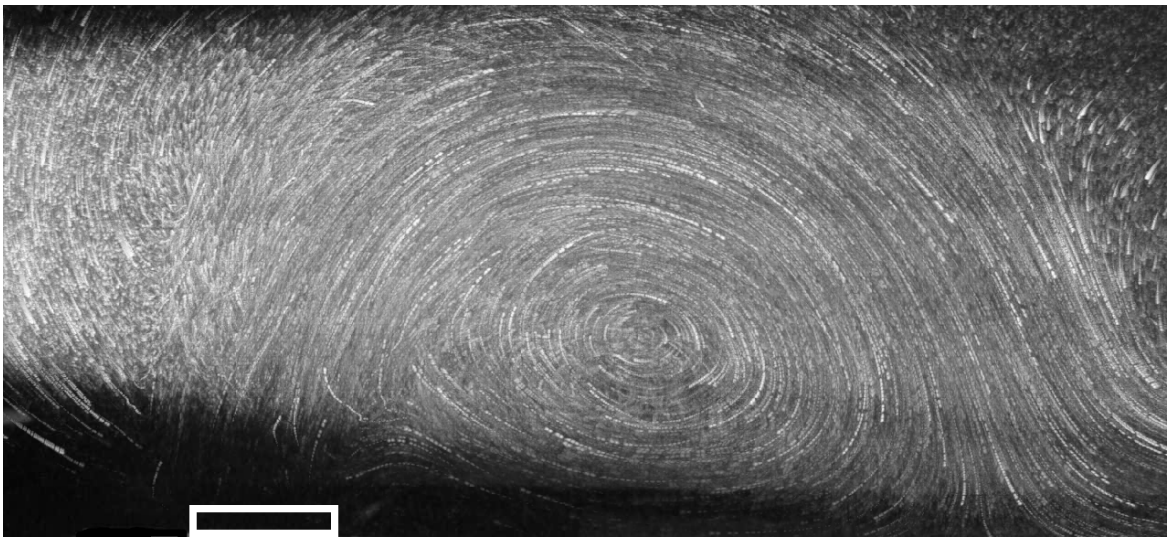

Figure 6.13 A streak image displaying the paths of particles in the vortex. The location of the source is shown by the white rectangle which has a width of 5 cm for scale. The image is taken from an experiment with $I^* = 0.84$.

tion of the source is indicated by the white rectangle and the light plane is at a depth of $\sim 0.5 - 1.5$ cm. The image shows a clear anticyclonic circulation in the vortex, which strengthens away from the vortex centre. The flow of the current from the source around the edge of the vortex is also visible. The division of the flow between recirculation in the vortex and propagation into the boundary current can be seen at the bottom right-hand edge of the image. As the vortex grows in size, the point of division progresses further downstream.

Figure 6.14 displays the velocity profiles across the vortex in the direction perpendicular to the wall at different times from an experiment at a low value of $I^* = 0.42$. The boundary wall is located at $y/R = 0$ and the profile extends outwards away from the wall. At late times the far edge of the vortex is no longer contained within the area of measurement and as such the profiles end abruptly. This is a constraint of the experimental setup (see section 2 for more details). The distance y across the vortex has been scaled with the vortex radius at the time the velocity profile is measured. We do not have simultaneous measurements of the vortex radius and velocity field available from the same experiment and thus have used the radius measurements from a dye attenuation experiment with a similar value of I^*. Scaling the plots in this manner enables the velocity profiles to be viewed in the context of the vortex. The surface velocity profiles for the intermediate I^* regime are displayed in figure 6.15. The data in figures 6.14 and 6.15 show three important features of the flow in the vortex. Firstly, using the maximum negative velocity measurements (since the data are unavailable for the

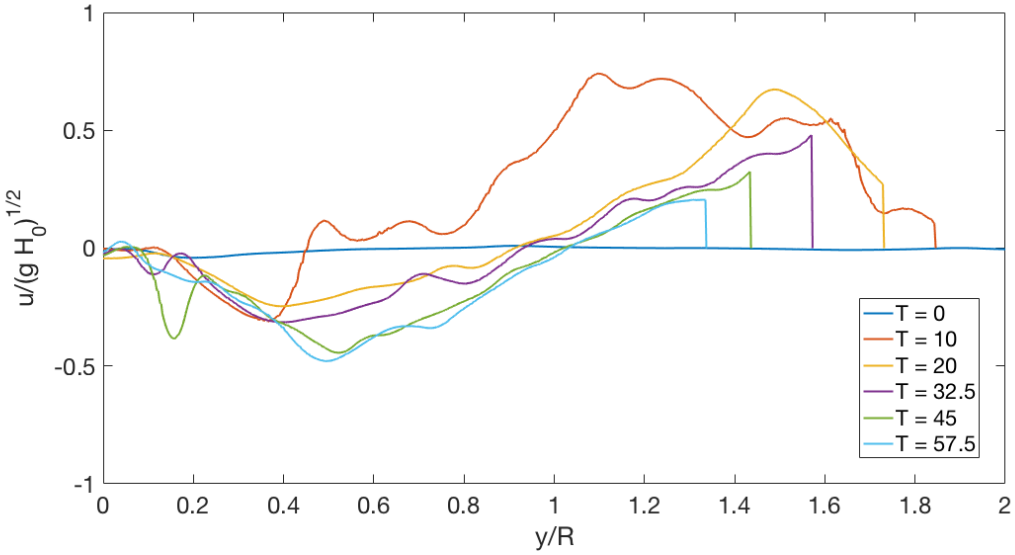

Figure 6.14 A plot of the vortex velocity from an experiment with a low value of $I^* = 0.42$ along a cross-section through the vortex centre perpendicular to the boundary wall. Profiles are shown at six different times which are given in the legend. The velocity is scaled with $\sqrt{g'H_0}$ for H_0 the depth of the source.

maximum positive velocity values at late times), we see an increase in the vortex velocity with time initially, before it then remains approximately constant for late times. Secondly, the velocity profiles remain approximately linear for the duration of the experiment and the gradient of the velocity profile seems to decrease with time, particularly in figure 6.14. Thirdly, the centre of the vortex, defined by the point of zero velocity, migrates further away from the boundary wall as the experiment progresses.

Figure 6.16 dispays the surface velocity profiles in the vortex for an experiment with high $I^* = 1.90$. For this experiment the camera location was changed which resulted in the velocity field closest to the boundary wall being excluded from the field of measurement. The profiles for the high I^* regime show different behaviour to that seen for low and intermediate I^* values with the maximum vortex velocity seeming to decrease at late times. For $T < 85$ we see an increase in the maximum velocity with an approximately linear velocity profile. The vortex goes unstable after this point and we see a decrease in the maximum velocity at later times. The profile at $T = 145$ also shows evidence of a contraction of the vortex diameter with a sharp decrease in velocity towards the edge of the vortex at $y/R \sim 1.7$ and a shift in the vortex centre back towards the boundary.

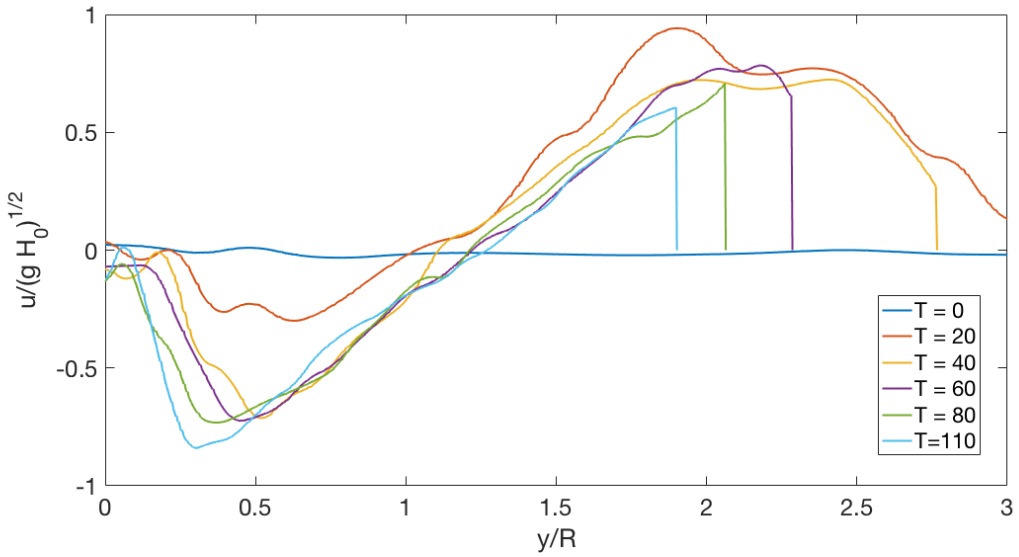

Figure 6.15 A plot of the vortex velocity from an experiment with an intermediate value of $I^* = 0.84$ along a cross-section through the vortex centre perpendicular to the boundary wall. Profiles are shown at six different times which are given in the legend. The velocity is scaled with $\sqrt{g'H_0}$ for H_0 the depth of the source.

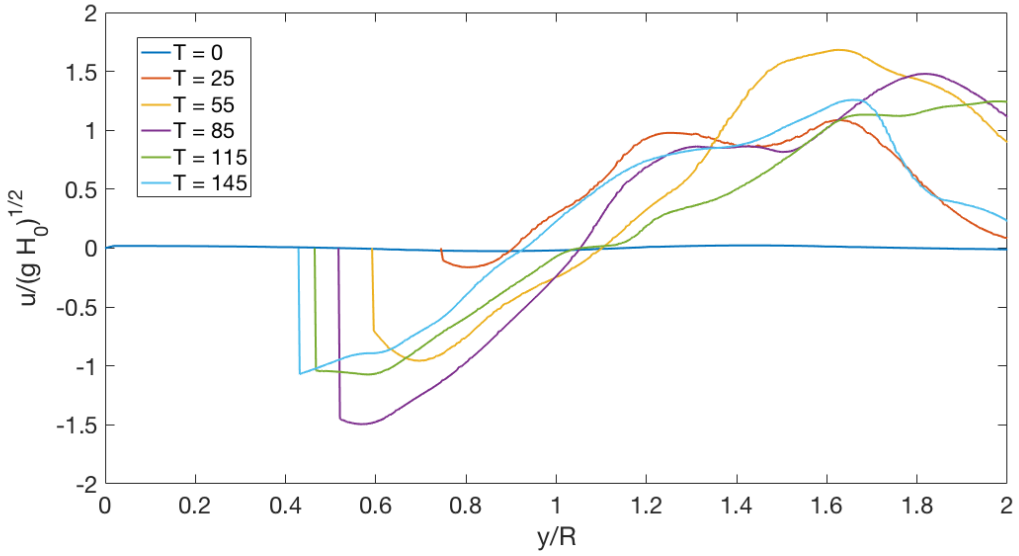

Figure 6.16 A plot of the vortex velocity from an experiment with a high value of $I^* = 1.90$ along a cross-section through the vortex centre perpendicular to the boundary wall. Profiles are shown at six different times which are given in the legend. The velocity is scaled with $\sqrt{g'H_0}$ for H_0 the depth of the source.

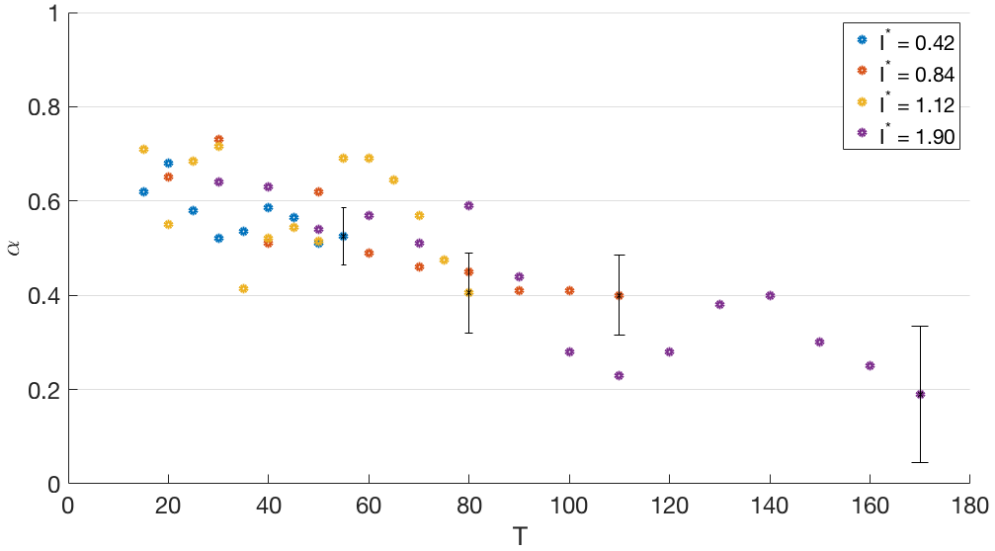

Figure 6.17 A plot of the estimated value of the vorticity ratio α using the gradient of the vortex velocity profiles. Typical error bars are shown.

In figure 6.14 we see evidence that the gradient of the velocity profiles is decreasing over time. The theoretical models of chapter 5 assume a linear velocity profile in the vortex, which is supported by the data in figures 6.14 - 6.16. The gradient of the velocity profiles is given by $\alpha f/2$ and therefore the PIV data suggests that the value of α is decreasing over time, rather than remaining constant as is assumed in the theoretical models of chapter 5. To investigate this further we plot the estimated value of α obtained from the gradient of the velocity profiles as a function of time in figure 6.17. The data in figure 6.17 show a decrease in the value of α over time across all I^* values. This behaviour is not captured in the shallow vortex and NP vortex growth models which use a constant value of α. The results here show that a time-dependent vorticity model is required to fully describe the flow within the vortex accurately and as such will be introduced in chapter 7.

We have seen above in section 6.2.1 that the vortex radius is smaller in the direction perpendicular to the boundary as the presence of the wall causes an asymmetrical vortex shape. We now investigate whether or not the reduction in the vortex radius also leads to a decrease in the vortex maximum velocity in the perpendicular direction. Figure 6.18 plots the ratio of the maximum velocities in the parallel direction and the perpendicular direction over time for the PIV experiments. For early times the velocity is greater for the parallel cross-section as the effects of rotation cause the current to turn to the right after leaving the source and the initial momentum from the source acts to speed up the current in the

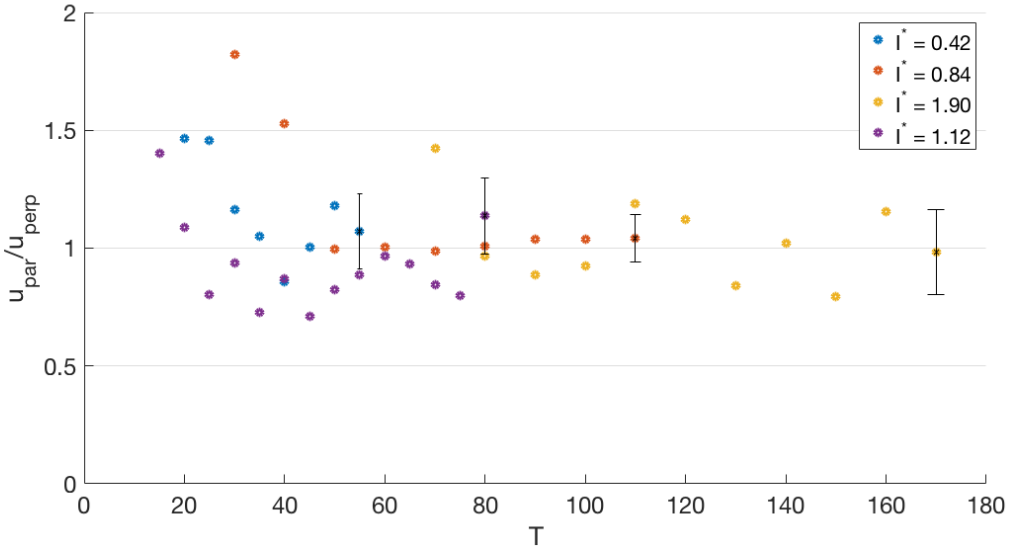

Figure 6.18 A plot of the ratio of the maximum experimentally measured vortex velocity in the parallel and perpendicular directions over time.

direction parallel to the boundary. After this initial adjustment period during which the vortex formation occurs, the maximum velocities in each direction are very similar, with the ratio of the velocities fluctuating around the value of 1 for all four of the PIV experiments. The data in figure 6.18 show that the vortex velocity remains consistent both parallel to and perpendicular to the boundary wall. Combined with the decrease in the vortex radius in the perpendicular direction seen in section 6.2.1, this means that the gradient of the linear velocity profile across the vortex perpendicular to the wall must increase to compensate. Since we expect that α will remain consistent across the vortex, the steepening of the velocity profile gradient in the perpendicular direction must be accounted for by a radius scaling factor. The vortex growth models from chapter 5 provide two choices for this scaling factor. For the shallow vortex model we expect the perpendicular radius to grow at approximately half of the rate of the parallel radius, giving a scaling factor of two. For the NP model, we take a mean value for the radius and therefore a scaling factor of $1/\sqrt{D^*}$ is appropriate. The use of these scaling factors will be analysed in more detail in chapter 8 where we compare the vortex velocity profile with the theoretical predictions for a time-dependent vorticity ratio.

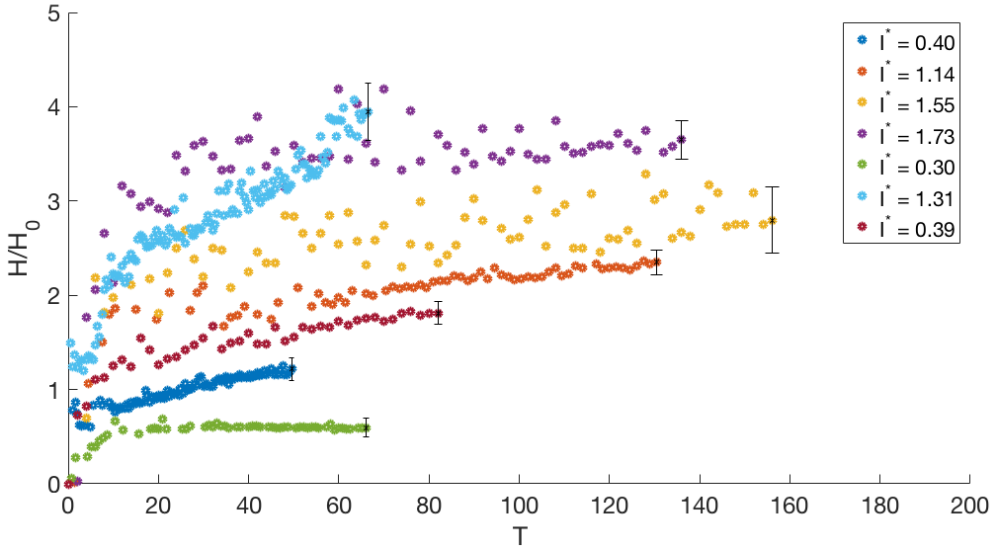

Figure 6.19 The experimentally measured dimensionless maximum vortex depth plotted versus dimensionless time for a subset of the experiments.

6.3 Vortex growth

From our experiments we have collected quantitative data relating to two key properties of the outflow vortex: the maximum vortex depth and the vortex radius. In this section we consolidate the data from the individual experiments to examine the behaviour across the full range of experimental parameters. The issue of vortex stability has been addressed above in section 6.2.3 and we choose to exclude the experiments in which the vortex goes unstable from our analysis. This means that we are only considering the experiments for low and intermediate values of the aspect ratio ratio I^*. The parameter ranges of the experiments considered in this section are: $0.5 \leq f \leq 2$ s^{-1}, $42 \leq Q \leq 100$ cm^3 s^{-1}, $2.1 \leq g' \leq 71.6$ cm s^{-2}, $2 \leq H_0 \leq 4$ cm and $2.5 \leq D \leq 5$ cm, giving the range $0.19 \leq I^* \leq 1.73$.

6.3.1 Vortex depth

We begin our analysis with the maximum vortex depth. This is measured in one second intervals throughout each experiment and is defined simply as the deepest point in the vortex. As the vortex grows in size we would expect its centre and therefore the location of the maximum depth point to move, which is accounted for in the method of measurement.

I^*	Q [cm^3 s^{-1}]	f [s^{-1}]	g' [cm s^{-2}]	H_0 [cm]	D [cm]
0.30	42	1	71.5	2	5
0.39	72	2	68.1	4	5
0.40	47.5	0.5	14.3	2	5
1.14	45	1.5	15.1	2	5
1.31	61	0.5	2.1	2	5
1.55	45	2	14.7	2	5
1.73	62	2	13.5	2	5

Table 6.5 Experimental parameters for the experiments shown in figure 6.19.

Figure 6.19 displays the maximum vortex depth over time for a subset of the experiments with $0.30 \leq I^* \leq 1.73$. The depth is scaled with the source depth H_0 and time with the rotation rate f. We have used these scalings here, rather than the theoretical scalings of $\hat{H} = f^2 H/g'$ and $\hat{t} = Qf^6 t/g'^3$, to allow the data to be displayed clearly on the same plot. The theoretical scalings will be used when comparing the data to the models in section 6.3.3. The experimental parameters are given in table 6.5.

The data in figure 6.19 show some fluctuations at early times but in general the measurements are consistent at later times. The maximum vortex depth increases sharply initially, with the rate of increase gradually slowing down over time. Some of the experiments, for example for $I^* = 0.30$, reach a constant vortex depth which in the case of the run for $I^* = 0.30$ persists for a considerable time of $T \sim 20 - 60$. This is equivalent to the time taken for the current to propagate around half of the tank perimeter ~ 180 cm. For the majority of the experiments we see a constant rate of growth for the vortex depth at late times. This can be seen in figure 6.19 for runs with I^* values $0.40, 1.14$ and 0.39. For runs with I^* values $1.55, 1.73$ and 1.31 we see fluctuations in the depth measurements which may indicate the presence of waves along the interface between the freshwater current and the saltwater ambient.

6.3.2 Vortex radius

The measurements of the vortex radius are dispayed in figure 6.20 for a subset of the experiments that provide a good representation of the range of behaviours seen across the full experimental parameter range. The exact parameters are displayed in table 6.6.

I^*	Q [cm^3 s^{-1}]	f [s^{-1}]	g' [cm s^{-2}]	H_0 [cm]	D [cm]
0.19	74	1	71.5	2	2.5
0.60	42	2	68.1	2	5
0.75	47.5	1	14.3	2	5
0.96	100	1	15.1	2	5
1.14	45	1.5	2.1	2	5
1.31	61	0.5	14.7	2	5
1.73	62	2	13.5	2	5

Table 6.6 Experimental parameters for the experiments shown in figure 6.20.

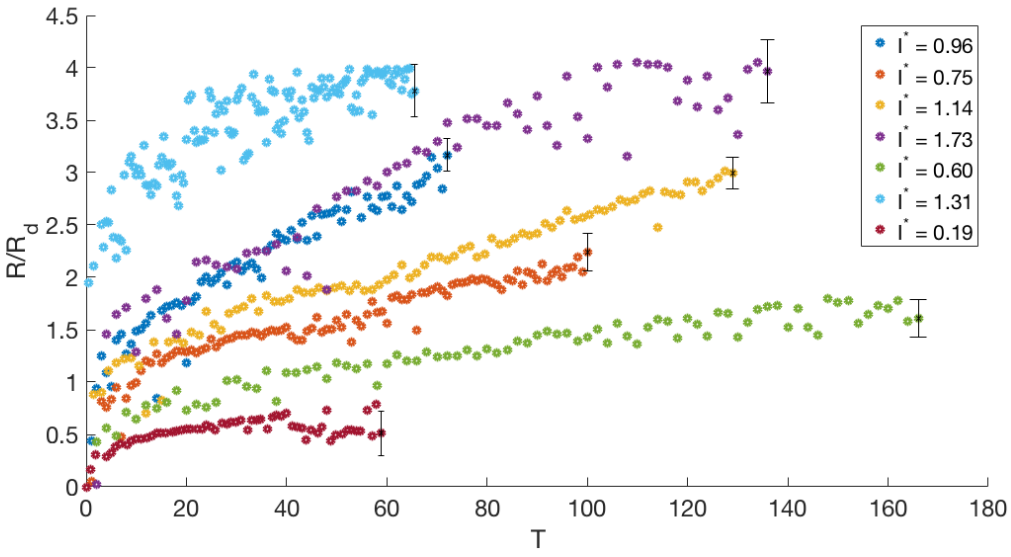

Figure 6.20 A plot of the experimentally measured vortex radius perpendicular to the boundary, scaled with R_d, versus dimensionless time $T = tf$ for a subset of the stable experiments.

The data in figure 6.20 show the same general trends as seen for the maximum vortex depth in figure 6.19, namely a sharp initial increase, followed by a slower but continued increase with time. For the run with $I^* = 1.14$ for example we see a constant rate of increase from $T = 20 - 130$. Similar behaviour is visible for runs with I^* values $0.96, 0.75, 0.60$ and 0.19 with the rate of increase at late times differing across the experiments. The fluctuations in the data present in the depth measurements in figure 6.19 can also be seen here, particularly in the runs with $I^* = 1.73$ and $I^* = 1.31$. The growth of the radius for both I^* values seems to reach a plateau towards the end of the experiment, with an approximately constant value at late times which is in contrast to the other experiments.

6.3.3 Time-dependence

In chapter 7 we present a time-dependent vorticity model of the full flow behaviour linking the outflow vortex and the boundary current, which incorporates the shallow vortex and NP vortex growth models. Here, we analyse the ability of these models to capture the time-dependent growth of the vortex to ensure that they are valid. The dependence on the vorticity ratio α is investigated in chapter 8 alongside the time-dependent vorticity model.

The maximum vortex depth is predicted by both models to increase as $\hat{t}^{1/2}$. To obtain the explicit time dependence in the shallow vortex model, recall that we are using the approximation under the assumption of a shallow vortex, $H/H_a << 1$, to allow for the series expansions of the Bessel functions to be used. This approximation is valid in our experiments where we have a fixed ambient depth $H_a = 32$ cm and the largest maximum vortex depth seen in any of the experiments is ~ 10 cm. We also saw in chapter 5 that the approximated solution showed the best agreement with the exact solution for small values of $T_R = Qt/(H_a R_{da}^2) \lesssim 1$. For the experiments considered in this section $0.01 \leq T_R \leq 0.95$ where we have used the end time of the experiment t_f to calculate T_R. The experimentally measured vortex depth, non-dimensionalised by g'/f^2, is plotted versus dimensionless time $\hat{t} = tQf^6/g'^3$ in figure 6.21. The choice of non-dimensionalisation is the same as that in the work of GL on which our finite PV extended model is based. The data are displayed on a log-log plot and fitted with a linear curve. The data in figure 6.21 show good collapse with an R^2 value of 0.91. The linear curve fitted to the data gives an index of 0.46 ± 0.03 allowing for experimental error, which demonstrates good agreement between the experimental data and the theoretical

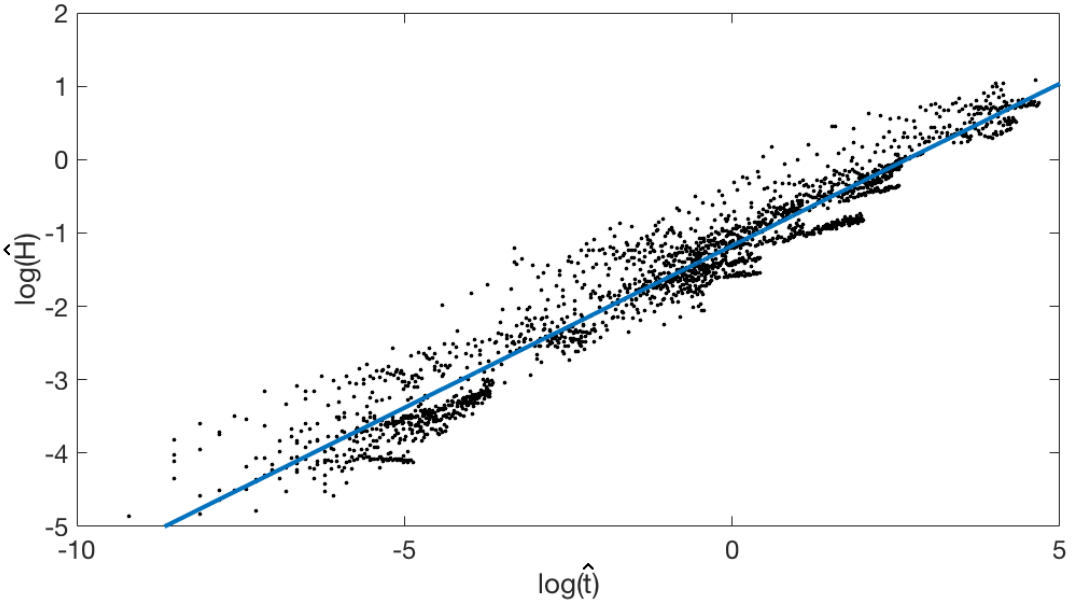

Figure 6.21 The experimentally measured dimensionless maximum vortex depth versus dimensionless time for all of the experiments as a log-log plot. A linear curve is fitted to the data.

models.

The vortex radius is predicted by both models to grow over time as $\hat{t}^{1/4}$. In section 6.2.1 we found the diameter ratio D^* to be approximately constant over time and therefore to analyse the time-dependent growth we may consider the vortex radius in either direction. Figure 6.22 displays the vortex perpendicular radius data from all of the stable experiments on a log-log plot which is fitted with a linear curve. We have used the same dimensionless variables as GL, namely $\hat{R} = f^2R/g'$ and $\hat{t} = Qf^6t/g'^3$. As with the vortex depth measurements we see good collapse in the data with a R^2 value of 0.87. The linear curve fitted to the data gives an index of 0.26 ± 0.03 which again shows good agreement between the data and the theory.

Overall, both the shallow vortex and NP models show capability of capturing the time-dependent growth of the vortex maximum depth and radius across the full range of experimental parameters. The time-dependence predicted by both models will form the foundation of the time-dependent vorticity model derived in chapter 7.

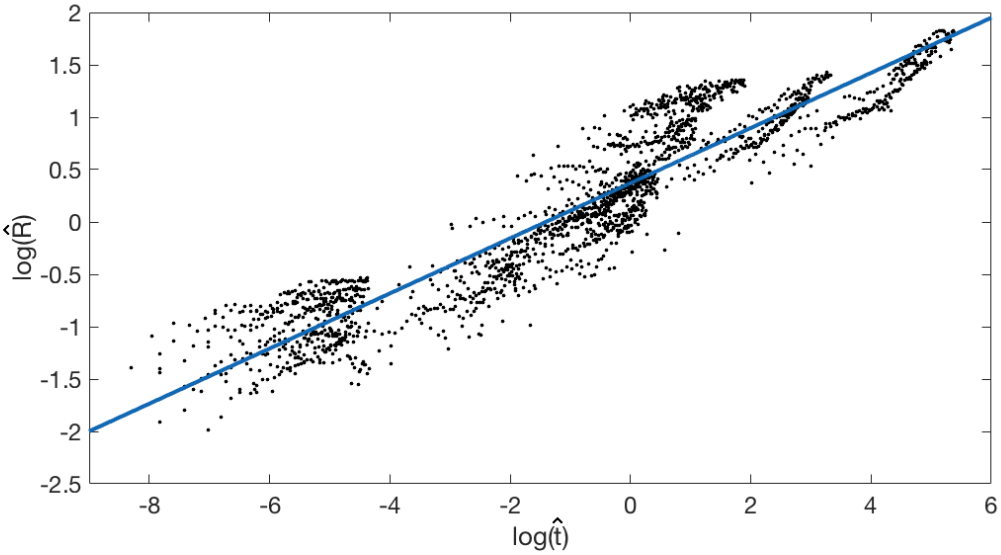

Figure 6.22 The experimentally measured dimensionless vortex perpendicular radius versus dimensionless time for all of the experiments as a log-log plot. A linear curve is fitted to the data.

6.4 Discussion

Laboratory experiments were conducted analysing the growth of the outflow vortex formed when a source of buoyant water enters into a rotating environment. The experiments were designed to simulate an outflow of freshwater entering into the ocean from a localised source such as a river. The source used in the experiments was designed to replicate such a scenario and its non-zero depth meant that a finite value of PV was introduced into the flow. A theoretical model for the growth of a vortex from a finite PV source was introduced in chapter 5 and here we have compared it with the experimental observations of the outflow vortex.

Qualitative observations of the flow revealed that the vortex shape is not circular, as assumed in the work of NP, but is in fact closer to a semi-circle across a large range of the experimental parmeters. The shape of the vortex at the surface is classified according to the diameter ratio $D^* = D_{perp}/D_{par}$ with a value of $D^* < 1$ found for all of the experiments for which the vortex remains stable. The vortex radius is therefore larger in the direction parallel to the boundary wall than in the direction perpendicular to the wall. The vortex depth profiles were analysed across the regimes of low, intermediate and high values of I^*, with the intermediate I^* regime showing the best agreement with the theory. For the high I^* regime the outflow vortex was found to go unstable once it reached a critical radius of $R/R_{dV} \sim 2$. The instability is analysed as a baroclinic instability and we see agreement with the stability

analysis of GL.

Analysis of the vortex velocity profiles across all I^* regimes shows the velocity profile to be approximately linear as predicted by the theory. The gradient of the profile is seen to decrease over time which necessitates the introduction of a time-dependent vorticity ratio α_T to account for the decrease, providing the motivation for the time-dependent vorticity model presented in chapter 7. Finally, measurements of the vortex maximum depth and radius were compared with the shallow vortex and NP models to evaluate the ability of the theory to capture the time-dependent growth of the vortex. Good agreement is found for both the vortex depth and radius.

Now that we have a theoretical understanding of the growth of the outflow vortex which shows reasonable agreement with the experimental observations, we are able to begin to fully answer the second key question that this thesis looks to address: what role does the presence of the outflow vortex play in determining the flow behaviour? This will be investigated in chapters 7 and 8 with the introduction of a time-dependent vorticity model linking the outflow vortex and the boundary current.

Chapter 7

Time-dependent theoretical model

7.1 Problem description

We have so far analysed two of the main features of buoyant outflows: the boundary current and the outflow vortex. In chapter 3 we introduced a steady state model for the boundary current for a finite potential vorticity source. This model neglected the presence of the outflow vortex and considered the current in a steady state. In chapter 5 we introduced a theoretical model for the growth of the outflow vortex from a finite potential vorticity source of constant volume flux. This model accounted for the presence of the boundary current via a change in the vortex shape to be approximately semi-circular, with the mass lost by the reduction in the vortex volume assumed to enter into the current. We also analysed the model of NP for the growth of a finite PV outflow bulge where the presence of the boundary current was included via a reduction in the volume flux into the vortex.

Analysis of the vortex velocity profiles in chapter 6 revealed that the vorticity ratio α decreases over time. In this chapter we introduce a theoretical model that includes a time-dependent vorticity ratio α_T and investigate what effect this has on the growth of the vortex and subsequently the boundary current. The model provides a link between the two theoretical models for the outflow bulge and the boundary current and thus formulates a complete theoretical description of the flow. This will help to establish the role that the presence of the outflow vortex plays in determining the current properties.

7.2 Theoretical model

The setup of the model follows that of PN and the idea of the 'momentum imbalance paradox' (Pichevin and Nof, 1997). The key idea is that a steady boundary current cannot be established due to the impossiblity of balancing the momentum flux leaving in the current. To offset the momentum-flux lost in the current, the outflow forms a large anticyclonic bulge next to the source which slowly migrates offshore. The model is therefore intrinsically time-dependent with a slowly-varying timescale set by the slow offshore bulge migration and as such we will no longer consider the boundary current in a steady state. The outflow vortex forms as an intermediary feature between the source and the boundary current and acts as a time-varying source for the current where the properties of the flow are conserved at each timestep. We model the freshwater outflow and the saltwater ambient as a two-layer fluid with zero mixing between the layers. This allows the use of the shallow water equations discussed in chapter 1. The setup of the model here is the same as for the steady-state current model and the vortex growth models, allowing us to use the previous results of the theory in chapters 3 and 5.

7.2.1 Model outline

The model is centred on the idea of the conservation of potential vorticity with the value of the initial PV at the source being conserved throughout the flow in both the vortex and the boundary current. This results in the following flow description:

- After the initial release of the freshwater from the source and the formation of the outflow vortex, the flow into the vortex is larger than that which is leaving and as such the vortex depth must increase over time.
- For PV to be conserved the vorticity ratio $\alpha = -\zeta/f$ must decrease over time, reaching the limit $\alpha = 0$ at large times. Once it is zero the vortex depth can no longer continue to increase and as a result the vortex radius must continue to grow. The growth of the radus is also required to satisify the force balance across the system.
- The velocity field in the vortex fixes the current velocity via a Bernoulli condition applied to a streamline along the outermost edge of the vortex and the current. The velocity is a linear function of the radius and the vorticity ratio. The increase in the radius maintains a non-zero velocity, despite the decrease in α, which enables the current to continue to propagate.

- For a finite wall velocity model, the decrease in the current velocity over time, combined with the maximum current depth h_0 that remains fixed by geostrophy, results in an increase in the current width to maintain the constant flux through a cross-section of the current. For a zero wall velocity model the steady state current width remains unchanged and is fixed by the conditions at the source.

The key result of the model is the importance of the continued growth of the vortex radius at late times. This not only accounts for the limit of the maximum vortex depth and the continued conservation of PV, but also enables the current to continue to propagate by supplying it with a non-zero velocity via a Bernoulli condition applied along the outer edge of the vortex and the current.

The details of the model formulation are presented below beginning with the derivation of the time-dependent vorticity ratio in the outflow vortex. The effects of this on the vortex properties are then discussed. The conditions in the vortex feed into the boundary current resulting in changes to the current velocity and current width which will be analysed in turn. We finish the chapter with a discussion of the initial PV at the source.

7.2.2 Vorticity ratio

We begin by considering the conservation of PV equation for the outflow vortex under the assumption of shallow water theory (see chapter 1). Using the vorticity ratio parameter $\alpha = -\zeta/f$, the PV in the vortex is given by

$$q_v = \frac{f(1-\alpha)}{H}, \tag{7.1}$$

where H is the vortex maximum depth. Since PV is conserved throughout the flow, for a source with initial uniform PV $q_0 = f(1-\alpha_i)/H_0$, according to (7.1) we must have

$$\frac{H}{H_0} = \frac{1-\alpha}{1-\alpha_i}. \tag{7.2}$$

In the vortex growth models of chapter 5 the vortex depth was predicted to increase with time as $t^{1/2}$, while the vorticity ratio α was assumed to remain constant. These results appear at first to be contradictory to the PV conservation equation in (7.2). The experimental results of chapter 6 showed that the vortex depth does indeed increase with time. We also saw from

the analysis of the vortex velocity profiles that the vorticity ratio α decreases over time. Therefore, combining the two observations (7.2) remains valid, provided that we model α as a time-dependent parameter.

We recall the work of NP where their model for the growth of the outflow vortex relied on the assumption that the vorticity ratio α only changed on the slow timescale associated with the offshore migration of the centre of the outflow bulge. The numerical studies showed that the value of α decreased, but only at long times due to the accumulation of small frictional effects. On the fast timescale associated with geostrophic adjustment, $O(1/f)$, they treated the value of α as approximately constant which allowed solutions for the growth of the vortex to be obtained. Here, we are assuming that the value of α remains constant on the geostrophic adjustment timescale, $O(1/f)$, such that the vortex growth models of chapter 5 remain valid, but changes on a slower timescale. The timescale over which the value of α changes can be calculated from (7.2). Substitution of either of the vortex depth formulae from the shallow vortex or NP models gives the dimensionless time for the change in α as

$$T_\alpha = Q^{*2} f t, \tag{7.3}$$

where $Q^* = H^*(1-\alpha_i)$ is the dimensionless initial source PV. The timescale over which α varies is therefore $O(1/Q^*2f)$ which is in general much larger than the geostrophic adjustment timescale, provided $Q^* < 1$. We also see that as the initial PV of the source increases, the timescale over which α changes will decrease. For an outflow of small finite PV, the value of α changes on a very slow timescale and can be approximated by a constant value, such as in the vortex growth models of chapter 5. We expect that these models are able to capture the key properties of a small PV outflow. However, for outflows with a large initial value of PV, the value of α changes on a much shorter timescale comparable to the fast timescale of geostrophic adjustment and therefore a time-dependent vorticity ratio α_T is required to fully capture the flow behaviour. This will now be introduced into the model to give a complete time-dependent theoretical description of the flow dynamics.

Returning to the PV conservation equation (7.2) we have

$$\frac{H}{H_0} = \frac{1-\alpha_T}{1-\alpha_i}. \tag{7.4}$$

For $H > H_0$ the value of α_T must decrease below the initial source value of α_i and continue to decrease further as the vortex depth increases. This decrease in the local vorticity is

very important as it allows the vortex to maintain a constant level of PV despite the vortex maximum depth increasing. For $H < H_0$ we expect the flow to be unsteady during the initial phase of formation of the vortex and as such a different modelling approach will likely be required, meaning that we will not consider it here. The adjustment phase for $H < H_0$ is similar to that mentioned in the work of NP, where the model for the outflow vortex is only valid beyond a time T_i, at which point the bulge is much larger than the boundary current. The key value here of the source depth H_0 can be seen as equivalent to the H_i term in the NP model. Horner-Devine et al. (2006) also note the existence of a plume initiation time during which nonlinearity is very important. The timescale T_i for the vortex depth to reach the source depth H_0 will be measured experimentally and analysed in chapter 8. We expect that the vortex growth models of chapter 5 will only be valid for $T > T_i$ and thus we are unable to estimate the timescale theoretically with the models currently at our disposal.

Once the transition phase has passed we expect the vortex to continue to grow for $T > T_i$ according to the models outlined in chapter 6, but with the new time-dependent form of the vorticity ratio α_T. For the shallow vortex model we use the shallow vortex approximation for $H << H_a$ to allow the time dependence to be seen explicitly in the formulae for the vortex maximum depth and vortex radius. The experimental results of chapter 6 showed that the time-dependent growth rates predicted by the shallow vortex and NP models agree well with the measurements. The shallow vortex model gives the vortex depth as

$$\frac{H_{TSV}}{H_0} = \left(1 + \frac{H^{*2}\alpha_T(2-\alpha_T)(T-T_i)}{8\pi}\right)^{1/2}, \tag{7.5}$$

and for the NP model we have

$$\frac{H_{TNP}}{H_0} = \left(1 + \frac{H^{*2}\alpha_T^2(2-\alpha_T)(T-T_i)}{4\pi(1+2\alpha_T)}\right)^{1/2}. \tag{7.6}$$

We have used a different non-dimensionalisation to that of chapter 5 as we are now working with both the vortex and the current models together. The maximum vortex depth has been scaled with the source depth H_0 and dimensionless time is given by $T = tf$. We are able to model the decrease in α_T with time by substituting for the vortex maximum depth formulae from both of the shallow vortex and NP models into (7.4). The presence of the boundary current is accounted for in a different way for each model and therefore we will use both in our analysis and look to compare them with the experimental data in chapter 8. The shallow vortex model is derived from the conservation of PV within the vortex, whereas

the NP model is derived from a force balance across the whole system of the vortex and boundary current. The shallow vortex model can be modified to account for the presence of the boundary current, but we might expect the NP model to provide the most accurate description of the flow as the boundary wall is inherently present in the physical description of the flow dynamics. With the modification of the NP model to include the time-dependent vorticity ratio parameter α_T, the model will be renamed as the vortex current model to distinguish between the previous work of NP and the new original work presented in this thesis.

Substituting for the vortex depth from (7.5) into (7.4) we obtain a quadratic equation that the shallow vortex vorticity ratio α_{TSV} must satisfy. Solving the equation we must take the negative root for a value in the range $0 \leq \alpha_{TSV} \leq 1$, giving the solution

$$\alpha_{TSV} = \frac{2+H^{*2}(1-\alpha_i)^2\frac{(T-T_i)}{4\pi} - \sqrt{(2+H^{*2}(1-\alpha_i)^2\frac{(T-T_i)}{4\pi})^2 - 4(1-(1-\alpha_i)^2)(1+H^{*2}(1-\alpha_i)^2\frac{(T-T_i)}{8\pi})}}{2(1+H^{*2}(1-\alpha_i)^2\frac{(T-T_i)}{8\pi})}. \tag{7.7}$$

Making the substitution from (7.6) into (7.4) we find that the vortex current model vorticity ratio is given implicitly by

$$(2+H^{*2}(1-\alpha_i)^2\frac{T-T_i}{4\pi})\alpha_{TVC}^3 - (3+H^{*2}(1-\alpha_i)^2\frac{T-T_i}{2\pi})\alpha_{TVC}^2 - 2(1-\alpha_i)^2\alpha_{TVC} + 1 - (1-\alpha_i)^2 = 0. \tag{7.8}$$

The value of α_T for both models is a function of two independent parameters: the depth ratio $H^* = h_0/H_0$ and the source vorticity ratio α_i, both of which affect the value of the initial PV $Q^* = H^*(1-\alpha_i)$. The dimensionless timescale over which the value of α_T changes in both (7.7) and (7.8) is given by $T_\alpha = H^{*2}(1-\alpha_i)^2 ft$, which is the same as discussed in section 7.2.2.

We analyse the effect of both of the independent parameters on the vorticity ratio. Figure 7.1 plots α_T as a function of time T for five different values of the source vorticity ratio α_i for both models. The depth ratio $H^* = 1$ remains fixed. The shallow vortex model is represented by the dashed lines and the vortex current model by the solid lines. Across all values of α_i we see the same general behaviour in the value of α_T over time as it decreases from α_i towards zero at a gradually decreasing rate. As α_i is increased the value of α_T is higher for a fixed

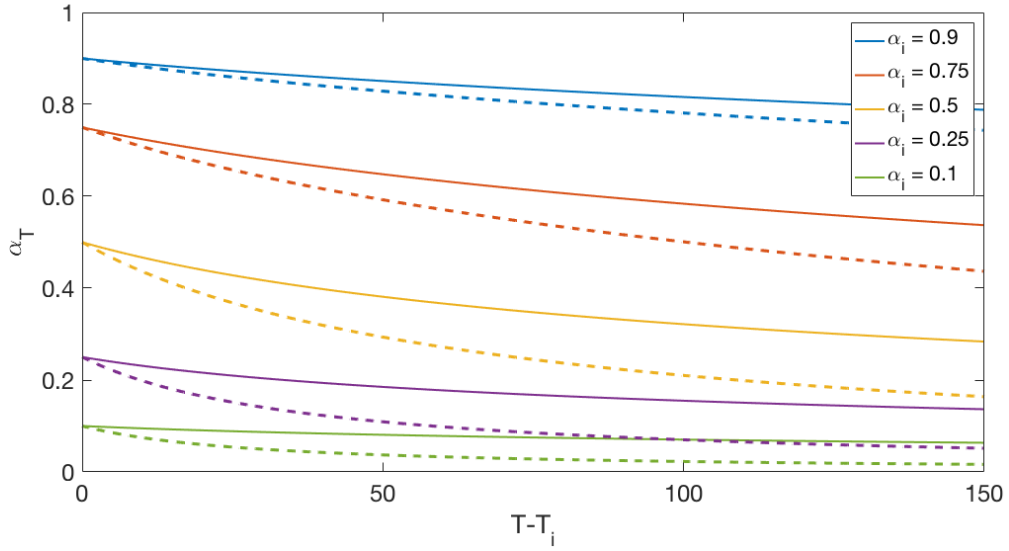

Figure 7.1 The vorticity ratio α_T for the shallow vortex and vortex current models as a function of dimensionless time $T = tf$ and initial source vorticity ratio α_i. Curves for five different values of α_i are shown while $H^* = 1$ remains fixed. The shallow vortex model is represented by the dashed lines and the vortex current model by the solid lines.

time. Comparing the models, we see a steeper rate of decay for the shallow vortex model compared to the same curve for the vortex current model.

Figure 7.2 plots α_T as a function of T also, but this time we fix the value of $\alpha_i = 0.5$ and allow H^* to vary. Again both models are shown, with the dashed line representing the shallow vortex model and the solid line the vortex current model. We see the same behaviour as for figure 7.1 with a decrease in the value of the vorticity ratio away from the initial value towards zero at long times. As the value of H^* is increased the initial decrease is steeper, meaning that the long time limit of zero will be reached more quickly. The shallow vortex model gives a faster rate of decay for the value of α_T.

We are able to approximate the leading order behaviour of α_T at large times using (7.7) and (7.8). For the shallow vortex model we have

$$\alpha_{TSV} \sim \frac{4\pi\alpha_i(2-\alpha_i)}{H^{*2}(1-\alpha_i)^2 T}, \tag{7.9}$$

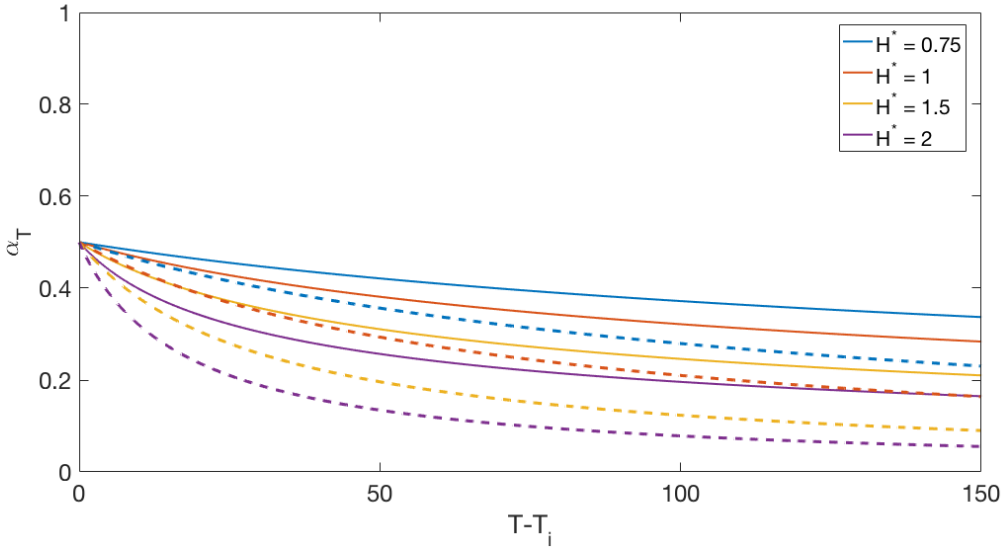

Figure 7.2 The vorticity ratio α_T for the shallow vortex and vortex current models as a function of dimensionless time $T = tf$ and depth ratio H^*. Curves for four different values of H^* are shown while $\alpha_i = 0.5$ remains fixed. The shallow vortex model is represented by the dashed lines and the vortex current model by the solid lines.

and for the vortex current model

$$\alpha_{TVC} \sim \sqrt{\frac{2\pi\alpha_i(2-\alpha_i)}{H^{*2}(1-\alpha_i)^2 T}}. \tag{7.10}$$

As we do not have the explicit behaviour of α_T as a function of time for the vortex current model, the approximation will prove useful in determining the long term behaviour of the flow properties.

7.2.3 Outflow vortex

Having obtained explicit formulae for the time-dependent vorticity ratio α_T we now investigate how the properties of the outflow vortex are affected. We use the theory of chapter 5 with a choice between the shallow vortex and vortex current models for the vortex growth.

7.2.3.1 Vortex depth

The vortex maximum depth is used to derive α_T via the conservation of PV and therefore for both the shallow vortex and vortex current models the depth is fixed according to (7.4). At large times the vorticity ratio reaches the limit $\alpha_T = 0$ which gives a maximum vortex depth that can be achieved,

$$\frac{H}{H_0} = \frac{1}{(1-\alpha_i)}. \tag{7.11}$$

A larger value of α_i corresponds to a smaller initial PV and thus the ultimate vortex depth decreases as the initial PV increases. We saw in section 7.2.2 that the vorticity ratio is a function of both the intial source vorticity ratio α_i and the depth ratio H^*. We investigate the effect that varying each of these parameters has on the vortex depth.

Figure 7.3 plots the vortex maximum depth with time dependent α_T according to both models (given in (7.4)) for five different values of the source vorticity ratio α_i, with $H^* = 1$. The shallow vortex model is represented by the dashed lines and the vortex current model by the solid lines. The general behaviour is the same across all values of α_i with the vortex depth increasing as time increases. In each case the rate of increase gradually slows over time as the depth tends to the long-time limit in (7.11). As the source vorticity ratio is increased the depth at any given time increases and we see a faster rate of increase for the vortex depth. For a larger α_i the flow initially contains more shear in the velocity field and thus the interface between the current and the ambient is more likely to deepen resulting in a deeper vortex. Comparison between the models shows that the depth increases at a faster rate for the shallow vortex model compared to the vortex current model.

Figure 7.4 plots the maximum vortex depth for time-dependent α_T as a function of time for four different values of H^* and fixed $\alpha_i = 0.5$. Again we see an increase in the depth over time at a gradually decreasing rate as it tends towards its final steady state value at long times. The shallow vortex model gives a faster rate of increase for the vortex depth and we see a smaller vortex depth for larger H^* at a fixed time. Since α_i is fixed, the initial PV increases as H^* increases and therefore the behaviour seen here is the same as in figure 7.3, with larger PV giving a smaller vortex depth. As H^* increases, the source depth becomes shallower and therefore we might expect a shallower vortex as a result.

In summary, the vortex depth reaches a long-time limit as the vorticity ratio $\alpha_T \to 0$. The limit of the vortex depth is seen to decrease as the initial PV is increased and the shallow

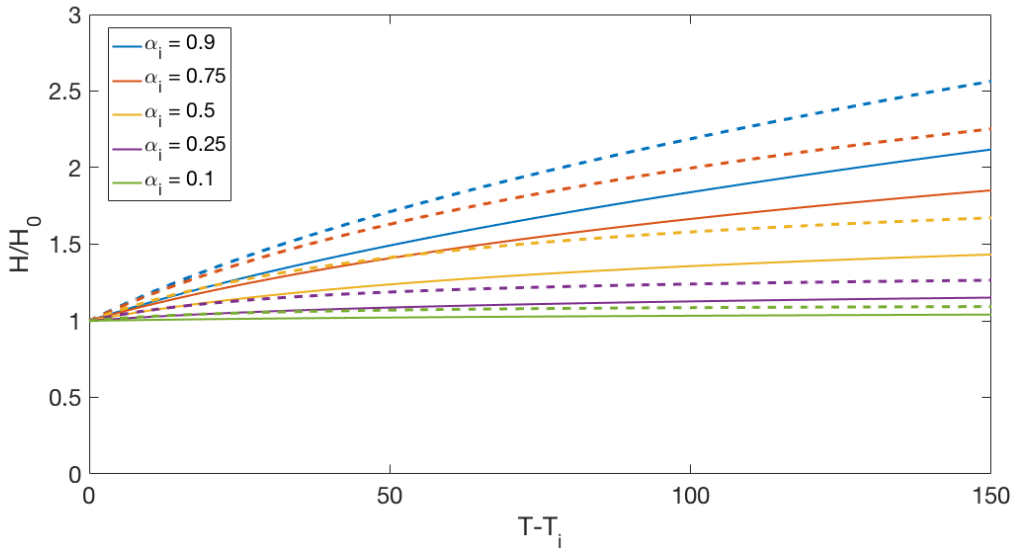

Figure 7.3 The maximum vortex depth for time dependent α_T for the shallow vortex and vortex current models versus dimensionless time T. Five curves are shown, each with a different value for the source vorticity ratio α_i with fixed $H^* = 1$. The shallow vortex model is represented by the dashed lines and the vortex current model by the solid lines.

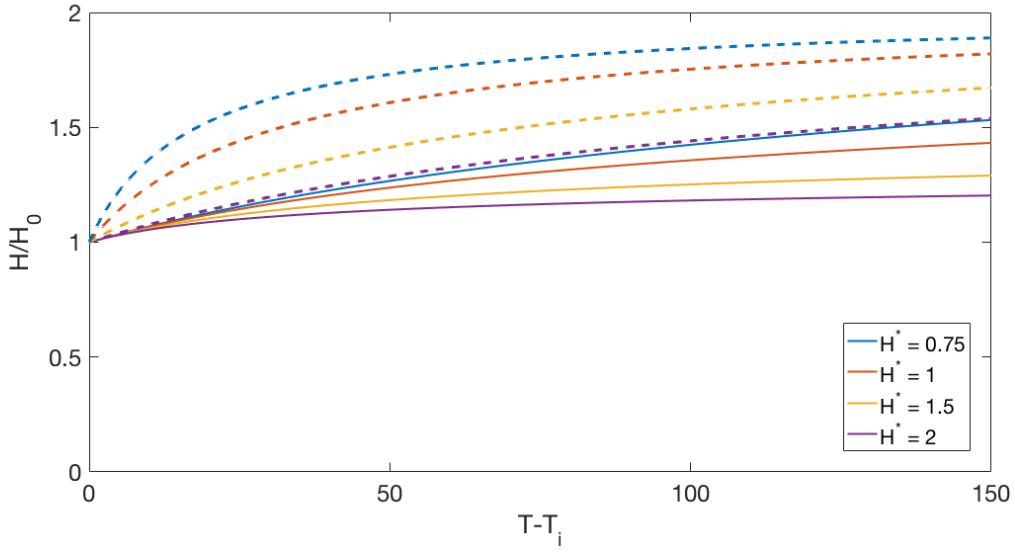

Figure 7.4 The maximum vortex depth for time dependent α_T for the shallow vortex and vortex current models versus dimensionless time T. Four curves are shown, each with a different value for the depth ratio H^* and fixed $\alpha_i = 0.5$. The shallow vortex model is represented by the dashed lines and the vortex current model by the solid lines.

vortex model shows a faster rate of increase for the vortex depth over time compared to the vortex current model.

7.2.3.2 Vortex radius

The effect of a time-dependent vorticity ratio on the vortex radius is particularly interesting. We have seen above that for PV to be conserved the vorticity ratio must decrease over time, reaching the limit $\alpha_T = 0$ at large times. Once it is zero the vortex depth can no longer continue to increase and as a result the vortex radius must continue to grow to absorb the excess of mass flux entering into the vortex compared to that leaving. Using the results from chapter 5 the vortex radius for time-dependent α_T is given by

$$\frac{R_{TSV}}{R_d} = \Big(\frac{R_i^4}{R_d^4} + \frac{8H^{*2}(T-T_i)}{\pi\alpha_T(2-\alpha_T)}\Big)^{1/4}, \tag{7.12}$$

for the shallow vortex model and

$$\frac{R_{TVC}}{R_d} = \Big(\frac{R_i^4}{R_d^4} + \frac{16H^{*2}(T-T_i)}{\pi(1+2\alpha_T)(2-\alpha_T)}\Big)^{1/4}, \tag{7.13}$$

for the vortex current model, where we have non-dimensionalised by the source deformation radius $R_d = \sqrt{g'H_0}/f$. The value of R_i in (7.12) and (7.13) is the vortex radius at time T_i when the vortex depth $H = H_0$ and the vorticity ratio $\alpha_T = \alpha_i$. It is determined using the relationship between the vortex depth and radius (which is the same for both the shallow vortex and vortex current models) given by

$$\frac{R}{R_d} = \frac{2\sqrt{2}}{\sqrt{\alpha_T(2-\alpha_T)}}\Big(\frac{H}{H_0}\Big)^{1/2}, \tag{7.14}$$

which gives $R_i/R_d = 2\sqrt{2}/\sqrt{\alpha_i(2-\alpha_i)}$.

Using the long time behaviour of α_T given by (7.9) and (7.10) we can substitute into (7.12) and (7.13) to get the leading order terms. We find that at large times when the vortex depth can no longer increase, the radius continues to increase according to

$$\frac{R_{TSV}}{R_d} \sim \Big(\frac{T^2H^{*4}(1-\alpha_i)^2}{\pi^2\alpha_i(2-\alpha_i)}\Big)^{1/4}, \tag{7.15}$$

for the shallow vortex model and

$$\frac{R_{TVC}}{R_d} \sim \left(\frac{8TH^{*2}}{\pi}\right)^{1/4}, \tag{7.16}$$

for the vortex current model. In both cases the radius does not reach a constant final value as seen for the vortex maximum depth, but instead continues to increase with time. The continued increase of the vortex radius is a result of the constant flux source meaning that fluid is still being supplied to the vortex. Since the vortex depth cannot increase any further the extra mass is absorbed by an increase in the vortex radius. The rate of increase is higher for the shallow vortex model and the growth rate increases with decreasing α_i and increasing H^* corresponding to an increase in the PV. For the vortex current model, the long-term radius growth rate is a function of H^* only and increases as the PV is increased.

As with the vortex maximum depth we investigate the effect of varying both α_i and H^* on the growth of the vortex radius. Figure 7.5 plots the vortex radius for time dependent α_T for five different values of α_i while $H^* = 1$ remains fixed. The shallow vortex model is represented by the dashed lines and the vortex current model by the solid lines. The general behaviour of the curves is the same across all α_i values with an increase in the radius over time. There is, however, a large difference in the initial value of the radius at $T = T_i$, with lower α_i values (corresponding to larger Q^* values) giving a larger initial vortex radius. Since the vortex depth is the same at $T = T_i$ this means that the initial vortex increases in size as the initial PV increases. The vortex radius is also higher at any fixed time for larger initial PV. The increase in vortex radius with decreasing α_i is expected as it follows the trend seen above in figure 7.3 where smaller α_i led to a shallower vortex. For a fixed volume flux, a shallower vortex depth must be compensated for by an increase in the vortex radius. Comparing the models we see a faster rate of increase for the vortex radius for the shallow vortex model.

Figure 7.6 displays the vortex radius for time-dependent α_T for a fixed value of α_i with varying H^*. For all values of H^* the vortex radius increases over time. The higher values of H^* show a sharper initial increase, which gradually slows down at later times towards a constant rate which is higher for larger values of H^*. At a fixed time, a larger value of H^* gives a larger vortex radius. This coincides with the behaviour seen in figure 7.4 with the vortex depth decreasing as H^* increases, as for a constant volume flux a shallower depth must be compensated for by an increase in the vortex radius. As the value of H^* increases the initial PV also increases as α_i is fixed and therefore figure 7.6 also shows that the vortex

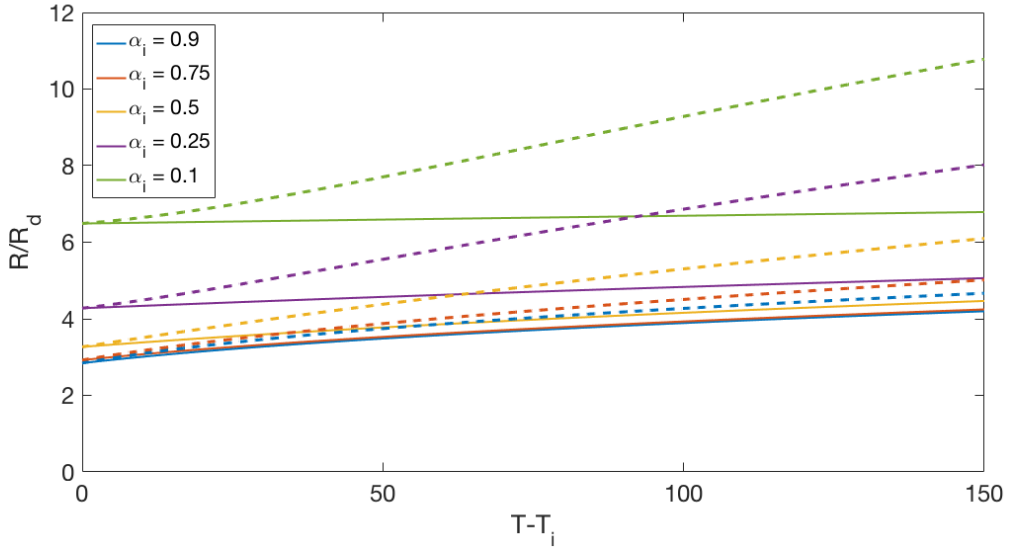

Figure 7.5 The vortex radius for time dependent α_T versus dimensionless time T. Five curves are shown, each with a different value for the source vorticity ratio α_i, while $H^* = 1$ remains fixed. The shallow vortex model is represented by the dashed lines and the vortex current model by the solid lines.

radius is greater for larger PV. The shallow vortex model predicts a more rapidly increasing and larger overall vortex radius at each value of H^*.

In summary, we see that at late times the excess fluid entering into the vortex compared to that leaving is absorbed by an increase in the vortex radius as the depth is unable to increase any further. The vortex radius is seen to increase as the PV is increased and we see a larger growth rate of the radius at late times for increased PV.

7.2.4 Boundary current

The effect of the introduction of a time-dependent vorticity ratio into the vortex growth models will now be discussed in terms of the boundary current. The outflow vortex acts as a time-varying source for the current with the PV in the vortex equal to that of the source, but with the initial depth and velocity changing over time. The time variability of the initial conditions in the vortex feeds into the boundary current and as a result the properties of the boundary current will now be time-dependent also.

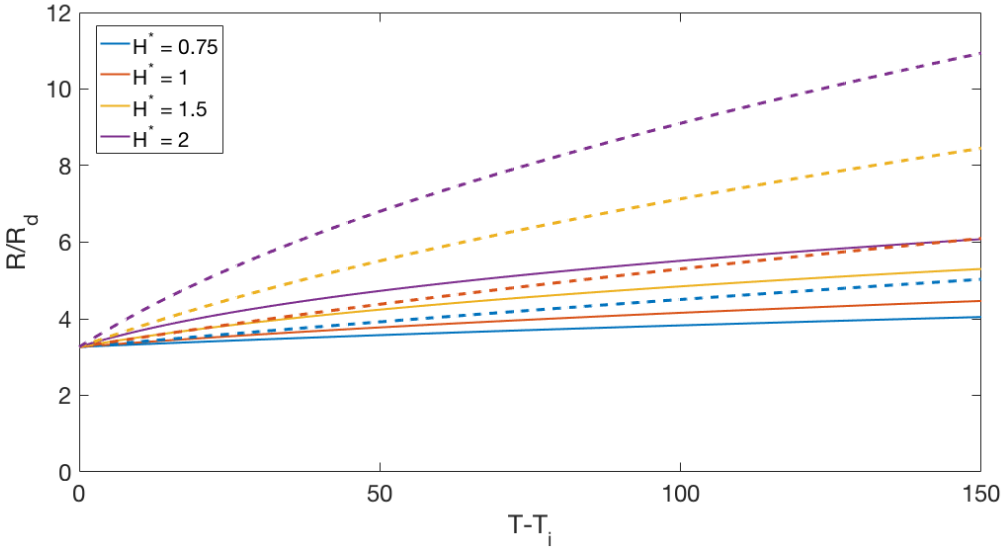

Figure 7.6 The vortex radius for time dependent α_T versus dimensionless time T. Four curves are shown, each with a different value for the depth ratio H^* and fixed $\alpha_i = 0.5$. The shallow vortex model is represented by the dashed lines and the vortex current model by the solid lines.

The current velocity is fixed according to a Bernoulli condition applied to the streamline around the outer edge of the vortex and the current (see section 7.2.4.1 for details). The maximum depth of the boundary current is fixed under the assumption of geostrophy as shown in chapter 3 and since we expect the boundary current to still be governed by geostrophy the value is unchanged. The current depth profile and subsequently the current width will differ depending on the choice of wall velocity. Analysis of the across-current velocity profiles and the experimentally measured current depth profiles in chapter 4 showed that both choices of a zero or finite value for the wall velocity in the steady state model saw agreement with the experimental data. It was unclear whether or not the experimental parameters determined which choice of wall velocity in the model provided the best fit to the data. In some instances a wall velocity of zero provided a good approximation and in others a finite value saw better agreement. With this in mind, we will therefore present a time dependent model for the boundary current using both a zero wall velocity and a finite value for the wall velocity.

We introduce a time dependent vorticity ratio α_T into the steady-state boundary current model of chapter 3 in the same way that it was introduced into the model for the outflow vortex in section 7.2.3. The initial PV entering into the boundary current is the same as the source PV and we therefore use the general current depth profile derived in chapter 3 for a source of dimensionless PV, $Q^* = H^*(1-\alpha_i)$ and a general wall velocity U_l, given by

$$\frac{h}{H_0} = \frac{1}{(1-\alpha_i)} + (H^* - \frac{1}{(1-\alpha_i)})\cosh(\sqrt{1-\alpha_i}\frac{y}{R_d}) - U_l^* \frac{1}{\sqrt{1-\alpha_i}}\sinh(\sqrt{1-\alpha_i}\frac{y}{R_d}). \quad (7.17)$$

We have non-dimensionalised by the source depth H_0 instead of the current depth h_0 which was used in chapter 3, giving $U_l^* = \sqrt{H^*}U_l = u_l/\sqrt{g'H_0}$. This is to ensure consistency with the non-dimensionlisation used for the vortex model in section 7.2.3. At this stage we have not yet specified the wall velocity U_l^*. There are two possible choices relating to the use of a zero wall velocity or a finite value fixed by a Bernoulli condition. We will look at each of these in turn below.

7.2.4.1 Current velocity

In the presence of the outflow vortex the current velocity is fixed by the velocity field of the vortex. We saw in chapter 4 that using the conditions at the source to fix the current velocity led to poor agreement between the theory and the experimental data. In the time-dependent model presented here, one of the roles of the presence of the vortex is to fix the current velocity. The vortex velocity field is a linear function of the radius and the vorticity ratio and the increase in the radius combined with the decrease in α_T results in a slowly decreasing velocity at the edge of the vortex. This feeds into the boundary current via a Bernoulli condition applied to a streamline along the outermost edge of the vortex and the current. Figure 7.7 shows the setup of the model, with the streamline in question extending from the edge of the vortex at A to a point B along the edge of the current downstream.

Applying the Bernoulli condition (see chapter 1 for details) along the streamline indicated in the figure gives

$$\frac{1}{2}u_l^2 = \frac{1}{2}\Big(\frac{\alpha_T f R_T}{2}\Big)^2, \quad (7.18)$$

where both the vortex and the current have a depth of zero at their respective edges and we have used the theoretical vortex velocity profile $v_\theta = -\alpha_T f r/2$ from chapter 5. Substituting for the vortex radius for time dependent α_T from (7.12) we have the time-dependent velocity for the shallow vortex model

$$U_{TSV}^* = \Big(\frac{4\alpha_{TSV}^4}{\alpha_i^2(2-\alpha_i)^2} + \frac{\alpha_{TSV}^3 H^{*2}(T-T_i)}{2\pi(2-\alpha_{TSV})}\Big)^{1/4}, \quad (7.19)$$

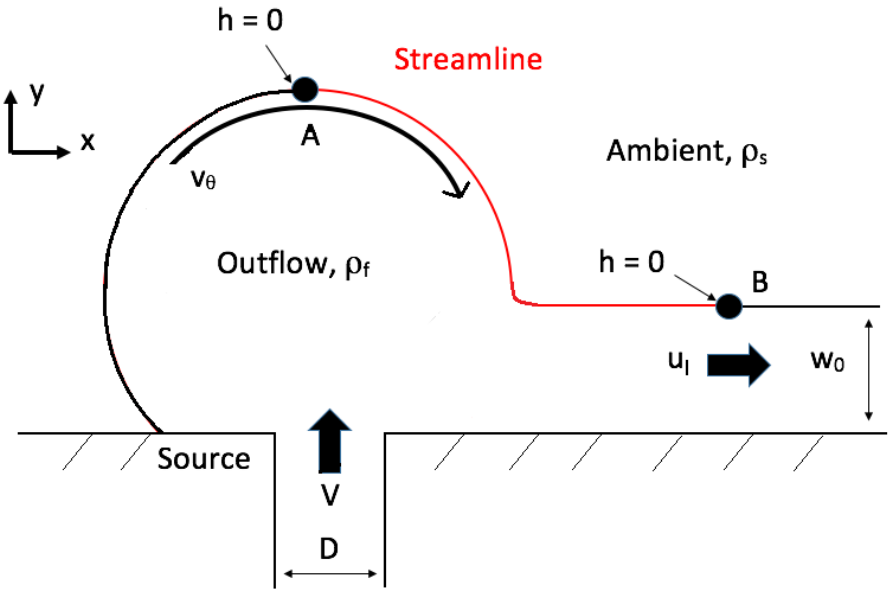

Figure 7.7 The idealised setup used to describe the problem. The Bernoulli condition is valid along the streamline from A at the edge of the vortex to B at the edge of the boundary current further downstream.

where we have non-dimensionalised by $\sqrt{g'H_0}$. For the vortex current model we substitute from (7.13) to obtain

$$U^*_{TVC} = \left(\frac{4\alpha^4_{TVC}}{\alpha_i^2(2-\alpha_i)^2} + \frac{\alpha^4_{TVC}H^{*2}(T-T_i)}{\pi(1+2\alpha_{TVC})(2-\alpha_{TVC})}\right)^{1/4}. \tag{7.20}$$

At late times as $\alpha \to 0$, the vortex depth can no longer increase and the excess fluid entering into the vortex is absorbed by the continued growth of the vortex radius. Using the results in (7.9) and (7.10) the late-time behaviour of the velocity is given by

$$U^*_{TSV} \sim \left(\frac{\alpha_i^3(2-\alpha_i)^3 16\pi^2}{(1-\alpha_i)^6 H^{*4}T^2}\right)^{1/4}, \tag{7.21}$$

for the shallow vortex model and for the vortex current model we have

$$U^*_{TVC} \sim \left(\frac{\alpha_i^2(2-\alpha_i)^2 2\pi}{(1-\alpha_i)^4 H^{*2}T}\right)^{1/4}. \tag{7.22}$$

The velocity will tend to zero eventually, but on a slower timescale than the decay of α_T. The increase in the vortex radius, which is proportional to the current velocity via a Bernoulli condition, at large times maintains a non-zero current velocity allowing the current to con-

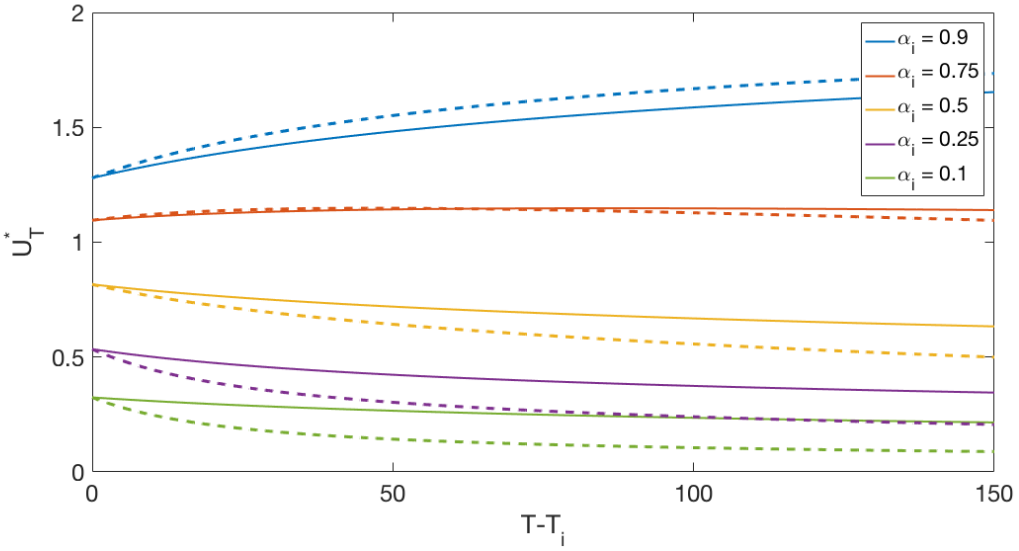

Figure 7.8 The time-dependent current velocity versus dimensionless time T for five different values of the source vorticity ratio α_i, while $H^* = 1$ remains fixed. The shallow vortex model is represented by the dashed lines and the vortex current model by the solid lines.

tinue to propagate. The results in (7.21) and (7.22) show that the rate of decay of the current velocity is faster for the shallow vortex model. We also see that as the value of α_i increases and as the value of H^* decreases, the velocity at late times is larger. Therefore for larger PV the current velocity will be lower.

As with the vortex properties, we investigate the effect of varying the source vorticity ratio α_i and the depth ratio H^* on the current velocity. Figure 7.8 plots the time-dependent current velocity for five different values of the source vorticity ratio α_i while $H^* = 1$ remains fixed. The shallow vortex model is represented by the dashed lines and the vortex current model by the solid lines. We see a change in the initial behaviour of the flow as the value of α_i is varied. For the two highest values of $\alpha_i = 0.9, 0.75$ the current velocity increases from its initial value, whereas for the smaller α_i values the velocity decreases throughout towards its long-time limit of zero. For $\alpha_i = 0.75$ the current velocity reaches a maximum at $T - T_i \sim 75$ before it then starts to decrease. The curve for $\alpha_i = 0.9$ continues to increase beyond $T - T_i = 150$, though at very late times we expect it will begin to decrease towards zero as seen in the long-time behaviour in (7.21) and (7.22). This change in the initial behaviour of the current velocity was seen in the work of TL and in our experimental results in section 4.4.3. The experimental data show a transition between currents that initially increase in velocity before slowing down and those which decrease in velocity throughout

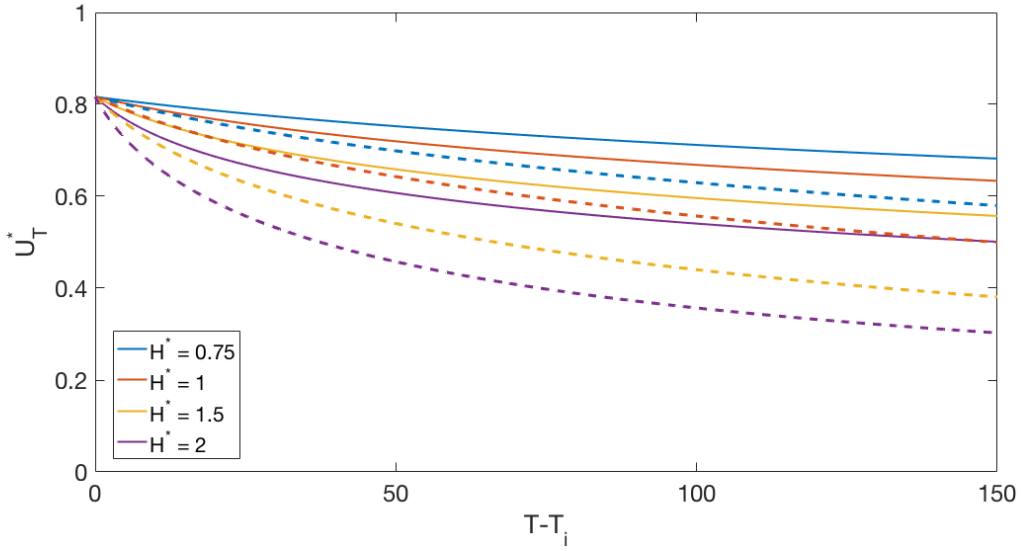

Figure 7.9 The time-dependent current velocity versus dimensionless time T for four different values of the depth ratio H^*, while $\alpha_i = 0.5$ remains fixed. The shallow vortex model is represented by the dashed lines and the vortex current model by the solid lines.

the experiment. The theoretical model derived here provides an explanation for the changes seen, with the value of the source vorticity α_i the key parameter.

Returning to figure 7.8 we see that in general, for a fixed time, the current velocity is greater for a lower initial PV (larger α_i). An increase in the initial local vorticity at the source corresponds to an increase in the velocity shear and therefore for a fixed source width, the source velocity must be higher. We expect that a higher initial velocity at the source will translate into a higher current velocity as seen in figure 7.8. Comparing the models we see that the shallow vortex model amplifies the trend in the velocity over time. This means that for an increasing current velocity, such as at early times for $\alpha_i = 0.9, 0.75$, the shallow vortex model predicts a higher value than the vortex current model and for a decreasing current velocity the shallow vortex model predicts a lower value. The shallow vortex model also predicts a faster decrease to zero for the current velocity over time as seen when comparing (7.21) and (7.22).

Figure 7.9 plots the current velocity over time for fixed α_i, while allowing H^* to vary. Curves for four different values of H^* are shown. At long times all of the curves decrease towards zero with a larger value of H^* giving a lower current velocity. The rate of decrease is also greater for larger H^*. Comparison of the two models shows that the shallow vortex

model gives a lower current velocity which decreases more rapidly towards zero than for the vortex current model.

In summary, our analysis has shown that the increase in the vortex radius at late times plays two important roles in the flow dynamics. Alongside absorbing the excess fluid entering into the vortex, the increase in the radius also allows a non-zero current velocity fixed by a Bernoulli condition to be maintained, allowing the current to continue to propagate. The current velocity is seen to decrease with increasing PV with the shallow vortex model giving a faster rate of decay.

7.2.4.2 Current depth profile

We now turn our attention to the choice of wall velocity U_l^* which will determine the shape of the current depth profile given in (7.17). Experimental measurements of the wall velocity in chapter 4 showed that its value changes as the experimental parameters are varied, with a range from approximately zero to approximately equal to the maximum current velocity. We will therefore model both scenarios by considering a zero wall velocity model and a finite wall velocity model. The use of a finite value for the wall velocity follows from the work of PN as discussed in chapter 3. Physically, the velocity at the wall must be zero, but here we are considering the current velocity at the edge of the thin bounday layer next to the wall and thus a finite value is allowed.

We first assume that the velocity at the wall is finite and equal to the current velocity U_T^*, which is given by (7.19) or (7.20) depending on the choice of vortex growth model. This follows the working of chapter 3 where the x-momentum equation in the shallow water limit fixes the wall velocity at its initial value. The vortex acts as the time-varying 'source' of the current, which means that the wall velocity is fixed at each time step according to the conditions in the vortex. The Bernoulli condition defined above in section 7.2.4.1 fixes the current velocity as U_T^*, which therefore gives our wall velocity $U_l^* = U_T^*$. As the source conditions feeding into the current change at each time step, so too does the wall velocity resulting in a time-dependent current depth profile. The profile will be the same for both the shallow vortex and the vortex current models, except for the value of U_T^*. The general profile is given by

$$\frac{h_{SV}}{H_0} = \frac{1}{(1-\alpha_i)} + (H^* - \frac{1}{(1-\alpha_i)})\cosh(\sqrt{1-\alpha_i}\frac{y}{R_d}) - U_T^* \frac{1}{\sqrt{1-\alpha_i}}\sinh(\sqrt{1-\alpha_i}\frac{y}{R_d}). \quad (7.23)$$

The time-dependence enters into the current depth profile in the U_T^* term, which will either increase or decrease over time depending on the value of α_i (see section 7.2.4.1). The changes to the current depth profile shape can be seen in chapter 3 where the current depth profile is plotted for varying values of the wall velocity. Due to the similarity of the depth profiles we do not provide a full analysis of the time-dependent profile here, but choose instead to concentrate on the effect that the time-dependent current velocity has on the current width in section 7.2.4.3.

The use of a zero wall velocity condition also arises from the x-momentum equation as discussed above, but in this case we are using the initial conditions at the source to fix U_l^*. The freshwater is discharged from the source perpendicular to the boundary and therefore intially the value of u is zero at $y = 0$. By the x-momentum equation it must remain zero for all time and hence the wall velocity is $U_l^* = 0$. The current velocity is still fixed by the vortex velocity via the application of the same Bernoulli condition as discussed above. Substituting a value of $U_l^* = 0$ into (7.23) we recover the same depth profile obtained for the steady state zero wall velocity model for the current in chapter 3. The difference in the current model here, however, is that we have a time-dependent current velocity, rather than the constant velocity obtained in chapter 3, but this does not affect the current profile. We will not repeat the analysis of the depth profiles here as the behaviour is unchanged from that presented in chapter 3.

7.2.4.3 Current width

We have seen so far that the continued increase in the vortex radius at late times is critical to provide a non-zero velocity that feeds into the boundary current, allowing it to continue to propagate. The current velocity does decrease at large time, however, and this decrease, combined with the fixed maximum current depth h_0, means that the current width must increase to maintain a constant flux through a cross-section of the current.

We are able to extract the explicit behaviour of the current width with time by solving (7.17) equal to zero for $y = w_{0T}$. The algebra is the same as that carried out in chapter 3 and thus we begin at the general form for the current width, substituting in our time-dependent velocity U_T^* to give

$$\frac{w_{0T}}{R_d} = \frac{1}{\sqrt{1-\alpha_i}} \operatorname{acosh}\Big(\frac{1-H^*(1-\alpha_i)-(1-\alpha_i)U_T^*\sqrt{2H^*+U_T^{*2}-H^{*2}(1-\alpha_i)}}{(H^*(1-\alpha_i)-1)^2-(1-\alpha_i)U_T^{*2}}\Big). \tag{7.24}$$

We have again non-dimensionalised by the source deformation radius $Rd = \sqrt{g'H_0}/f$ to ensure consistency across the model. At long times the current velocity U_T^* eventually reaches zero and therefore the final current width value at large time tends towards

$$\frac{w_{0T}}{R_d} \sim \frac{1}{\sqrt{1-\alpha_i}} \operatorname{acosh}\Big(\frac{1}{1-H^*(1-\alpha_i)}\Big). \tag{7.25}$$

We note here that this is also the value of the constant current width obtained in the zero wall velocity model. Once again we direct the reader to section 3.2.2.1 for a detailed analysis of the dependence of the zero wall velocity model current width on the initial PV. The current width for a finite wall velocity given in (7.24) will give two different values depending on the choice of vortex growth model. The wall velocity U_T^* is given by (7.19) for the shallow vortex model and (7.20) for the vortex current model. The large time limit of the current width in (7.25) shows that the width increases with increasing initial PV.

We now investigate the dependence of the current width on the independent parameters α_i and H^*, which together describe the effect of finite PV. Figure 7.10 plots the time-dependent maximum current width as a function of time for five different values of the source vorticity ratio α_i at fixed $H^* = 1$. The dashed lines represent the shallow vortex model for the vortex growth and the solid lines the vortex current model. For the three lowest values of α_i the general trend is the same, with an increasing current width over time. For the higher values of α_i there is an initial slight decrease in the current width at early times, but the long-time behaviour will see it increase. The initial decrease here is caused by the initial increase in the current velocity for high values of α_i seen in figure 7.8. At a fixed time the current width increases with increasing initial PV (lower α_i). Comparison of the two vortex growth models shows the same behaviour that has been seen in the current velocity in figure 7.8 with the shallow vortex model amplifying the behaviour over time. Here this means that for low values of α_i where the width is increasing, the shallow vortex model gives a larger current

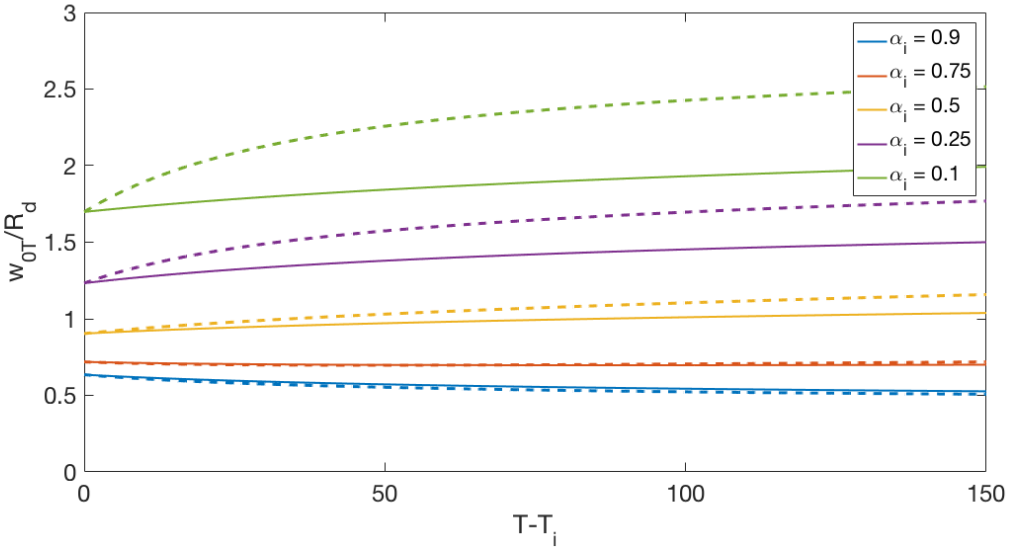

Figure 7.10 The time-dependent current width versus dimensionless time T for five different values of the source vorticity ratio α_i, with fixed H^*. The dashed lines represent the shallow vortex model for the vortex growth and the solid lines the vortex current model.

width and for high values of α_i where there is an initial decrease, the shallow vortex model gives a slightly lower current width. At long times we expect the shallow vortex model to give a larger current width as with the other values of α_i. The decrease in the current velocity is faster for the shallow vortex model and thus the long-time width limit of (7.25) is reached on a shorter timescale. The long-time limit also gives a larger current width for smaller values of α_i as seen in figure 7.10.

Figure 7.11 plots the current width as a function of time for four different values of the depth ratio H^* keeping $\alpha_i = 0.5$ fixed. The general behaviour is the same for each value of H^*, with an increasing current width over time. At a fixed time, the width increases with increasing H^*. We have seen above in figure 7.9 that the current velocity decreases with increasing H^*. Therefore, to maintain a constant flux through any cross-section of the current, the cross-sectional area must increase resulting in a greater current width. The increase in the current width at late times with increasing H^* is also consistent with the long-time width limit given by (7.25). The shallow vortex model follows the same pattern of behaviour as the vortex current model, but with a faster rate of increase. The width predicted by the shallow vortex model is larger than the vortex current model for each value of H^* at all times.

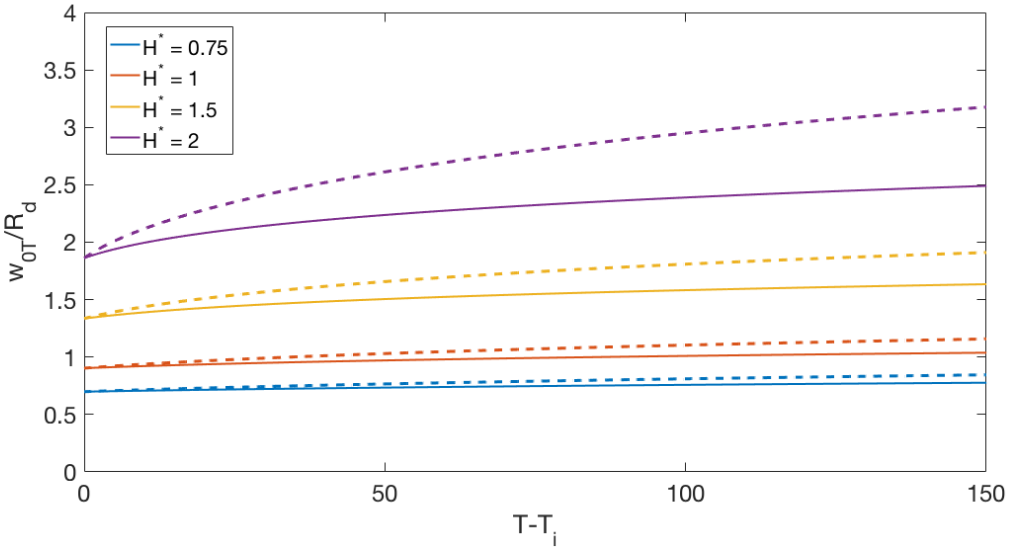

Figure 7.11 The time-dependent current width versus dimensionless time T for four different values of the depth ratio H^*, with fixed $\alpha_i = 0.5$. The dashed lines represent the shallow vortex model for the vortex growth and the solid lines the vortex current model.

In summary, the decrease in the current velocity with time, combined with the maximum current depth that remains fixed by geostrophy, results in an increase in the current width over time. The width is also seen to increase as the PV is increased and the rate of increase is once again greater for the shallow vortex model.

7.2.4.4 Model breakdown

Having analysed the various current properties for the case of a time-dependent vorticity ratio α_T, we turn our attention to the solvability conditions for the model. Looking back at the solvability conditions for the general current model of chapter 3 in (3.18), we see that the range of values of the initial PV for which the model is valid is given by

$$0 \leq Q^* < \frac{2H^* + U_T^{*2} + \sqrt{4U_T^{*2}H^* + U_T^{*4}}}{2H^*}. \tag{7.26}$$

where $Q^* > 1$. For $Q^* < 1$ the model is always valid. The limiting value of Q^* according to (7.26) will change in time since U_T^* is time dependent. At late times U_T^* tends to zero for both vortex growth models and therefore the solvability condition reduces to $Q^* < 1$. We also note that for the assumption in section 7.2.2 that the vorticity ratio varies on a slower

timescale than that of geostrophic adjustment to hold true, we must have $Q^* < 1$. This can be reformulated in terms of the vortex maximum depth limit $H_{max} = H_0/(1-\alpha_i)$ as

$$H_{max} > h_0. \tag{7.27}$$

Therefore, provided that the vortex is deeper than the maximum geostrophic depth, the boundary current model remains valid. The model for the growth of the outflow vortex remains valid for all values of Q^*.

7.3 Initial PV

In deriving the time-dependent vorticity model we have so far considered a general value for the source vorticity ratio α_i. In chapter 3 we explored the value of the source vorticity ratio further and presented a possible approximation for its value as the Rossby number $Ro = u_0/fw_0$. We used the theoretical results for the current velocity u_0 and current width w_0 to derive an implicit equation that could be solved for α_i and we will do the same here. Since our model is time-dependent, we use the value of the current velocity and current width at time $T = T_i$ since this coincides with $\alpha_T = \alpha_i$. The current velocity at $T = T_i$ is given by

$$U^*_{Ti} = \frac{u_{Ti}}{fR_d} = \frac{\alpha_i}{2}\frac{R_i}{Rd}, \tag{7.28}$$

where $R_i/Rd = \sqrt{8/\alpha_i(2-\alpha_i)}$ is the intial vortex radius at $T = T_i$. The current width at $T = T_i$ is given by

$$\frac{w_{0Ti}}{R_d} = \frac{1}{\sqrt{1-\alpha_i}}\,\mathrm{acosh}\Big(\frac{1-H^*(1-\alpha_i)-(1-\alpha_i)U^*_{Ti}\sqrt{2H^*+U^{*2}_{Ti}-H^{*2}(1-\alpha_i)}}{(H^*(1-\alpha_i)-1)^2-(1-\alpha_i)U^{*2}_{Ti}}\Big), \tag{7.29}$$

Combining the two results gives an implicit equation for $\alpha_i \sim U^*_{Ti}(\alpha_i)/fw_{0Ti}(\alpha_i)$. We are able to solve for α_i and find that a solution only exists for $H^* \gtrsim 1$ and that the estimated value of α_i increases with increasing H^*. As well as a minimum value of H^* for which this approximation is valid, there is also an uper limit of $H^* = 3$ at which $\alpha_i = 1$ and the model reduces to the case of zero PV. For $H^* \sim 1$, the estimated value of $\alpha_i = 0$ and thus the full

range of values of Q^* are covered by the approximation.

An alternative approximation for α_i can be obtained from the maximum vortex depth limit given by $H_{max} = H_0/(1-\alpha_i)$. In the case of a zero local vorticity source with $\alpha_i = 0$ the vortex depth cannot be greater than the source depth H_0. We also see that for the zero PV model with $\alpha_i = 1$, the vortex depth is able to grow indefinitely. In the case of finite PV for $0 < \alpha_i < 1$, the maximum vortex depth measured experimentally can be used to derive a lower bound on the estimated value of α_i. In practice, we expect that the minimum value of α_i fixed by using H_{max} alongside the experimentally measured maximum vortex depth will provide the best approximation for α_i to be used when comparing the model with the data in chapter 8. We in fact find that this minimum limit is greater than the theoretically estimated value for $\alpha_i \sim Ro$ for the vast majority of the experiments. The estimation of the value of α_i is discussed in more detail in chapter 8.

7.4 Discussion

We have presented a time-dependent theoretical model that describes the full dynamics of the flow formed when a buoyant outflow enters into a rotating environment. The model links together the two main features of such flows: the anticyclonic outflow vortex and the propagating boundary current by drawing on the key components of the steady-state boundary current model presented in chapter 3 and the vortex growth models discussed in chapter 5.

The conservation of PV within the flow is central to the derivation of the model and leads to the introduction of a time-dependent vorticity ratio α_T, guided by the experimental observations discussed in chapter 6. Initially, the vortex depth deepens as more fluid enters into the vortex compared to the amount leaving. For PV to be conserved the vorticity ratio must decrease over time, reaching the limit $\alpha_T = 0$ at large times. Once it is zero the vortex depth can no longer continue to increase and as a result the vortex radius must continue to grow to absorb the excess fluid and to satisfy the force balance across the system. The velocity field in the vortex fixes the current velocity via a Bernoulli condition applied to a streamline along the outermost edge of the vortex and the current. The continued increase in the radius maintains a non-zero velocity, despite the decrease in α_T, which enables the current to continue to propagate. For a finite wall velocity model, the decrease in the current velocity over time, combined with the maximum current depth h_0 that remains fixed by

geostrophy, results in an increase in the current width to maintain the constant flux through a cross-section of the current. For a zero wall velocity model the steady state current width remains unchanged and is fixed by the conditions at the source.

The key result of the model is the importance of the continued growth of the vortex radius at late times. This not only accounts for the limit of the maximum vortex depth and the continued conservation of PV, but also enables the current to continue to propagate by supplying it with a non-zero velocity. The model also demonstrates two of the roles played by the presence of the outflow vortex with it acting as a time-varying source for the current and fixing the current velocity via its own velocity field.

The features of the model were analysed to determine the effect that PV has on the flow properties. The vortex maximum depth and current velocity were seen to decrease with an increasing value of PV, while the vortex radius and current width increase with increasing PV. These results are consistent with the previous finite PV models of chapters 3 and 5. We will compare the time-dependent theoretical model derived in this chapter with the experimental data in chapter 8.

Chapter 8

Time-dependent experimental observations

8.1 Introduction

In chapter 7 we presented a time-dependent theoretical model that provides a link between the outflow vortex and the boundary current produced when a buoyant outflow enters into a rotating environment. This chapter looks to build upon this work by comparing the theory with the experimental results.

We began by introducing a steady state model for a finite PV boundary current in chapter 3 which was then compared with experimental results in chapter 4. The comparison suggested that a time-dependent model was required to capture the qualitative features of the current. We then introduced a model for the growth of a vortex produced by a finite PV source in chapter 5 which was also compared with experimental data in chapter 6. The experimental measurements of the vortex velocity profiles showed that the vorticity ratio decreased over time and thus a time-dependent vorticity model was required to capture this behaviour. These observations ultimately led to the derivation of a time-dependent theoretical model in chapter 7 which provides a full description of the flow dynamics for a buoyant outflow entering into a rotating environment. The model draws on the key components of the boundary current and vortex growth models and combines them to provide a link between the two features. By comparing this model with the experimental measurements we hope to verify the model results and gain insight into the first-order physics at play. We also hope to gain further understanding of the role played by the outflow vortex in determining the flow dynamics.

8.2 Model comparison

The qualitative aspects of both the boundary current and the outflow vortex have been addressed in chapters 4 and 6 respectively. We have also presented quantitative measurements of various properties of the current and vortex which were compared with the previous theoretical models. Here we will compare the experimental data with the theoretical model predictions from the time-dependent model introduced in chapter 7. We begin with a discussion of the estimation of the model parameters, and then follow the same structure as chapter 7. The time-dependent vorticity ratio α_T is analysed before we move onto the outflow vortex and a comparison of the experimental measurements of the vortex maximum depth and radius with the theory. We finish with the boundary current, which we now consider as time-dependent, rather than as a steady state feature. We compare the experimentally measured current velocity and current width with the theoretical predictions.

We will use only the data from the experiments that remain stable (unless otherwise stated), corresponding to low and intermediate values of I^*. The experimental parameter ranges are: $0.5 \leq f \leq 2$ s^{-1}, $42 \leq Q \leq 100$ cm^3 s^{-1}, $2.1 \leq g' \leq 71.6$ cm s^{-2}, $2 \leq H_0 \leq 4$ cm and $2.5 \leq D \leq 5$ cm, giving the range $0.19 \leq I^* \leq 1.73$.

The experimental data will be compared with the theoretical predictions from both the shallow vortex and the vortex current models throughout this chapter. We have chosen to carry both models through the comparison as each is derived using different physics and accounts for the presence of the boundary current in a different way. The vortex current model is derived from a force balance across the whole system of the vortex and boundary current, whereas the shallow vortex model relies on the conservaton of potential vorticity in the vortex and is modified to account for the presence of the current by a change in the vortex shape. Due to the fact that the boundary current is inherently a part of the physical decription of the flow dynamics in the vortex current model, we might expect that this will provide the most accurate description of the flow on physical grounds.

When analysing the agreement between the two theoretical models and the experimental data, we will rely on qualitative methods to determine which model demonstrates the best fit with the data. A full quantitative analysis of the performance of the models is left for future work, for two main reasons. Firstly, the choice of the initial source vorticity ratio α_i is made by fitting the theoretical curves to the data across the four main flow features

under consideration: the vortex depth, vortex radius, current velocity and current width, and then selecting the single value that provides the best qualitative fit to the data across all four features. The qualitative nature of this selection means that any statistical evaluation of the model fit would be biased. In future studies we plan to obtain accurate measurements of the source vorticity field within the source structure (see section 4.3.2) which will provide a fixed value for α_i that can be used in the models. With access to this data a full statistical analysis of the performance of the two models could then be carried out. The second reason for ony considering a qualitative evaluation of the theoretical models in this thesis is that here we are concentrating on providing a proof-of-principle evaluation of the time-dependent model to assess its capability to capture the first order physics of the flow. Further evaluation and analysis of the model will take place in future studies, including a statistical analysis of its performance against the experimental data.

8.2.1 Model parameters

There are two key model parameters that we will derive from the experimental data: the source vortcitiy ratio α_i and the transition timescale T_i beyond which the time-dependent model is valid. We also investigate the initial vortex radius R_i at $T = T_i$ and find that the theoretical values provide poor estimates of the values seen experimentally. This is discussed in detail in section 8.2.1.3.

8.2.1.1 Source vorticity ratio

We begin our analysis with the source vorticity ratio α_i. In chapter 4 we presented PIV data that provided an estimate of the source vorticity for a subset of the experimental parameters. To obtain estimates for the full parameter range we fitted the experimental data to the steady state current model. This gave some promising results, in particular demonstrating that a zero PV model is able to capture the key characteristics of the current in a steady state for $Ro/Fr_c \gtrsim 1/\sqrt{2}$. We look to follow the same method here, by fitting the data to the theory as closely as possible to provide estimated values for α_i.

The fitted values of α_i are derived by considering the qualitative fit to the experimental data across all features of the flow, that is: the vortex depth, vortex radius, current velocity and current width. The measurements of the vortex maximum depth are particularly important

to consider when deriving the value of α_i, as they impose a lower bound according to the theoretical model as discussed previously in chapter 7. The lower bound is given by

$$\alpha_i \geq 1 - \frac{1}{H_{max}}. \tag{8.1}$$

Furthermore, the measurements of the vortex depth are made using the method of dye attenuation, which results in relatively small measurement error. The vortex radius, current velocity and current width are all measured using the method of front-tracking, which is more susceptible to measurement errors. Typical errors will be given when the data are presented in later sections. This is all taken into account when deriving the fitted values of α_i from the data. We consider both of the vortex growth models presented in chapter 5 and in many cases we obtain different values of α_i when fitting the data to each of the shallow vortex and vortex current models. A subset of the experiments are chosen that allow for the best comparison with the theory. One particularly important criterion in selecting the experiments for comparison is the ratio of the transition timescale T_i and the end time of the experiments. To be able to compare the data with the theory we require that the transition time T_i is much less than the time at which the experiment ends. Unfortunately, this means that for many of the experiments with low values of I^* a comparison with the theory is not possible. For low values of I^* the vortex is elongated along the boundary wall with a weak circulation and a shallow depth, meaning that it takes a longer time for the vortex to deepen and reach the source value of H_0 which defines the transition time T_i. The current speed is also in general larger in this regime and the current rounds the perimeter of the tank in a shorter time forcing the experiment to be halted.

The fitted values of α_i for both of the shallow vortex and vortex current models are displayed in figure 8.1 versus the ratio of the aspect ratios I^*. A total of seventeen experiments are used in the comparison with the experimental data. The plot shows that the fitted values for the vortex current model are in general higher than for the shallow vortex model. This is due to the faster rate of decay of the vorticity ratio α_T for the shallow vortex model which results in more rapid changes to the flow properties, as seen in chapter 7. The α_i values range from $0.59 \leq \alpha_i \leq 0.99$ and do not appear to show any trend relating to the value of I^*.

We next consider the values of $Q^* = H^*(1-\alpha_i)$, which are plotted in figure 8.2 versus I^*. The data show that the flow has a finite value of PV across the majority of the experimental parameter range for both models, with $0.01 \leq Q^* \leq 0.74$. The value of the PV does, however,

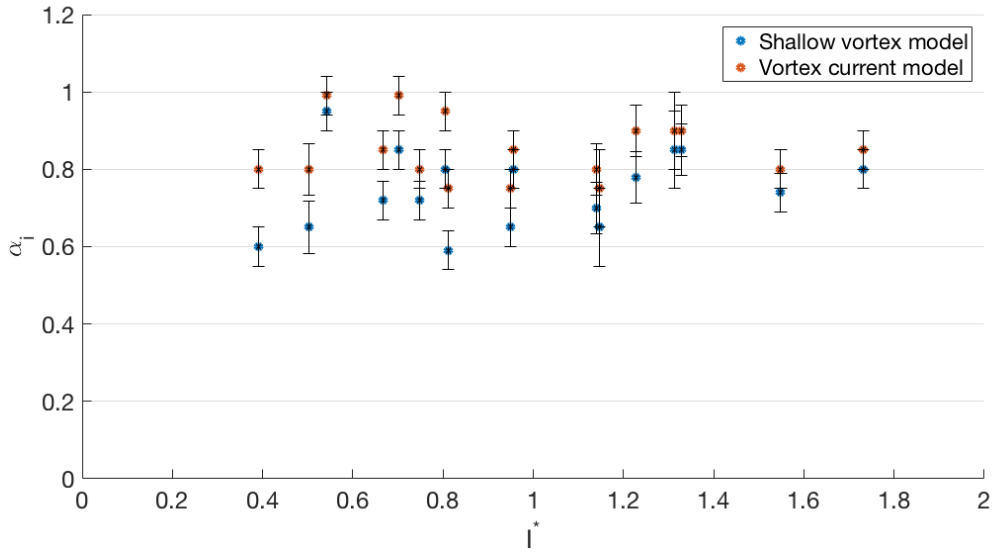

Figure 8.1 The fitted α_i values that give the best agreement between the theory and the experimental data, versus the aspect ratio ratio I^*.

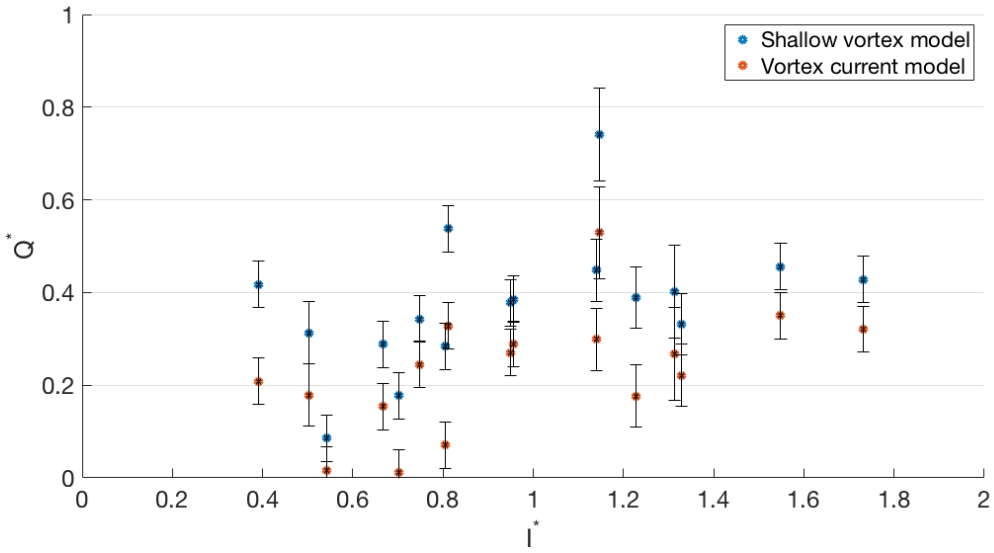

Figure 8.2 The fitted Q^* values that give the best agreement between the theory and the experimental data, versus the aspect ratio ratio I^*.

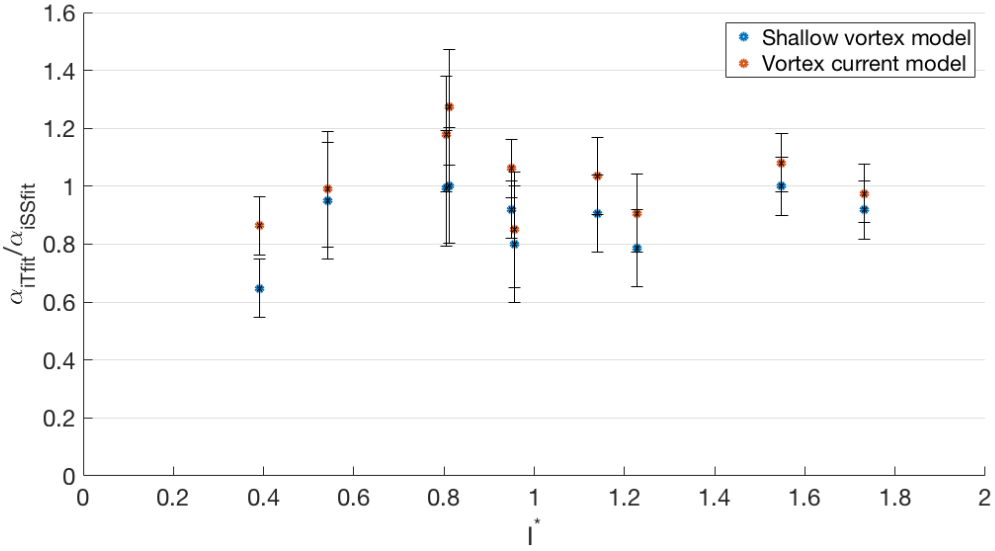

Figure 8.3 The ratio of the fitted values of α_i derived from the time-dependent theoretical model α_{iTfit} and the steady state current model α_{iSSfit}, versus I^*.

remain quite small which explains the ability of the zero PV steady state current model of TL to be able to capture the key properties of the current for $Ro/Fr_c \gtrsim 1/\sqrt{2}$ as seen in chapter 4. We also see that $Q^* < 1$ for each experiment, which ensures that the theoretical model remains valid.

Finally, we compare the fitted values of the source vorticity ratio α_i derived in this chapter for the time-dependent theoretical model, with those derived in chapter 3 for the steady state current model. Figure 8.3 plots the ratio of the values versus I^*. The data show that in general the fitted α_i values are slightly lower for the time-dependent shallow vortex model, whilst the values from the vortex current model agree very well with their steady-state counterparts. The mean value of the ratio for the shallow vortex model is 0.89 ± 0.14, while for the vortex current model the mean ratio value is 1.02 ± 0.14. The largest discrepancy is seen at the lowest value of I^*, which is unsurprising as the flow in the low I^* regime is shallow and wide making it susceptible to the largest measurement errors. The level of agreement between the fitted values is promising as it suggests that fitting the data to the theory provides a valid and consistent method for estimating the source vorticity ratio when accurate measurements are unavailable.

Before we move onto a comparison of both the shallow vortex and vortex current models with the experimental data in the remainder of this chapter, it is worth reiterating that the fitted

values of α_i for both models have been derived qualitatively. That is, the theoretical curves for all of the flow features: the vortex depth, vortex radius, current velocity and current width are fitted to the data and the value of α_i that provides the best qualitative fit across all four features is used. For the preliminary comparison with the data in this thesis such a method is okay as we are concentrating on a proof-of-principle type comparison with the time-dependent theoretical model to assess its capability to capture the first order time-dependent physics of the flow. For future studies, a rigorous framework for model evaluation will be required, where the fitted values of α_i are calculated in the same way for each experiment. One possible such method would be to use the value of α_i that minimises the least squares regression coefficient between the theoretical curves and the data across the four flow features.

8.2.1.2 Transition timescale

Another important parameter in the time-dependent model that must be derived from the experimental data is the transition timescale T_i. We saw in chapter 7 that the vorticity ratio α_T decreases from its initial value α_i for $T > T_i$, where T_i is defined as the time at which the the vortex depth is equal to the depth of the source H_0. Our model is only valid for $T > T_i$.

We are able to obtain estimates for the time $T = T_i$ for the vast majority of the experiments, with the exception of three runs where the vortex does not reach the source depth before the end of the experiment. These will be excluded from our analysis. Figure 8.4 plots the transition timescale as measured experimentally versus the depth ratio H^*. The data show a transition in the behaviour for $H^* \lesssim 1$. For $H^* \sim 1$ the maximum depth fixed by geostrophy, h_0, is approximately equal to the source depth. We expect geostrophic adjustment to occur after $1-2$ rotation periods, corresponding to $T_i \sim 4\pi - 8\pi$. The data show that for $H^* > 1$ the source depth is reached quickly as the outflow increases in depth towards the larger geostrophic value of h_0. This is in contrast to the behaviour for $H^* \sim 1$ where the transition time T_i varies on the order of the geostrophic adjustment timescale. The experiments with $H^* \sim 1$ and small $T_i < 10$ have a larger volume flux Q than those with larger T_i. This increases the source momentum-flux Q^2/A which acts to deepen the flow over a shorter timescale.

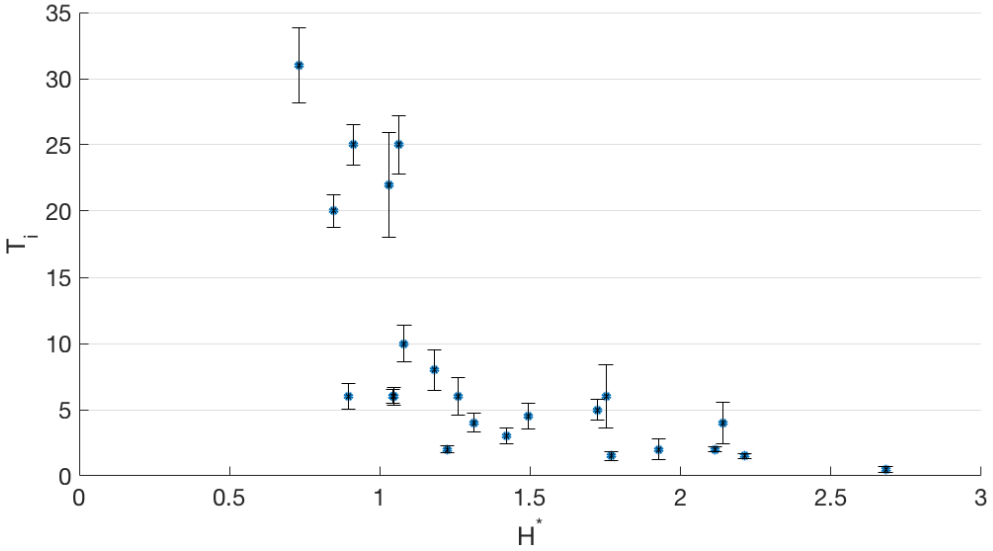

Figure 8.4 The experimentally estimated value of T_i from the vortex depth data versus $H^* = h_0/H_0$.

8.2.1.3 Initial vortex radius

The transition timescale T_i is defined to be the time taken for the vortex depth to increase to the source depth H_0. During this period of transition the vortex radius will also increase, reaching a value of R_i at time T_i. The thoeretical model introduced in chapter 7 estimates the value of R_i to be

$$\frac{R_i}{R_d} = \frac{2\sqrt{2}}{\sqrt{\alpha_i(2-\alpha_i)}}, \tag{8.2}$$

which is the same for both the vortex current and shallow vortex models for the vortex growth. In this section we compare the experimental measurements for the vortex radius with the theoretical predictions for R_i. The theoretical predictions according to (8.2) are calculated using the fitted values for α_i discussed in section 8.2.1.1 and we use the experimentally measured values of T_i from the vortex depth data in section 8.2.1.2.

Figure 8.5 plots the ratio of the experimentally estimated R_i value and the theoretically predicted value, versus I^*. The theoretical predictions for the shallow vortex model in both the parallel and perpendicular directions and those of the vortex current model are compared with the data. The figure shows that in general the value of R_i achieved experimentally is less than that predicted by the theory. The best agreement is seen for the shallow vortex model for the radius in the perpendicular direction, but there is still a consistent overestimation of the intial radius by the theory. This is perhaps not too suprising as we have used a relationship

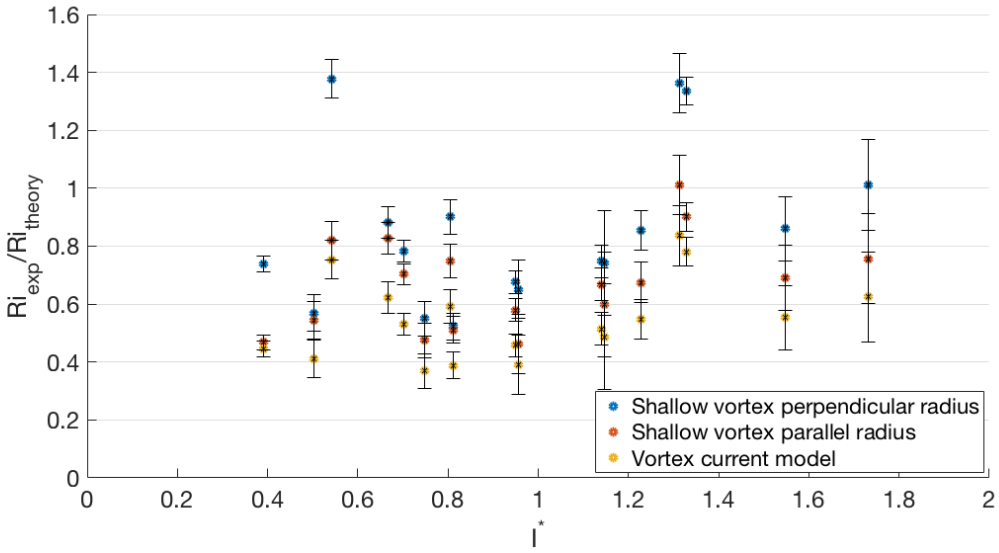

Figure 8.5 The ratio of the experimentally estimated R_i value and the theoretically predicted value versus I^*.

between the vortex maximum depth and radius to derive the equation for R_i given in (8.2), which we expect only to be valid for $T \geq T_i$. The data show that this relationship does not hold during the intial vortex formation for $T < T_i$.

The results seen here mean that we will use the experimental values for R_i when comparing the theory with the data in later sections. We only expect the time-dependent theoretical model of chapter 7 to be valid for $T > T_i$ and therefore by using the experimental values for R_i and T_i we will ensure a fair comparison with the data that is not skewed by the inability of the theory to predict the initial conditions of the vortex at $T = T_i$.

8.2.2 Vortex vorticity ratio

Alongside the main group of experiments used in the model comparison, four further experiments were conducted that enabled velocity measurements to be made at the surface of the vortex using PIV. These are the same group of experiments discussed in section 6.2.4 when analysing the vortex velocity profiles. Here we discuss measurements of the vorticity ratio for the outflow vortex and compare the experimental data with the value of α_T predicted by the theoretical model in chapter 7.

Regime	Q [cm^3 s^{-1}]	f [s^{-1}]	g' [cm s^{-2}]	H_0 [cm]	D [cm]	I^*
low I^*	48	0.5	13.2 - 14.3	2	5	0.40 - 0.42
intermediate I^*	48	1	13.1 - 15.8	2	5	0.75 - 0.84
high I^*	42 - 48	1	2.3 - 3.4	2	5	1.90 - 2.30

Table 8.1 Experimental parameters for the PIV experiments and the corresponding dye attenuation experiments with which they are matched.

The vorticity ratio is measured experimentally using two methods. In chapter 6 we used the gradient of the vortex velocity profiles to estimate the value of α_T at each timestep. The theory assumes that the vortex velocity profile is given by

$$v_\theta = -\frac{\alpha_T f r}{2}. \tag{8.3}$$

The results in chapter 6 showed that in general, the maximum vortex velocity increases with time initially, but then remains approximately constant for the remainder of an experiment. The vortex radius was shown to increase with time, while the gradient of the velocity profile decreases with time. The gradient is given by $\alpha_T f/2$ and therefore its decrease corresponds to a decrease in the vorticity ratio, which we saw in chapter 7 is required in order to conserve PV. This decrease, combined with the increase in the vortex radius, is the cause of the approximately constant velocity seen in the vortex velocity profiles at late times. We also saw in section 6.2.4 that the maximum magnitude of the vortex velocity was the same for the parallel and perpendicular cross-sections, whilst the radius was smaller in the perpendicular direction. This difference is accounted for in the velocity profile in (8.3) by ensuring that the vortex radius is scaled appropriately depending on the direction in which it is measured and the vortex growth model being used. For the shallow vortex model we expect the perpendicular radius to grow at approximately half of the rate of the parallel radius, giving a scaling factor of two (plotted as $1/2$ perpendicular velocity in figures). For the vortex current model, we take a mean value for the radius and therefore a scaling factor of $1/\sqrt{D^*}$ is appropriate (plotted as mean velocity in figures). When comparing the experimental data we present both the parallel velocity measurements and the appropriately scaled perpendicular velocity measurements. The second method for calculating the vorticity ratio experimentally is to use the full PIV data across the entire vortex surface to estimate the mean vorticity in the vortex. The details of the method used are given in chapter 2.

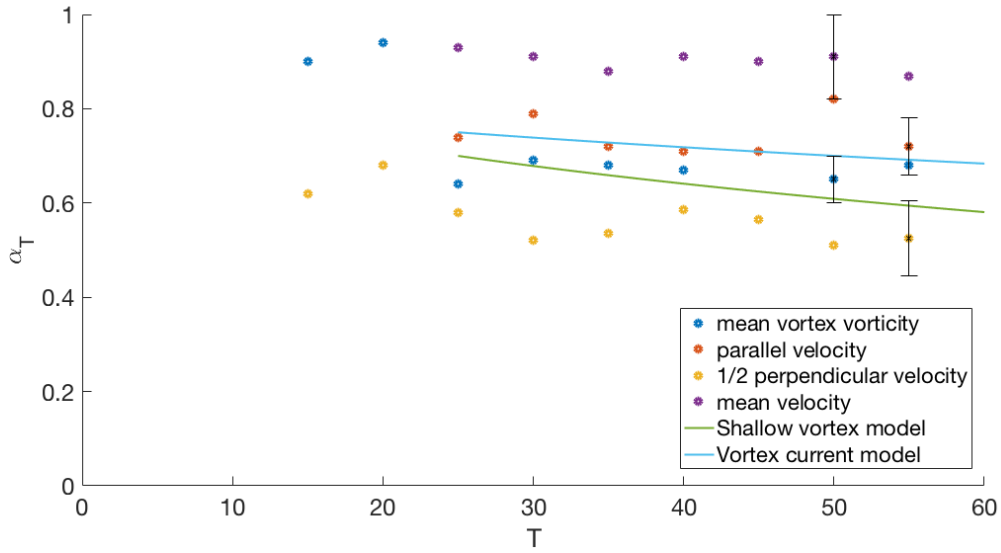

Figure 8.6 The estimated value for the vortex vorticity ratio over time from the experimental data for low I^*. The theoretical predictions for the shallow vortex and vortex current models are also shown.

The theoretical curves for the time-dependent vorticity ratio derived in chapter 7 for both the shallow vortex and vortex current models will be compared with the experimental data for the mean vortex vorticity estimates and the velocity profile estimates for α_T. In order to make this comparison the PIV experiments are matched with a dye attenuation experiment with similar parameter values to enable a fitted value of α_i to be calculated. The experimental parameters are given in table 8.1. The value of α_i for each experiment is taken to be the fitted value as discussed in section 8.2.1.1 and the value of T_i is also estimated from the experimental data as discussed in section 8.2.1.2. We expect the mean vortex vorticity data to provide the best estimates for the vorticity ratio, with the estimates from the velocity data being slightly higher. This is due to the outflow vortex increasing in size beyond the field of measurement in the PIV experiments, which prevents the full radius of the vortex from being used when calculating the gradient of the velocity profiles. This issue is overcome for the mean vorticity measurements by averaging the vorticity over the central area of the vortex that remains in the field of view.

Figure 8.6 displays the data for the estimated α_T values for the low I^* regime over time. Four different sets of data are shown corresponding to different estimates for the value of α_T along with the theoretical predictions from the shallow vortex and vortex current models. The estimates from the parallel velocity data show good agreement with the mean vortex vorticity measurements and the theory. For the perpendicular velocity data the estimates for α_T are

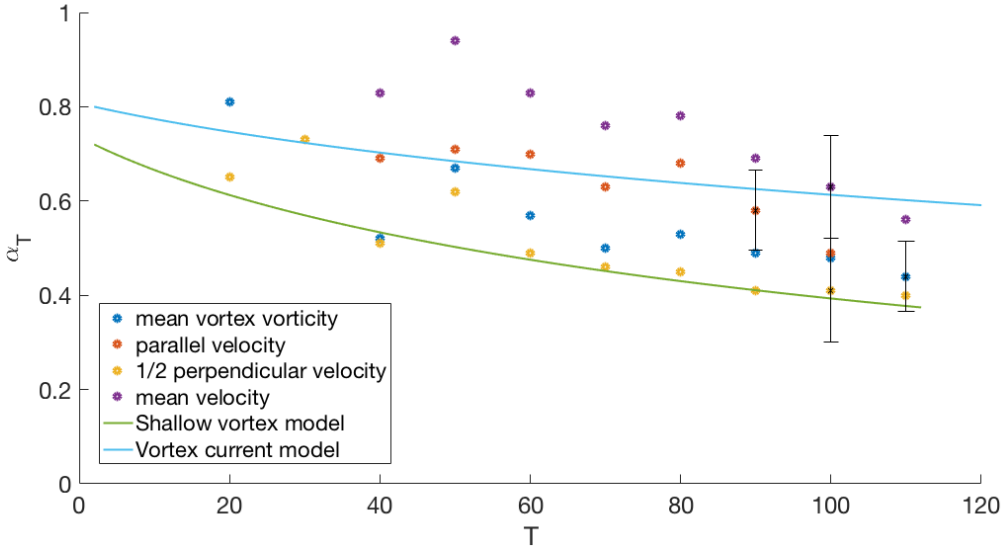

Figure 8.7 The estimated value for the vortex vorticity ratio over time from the experimental data for intermediate I^*. The theoretical predictions for the shallow vortex and vortex current models are also shown.

larger which can be seen in the mean velocity data in figure 8.6. The mean value is used for a comparison with the vortex current model, and we see that the model underestimates the values. Adjusting the perpendicular velocity data for the smaller radius according to the shallow vortex model gives better agreement with the theory and reduces the estimates to a similar magnitude as seen for the parallel velocity and mean vortex vorticity data. This suggests that the shallow vortex model provides a good prediction for the change in the vortex shape with the presence of the boundary wall.

The same data for the intermediate I^* regime are displayed in figure 8.7. The mean vortex vorticity data and the adjusted perpendicular velocity data show good agreement with the shallow vortex theory for $T > 60$. The parallel velocity data give larger values for α_T in general, but decrease towards the mean vortex vorticity estimates at late times. The larger values for the mean velocity give better agreement with the vortex current model. Overall, the data show that both models perform reasonably well in capturing the magnitude and the rate of decay of the vorticity ratio in the vortex.

Figure 8.8 plots the estimates for α_T from the experiments in the high I^* regime. The experimental data show large fluctuations which are a consequence of the unstable nature of the vortex in the high I^* regime. The estimated values of α_T at early times are large, but

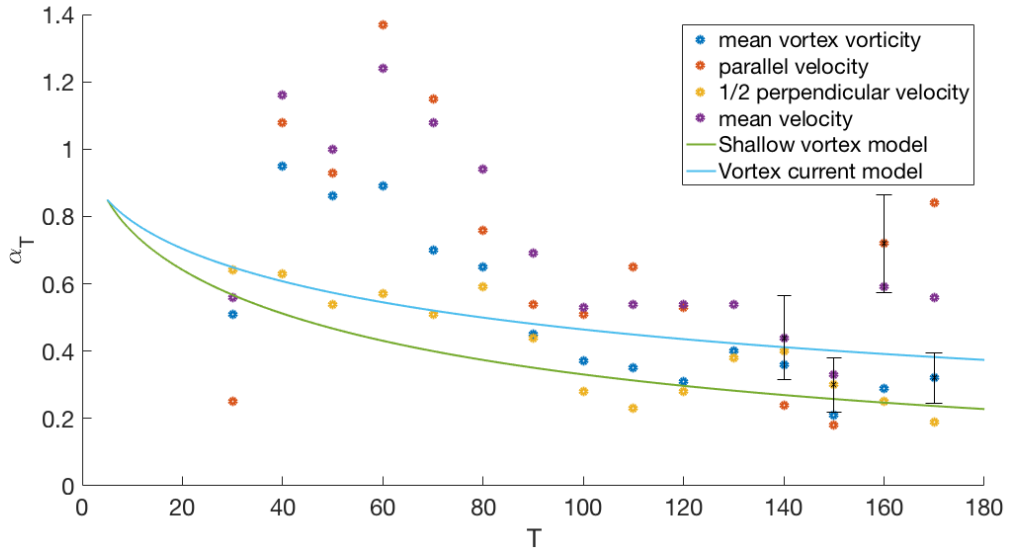

Figure 8.8 The estimated value for the vortex vorticity ratio over time from the experimental data for high I^*. The theoretical predictions for the shallow vortex and vortex current models are also shown.

decrease towards the order of magnitude predicted by the theory for the second half of the experiment $T \gtrsim 80$. We will concentrate on the values in this range for our comparison. The adjusted perpendicular velocity estimates agree well with both the mean vortex velocity estimates and the shallow vortex theory. The parallel velocity data show an increase for $T > 150$ which is likely a result of the vortex becoming unstable. Neglecting these last two data points, the mean velocity estimates show reasonable agreement with the vortex current model and the mean vorticity estimates.

In summary, we see promising agreement with the theory and the experimental data across the full range of the experimental parameters. It is difficult to compare the performance of the the shallow vortex and vortex current models against one another as the errors in the data are quite large. What the data show, however, is that the decay of α_T shows reasonable agreement with the theory in terms of its magnitude and the rate of decay over time and perhaps most importantly that the value of α does not remain constant during an experiment. The data also suggest that the factor of $1/2$ used in the shallow vortex model to account for the contraction of the radius perpendicular to the boundary wall works well as a first approximation. This will be discussed in more detail in section 8.2.4 when analysing the vortex radius measurements.

I^*	Q [cm^3 s^{-1}]	f [s^{-1}]	g' [cm s^{-2}]	H_0 [cm]	D [cm]
0.39	74	2	68.0	2	2.5
0.80	62	1	15.3	2	5
1.14	45	1.5	15.1	2	5
1.15	42	0.5	2.3	2	5
1.33	100	1.5	15.3	2	5
1.73	62	2	13.5	2	5

Table 8.2 Experimental parameters for the experiments shown in figure 8.9.

8.2.3 Vortex depth

In this section we compare the experimental measurements of the vortex maximum depth with both of the theoretical models. We present the comparison for six experiments in detail, which cover the full range of behaviours seen in the experimental data. The data are shown in figure 8.9 alongside the theoretical curves for both the shallow vortex and vortex current models. We use the fitted values of α_i in the theoretical models, which are chosen to give the best fit between the theory and the data across all of the flow features. The experimental values for the transition time T_i are also used. The controlled experimental parameters are given in table 8.2.

The data in figure 8.9 in general show good agreement with the theory across the full I^* parameter range. Of the seventeen experiments considered, eight of them show good agreement comparable to (d), (e) and (f), seven show a slight underestimation of the depth comparable to (b) and the remaining two show an initial underestimation of the depth, but good agreement at late times comparable to the behaviour seen in (c). We will comment on each plot in figure 8.9 turn, beginning with (a). The general agreement for $I^* = 1.14$ is good for both models. The depth measurements at early times fluctuate greatly, but settle down for $T > 50$ suggesting that the initial fluctuations are the result of measurement errors. For $I^* = 0.80$ in (b) the data fluctuates throughout, suggesting the possible presence of waves at the density interface, but the general growth rate is captured reasonably well by the theory. There is a slight underestimation of the magnitude of the depth by both models. For $I^* = 1.73$ in (c) the theory underestimates the initial increase in the magnitude of the depth, however, at later times the rate of increase and the magnitude are captured well, particularly by the shallow vortex model. For $I^* = 1.33$ in (d) we see good agreement between the shallow vortex model and the data. The vortex current model slightly underestimates the magnitude of the depth, but is able to predict the growth rate well. Finally for $I^* = 1.15$ in (e) and

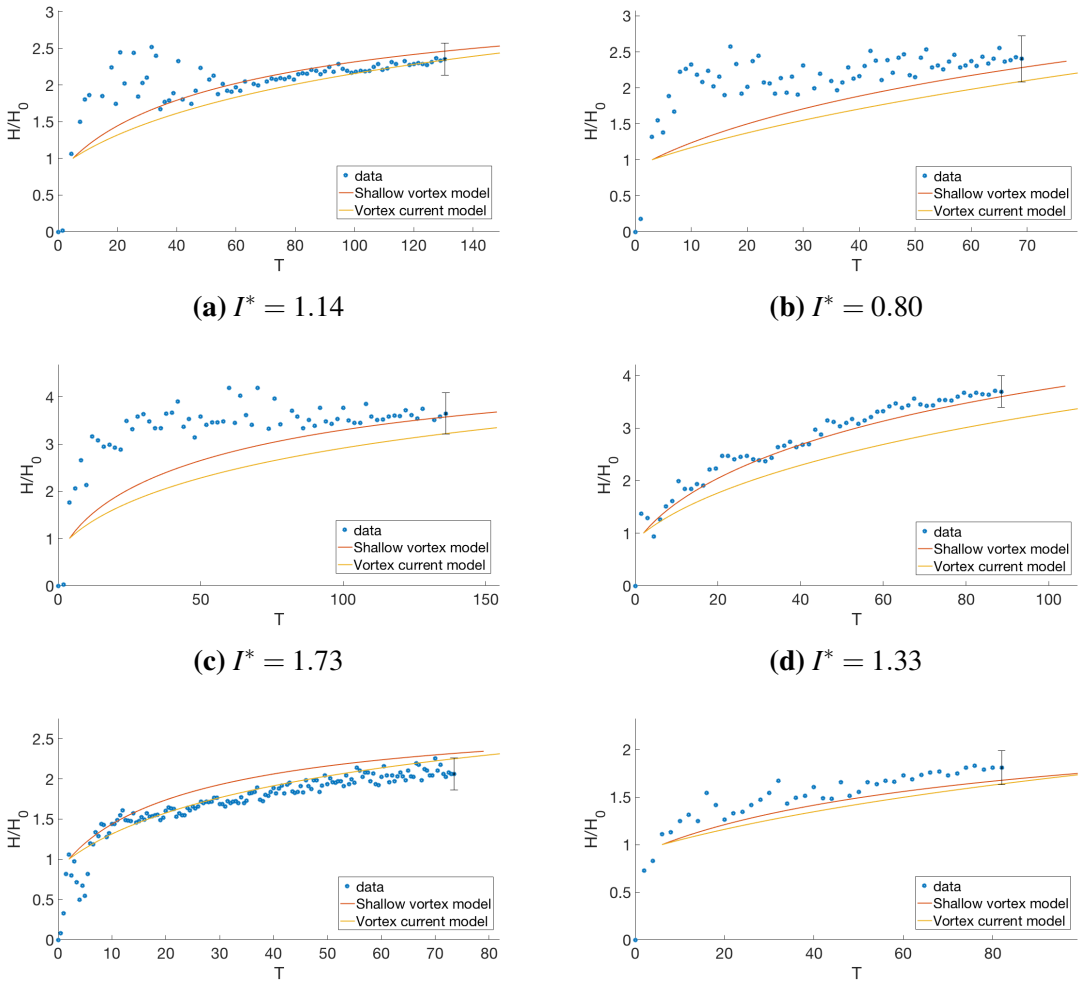

(a) $I^* = 1.14$ **(b)** $I^* = 0.80$

(c) $I^* = 1.73$ **(d)** $I^* = 1.33$

(e) $I^* = 1.15$ **(f)** $I^* = 0.39$

Figure 8.9 The experimentally measured maximum vortex depth and the theoretical predictions using the fitted values of α_i, versus time T.

$I^* = 0.39$ in (f) the overall agreement between the data and the theory is good with the vortex current model performing particularly well in modelling the data in (e).

In summary, the overall agreement between the data and the theory is promising considering the simplicity of the models. The theory models the flow as a two-layer fluid and does not contain a number of effects such as mixing and Ekman layers, which are likely relevant. Despite these simplifications, the models show good capability at predicting the rate of increase in the vortex maximum depth over time, though they show a tendency to underestimate its magnitude. NP saw the same underestimation of the vortex depth by their model with a constant vorticity ratio when compared with the numerical simulatons. The values predicted by their analytical model were on the order of $10-25\%$ smaller than those seen in the numerical simulations. In terms of a comparison of the models, there is little to choose between them. Both are able to capture the growth rate well, but in general underestimate the magnitude of the depth in most cases.

8.2.4 Vortex radius

The time-dependent theoretical models of chapter 8 also provide predictions for the change in the vortex radius for $T > T_i$. We compare the experimental measurements of the vortex radius with the theory for the same subset of seventeen experiments as in section 8.2.3. The fitted values of α_i will again be used in the models and the experimental values for the transition time T_i, and the initial radius R_i will be used. The results from six experiments are presented in detail in figure 8.10 covering the parameter range $0.39 \leq I^* \leq 1.73$. The full experimental parameters are given in table 8.3. The radii in the perpendicular and parallel directions from the shallow vortex and vortex current models have been accounted for by multiplying the theoretical curves by the appropriate scaling factor. In the case of the vortex current model we have used the effective radius calculated from the vortex area and for the shallow vortex model the perpendicular radius is half that in the parallel direction.

Overall, figure 8.10 demonstrates similar qualitative behaviour between the data and the theory, particularly for the shallow vortex model perpendicular radius. For the seventeen experiments considered, seven demonstrated good agreement with the shallow vortex perpendicular radius, with the vortex current model and the shallow vortex parallel radius overestimating the values. Such behaviour is comparable to that seen in (a) and (f). For

I^*	Q [cm^3 s^{-1}]	f [s^{-1}]	g' [cm s^{-2}]	H_0 [cm]	D [cm]
0.39	72	2	68.1	4	5
0.54	100	1.5	68.4	2	5
0.70	100	2	71.6	2	5
0.96	100	1	13.5	2	5
1.15	42	0.5	2.3	2	5
1.73	62	2	13.5	2	5

Table 8.3 Experimental parameters for the experiments shown in figure 8.10.

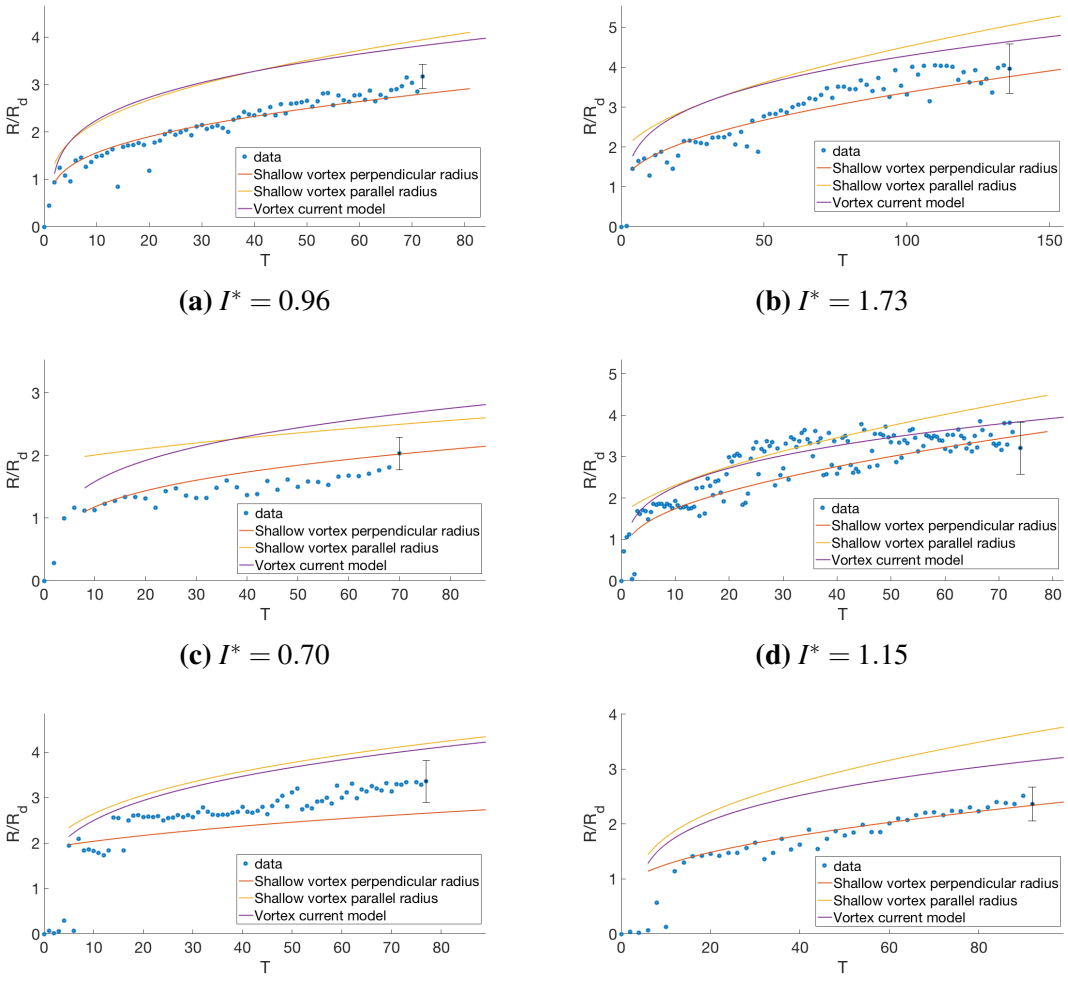

(a) $I^* = 0.96$ **(b)** $I^* = 1.73$

(c) $I^* = 0.70$ **(d)** $I^* = 1.15$

(e) $I^* = 0.54$ **(f)** $I^* = 0.39$

Figure 8.10 The experimentally measured vortex radius and the theoretical predictions using the fitted values of α_i, versus time T.

five of the experiments the theory overestimated the data in general with the shallow vortex perpendicular radius showing the best agreement, comparable to the behaviour in (c). For the remaining five experiments the data were seen to lie in-between the theoretical curves as seen in (b), (d) and (e). We will comment on each plot in figure 8.10 in turn. For $I^* = 0.96$ in (a), we see good agreement for the shallow vortex model perpendicular radius, but an overestimation in the parallel direction. For $I^* = 1.73$ in (b), the shallow vortex model perpendicular radius matches the data at early times, but then slightly underestimates the radius later in the experiments. The vortex current model predictions match reasonably well with the data at later times. In (c) for $I^* = 0.70$ the best agreement is given by the shallow vortex model perpendicular radius once again, with both the shallow vortex model parallel radius and the vortex current model overestimating the data. For $I^* = 1.15$ in (d) the data show quite large fluctuations with the three theoretical curves approximating the values quite well. The vortex current model perhaps shows the best overall agreement. For $I^* = 0.54$ in (e) the shallow vortex model perpendicular radius underestimates the values, while the shallow vortex model parallel radius and vortex current model overestimate the data by approximately the same amount. Finally for $I^* = 0.39$ in (f) there is again good agreement between the data and the shallow vortex model perpendicular radius, while the data are overestimated by the other two theoretical curves.

In summary, we see that the shallow vortex model shows capability of modelling the growth of the vortex radius in the direction perpendicular to the boundary wall. We recall that the shallow vortex model assumes that the presence of the boundary wall acts to split the vortex in half, such that the vortex diameter, rather than the radius, in the direction perpendicular to the wall grows according to the radius growth rate predicted by the model. While the data in figure 8.10 suggest that this appears to be the case, they also show that the radius in the parallel direction grows at a slower rate than is predicted by the model. Understanding the relationship between the different growth rates of the vortex radius in the directions perpendicular to and parallel to the boundary wall will be key in modelling the vortex growth effectively in the future. What our results show here is that the vortex diameter perpendicular to the boundary wall appears to grow according to the vortex radius growth rate of the shallow vortex model. This behaviour is in agreement with the measurements of the diameter ratio D^* in chapter 6 which showed that the vortex is not circular with the mean value $D^* \sim 0.6$. The vortex current model uses an average value of the vortex radius across both directions and the data in figure 8.10 show that this in general overestimates the values seen experimentally. The same overestimation of $\sim 20-30\%$ was seen in the

work of NP when comparing the numerical simulations with their analytical model for a constant vorticity ratio. The qualitative behaviour seen in our experiments agrees with that seen numerically by NP, suggesting that the overestimation is a result of the assumption of an approximately circular vortex. The overestimation of the vortex radius is also consistent with the underestimation of the vortex maximum depth for the mass flux into the vortex to be conserved. Finally, we remark on a comment made by GL that friction causes the radius to increase and the depth to decrease. Both behaviours are seen here when comparing the experimental data with the theory and thus a future modification to the model to include the effects of friction may lead to better agreement.

8.2.5 Boundary current

When deriving the time-dependent theoretical model in chapter 7 our main aim was to provide a link between the outflow vortex and the boundary current in order to determine the role played by the vortex. Having analysed the experimental data in comparison with the model predictions for the outflow vortex, we now move onto the boundary current focussing on two key properties: the current velocity and the current width.

8.2.5.1 Current velocity

The current velocity is fixed by the velocity field of the outflow vortex via a Bernoulli condition and is equal to vortex velocity at the outermost edge of the vortex. Details of the Bernoulli condition and the streamline used are given in chapter 7. As with the calculations in the previous sections, we use the fitted values of α_i in the theoretical models. We also use the experimentally measured transition times T_i from section 8.2.1.2 and the experimentally measured values for the initial vortex radius R_i from section 8.2.1.3. We present the data from six of the experiments in figure 8.11 with $0.39 \leq I^* \leq 1.73$. The full experimental parameter values are displayed in table 8.4. The experimental data for the current velocity is the mean current velocity defined by l/t for a current of length l, rather than the instantaneous velocity dl/dt. The reasons for using the mean velocity are the same as those given in chapter 4.

The plots in figure 8.11 overall demonstrate reasonable agreement between the theory and the experimental data across the full parameter range. For the seventeen experiments compared with the theory, seven show good agreement between the data and the shallow

I^*	Q [cm^3 s^{-1}]	f [s^{-1}]	g' [cm s^{-2}]	H_0 [cm]	D [cm]
0.39	74	2	68.0	2	2.5
0.70	100	2	71.6	2	5
0.75	47.5	1	15.8	2	5
1.31	61	0.5	2.1	2	5
1.33	100	1.5	15.3	2	5
1.73	62	2	13.5	2	5

Table 8.4 Experimental parameters for the experiments shown in figure 8.11.

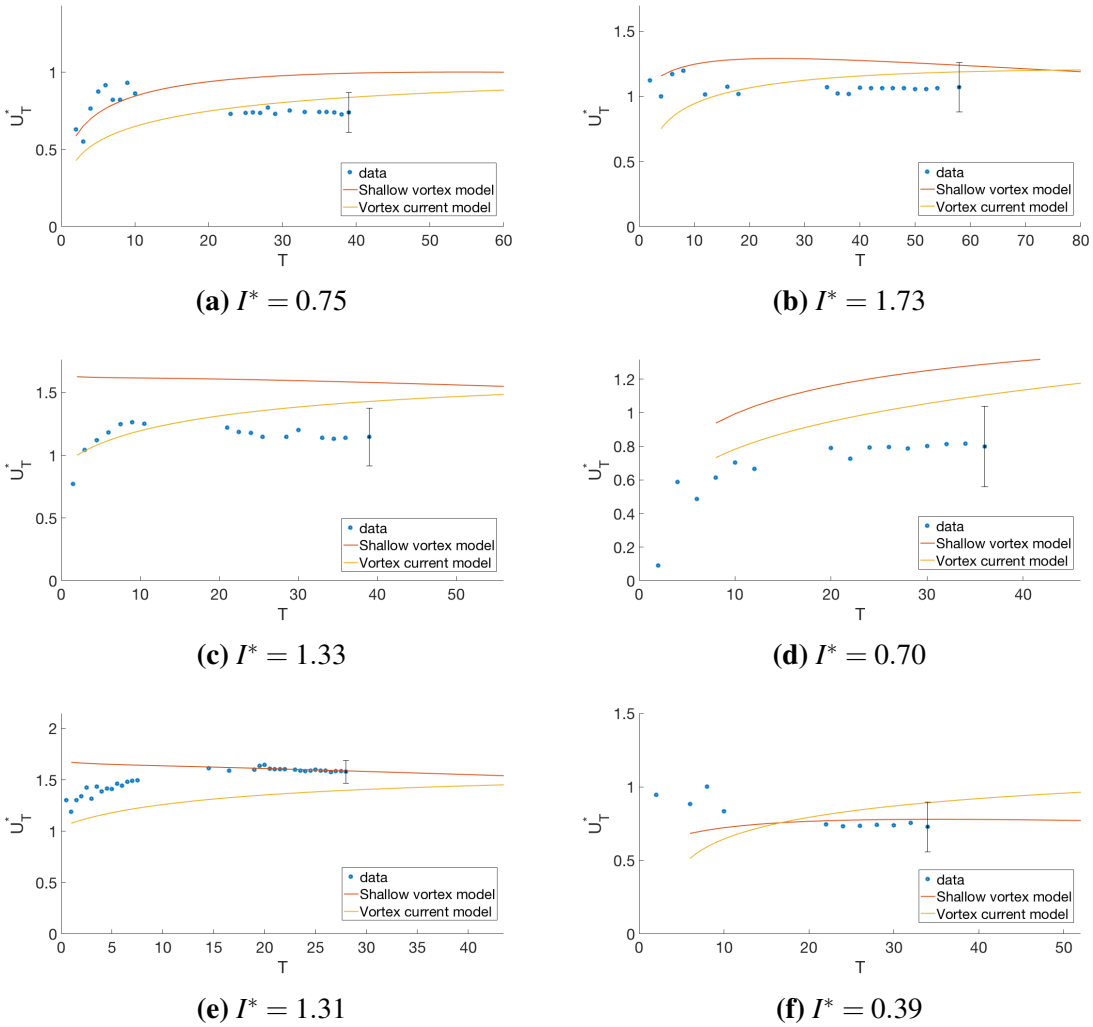

(a) $I^* = 0.75$ **(b)** $I^* = 1.73$

(c) $I^* = 1.33$ **(d)** $I^* = 0.70$

(e) $I^* = 1.31$ **(f)** $I^* = 0.39$

Figure 8.11 The experimentally measured mean current velocity and the theoretical predictions using fitted values for α_i, versus time T.

vortex model, comparable to (e) and (f). For five of the experiments we see good agreement with the shallow vortex model initially, but with an overestimation of the velocity at later times meaning that the vortex current model performs better later in the experiment. Such behaviour is comparable with (a) and (b). In the remaining six experiments we see a general overestimation of the current velocity comparable to that seen in (d), though in all of the cases the vortex current model is most closely aligned with the data. In (c) we see a further interesting behaviour with the vortex current model providing the best fit to the magnitude of the current velocity, but with the shallow vortex model demonstrating a better capability to capture the time-dependent behaviour. We will now discuss the plots shown in more detail. For $I^* = 0.75$ in (a) the shallow vortex model captures the early behaviour of the velocity well with the vortex current model underestimating the initial magnitude. However, at later times the vortex current model shows good agreement with the data. Similar behaviour is seen in (b) with $I^* = 1.73$. The run with $I^* = 1.33$ in (c) shows that both models are able to capture different features of the flow well, with the shallow vortex model capturing the decrease in the velocity over time, but overestimating its magnitude, while the vortex current model provides a better fit to the magnitude of the velocity but predicts an increasing value not seen in the data. For $I^* = 0.70$ in (d) both models overestimate the current velocity, but capture its growth rate reasonably well with the vortex current model the best fit overall. For $I^* = 1.31$ in (e) the shallow vortex model shows good agreement with the theory beyond the initial stage. The vortex current model again provides a reasonable estimate of the magnitude of the velocity, but is unable to capture the change in behaviour with time as well as the shallow vortex model. Finally, for $I^* = 0.39$ in (f) the agreement at late time is good between the shallow vortex model and the data. The vortex current model also performs well.

In summary, the overall agreement between the theory and the data is quite promising. The shallow vortex model shows an ability to capture the time-dependent behaviour of the velocity, whilst tending to overestimate its magnitude in general. The vortex current model seems less capable of accurately predicting the change in the current velocity over time, but in general provides a better representation of the magnitude of the velocity. This means that overall the vortex current model perhaps shows the best agreement with the data. We expect that with more accurate measurements of the instantaneous current velocity from a method such as PIV, rather than the mean velocity measurements used here, the agreement with the models would likely improve. The use of PIV to measure the current is an improvement that will be made for future studies. Finally, the reasonable level of agreement between the data and the theory across the full experimental parameter range in figure 8.11 suggests that the

I^*	Q [cm^3 s^{-1}]	f [s^{-1}]	g' [cm s^{-2}]	H_0 [cm]	D [cm]
0.39	72	2	68.1	4	5
0.54	100	1.5	68.4	2	5
0.96	100	1	13.5	2	5
1.14	45	1.5	15.1	2	5
1.15	42	0.5	2.3	2	5
1.73	62	2	13.5	2	5

Table 8.5 Experimental parameters for the experiments shown in figure 8.12.

current velocity is potentially related to the velocity within the vortex as suggested by the time-dependent theoretical model of chapter 7, at least in terms of the first-order physics present in the system. In future studies we intend to further analyse this link with more accurate velocity measurements.

8.2.5.2 Current width

We now come to the final aspect of the flow that we will consider: the current width. The current width is determined by solving the current depth profile equal to zero at $y = w_{0T}$. The current depth profile depends on the choice of wall velocity U_l and therefore the current width will do so as well. We consider the two cases of a zero wall velocity and a finite wall velocity equal to the current velocity U_T^*. The reasoning behind the consideration of both choices has been presented in chapters 3 and 7. For a zero wall velocity the depth profile reduces to the steady state zero wall velocity current depth profile of chapter 3. The fitted values of α_i for both the shallow vortex and vortex current models will be used to determine the theoretical value of the steady state width which we expect will only be reached at late times. The case of a finite wall velocity equal to the current velocity U_T^* results in a time-dependent current width, with a different value of U_T^* depending on the choice of vortex growth model. As with the other flow properties, we consider both the shallow vortex and vortex current models in comparison with the experimental data. Again we will use the fitted values for α_i, the experimentally measured transition timescale T_i and the experimentally measured initial vortex radius R_i. Figure 8.12 displays the current width as a function of dimensonless time $T = tf$ for six experiments with $0.39 \leq I^* \leq 1.73$. Full parameter values are given in table 8.5. The theoretical predictions for the four different models are also shown.

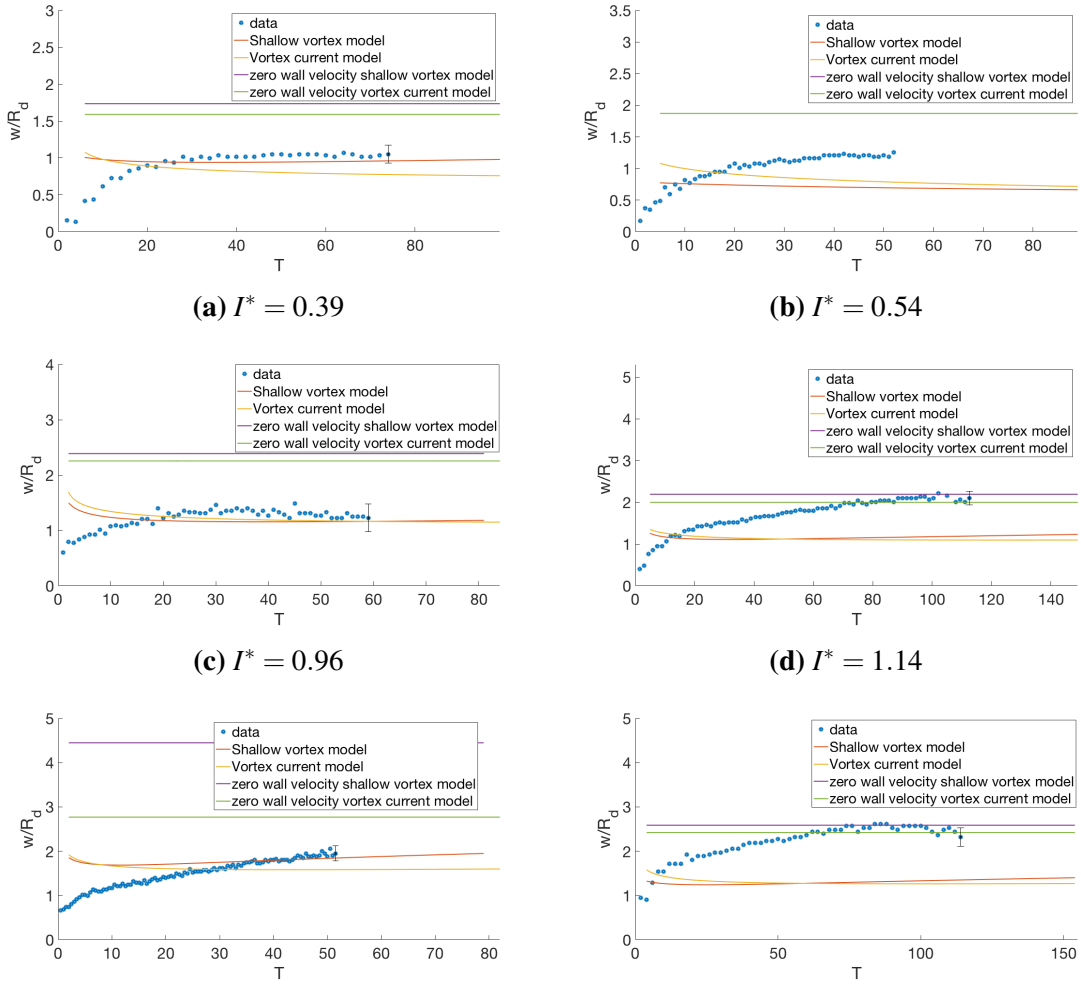

(a) $I^* = 0.39$ **(b)** $I^* = 0.54$

(c) $I^* = 0.96$ **(d)** $I^* = 1.14$

(e) $I^* = 1.15$ **(f)** $I^* = 1.73$

Figure 8.12 The experimentally measured current width and the theoretical predictions using the fitted values for α_i, versus time T. The general shallow vortex and vortex current models use a finite value for the wall velocity.

A broad range of different behaviours are seen in the current width data in figure 8.12. Out of the seventeen experiments that were compared with the theory, six showed better agreement with the time-dependent theory comparable to the behaviour seen in (a), (c) and (e) while nine showed better agreement with the steady state theory as seen in (d) and (f). The remaining two experiments had current width values that were between both models, similar to the behaviour in (b). We will now discuss each plot individually. For $I^* = 0.39$ in (a) the magnitude of the current width data matches well with the finite wall velocity shallow vortex model beyond the initial growth phase. The initial increase in the width is not seen in the theory. For $I^* = 0.54$ in (b) the time-dependent theory underestimates the data, while the steady state values are too high for both models. At $I^* = 0.96$ in (c) we see good agreement between the data and the time-dependent models in terms of predicting the magnitude of the current width, however, the theory predicts an initial decrease in the current width which is a feature not present in the data. For $I^* = 1.14$ in (d) the time-dependent models underestimate the data while the zero wall velocity models show good agreement at late times. The suitability of the zero wall velocity model does not seem to be related to the value of I^* as for $I^* = 1.15$ in (e) the zero wall velocity models overestimate the current width, with the time-dependent models showing better agreement with the data. The shallow vortex model captures the late-time increase in the current width well, but again it predicts an initial decrease not seen in the data. Finally, for the highest value of $I^* = 1.73$ in (f) the zero wall velocity models predict the steady state width value very well.

The range of behaviours seen in the plots in figure 8.12 make it difficult to evaluate the performance of the theoretical models. In some instances, for example the plots in (a), (c) and (e), the time-dependent theory matches the magnitude of the current width well, but predicts an initial decrease in the width not seen in the data. This may suggest that the time-dependent model for the boundary current is only valid at later times or that the choice of U_T^* for the finite wall velocity is perhaps incorrect. For other experiments, such as those for the plots in (d) and (f), the use of a zero wall velocity model and the resulting steady state value for the current width shows good agrement with the data. For these experiments the time-dependent theory underestimates the current width magnitude. An analysis of the experiments reveals that for those with the lowest Rossby number the zero wall velocity model shows good agreement with the data, while for the experiments at higher Rossby number it overestimates the current width. This is consistent with the approximations made in the model, in particular the use of the shallow water x-momentum equation in (3.20) is only valid for small Rossby number. For the experiments at higher Rossby number, the use

of a finite wall velocity gives better agreement with the data, but the time-dependent current velocity U_T^* is perhaps not the right choice due to the initial decrease in the current width predicted by the model which is not seen in the data. The current velocity profiles presented in chapter 4 show that while the near-wall velocity ranges from $0-1/2$ times the peak value in the current, in most cases it remains reasonably consistent at approximately $1/4-1/2$ times the peak value. This suggests that the use of a finite wall velocity equal to a constant fraction of the peak current velocity may perhaps improve the fit to the width data. The PIV data are only available for a subset of the experimental parameter range, however, so we are wary of drawing any strong conclusions. Ultimately, the data presented in this section show that a zero wall velocity model is able to predict the value of the current width at late times well for the experiments with low Rossby number $Ro_{exp} \lesssim 0.4$. For the experiments at higher Rossby number, a finite wall velocity model is required, though the choice of U_T^* is perhaps not the most appropriate.

8.3 Discussion

The role of the presence of the outflow vortex in determining the flow dynamics has been investigated via a comparison of the experimental data and the time-dependent theoretical model introduced in chapter 7. The source vorticity ratio was estimated from the data as in chapter 4 and the values are found to be similar to those derived from the steady state current properties. The transition timescale and the initial vortex radius were also estimated from the data and used in the model.

The experimental data for the velocity field in the vortex showed that the vorticity ratio decayed over time in agreement with the theory. Both the vortex current and shallow vortex models showed reasonable agreement with the values measured experimentally. The growth rate of the vortex maximum depth was also captured well by the theory, though both models tended to underestimate the magnitude of the vortex depth. The growth of the vortex radius in the direction perpendicular to the boundary wall was shown to be modelled well by the shallow vortex model under the assumption of a semi-circular vortex shape. The growth of the radius in the direction parallel to the wall was overestimated by both theoretical models, but improved agreement was seen in comparison to the work of NP and their analytical model with a constant vorticity ratio. Ultimately, further work is required to understand the relationship between the different growth rates of the vortex radius in the directions parallel

to and perpendicular to the boundary wall.

The use of the vortex velocity field to fix the current velocity and provide a theoretical link between the outflow vortex and the boundary current, showed promising agreement with the experimental data. The shallow vortex model was able to capture the qualitative change in the current velocity over time, but overestimated its magnitude, meaning that the vortex current model provided the best agreement overall. The experimental data showed a generally decreasing current velocity during an experiment and thus the use of a time-dependent vorticity ratio that decays with time is needed to capture this decrease as use of a constant vorticity ratio would predict a velocity that increased with the vortex radius. Analysis of the current width revealed that for low Rossby number a zero wall velocity model provides the best fit to the data at late times, while for larger Rossby number a finite wall velocity model is required. The use of the time-dependent current velocity U_T^* was able to capture the magnitude of the width well at late times, but predicted an initial decrease in the width that was not seen in the data, suggesting that a different choice of finite wall velocity in the model may be required.

A qualitiative evaluation of the two theoretical models suggests that both show capability of modelling the features of the flow, but overall the vortex current model demonstrates the best agreement with the data. As mentioned at the beginning of the chapter, this is perhaps as expected since the vortex current model is derived from a force balance across both the vortex and the boundary current and thus the effect of the current on the vortex growth is inherently present in the physics of the flow. This is in comparison to the shallow vortex model which is derived from PV conservation in the vortex and thus provides a model for pure unimpeded vortex growth with the effect of the presence of the boundary current added via a change in the vortex shape from circular to semi-circular. This is only an approximation, though as we have seen in this chapter it seems to perform well at first-order.

Overall, we have shown the capability of the time-dependent theoretical model of chapter 7 to capture many of the key flow features. In particular, we have shown that the current velocity may be fixed according to the vortex velocity field, demonstrating a potential new role played by the vortex in determining the current properties.

Chapter 9

Grid-generated turbulence

9.1 Introduction

For a buoyant outflow entering into the ocean the turbulent nature of the environment will provide momentum and mass transfers between the current and the sea resulting in a change to the flow properties. We have modified the experimental setup to include a non-quiescent ambient to recreate the turbulent environment of the ocean in the laboratory. Background turbulent motion is imposed by an oscillating grid of the same shape and size as is the norm for this area of study (eg. Turner 1968, Thompson and Turner 1975, Hopfinger and Toly 1976, Nokes 1988).

In this chapter we outline the key theoretical aspects of the problem of grid-generated turbulence in both a non-rotating and rotating frame. For a non-rotating frame we compare the turbulence in our experimental setup with the literature to verify the robustness of its properties. With the addition of rotation the problem is more complex and the effects seen in our experiments will be compared with those seen elsewhere in the literature. We will ultimately introduce a freshwater outflow into the experimental setup in chapter 10 and investigate the effects of the background turbulence on the flow properties as we look to address the third key question of this thesis. Here, we analyse the properties of the grid-generated turbulence to ensure that the theoretical description agrees with the results seen experimentally. We also want to ensure that the turbulence produced in our experimental setup demonstrates the same properties seen in similar mixing grid studies.

9.2 Non-rotating turbulence

The properties of grid-generated turbulence have been studied extensively in the past. The values of the turbulent rms velocity u^* and the integral lengthscale l are modelled according to the work of Hopfinger and Toly (1976) as

$$u^* = \frac{K_1(sM)^{1/2}u_0}{z}, \tag{9.1}$$

$$l = K_2 z, \tag{9.2}$$

with K_1 and K_2 empirical constants determined experimentally, s the stroke height of the grid, M the grid mesh size, z the distance from the grid and $u_0 = ns$ the initial grid velocity for a stroke frequency n. In general, the values of the empirical constants are taken to be $K_1 = 0.25$ and $K_2 = 0.10$ though they are dependent on the method of turbulence generation being used. The value of K_2 in particular varies greatly in the literature from 0.1 (Hopfinger and Toly 1976), to 0.25 (Fleury et al. 1991). The distance from the grid z is measured from a virtual origin which is also defined differently across the literature. Hopfinger and Toly (1976) describe the choice of origin to be 'crucial to the determination of the exponent in the power law of decay'. For their fit to a z^{-1} curve in (9.1), they define a virtual origin by the point at which the integral lengthscale reaches zero. This was found to be 1 ± 0.5 cm below the mid-point of the grid oscillation. Thompson and Turner (1975) also reported that the virtual origin should be ~ 1 cm below the mid-position of the grid when using square bars. Nokes (1988) used the mean-point of the oscillation as the virtual origin from which to measure the distance from the grid.

9.2.1 Experimental results

The properties of grid-generated turbulence have been shown to be robust across a wide-range of different experimental setups seen in the literature (e.g. Hopfinger and Toly 1976, Thompson and Turner 1975, Nokes 1988). The values of the constants K_1 and K_2 and the choice of virtual origin from which the distance from the grid is measured vary depending on the method of turbulence generation and the properties of the experimental setup being used. We have conducted calibration experiments across the full range of parameters in order to determine the constants empirically for our particular experimental setup. Experiments are conducted with the addition of a mixing grid to the experimental setup as described in

chapter 2. We use two alternative forms of visualisation of the turbulent flow in both the horizontal and vertical planes. In the horizontal plane, the turbulent properties are averaged over both the x and y directions at a fixed height, while for the vertical plane the properties are averaged in the x direction only at each fixed height. Both sets of data will be used in the analysis. The velocity is measured using PIV and the in-built Digiflow algorithm (Dalziel, 2006) and the integral lengthscale calculated using an autocorrelation function. The grid mesh size is fixed at $M = 5$ cm and we fix the stroke height at $s = 3$ cm. The stroke frequency is varied across $n = 0.5, 1, 1.5$ and 2 Hz. Full details of the experimental methods used are given in chapter 2.

Before presenting an analysis of the turbulent properties we begin with a qualitative look at the mean vorticity field in a vertical slice through the turbulent flow. In figure 9.1 the time-averaged mean vorticity field in the plane of motion is shown for two experiments with different values of the stroke frequency n. The mixing grid is switched on once solid body rotation has been reached and the images recorded for ~ 60 seconds. The images are then time-averaged via an arithmetic mean taken over the final ~ 5 seconds. The vorticity scale increases from black at -1 rad s^{-1} to white at $+1$ rad s^{-1}. As the value of n is increased from 0.5 Hz to 1 Hz we see an increase in the strength of the turbulence generated by the grid, with the regions of large vorticity (black and white) extending further from the mid-point of the grid stroke. At large distances from the grid the turbulence has decayed significantly.

We plot the experimentally measured value of u^*, non-dimensionalised by $u_0 = ns$, against the proposed velocity scaling $(sM)^{1/2}z^{-1}$ given in (9.1). Plotting the data in this way means that the value of the constant K_1 will be equal to the gradient. The data are shown in figure 9.2 for four different stroke frequencies. A typical error bar is also shown. We fit a linear curve to the data to give an estimate for the value of the constant K_1. This is done for all of the data together and also separately for each value of the stroke frequency. The estimates for K_1 and the corresponding R^2 values for the linear fit are given in table 9.1. The values for K_1 are very similar for each value of n with perhaps a slight decrease as the value of n is increased.

Experimental measurements of the turbulent integral lengthscale are plotted as a function of distance from the grid in figure 9.3. Data are shown for four different stroke frequencies, $n = 0.5, 1, 1.5$ and 2 Hz. The estimated values of K_2 obtained from a linear fit to the data are given in table 9.2 for each value of n. We see a larger spread in the lengthscale measurements

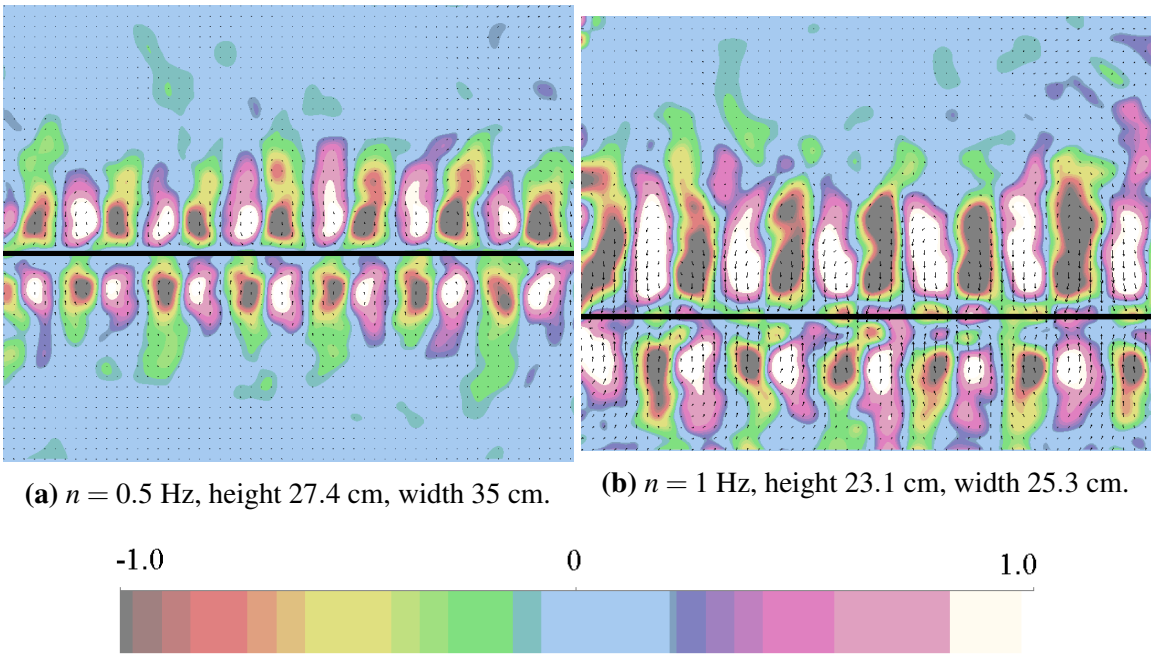

(a) $n = 0.5$ Hz, height 27.4 cm, width 35 cm.

(b) $n = 1$ Hz, height 23.1 cm, width 25.3 cm.

Figure 9.1 The time-averaged mean vorticity field in a vertical plane through the turbulent flow. The stroke height is fixed at $s = 3$ cm while the stroke frequency increases from $n = 0.5$ Hz to $n = 1$ Hz. The location of the mid-stroke of the mixing grid is indicated by a black line. A scale bar is shown for the vorticity in rad s^{-1} and the size of each plot is indicated.

compared to those of the turbulent velocity in figure 9.2, which is reflected in the larger error in the estimates for K_2 and the smaller R^2 values. The increased uncertainty is a result of the difficulty of accurately measuring the turbulent lengthscale via an autocorrelation function.

Applying a linear fit to the lengthscale data also gives estimates of the location of the virtual origin from which the distance z from the grid is measured. We saw in section 9.2 that the choice of virtual origin differs in the literature, but in general is located at or below the mid-point of the grid stroke. We follow the method of Hopfinger and Toly (1976) and define

n [Hz]	K_1	R^2
0.5	0.27 ± 0.04	0.94
1	0.27 ± 0.02	0.97
1.5	0.23 ± 0.02	0.99
2	0.22 ± 0.03	0.97
0.5 - 2	0.25 ± 0.02	0.95

Table 9.1 Estimates for the empirical constant K_1.

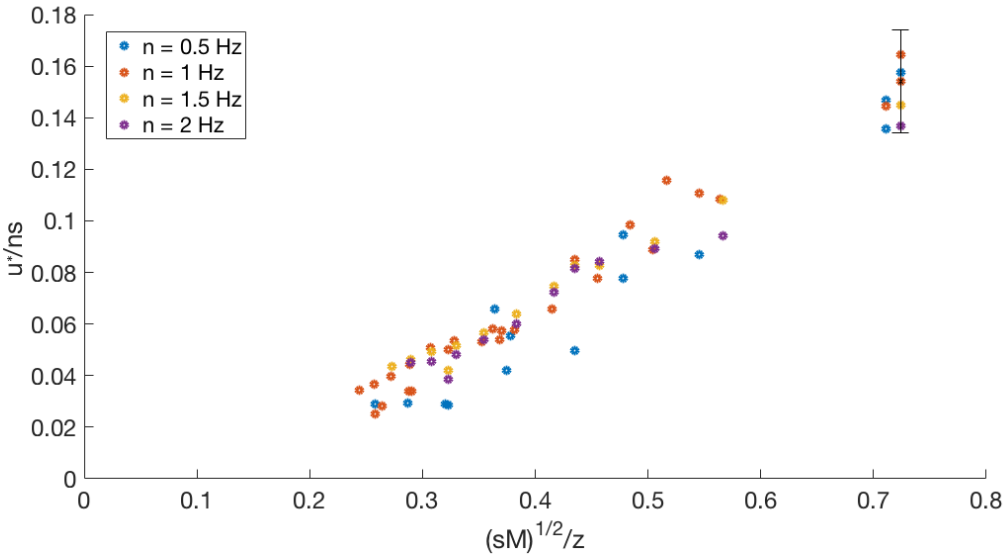

Figure 9.2 The horizontal turbulent rms velocity, u^* scaled with $u_0 = ns$, plotted against the proposed scaling $(sM)^{1/2}z^{-1}$. The stroke frequency varies across $n = 0.5, 1, 1.5$ and 2 Hz.

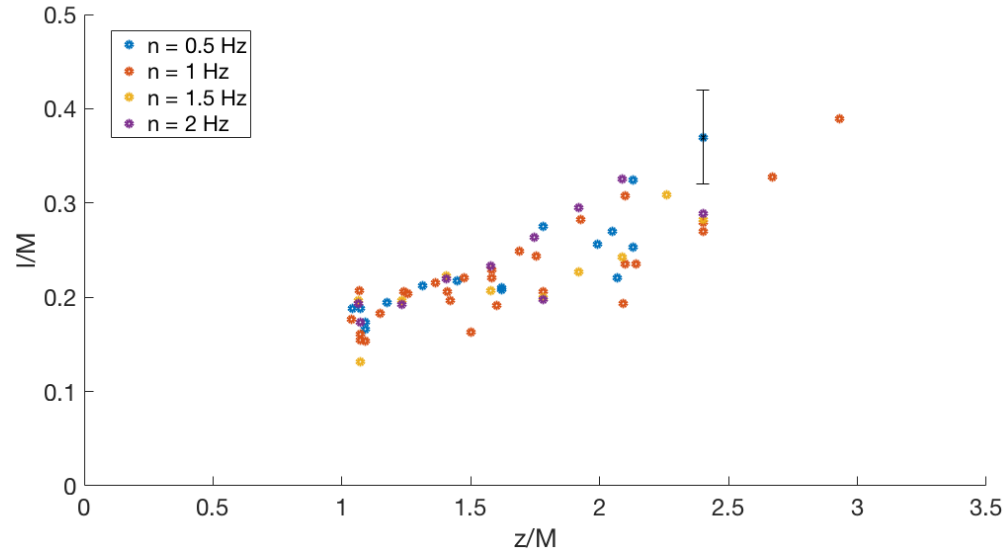

Figure 9.3 The turbulent integral length scale, l scaled with the grid mesh size M, plotted against the distance form the grid, z also scaled with M. The stroke frequency varies across $n = 0.5, 1, 1.5$ and 2 Hz.

n [Hz]	K_2	R^2
0.5	0.10 ± 0.03	0.75
1	0.09 ± 0.02	0.74
1.5	0.09 ± 0.04	0.74
2	0.10 ± 0.05	0.73
0.5 - 2	0.09 ± 0.02	0.72

Table 9.2 Estimates for the empirical constant K_2.

our virtual origin to be the height in the fluid where the integral lengthscale decreases to zero. The lengthscale data suggests a choice of origin at 2.5 ± 1.5 cm below the mid-position of the grid stroke. Adjusting the data to account for the virtual origin gives $K_1 = 0.23 \pm 0.05$ and $K_2 = 0.10 \pm 0.02$.

In summary, the turbulence generated by the mixing grid in our experimental setup is similar to that seen in previous studies of this nature. The turbulent velocity u^* and turbulent lengthscale l fit the model of Hopfinger and Toly (1976) and behave according to (9.1) and (9.2) respectively. The constants K_1 and K_2 determined empirically from the experiments are within the ranges used in the literature. We will use the values $K_1 = 0.23$ and $K_2 = 0.10$ in our analysis.

9.3 Rotating turbulence

The addition of rotation modifies the behaviour of the grid-generated turbulence that we are considering in our experimental setup. The effect of rotation on turbulent mixing across an interface has been studied by Hopfinger et al. (1983) and Fleury et al. (1991) amongst others. The major result is that the addition of rotation leads to non-isotropic turbulence with the integral lengthscale parallel to the rotation axis being much larger than the integral lengthscale in a direction perpendicular to the axis.

Fleury et al. (1991) considered three cases depending on whether the distance from the grid is smaller than a typical distance Z_T, greater than a typical distance Z_R, or lies in the range $Z_T < z < Z_R$. For $z < Z_T$ they found that the effect of rotation is negligible and the non-rotating oscillating grid turbulence laws according to Hopfinger and Toly (1976) hold. For $Z_T < z < Z_R$ the decay of u^* with z slows down suddenly and the increase of l with z

is much slower. For $z > Z_R$ the turbulence is quasi-two-dimensional and u^* and l remain approximately constant. Their values can be related to those at the transition value, Z_T, by

$$u(z > Z_R) \approx 0.55u(Z_T), \tag{9.3}$$

$$l(z > Z_R) \approx l(Z_T)/0.55. \tag{9.4}$$

This gives $u(Z_R)l(Z_R) \approx u(Z_T)l(Z_T)$ meaning that the Reynolds number is approximately the same at the two positions in the tank. Another result of interest is from the work of Hopfinger et al. (1983). They estimated the Rossby number at the transition height $Ro(Z_T) = 0.2$, where Ro is defined as

$$Ro = \frac{u^*(z)}{fl(z)}. \tag{9.5}$$

We can use this value of Ro and the form for u^* and l given in equations (9.1) and (9.2) to estimate the transition height Z_T as

$$Z_T = \left(\frac{K_1 M^{1/2} s^{3/2} n}{K_2 f Ro(Z_T)}\right)^{1/2}. \tag{9.6}$$

Using the relations for $z > Z_R$ in equations (9.3) and (9.4) we estimate the Rossby number at $z = Z_R$ to be

$$Ro(Z_R) = (0.55)^2 \frac{u(Z_T)}{fl(Z_T)} = 0.3Ro(Z_T) = 0.06. \tag{9.7}$$

The values of $Ro(Z_T) = 0.2$ and $Ro(Z_R) = 0.06$ will be compared with the experimental data below.

9.3.1 Experimental results

In the same way as for the non-rotating experiments, we wish to verify that the grid-generated turbulence in our experimental setup behaves in the same way as for previous studies. In the case of rotating turbulence, the transition from three-dimensional turbulence near to the grid to quasi-two-dimensional turbulence far from the grid is of particular interest as it will change the nature of the turbulence that is acting on the freshwater outflow in our experiments. The analysis presented in this section will look to identify this transition and estimate the height at which it occurs. The experimental results presented here will also provide a guideline for the choice of the most suitable parameter regime for the grid-generated turbulence to use in

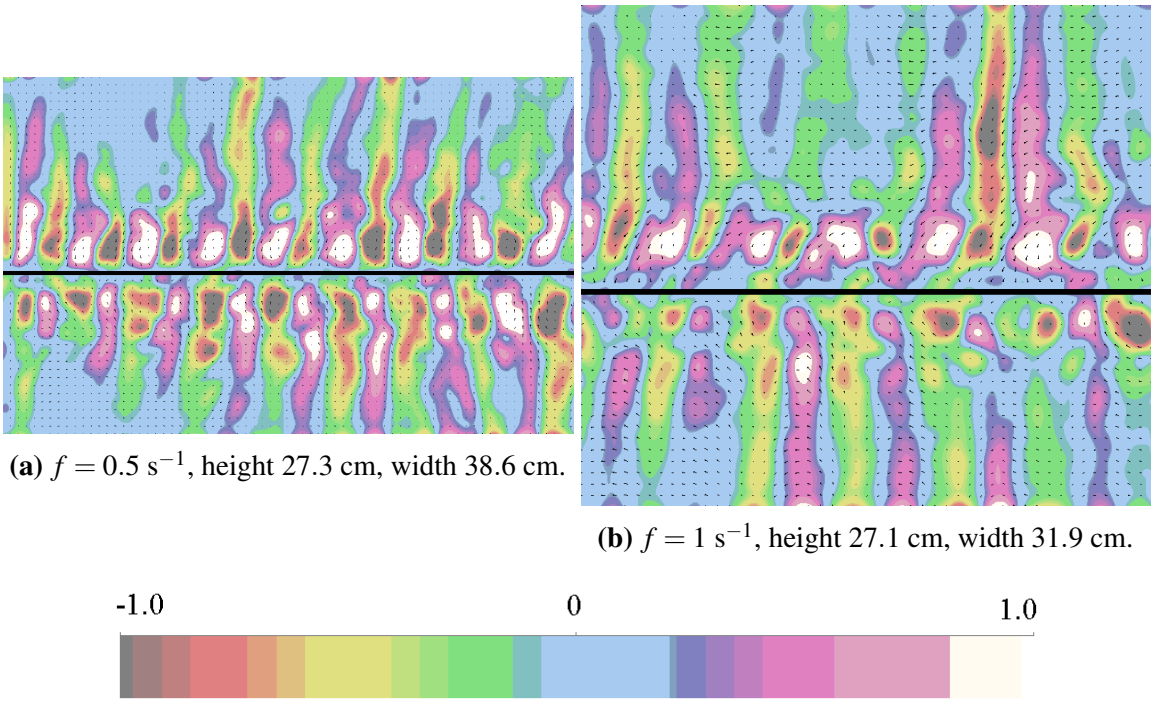

(a) $f = 0.5$ s^{-1}, height 27.3 cm, width 38.6 cm.

(b) $f = 1$ s^{-1}, height 27.1 cm, width 31.9 cm.

Figure 9.4 The time-averaged mean vorticity field in the vertical plane. The stroke height is fixed at $s = 3$ cm and the stroke frequency fixed at $n = 0.5$ Hz. The rotation rate is increased from $f = 0.5$ s^{-1} to $f = 1$ s^{-1}. The location of the mid-point of the grid stroke is indicated by a black line. A scale bar is shown for the vorticity in rad s^{-1} and the size of each image is indicated.

our experiments.

We begin with a qualitative look at the turbulence generated by the mixing grid in the presence of rotation, with an analysis of the mean vorticity fields through a vertical slice in the flow. Figure 9.4 displays the mean vorticity profiles for a fixed stroke frequency $n = 0.5$ Hz, with a varying rotation rate. Long vortex tubes extending away from the grid towards the surface are visible in both images and represent the transition to quasi-two-dimensional turbulence away from the grid. The region of three-dimensional turbulence close to the grid is identifiable by the areas of high vorticity (white and black) and we can see that it extends for a larger distance for smaller f. This means that the transition height decreases as the rotation rate is increased, which is in agreement with the theory in (9.6).

Figure 9.5 shows the mean vorticity field in a horizontal plane through the flow at three different heights above the grid, with and without rotation. The stroke height and stroke oscillation frequency remained fixed at $s = 3$ cm and $n = 1$ Hz respectively. The images at

$z = 2.75$ cm are very similar with and without rotation. This follows the expected behaviour of the turbulence with the rotation not affecting the turbulence close to the grid. At $z = 8$ cm we begin to see the effects of rotation with the right-hand image displaying a more coherent flow structure compared to the left-hand image without rotation. For the largest height of $z = 13.35$ cm the rotating turbulence becomes quasi-two-dimensional with the formation of vortex columns extending to the surface. In contrast the strength of the turbulence in the left-hand image without rotation has decreased considerably. There is a very obvious change in the structure of the turbulence with and without rotation at large heights from the grid.

The turbulent velocity data are analysed in comparison to the three stage model of Fleury et al. (1991) to provide estimates for the transition heights Z_T and Z_R. Figure 9.6 plots the rms velocity as a function of height from the grid for two different rotation rates $f = 0.5$ and 1 s^{-1}, with the stroke frequency fixed at $n = 0.5$ Hz. The data show that the turbulent velocity decreases with increasing distance from the grid and increases as the value of f is increased. This behaviour is in agreement with the theory presented in section 9.3. The theory predicts that the transition to quasi-two-dimensional turbulence will occur at a lower height for increased f and therefore the turbulent velocity at the transition height will be higher and thus a larger velocity is maintained for $Z > Z_R$. The data in figure 9.6 are displayed on a log-log plot which allows us to estimate the transition heights Z_T and Z_R. We estimate the value of Z_T as the height at which the initially linear gradient of the velocity curve changes, following the method used by Hopfinger et al. (1983). The value of Z_R can also be estimated from the data as the height beyond which the velocity remains approximately constant. For $f = 0.5$ s^{-1} we estimate $Z_T \sim 14.2 \pm 2$ cm with Z_R greater than the field of measurement. For $f = 1$ s^{-1} we estimate $Z_T \sim 5.5 \pm 2$ cm with $Z_R \sim 8.6 \pm 2$ cm.

Estimates for the transition heights Z_T and Z_R are made for the experiments at $n = 1$ Hz also, using the same methods as above. Figure 9.7 plots the estimated values of Z_T from the data versus f/n. The theoretical curve for Z_T according to the theory of Hopfinger et al. (1983) given in (9.6) is also shown, where we have used their transition Rossby number value of $Ro = 0.20$. The data in figure 9.7 show good agreement with the theory for Z_T which demonstrates that the behaviour expected from grid-generated turbulence is seen in our experimental setup.

Figure 9.8 plots the Rossby number $Ro = u^*/(fl)$ for the experiments at different values of f/n. The Rossby number decreases initially as z is increased as the velocity decays and the

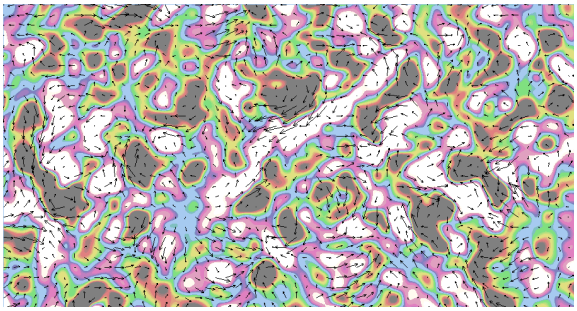

(a) $z = 2.75$ cm, height 13.4 cm, width 26.6 cm.

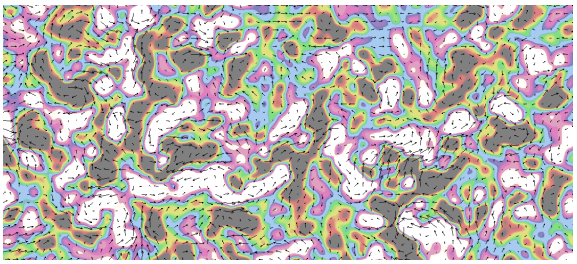

(b) $z = 2.75$ cm, height 12.9 cm, width 30.3 cm.

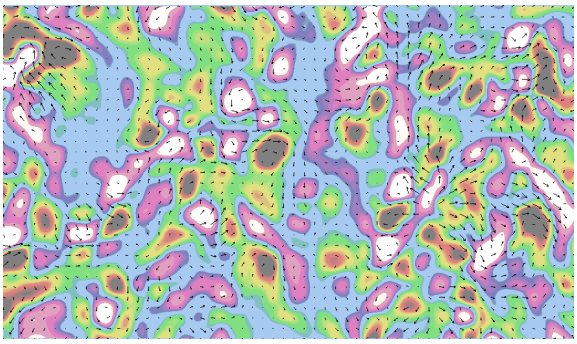

(c) $z = 8$ cm, height 16.7 cm, width 27.9 cm.

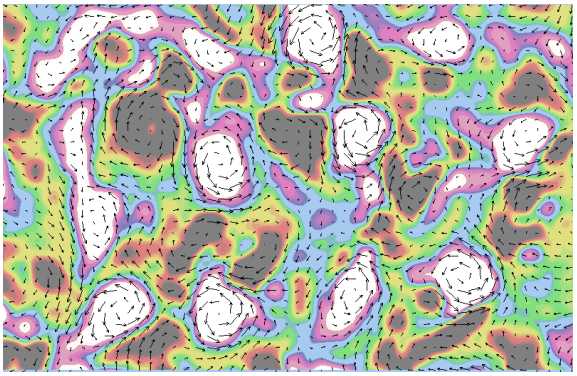

(d) $z = 8$ cm, height 16 cm, width 26.4 cm.

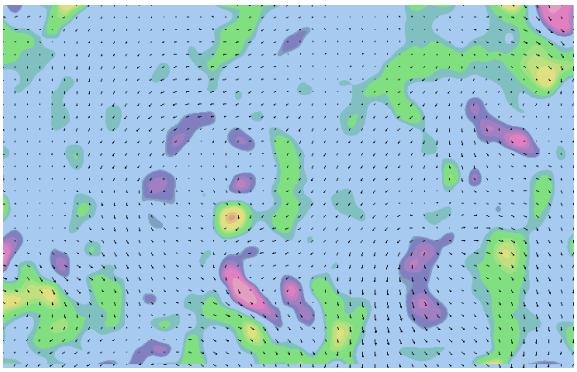

(e) $z = 13.35$ cm, height 15.2 cm, width 23.3 cm.

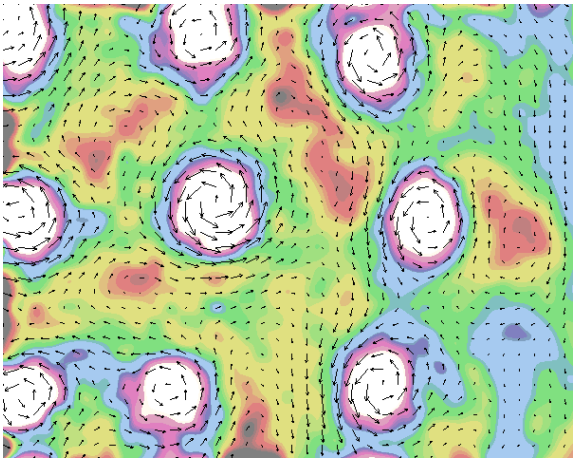

(f) $z = 13.35$ cm, height 16.2 cm, width 20.3 cm.

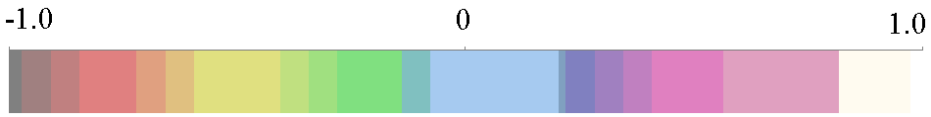

Figure 9.5 The time-averaged mean vorticity field for $z = 2.75, 8$ and 13.35 cm. Adjacent images show $f = 0$ (left-hand image) and $f = 1$ s^{-1} (right-hand image). The stroke height and stroke oscillation frequency are fixed at $s = 3$ cm and $n = 1$ Hz respectively. A scale bar is shown for the vorticity in rad s^{-1} and the size of each image is indicated.

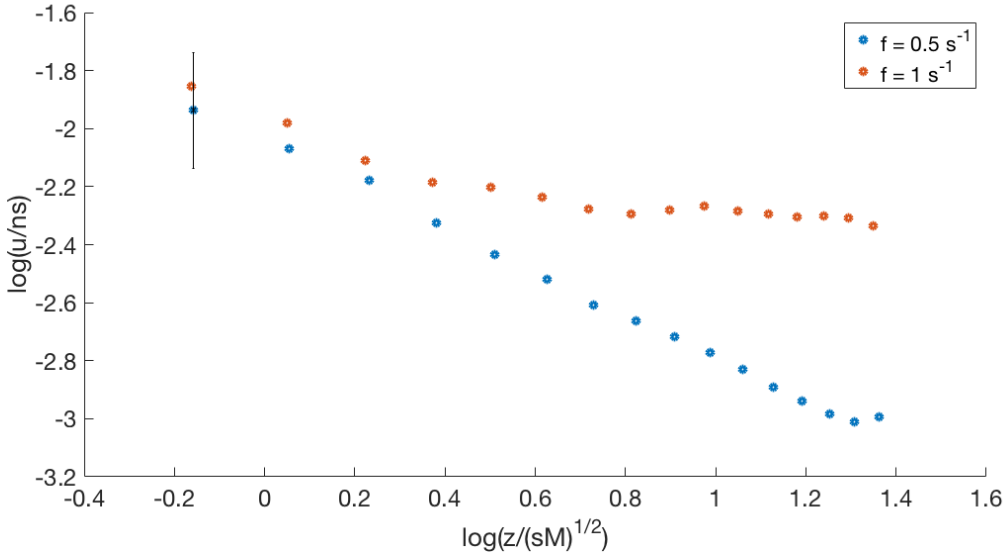

Figure 9.6 The experimentally measured turbulent rms velocity u^*, scaled with $u_0 = ns$, plotted as a function of height from the grid, z, scaled with the grid mesh size M and stroke amplitude s. The data are shown as a log-log plot. The rotation rate is varied across $f = 0.5$ and 1 s^{-1}.

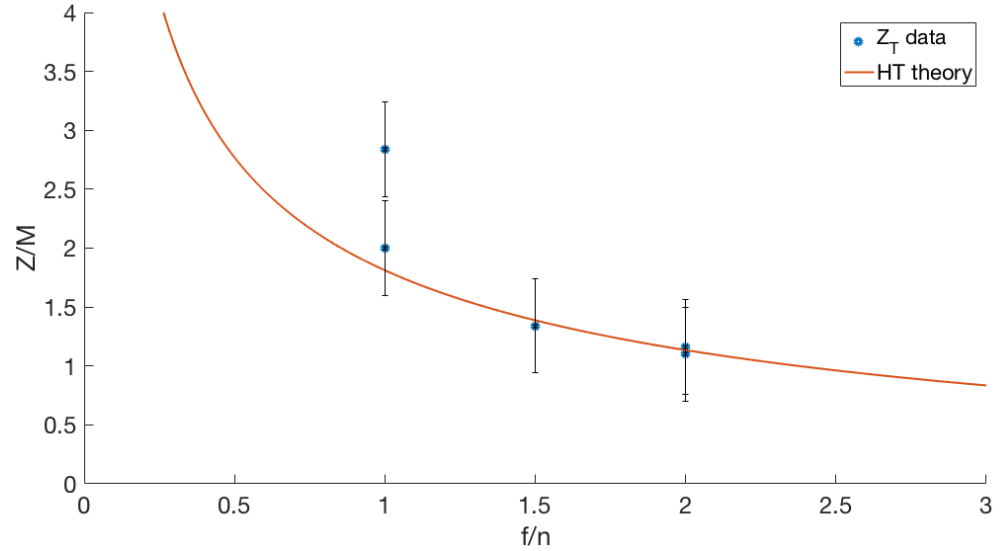

Figure 9.7 The estimated values of Z_T scaled with M and plotted versus f/n. The theoretical curve according to the theory of Hopfinger et al. (1983) given in (9.6) is also shown with a Rossby number of $Ro = 0.20$.

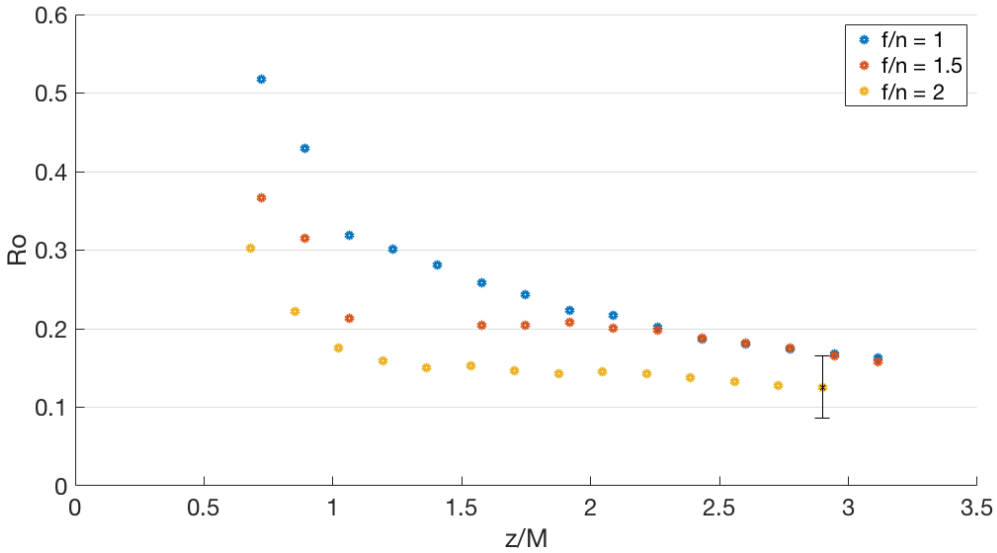

Figure 9.8 The experimentally measured Rossby number, where $Ro = u^*/fl$, versus height above the grid z, scaled with the grid mesh size M.

turbulent lengthscale grows. At larger values of z/M, it remains at an approximately constant value as the turbulence transitions to quasi-two-dimensional turbulence. The estimated transition value of $Ro(Z_T) = 0.2$ from the work of Hopfinger et al. (1983) provides a good approximation for the transition height Z_T. The data show an increase in the value of z/M at $Ro = 0.2$ for smaller f/n as predicted by the theory in (9.6). The estimated final constant Rossby number of $Ro(z > Z_R) \sim 0.06$ using the relations found by Fleury et al. (1991) in (9.3) and (9.4) is smaller than the values seen in our experimental setup. The data in figure 9.8 suggest a value of $Ro \sim 0.14 \pm 0.06$.

Overall, the rotating grid-generated turbulence produced by our experimental setup exhibits the same features seen in similar studies described in the literature. In particular, we see a transition from three-dimensional turbulence close to the gird to quasi-two-dimensional turbulence at larger distances from the grid as described by Fleury et al. (1991). The height at which the transition occurs is found to be similar to that seen in the work of Hopfinger et al. (1983) with a transition Rossby number value of $Ro(Z_T) = 0.2$ showing good agreement with the data.

9.4 Discussion

We have seen that the grid-generated turbulence produced in our experimental setup exhibits the same behaviours seen in other studies in the literature. In the case of non-rotating grid-generated turbulence, the scalings for the turbulent rms velocity and turbulent integral lengthscale from the work of Hopfinger and Toly (1976) agree well with our experimental data. Fitting the expressions in (9.2) and (9.1) to the data we obtain constants $K_1 = 0.23$ and $K_2 = 0.10$ which are within the same range as those used in the literature. The choice of virtual origin when measuring the height above the grid and fitting the data to the expressions in (9.2) and (9.1) is debated in the literature, with different values being used depending on the experimental setup. For our setup we find that a distance of $\sim 2.5 \pm 1.5$ cm below the mid-point of the grid-oscillation is the appropriate choice.

With the addition of rotation we see a change in the structure of the turbulence from three-dimensional close to the grid, to quasi-two-dimensional at larger heights with approximately constant values for u^* and l. The theory predicts that the transition between the regimes decreases in height as the rotation rate is increased and increases in height as the stroke frequency is increased, both of which are seen in our experiments. The transitional Rossby number of $Ro(Z_T) = 0.2$ from the work of Hopfinger et al. (1983) provides a good approximation to the values seen in our experiments.

Combining all of the information and analysis conducted in this chapter, we choose to use a stroke frequency of $n = 1$ Hz and rotation rates of $f = 0.5, 1$ s^{-1} for the experiments where a source of freshwater is released into a turbulent ambient. The experimental results from this setup will be discussed in chapter 10.

Chapter 10

Experimental observations for a turbulent ambient

10.1 Problem description

In chapter 9 we investigated the properties of grid-generated turbulence in a non-rotating and rotating frame. The turbulence was found to demonstrate the same properties as seen in similar studies of grid-generated turbulence (eg. Hopfinger and Toly 1976, Hopfinger et al. 1983 and Fleury et al. 1991). By positioning the mixing grid at varying depths in the tank we were able to alter the nature of the turbulence impacting on the flow. At shallow grid depths the three-dimensional turbulence produced models a river outflow entering into a shallow sea where the bottom topography of the sea bed will act as a source of turbulent friction (e.g. Simpson et al. 1996, Fisher et al. 2002, Jacobs 2004). At larger grid depths the turbulence produced is quasi-two-dimensional and forms surface eddies that resemble those seen in currents along the coasts of Norway (Mork 1981, Johannessen et al. 1989) and California (Brink et al. 1991).

The addition of turbulence to the saltwater ambient will lead to increased levels of mixing at the interface with the freshwater current. In the previous experiments with a quiescent ambient, mixing at the interface between the two layers of the flow was assumed to be negligible and as such was neglected in the theoretical modelling. Here, we use the work of Turner (1968) to model the entrainment across the density interface and investigate the effect of turbulent mixing on the flow properties. Turner models the entrainment velocity at the

interface as

$$\frac{u_e}{u^*} \sim Ri^{-N}, \tag{10.1}$$

where u^* is the turbulent velocity at the interface, N is an empirical constant and Ri is a Richardson number. The Richardson number is defined as

$$Ri = \frac{g'l}{(u^*)^2} \tag{10.2}$$

with l the turbulent integral lengthscale at the interface. The experiments of Turner found two different values for the empirical constant N depending on the stratifying agent: for heat $N = 1$ and for salt $N = 1.5$ at high values of Ri.

In this chapter we address the third key question of this thesis as we investigate the effects of a turbulent ambient on the properties of the boundary current and the outflow vortex. The turbulence generated by the mixing grid is quantified by a turbulent Richardson number as defined by Turner (1968). We analyse the effect of turbulent mixing across a large range of Richardson numbers on the current depth, current velocity, current width, vortex radius and vortex depth. The structure of the turbulence is also varied from three-dimensional to quasi-two-dimensional and the effects of this change on the flow properties investigated.

10.2 Experimental results

The setup of the experiments remains the same as that described in chapter 2 with the addition of a mixing grid into the rotating tank. The strength and structure of the turbulence is varied by changing the depth of the mixing grid. We use a fixed stroke amplitude $s = 3$ cm, a fixed stroke frequency $n = 1$ Hz and a fixed grid mesh size of $M = 5$ cm. The depth of the mixing grid is varied across $z = 16$ cm, $z = 8$ cm and $z = 4$ cm. The frequency of the stroke was chosen based on the observations in chapter 9. A value of $n = 1$ Hz means that for the three heights considered we have qualitatively different turbulence. At large $z = 16$ cm the turbulence is in general quasi-two-dimensional, while at small $z = 4$ cm the turbulence is three-dimensinal in nature. At $z = 8$ cm we lie in the transition regime. The turbulent properties at each height above the grid are calculated according to the results in chapter 9.

The strength of the turbulence produced in each experiment is quantified by a Richardson number as defined in (10.2). The values of the turbulent velocity u^* and the integral

lengthscale l are calculated at the depth at which the turbulence acts on the flow property in question. For example, for the maximum current depth h_0, we calculate the turbulent properties at a distance $z - h_0$ from the grid. The current velocity, current width and vortex radius are measured at the surface and therefore the turbulent properties are calculated at a distance z from the grid. For the vortex maximum depth the data from the experiments with a non-turbulent ambient are used to estimate the mean vortex depth during an experiment, H_{mean}, and the turbulent properties calculated at a distance $z - H_{mean}$ from the grid. Four different sets of experimental parameters were considered that cover the three different flow regimes at low, intermediate and high values of I^*. The parameter values were chosen such that we are able to cover the majority of the different flow behaviours seen in the previous experiments with a quiescent ambient. The range of experimental parameter values used and the corresponding values of I^* vary slightly for each flow property considered and thus are given in each section.

10.2.1 Boundary current

The effect of a turbulent ambient on the boundary current is analysed by considering the change in three key current properties: the current velocity, the current width and the current depth. For each current property, we compare the results from experiments with a non-turbulent ambient and those with a turbulent ambient for grid depths of $z = 16$ cm and $z = 8$ cm. For a grid depth of $z = 4$ cm the propagation of the boundary current was dramatically reduced and halted entirely in some instances, preventing measurements of the current properties from being made. The issue of stopping the current will be addressed in section 10.2.3.

For the experiments conducted with a turbulent ambient a cyclonic mean-flow was present around the boundary of the tank. The flow was strongest at the surface and extended to a depth of $\sim 3-5$ cm. Figure 10.1 displays a long-exposure image of the flow next to the boundary where the movement of the particles can be seen as streaks, whose length is proportional to the magnitude of the velocity. The motion of the mean flow along the boundary of the tank is visible up to a distance of $\sim 4-5$cm from the wall and moves from right to left in the figure. We expect that the mean flow will reduce the current velocity and deepen the current as it acts in the direction opposing the motion of the current. Its effects will be discussed in section 10.2.1.1 with analysis of velocity profiles taken across the current

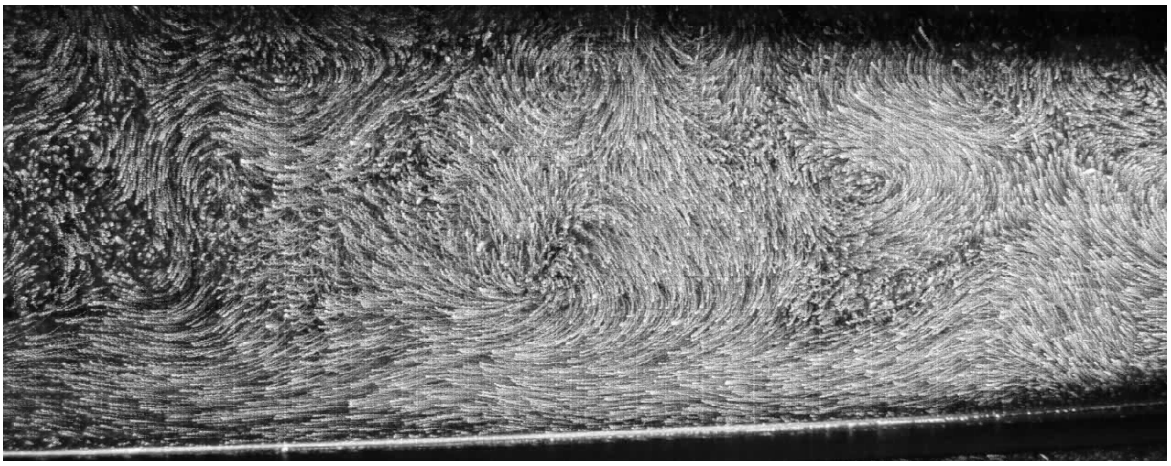

Figure 10.1 A streak-image showing the velocity field at the surface ($z = 15 \pm 0.5$ cm) with $f = 0.5$ s^{-1} and $n = 1$ Hz. The light sheet has a width of 15 cm at the right-hand edge of the image for scale.

and in section 10.2.1.3 when analysing the current depth measurements.

We briefly present a possible modification that could be made to the experimental setup to potentially alleviate the problem of the mean flow around the boundary of the tank in future studies. The opposing mean flow was only observed at the boundary of the tank and thus by inserting a second partial wall in front of the tank boundary the effect of the mean flow on the current may be reduced, whilst still allowing the grid to move freely at depth. The modified setup is displayed in figure 10.2 with an aerial view showing the position of the partial barrier in relation to the current setup and a side view showing how the grid will still be able to oscillate at depth. By positioning the partial barrier in this way the mean flow around the tank boundary will still occur, but will now be separated from the propagating freshwater current along the first wall of the tank, thus preventing it from interfering with the measurements made there. This will allow for the effects of the mean flow to be separated from those of the turbulent ambient.

10.2.1.1 Current velocity

The current velocity was measured using PIV. Particles were added to both the ambient fluid and the freshwater current and the measurements made in a horizontal light sheet $\sim 0.5 - 1.5$ cm below the surface of the fluid. The experimental parameters are displayed in table 10.1. The nature of the turbulence acting on the current at the surface for grid depths of $z = 16$ cm

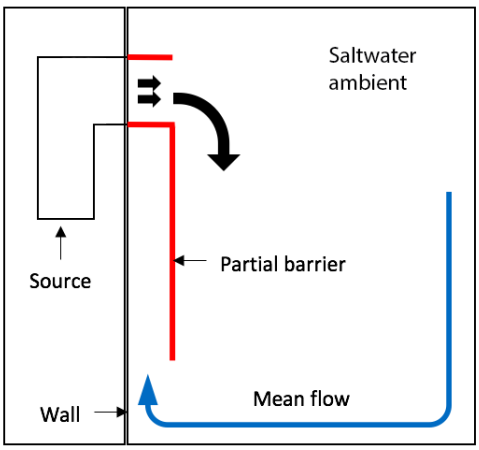

(a) Aerial view of location of partial barrier.

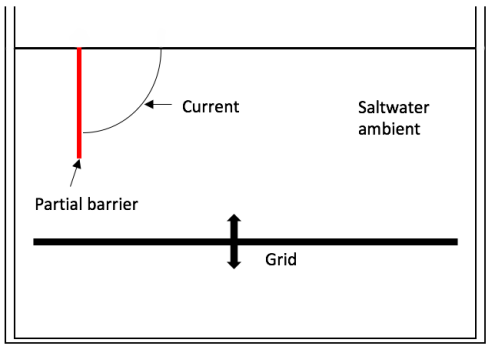

(b) Side view of location of partial barrier.

Figure 10.2 Modified experimental setup that could be used to reduce the mean flow effects on the freshwater current in future studies. The red lines indicate the new partial barrier that would be added to the current experimental setup.

Exp. group	Q [cm^3 s^{-1}]	f [s^{-1}]	g' [cm s^{-2}]	I^*	$z = 16$ cm	$z = 8$ cm
1	48	0.5	13.3 - 13.7	0.41 - 0.42	2D	3D
2	48	1	13.4 - 14.5	0.79 - 0.83	2D	Transition
3	48	0.5	2.9 - 4.4	0.81 - 1.04	2D	3D
4	48	1	3.1 - 3.7	1.80 - 2.00	2D	Transition

Table 10.1 Experimental parameters for the experiments measuring the current velocity and current width in a turbulent ambient.

and $z = 8$ cm is also indicated.

We present two forms of the velocity data, one consisting of the current velocity profile at late times during the experiment and the other showing the development of the maximum current velocity over time. The time development of the velocity shows the same qualitative behaviour across the three regimes of low, intermediate and high I^* and thus we present the data from only one regime to demonstrate the behaviour seen. We begin with the current velocity profiles with and without turbulence. The profiles are taken across the current at the same position for each flow regime, approximately one-fifth of the way around the perimeter of the tank. A total of six profiles are displayed for each value of I^*, with three taken at $T = 0$ at the beginning of each experiment before the release of the current and three taken at the end of the experiment. The data for the non-turbulent ambient is displayed with a solid

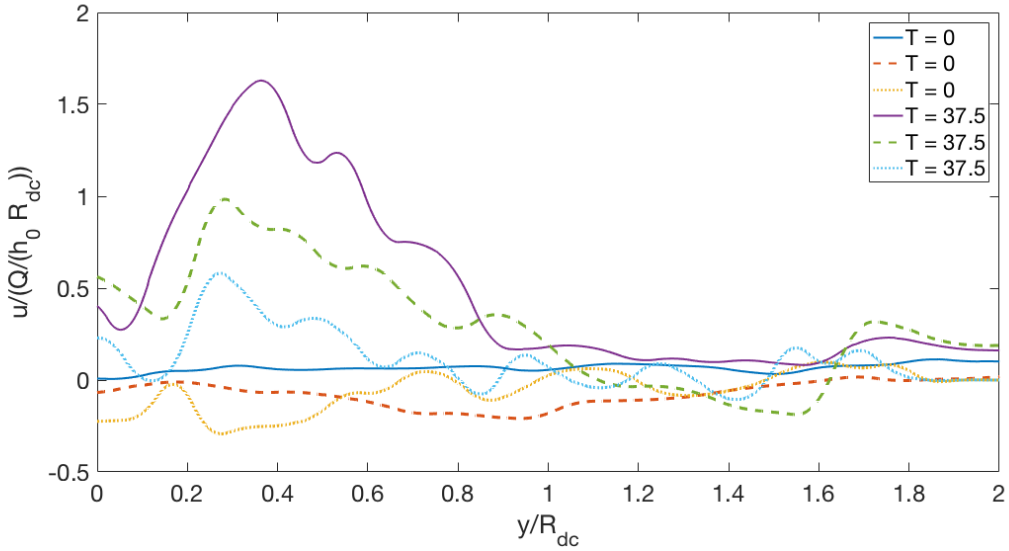

Figure 10.3 Across current velocity profiles taken at the beginning and end of an experiment for the low I^* regime. Three sets of profiles are shown, with the solid line denoting no ambient turbulence, the dashed line a grid depth of $z = 16$ cm and the dotted line a grid depth of $z = 8$ cm.

line, with the dashed line denoting a grid depth of $z = 16$ cm, and the dotted line representing a grid depth of $z = 8$ cm. This is the same across figures 10.3 - 10.5.

Figure 10.3 displays the velocity profiles for the experiments with a low value of I^*. As the strength of the turbulence is increased we see a reduction in the current velocity but the same general profile shape is maintained. The largest velocities are seen towards the centre of the current with a decrease towards zero at either edge. The wall velocity remains non-zero for all of the experiments at less than or equal to half of the maximum value. For the experiment with a grid depth of $z = 8$ cm the current propagation is severely disrupted by the turbulence as can be seen by the small current velocities in the figure. The mean flow along the boundary present for rotating turbulence is visible in the profiles at $T = 0$ for the turbulent experiments. It has a magnitude of $\sim 0.20 \pm 0.1$ in dimensionless units and is stronger for the shallower grid depth.

Figure 10.4 displays the across current velocity profiles for the intermediate I^* experiments. As the strength of the turbulence in the ambient is increased we again see a reduction in the maximum current velocity. The mean flow along the boundary can be identified in the profiles at $T = 0$ for the turbulent ambient experiments and has a velocity of ~ 0.4 in dimensionless units. The reduction in the maximum current velocity is of the same order

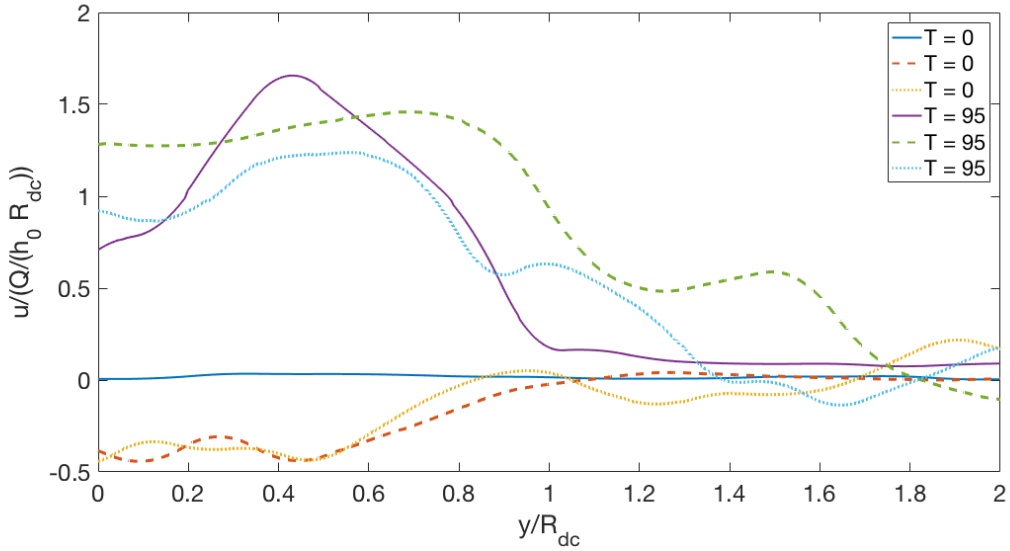

Figure 10.4 Across current velocity profiles taken at the beginning and end of an experiment for the intermediate I^* regime. Three sets of profiles are shown, with the solid line denoting no ambient turbulence, the dashed line a grid depth of $z = 16$ cm and the dotted line a grid depth of $z = 8$ cm.

of magnitude as the mean flow. The velocity profile also becomes wider and less peaked with the addition of turbulence. For the $z = 16$ cm case we see an approximately constant current velocity from $y/R_{dc} = 0 - 0.8$ suggesting that the turbulence acts to increase the level of uniformity in the velocity profile. The increased profile width for a turbulent ambient suggests increased levels of entrainment and subsequent mixing at the horizontal interface between the two layers.

Figure 10.5 displays the across current velocity profiles for the high I^* regime experiments. Again, we see a reduction in the current velocity as the strength of the turbulence is increased, with the current almost halted entirely for a grid depth of $z = 8$ cm. For this grid depth the profile width is much smaller than in the other experiments and the magnitude of the current velocity is the same as that of the turbulent velocity seen at $T = 0$ before the release of the current. The reduction in the current velocity from the non-turbulent case to a grid depth of $z = 16$ cm, is similar to the magnitude of the mean flow at the tank boundary, which can be identified for both grid depths at $T = 0$. The magnitude of the mean flow is similar to that seen in figure 10.4 and both are larger than the mean flow in figure 10.3 due to the experiments having a larger rotation rate. The turbulence also acts to increase the profile width and increase the uniformity of the velocity profile as seen for the intermediate I^* regime.

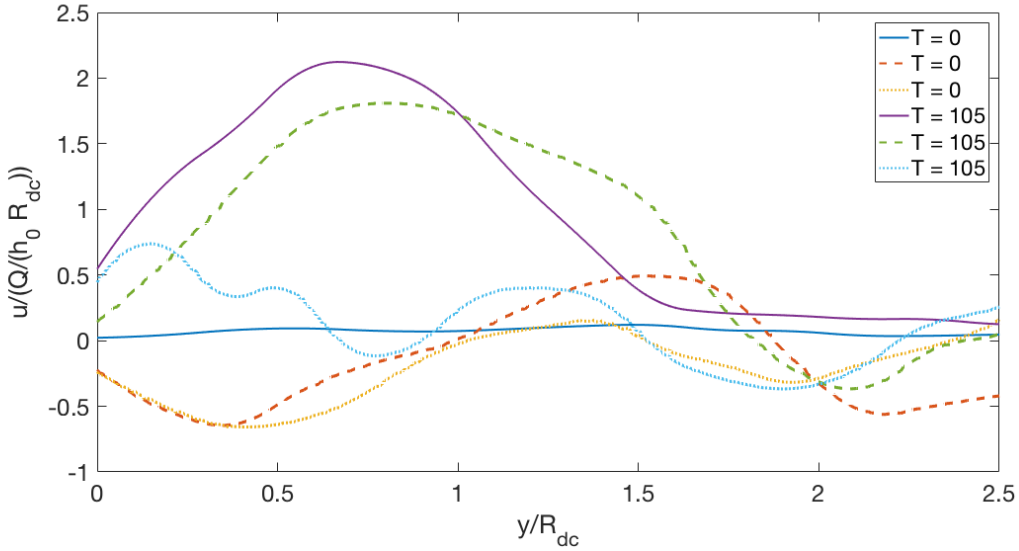

Figure 10.5 Across current velocity profiles taken at the beginning and end of an experiment for the high I^* regime. Three sets of profiles are shown, with the solid line denoting no ambient turbulence, the dashed line a grid depth of $z = 16$ cm and the dotted line a grid depth of $z = 8$ cm.

Measurements of the maximum current velocity seen in the across current velocity profiles are made at 5 second intervals for each experimental parameter regime, both with and without turbulence. Figure 10.6 displays the data for the high I^* experiments as a function of dimensionless time T. The data for the low and intermediate I^* regimes show the same qualitative behaviour as that seen in figure 10.6. The general effect of the turbulent ambient on the current velocity for these regimes can be seen in figures 10.3 and 10.4. The velocity in figure 10.6 is very similar for the non-turbulent case and the case of quasi-two-dimensional turbulence ($Ri = 82$), with a slight reduction for the turbulent ambient. As the turbulence strength is increased to $Ri = 43$ there is a clear decrease in the maximum current velocity. For both of the experiments with a turbulent ambient we estimate the mean flow around the boundary of the tank evident in figure 10.5, to be 0.40 ± 0.20 in dimensionless units. This is much larger than the decrease in velocity seen for $Ri = 82$ and smaller than the decrease seen for $Ri = 43$.

Figure 10.7 plots the change in the current velocity u_e versus the turbulent Richardson number Ri for all values of I^*. The change in velocity is calculated as the value for a turbulent ambient minus the velocity measured for a quiescent ambient. The nature of the turbulence acting on the current is also indicated in the legend. The data show that in general the current velocity is reduced by a greater amount for a smaller Richardson number. The largest

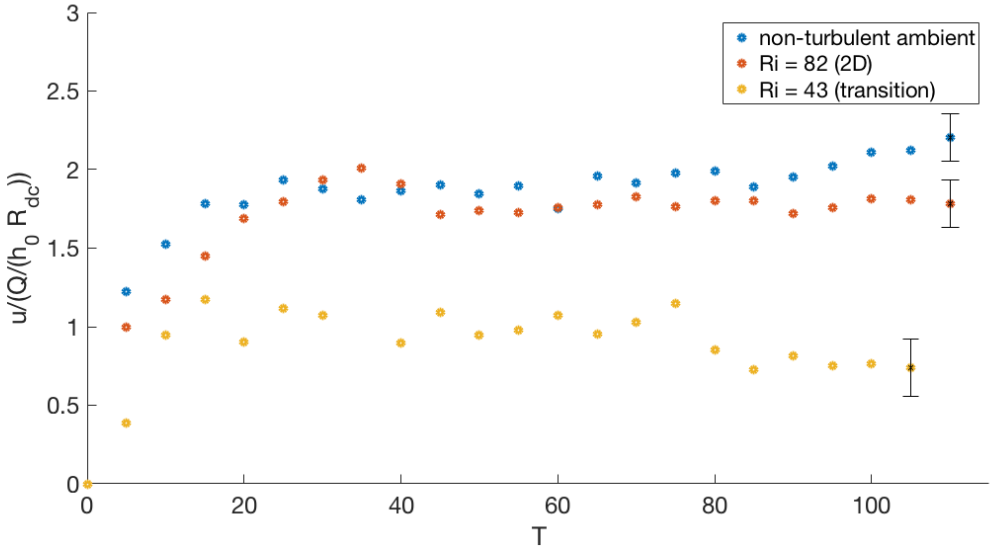

Figure 10.6 The maximum current velocity versus time for the high I^* regime experiments. Three sets of data are shown for a non-turbulent ambient, a grid depth of 16 cm and a grid depth of 8 cm.

decreases in velocity also occur for the three-dimensional and transitional turbulence regimes. For the quasi-two-dimensional turbulence we see a slight increase in the current velocity at $Ri = 366$, which is a behaviour unique to this regime.

10.2.1.2 Current width

Using the velocity profiles presented in section 10.2.1.1, estimates of the current width were made. The distance from the boundary wall of the tank at $y/R_{dc} = 0$ to the point at which the dimensionless current velocity decreases below a threshold value was used to approximate the current width every 5 seconds (see chapter 2 for full details). The current width estimates are plotted in figure 10.8 versus dimensionless time for the intermediate I^* regime. The qualitative behaviour is the same for the low and high I^* regimes with the width initially increasing and then remaining approximately constant. The general effect of the turbulent ambient on the current width for these regimes can be seen in figures 10.3 and 10.5 respectively. In figure 10.8 we see that overall the presence of turbulence acts to increase the current width. The data show an interesting trend with the current width increasing from its value for a non-turbulent ambient for $Ri = 366$, but then decreasing for stronger turbulence at $Ri = 186$. The structure of the turbulence changes from the quasi-two-dimensional regime at $Ri = 366$ to the transition regime for $Ri = 186$, which suggests that

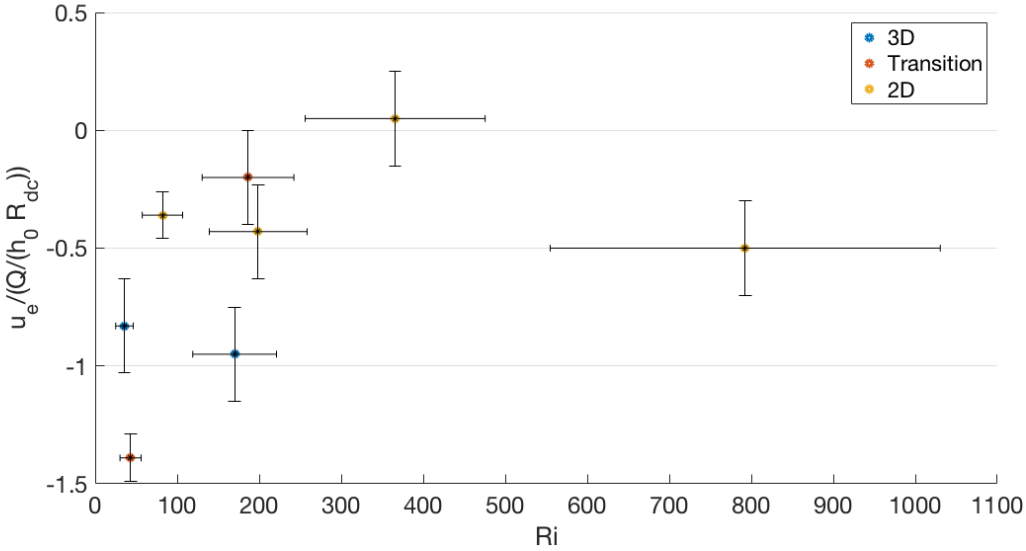

Figure 10.7 The change in the maximum current velocity versus turbulent Richardson number *Ri*.

the effect of the turbulence on the current width may be linked to its structure. This will be discussed in terms of the possible physical mechanisms at work in the flow in section 10.2.1.4.

The estimated change in the current width with the addition of turbulence to the ambient w_e is plotted against the Richardson number in figure 10.9. The change in the width is calculated as the value for a turbulent ambient minus the value measured in a quiescent ambient. For the smallest Richardson numbers, the current width is reduced in the presence of turbulence. As the intensity of the turbulence is reduced and the Richardson number increased, the current width is seen to increase. The largest values of the reduction in the width occur for the three-dimensional and transitional turbulence regimes, while the largest values for increases in the width are seen for quasi-two-dimensional turbulence.

10.2.1.3 Current depth

The current depth is measured experimentally using the same method of dye attenuation as that employed for a quiescent ambient. The depth is measured at a fixed point approximately one-third of the way around the perimeter of the tank and between $0.1 - 1$ cm from the tank wall. The exact value varies for each experiment due to interference in the measurements from the grid (see chapter 2 for more details). The experimental parameters for each group of experiments are given in table 10.2. The nature of the turbulence acting on the current

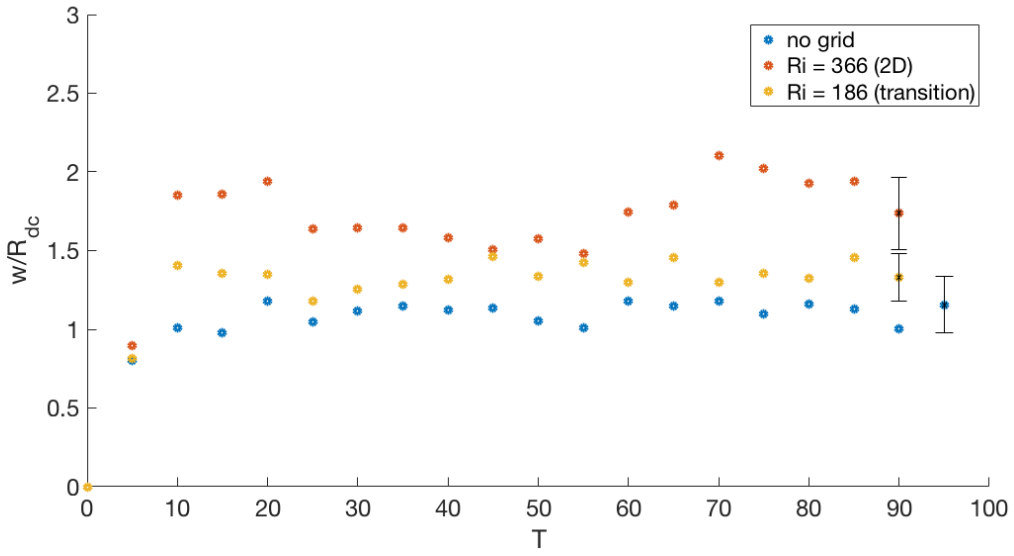

Figure 10.8 The estimated current width versus time for the intermediate I^* regime experiments. Three sets of data are shown for a non-turbulent ambient, a grid depth of 16 cm and a grid depth of 8 cm.

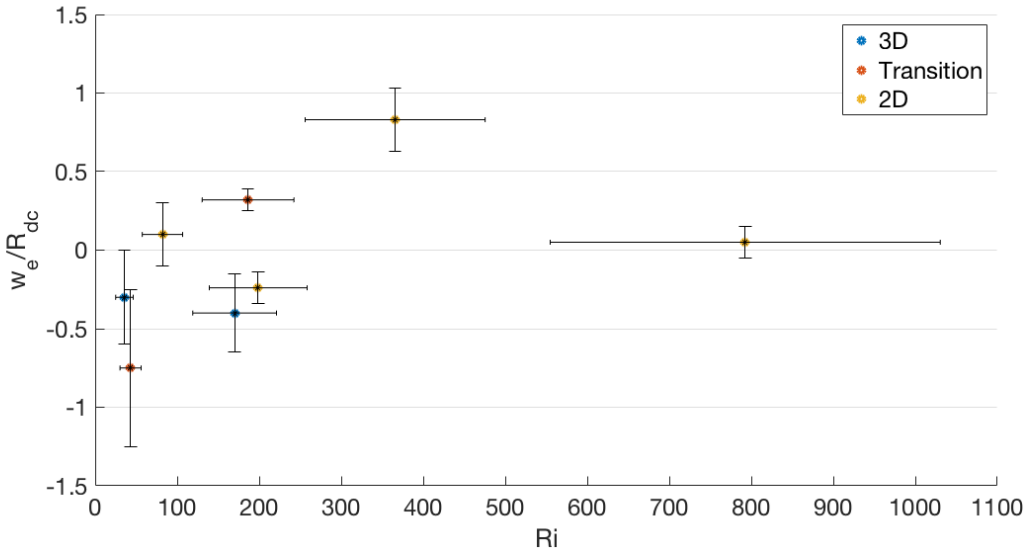

Figure 10.9 The estimated change in the current width versus turbulent Richardson number *Ri*.

Exp. group	Q [cm^3 s^{-1}]	f [s^{-1}]	g' [cm s^{-2}]	I^*	$z = 16$ cm	$z = 8$ cm
1	40 - 48	0.5	14.3 - 17.4	0.34 - 0.40	2D	3D
2	40 - 48	1	11.8 - 15.9	0.72 - 0.86	2D	3D
3	40 - 42	0.5	2.3 - 4.7	0.75 - 1.15	2D	3D
4	40 - 42	1	2.3 - 4.6	1.52 - 2.31	2D	3D

Table 10.2 Experimental parameters for the experiments measuring the current depth in a turbulent ambient.

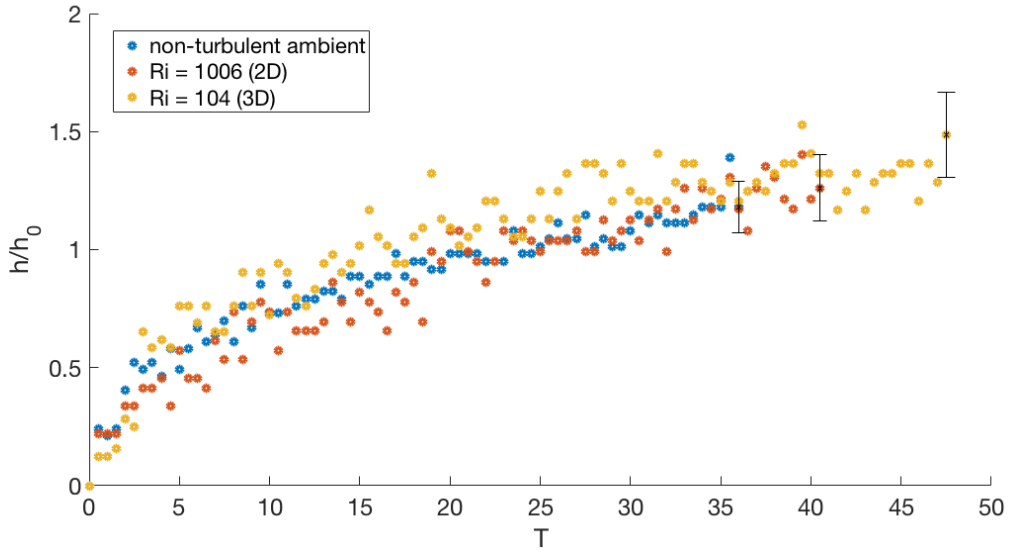

Figure 10.10 The current depth scaled with h_0 versus dimensionless time T for the low I^* parameter regime. Measurements from three experiments are shown with differing strengths of ambient turbulence.

depth for grid depths of $z = 16$ cm and $z = 8$ cm is also indicated.

The measurements of the current depth for the low I^* regime are shown in figure 10.10 versus time. There appears to be little difference between the current depth measurements across the three experiments for a quiescent ambient, $Ri = 104$ and $Ri = 1006$. There is perhaps a slight increase in the depth for $Ri = 104$ where the turbulence is three-dimensional and a slight decrease for $Ri = 1006$ with quasi-two-dimensional turbulence, but the scatter in the data makes it difficult to identify.

Figure 10.11 plots the current depth measurements versus time for the intermediate I^* regime. The data for three experiments are shown for a non-turbulent ambient and for two

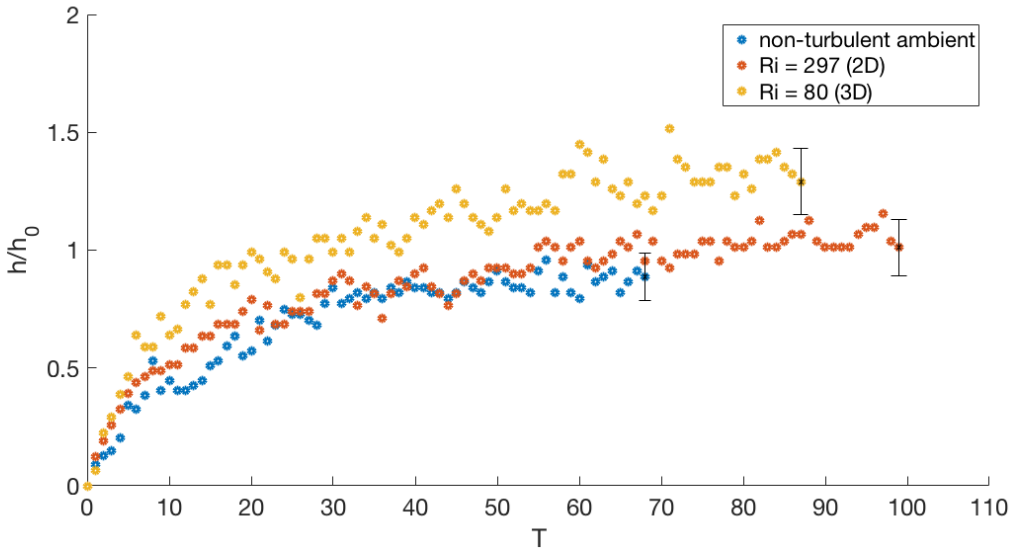

Figure 10.11 The current depth scaled with h_0 versus dimensionless time T for the intermediate I^* parameter regime. Measurements from three experiments are shown with different intensities of ambient turbulence.

different values of Ri. For the experiments with no turbulence and weak two-dimensional turbulence ($Ri = 297$) the current depth is very similar with a slight increase for the turbulent ambient. However, for the stronger three-dimensional turbulence ($Ri = 80$) the current depth increases.

The data for the current depth in the high I^* parameter regime is displayed in figure 10.12. With the introduction of turbulence we see an increase in the current depth to the theoretically predicted depth of h_0, which is not reached in the experiment with a non-turbulent ambient. The increase in the current depth is very similar for both $Ri = 8$ with three-dimensional turbulence and for quasi-two-dimensional turbulence at $Ri = 84$.

The results are summarised for all values of I^* in figure 10.13 where the estimated change in the current depth h_e is plotted versus the Richardson number. The value of h_e is calculated as the current depth for a turbulent ambient minus the current depth for a quiescent ambient. For small Ri the current depth deepens, with the increase in depth decreasing as Ri is increased. At large $Ri \sim 1000$ we see little or no change in the current depth. The nature of the turbulence appears to have little impact on the effect on the current depth with both quasi-two-dimensional and three-dimensional turbulence showing the same trend.

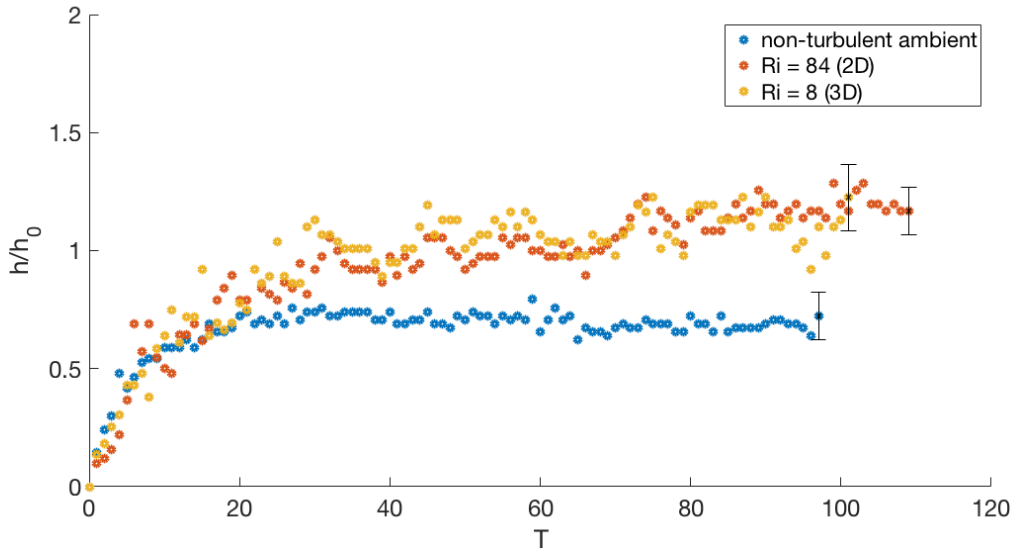

Figure 10.12 The current depth scaled with h_0 versus dimensionless time T for the high I^* parameter regime. Measurements from three experiments are shown with differing strengths of ambient turbulence.

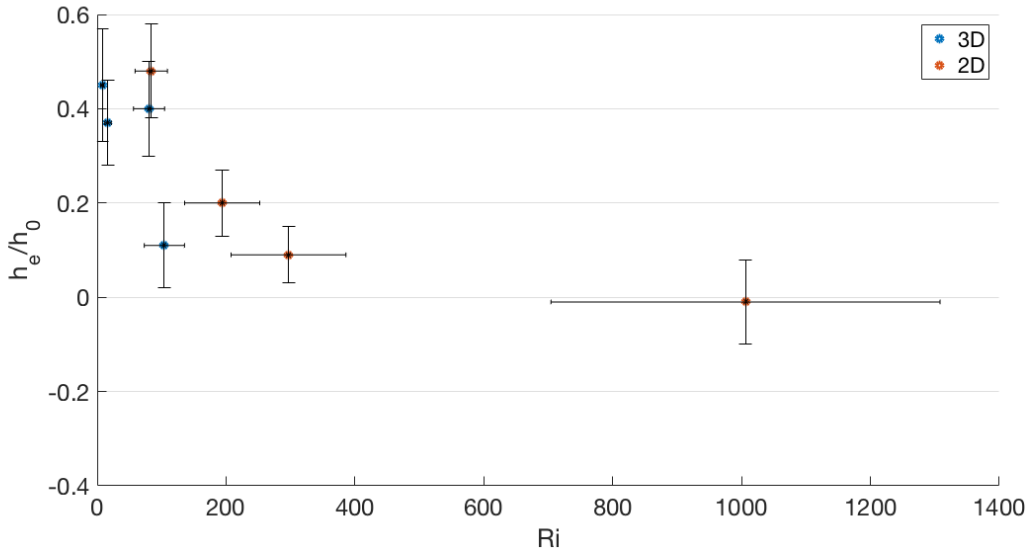

Figure 10.13 The change in the current depth scaled with h_0 versus turbulent Richardson number Ri.

10.2.1.4 Discussion

The addition of turbulence to the ambient has seen changes to the three current properties considered. For the current velocity the maximum value is reduced with a turbulent ambient. The mean flow around the boundary of the tank generated by the rotating turbulence opposes the direction of the current propagation and is likely the main cause of the reduction in the current velocity. The largest decreases occur for small Ri and three-dimensional turbulence where the expected increase in the level of mixing appears to enhance the effect of the mean flow. The relationship between the current velocity and the mean flow is not a simple linear addition with reductions up to $2-3$ times the magnitude of the mean flow seen in the experiments at small Ri. This is in contrast to the experiments at larger Ri, for example $Ri = 793$ in figure 10.7, where the reduction in the current velocity is of the same order of magnitude as the mean flow velocity of 0.3 ± 0.1 in dimensionless units. Here the change in the current velocity can be approximated by a simple linear relationship. A further behaviour is seen for the experiment at $Ri = 366$ where we see a slight increase in the current velocity. The mean flow for this experiment has a dimensionless value of 0.44 ± 0.1 and thus the current velocity must have increased significantly to overcome the opposing flow. For the quasi-two-dimensional (2D) turbulence regime we see large cyclonic vortices at the surface of the flow (see chapter 9) and the direction of the circulation within these vortices is the same as the direction of the current propagaton. A possible explanation for the increased current velocity is that the vortices at the edge of the current align themselves with the direction of the flow providing the extra energy required to speed up the current. The increased current velocity is only seen for one of the experiments in the 2D regime, however, and thus further investigation (including an assessment of the repeatability of the experimental results) is required before we are able to draw any firm conclusions.

The action of a turbulent ambient on the current width appears to depend not only on the strength of the turbulence, but also on its structure. For intense three-dimensional (3D) turbulence the current width is seen to decrease, while for quasi-two-dimensional turbulence the current width in general increases. In the 3D turbulent regime we might expect the vigorous stirring to strengthen the horizontal density interface at the surface, thus reducing the current width. As the turbulence transitions to quasi-two-dimensional we see the formation of cyclonic eddies at the surface. These eddies may act to entrain fluid across the horizontal density interface causing the current width to increase.

The current depth is seen to increase in the presence of turbulence, which is perhaps not the expected behaviour. For the Richardson numbers considered in the experiments, comparison with other mixing grid studies suggests that the turbulence will act to scour the interface from below making the current shallower. As this does not appear to be the case in our experiments, we must consider other possible explanations for the deepening of the current. One such explanation is the effect of the mean flow along the tank boundary that is generated by the rotating turbulence. The current depth showed little change in the presence of turbulence for the low I^* regime as shown in figure 10.10, whilst for the intermediate and high I^* experiments the current depth increases for a turbulent ambient as seen in figures 10.11 and 10.12. In section 10.2.1.1 the mean flow for the low I^* experiments was seen to be quite small $\sim 0.1 \pm 0.1$ (dimensionless units) in comparison to the mean flow at a higher rotation rate for intermediate and high I^* at $\sim 0.4 \pm 0.2$ (dimensionless units). The increase in the magnitude of the mean flow provides a possible explanation for the increase in the current depth. As the current collides with the opposing mean flow we would expect mixing to occur resulting in a deepening of the current. Another possible mechanism for the deepening of the current is vortex stretching. In the case of quasi-two-dimensional turbulence long vortex tubes are formed which extend upwards to the surface. As the current interface comes into contact with these vortices, it is possible that the current is entrained into the vortex and stretched vertically resulting in an increase in depth. To examine this behaviour in more detail we would need to remove the mean flow from the tank, which provides a possible route of further study.

10.2.2 Outflow vortex

The properties of the outflow vortex were also measured in the presence of a turbulent ambient. We investigate the effect of turbulence on the vortex maximum depth, vortex velocity field and the vortex radius. We again concentrate on the change seen in these properties when introducing the outflow into a turbulent environment compared to a quiescent one. Grid depths of $z = 16$ cm and $z = 8$ cm are used to vary the strength and nature of the turbulence.

10.2.2.1 Vortex depth

The vortex depth is estimated using PIV data. A vertical profile of the velocity field in the y-direction through the vortex is taken $\sim 2-4$ cm downstream of the source opening and the

Exp. group	Q [cm^3 s^{-1}]	f [s^{-1}]	g' [cm s^{-2}]	I^*	$z = 16$ cm
1	48	0.5	15.4	0.38	2D
2	48	1	14.6 - 16.5	0.73 - 0.79	2D
3	48	0.5	1.9 - 2.2	1.22 - 1.33	Transition
4	48	1	2.7 - 3.5	2.03 - 2.39	3D

Table 10.3 Experimental parameters for the experiments measuring the vortex depth in a turbulent ambient.

depth estimated by the decay of the velocity towards zero at the base of the vortex. We are unable to use the previous method of dye attenuation to obtain measurements as the presence of the mixing grid blocks the light source situated beneath the tank. To ensure the accuracy of this method, each PIV experiment is matched with a dye attenuation experiment with similar parameters and the depth on the vertical velocity plots is scaled with the vortex depth measured experimentally H. This allows the vertical velocity profiles to be viewed in the context of the vortex. We see below in figures 10.14 - 10.16 that the vortex depth estimated by the vertical profiles in this way provides a good approximation. Vertical velocity profiles are measured every 5 seconds and are averaged over five frames (1 second) to smooth the data. The profiles are taken passing through the approximate centre of the vortex where we expect the maximum depth to be achieved. For full details of the method used see chapter 2. The experimental parameter ranges for the four groups of experiments are displayed in table 10.3. The nature of the turbulence acting on the vortex is also indicated.

Measurements are made across the three I^* regimes for a non-turbulent ambient and a grid depth of $z = 16$ cm. Unfortunately, the motion of the mixing grid at $z = 8$ cm blocked the light source used for the PIV imaging and as such we were unable to make depth measurements for shallower grid depths. Before presenting the estimated vortex depth measurements, we first analyse the vertical velocity profiles from which they were obtained. Figure 10.14 displays the velocity profile through the outflow vortex at the beginning and end of an experiment, both with and without turbulence, for the low I^* regime. At $T = 0$ the freshwater has yet to be released. The solid line denotes no ambient turbulence and the dashed line a grid depth of $z = 16$ cm. A positive velocity represents motion away from the source. In both cases the vortex is shallow with a maximum depth of $H \sim 3$cm. The velocity decays with increasing depth, but never quite reaches zero, remaining finite beyond a depth of $z/H = -4.5$. This is a common feature of all of the experiments and suggests that the vortex induces a small circulation in the ambient flow beneath it. For a grid depth of $z = 16$ cm, the initial velocity

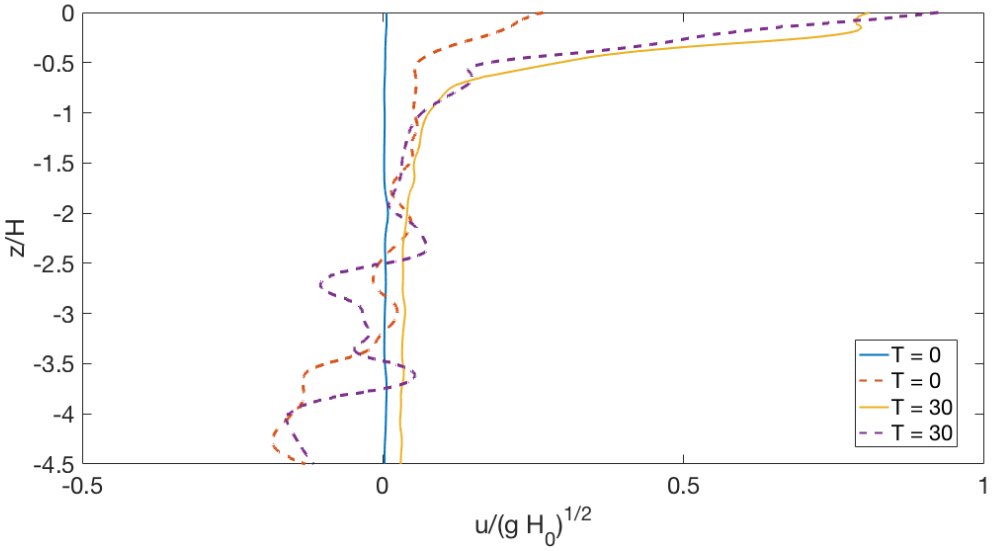

Figure 10.14 Vertical velocity profiles passing through the centre of the outflow vortex taken at the beginning and end of an experiment for the low I^* regime. Two sets of profiles are shown, with the solid line denoting no ambient turbulence and the dashed line a grid depth of $z = 16$ cm.

profile before the release of the freshwater current shows a positive velocity moving away from the source at the surface, with a negative velocity moving towards the source at depth. At $T = 30$ the negative velocity at depth remains, while the positive velocity at the surface increases in magnitude beyond that seen for a non-turbulent ambient. The depth of the profile seems to remain approximately the same.

Figure 10.15 displays the vertical velocity profiles through the vortex for the intermediate I^* regime. The lower value of g' leads to a deeper vortex than that seen for the low I^* regime with $H \sim 4.5$ cm. For the non-turbulent case the same features can be seen with a large positive velocity at the surface and a non-zero positive velocity beneath the vortex. With the introduction of turbulence, the initial profile at $T = 0$ also shows the same features as seen for the low I^* experiments, with a positive surface velocity and a negative velocity at large depths. At $T = 40$ the velocity profile looks very similar to that without turbulence, though with a generally larger magnitude of velocity. The profile also extends to a greater depth in the presence of turbulence.

The largest velocities are seen in the high I^* regime profiles which are displayed in figure 10.16. For this experiment the volume flux is larger which will cause an increase in the velocity as seen in the figure and also an increase in the vortex depth with $H \sim 12$ cm.

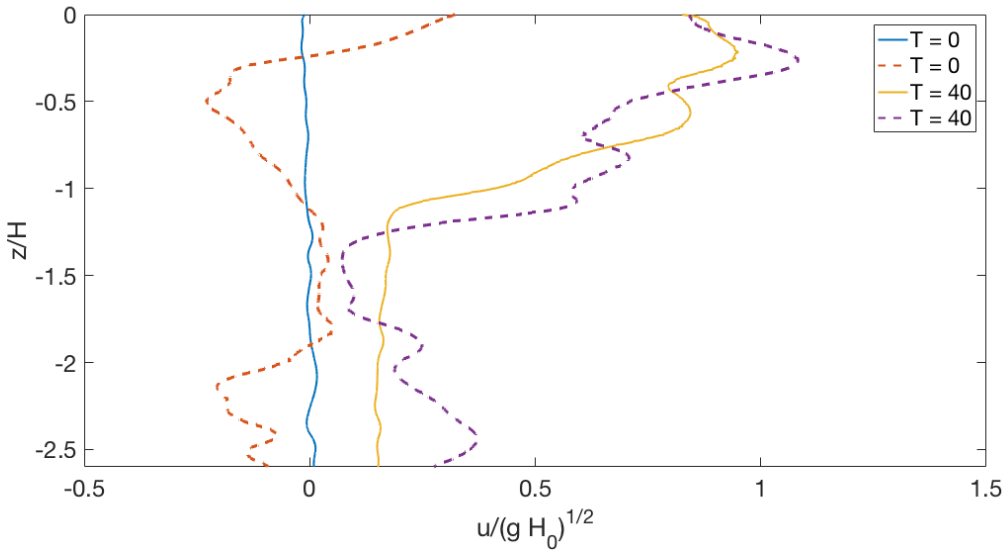

Figure 10.15 Vertical velocity profiles passing through the centre of the outflow vortex taken at the beginning and end of an experiment for the intermediate I^* regime. Two sets of profiles are shown, with the solid line denoting no ambient turbulence and the dashed line a grid depth of $z = 16$ cm.

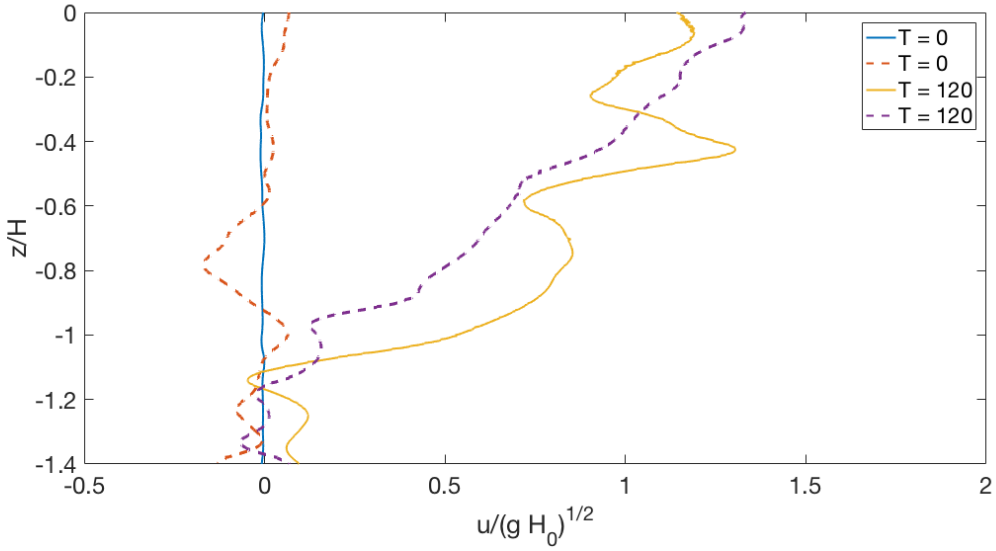

Figure 10.16 Vertical velocity profiles passing through the centre of the outflow vortex taken at the beginning and end of an experiment for the high I^* regime. Two sets of profiles are shown, with the solid line denoting no ambient turbulence and the dashed line a grid depth of $z = 16$ cm.

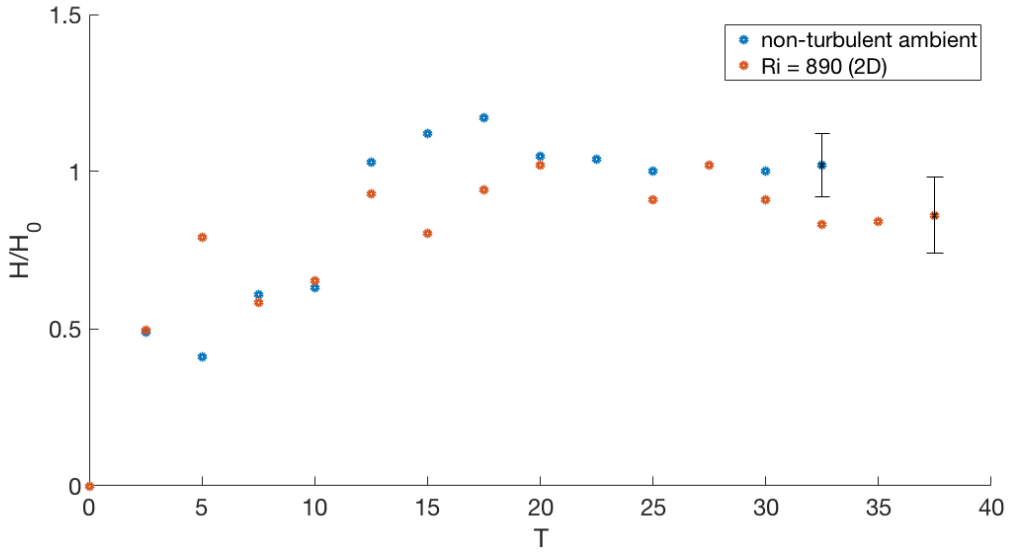

Figure 10.17 Estimates of the vortex maximum depth taken from the vertical velocity profiles versus time for the low I^* regime. Two sets of data are shown for no turbulence and a grid depth of 16 cm. The vortex depth is scaled with the source depth H_0.

For the non-turbulent case the velocity decreases from the surface with some fluctuations at depth. The peak in the velocity profile at a depth of $z/H \sim -0.4$ is not a persistent feature, with the profile generally fluctuating over time around its basic shape. With the addition of turbulence the magnitude of the velocity remains similar with a slight increase at the surface. The velocity decreases from the surface at a reasonably consistent rate to a depth of $z/H \sim -1$. The grid is located at a depth of $z/H \sim -1.25$ and reaches a depth of $z/H \sim -1.2$ at its maximum extent during oscillation. The velocity profile gives a mean velocity of approximately zero for the bottom part of the profile $z/H \lesssim -1.2$ at $T = 0$ and $T = 120$ due to the presence of the grid.

We now consider the change in the vortex depth over time, with and without the presence of turbulence in the ambient. Figure 10.17 plots the estimated vortex depth from the vertical velocity profiles for the low I^* regime experiments versus time. The same qualitative behaviour is also seen in the intermediate and high I^* regimes with the vortex depth increasing over time. The general effect of the turbulent ambient on the vortex depth for these regimes can be seen in figures 10.15 and 10.16. The data in figure 10.17 show that the vortex depth remains reasonably consistent with and without turbulence for $T > 12.5$, but is decreased by the presence of turbulence at later times.

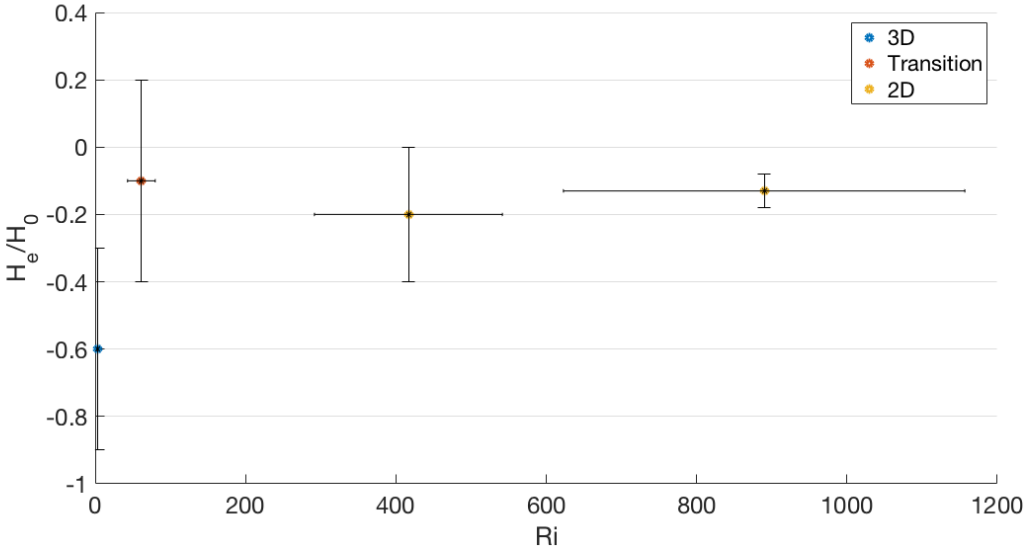

Figure 10.18 The estimated change in the vortex maximum depth, scaled with the source depth H_0, versus turbulent Richardson number Ri.

The estimated change in the vortex maximum depth H_e is plotted as a function of Ri in figure 10.18. The vortex depth decreases across all Richardson numbers and all turbulent regimes, though the lack of data points and large error bars make it difficult to draw any firm conclusions. The largest decrease occurs at the smallest value of Ri for the three-dimensional turbulence regime, with the decrease in the depth reduced as the value of Ri is increased and the turbulence transitions to become quasi-two-dimensional.

10.2.2.2 Vortex surface velocity field

As well as the vertical velocity profiles through the vortex centre presented in section 10.2.2.1, velocity profiles were also measured across the surface of the vortex. The profiles are taken along a horizontal cross-section through the vortex centre, beginning at the boundary and moving outwards. The light sheet for the PIV is at a depth of $\sim 0.5 - 1.5$ cm. The experimental parameters used are given in table 10.4 alongside the nature of the turbulence acting on the vortex at the surface for the two grid depths of $z = 16$ cm and $z = 8$ cm. The vortex velocity profile is predicted by the theory to be linear, with a value of zero at the centre that increases outwards with the radius (see chapters 5 and 7). We analyse the velocity profiles for three different cases of a non-turbulent ambient (solid line), a grid depth of $z = 16$ cm (dashed line) and a grid depth of $z = 8$ cm (dotted line) across the three I^* regimes. The

Exp. group	Q [cm^3 s^{-1}]	f [s^{-1}]	g' [cm s^{-2}]	I^*	$z = 16$ cm	$z = 8$ cm
1	48	0.5	13.1 - 15.9	0.37 - 0.42	2D	3D
2	48	1	13.1 - 15.5	0.76 - 0.84	2D	Transition
3	48	0.5	1.8 - 3.1	0.99 - 1.36	2D	3D
4	48	1	3.4 - 4.1	1.70 - 1.90	2D	Transition

Table 10.4 Experimental parameters for the experiments measuring the vortex velocity field and the vortex radius in a turbulent ambient.

boundary wall is located at $y/R_d = 0$.

Figure 10.19 displays the vortex velocity profiles for the low I^* regime. The profiles at $T = 0$ were measured at the beginning of an experiment before the release of the freshwater. We see an approximately linear profile for both the non-turbulent and turbulent experiments, with a negative velocity nearest to the wall and a positive velocity far from the wall signifying, the anticyclonic circulation of the vortex. The negative peak in the velocity is achieved away from the boundary with the velocity decreasing towards zero closer to the wall. For the non-turbulent case the velocity decreases to zero, while it remains finite with the presence of turbulence. The gradient of the profiles is similar for the turbulent and non-turbulent cases, though the centre of the vortex at zero velocity is closer to the wall for the turbulent ambient.

The vortex velocity profiles for the intermediate I^* regime are displayed in figure 10.20. For the two experiments with a turbulent ambient the initial profiles at $T = 0$ fluctuate around zero in comparison to the flat profile for the non-turbulent case. We see an approximately linear velocity profile across all three cases and as seen for the low I^* regime, the point of zero velocity moves closer to the boundary wall as the turbulence intensity is increased. The gradient of the profiles also seems to increase slightly with stronger turbulence, while the maximum velocity decreases for the mixing grid depth of $z = 8$ cm compared to the other two cases of weak or no turbulence.

The final vortex velocity profiles are displayed in figure 10.21 for the high I^* regime. For the non-turbulent case the profile is approximately linear with a maximum negative velocity close to the wall that increases at an approximately constant rate across the diameter of the vortex. For a grid depth of $z = 16$ cm we see reduced velocities in general and the profile oscillates around a base linear shape. At a grid depth of $z = 8$ cm, the profile is no longer linear and has lost most of its structure. The velocity is positive across the full width of the

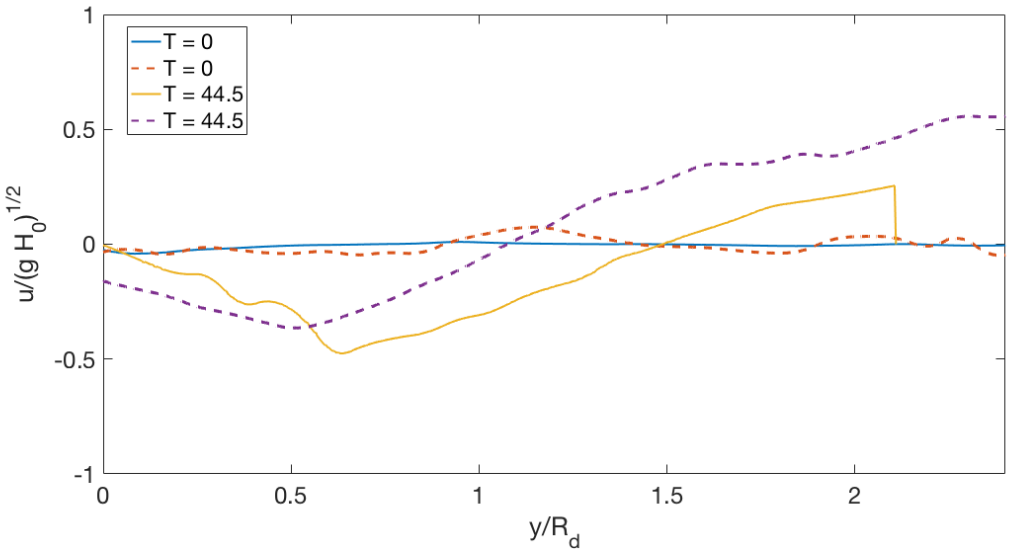

Figure 10.19 Velocity profiles across the surface of the outflow vortex taken at the beginning and end of an experiment for the low I^* regime. Two sets of profiles are shown, with the solid line denoting no ambient turbulence and the dashed line a grid depth of $z = 16$ cm. The boundary wall is located at $y/R_d = 0$.

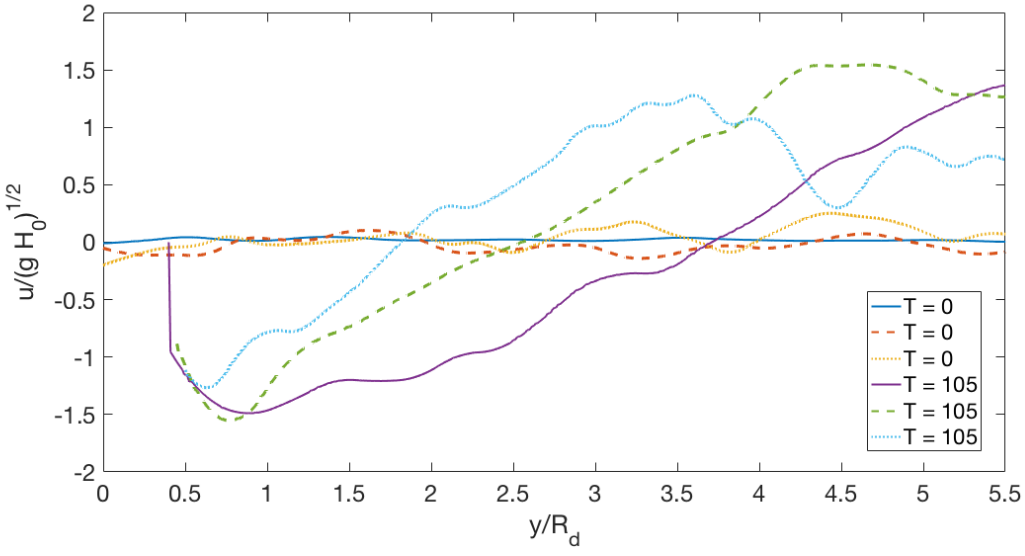

Figure 10.20 Velocity profiles across the surface of the outflow vortex taken at the beginning and end of an experiment for the intermediate I^* regime. Three sets of profiles are shown, with the solid line denoting no ambient turbulence, the dashed line a grid depth of $z = 16$ cm and the dotted line a grid depth of $z = 8$ cm. The boundary wall is located at $y/R_d = 0$.

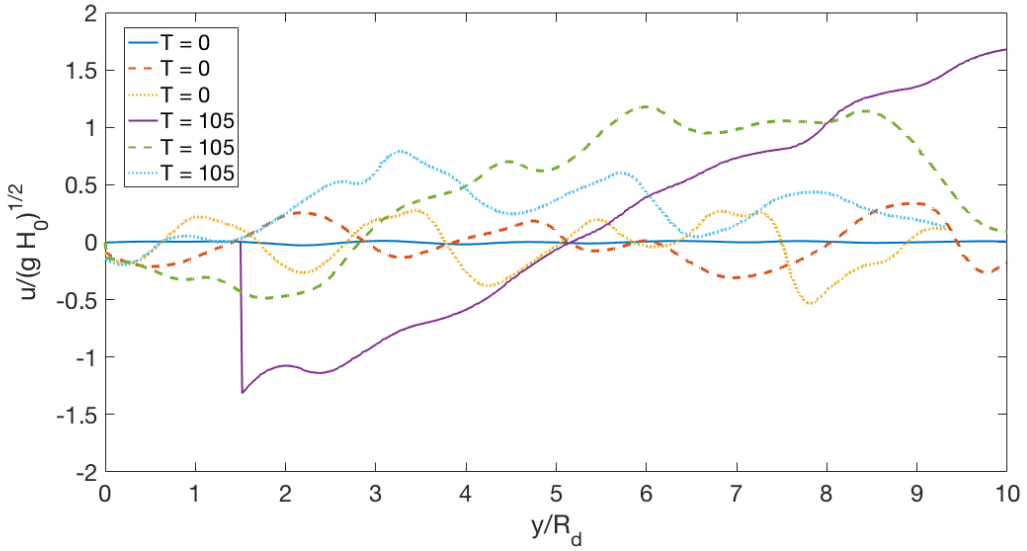

Figure 10.21 Velocity profiles across the surface of the outflow vortex taken at the beginning and end of an experiment for the high I^* regime. Three sets of profiles are shown, with the solid line denoting no ambient turbulence, the dashed line a grid depth of $z = 16$ cm and the dotted line a grid depth of $z = 8$ cm. The boundary wall is located at $y/R_d = 0$.

vortex suggesting that its formation has been significantly disrupted by the turbulence. The Richardson number is low with a value of $Ri = 56$ at the surface and a higher value at depth. We saw in section 10.2.2.1 that the vortex depth is large for the high I^* experiments and thus it seems here that the turbulence is of sufficient strength that it is almost able to halt the formation of the outflow vortex.

In summary, the vortex velocity profiles in general demonstrate the same features for a turbulent ambient as seen for a quiescent ambient. The circulation in the vortex remains anticyclonic and the velocity profile remains approximately linear in most cases. For a turbulent ambient the point of zero velocity at the vortex centre appears to move closer to the boundary wall, suggesting a smaller vortex size. This will be investigated in the next section.

10.2.2.3 Vortex radius

In the same way that the vertical velocity profiles enabled estimates of the vortex depth, the horizontal profiles allow estimates of the vortex radius to be made. The radius is estimated as the distance between the point of maximum velocity and the point of zero velocity. This assumes a linear profile, which is verified by the velocity profiles in section 10.2.2.2. For

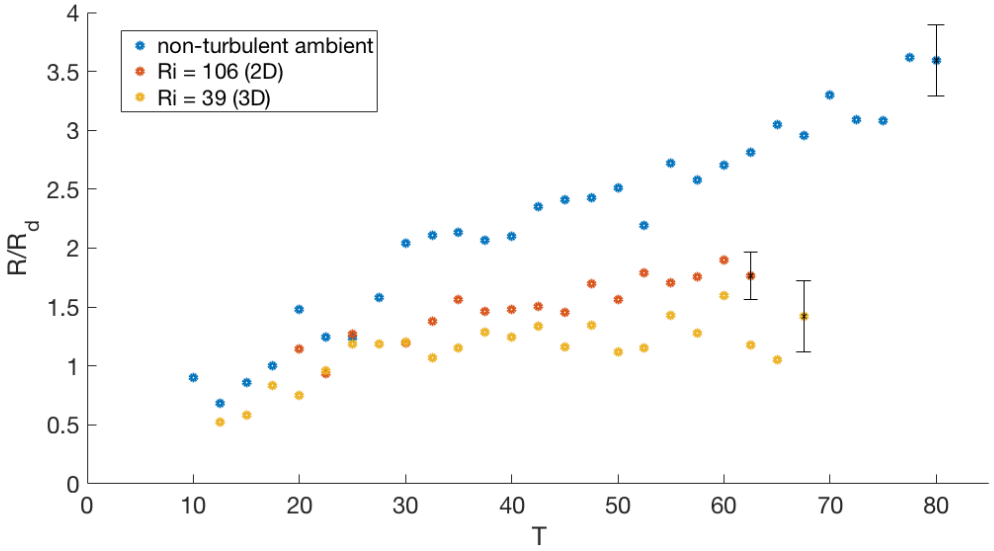

Figure 10.22 Estimates of the vortex radius taken from the across vortex velocity profiles, versus time for the intermediate I^* regime. Three sets of data are shown for no turbulence, a grid depth of 16 cm and a grid depth of $z = 8$ cm.

full details of the method see chapter 2. The vortex radius estimates for the intermediate I^* regime over time are displayed in figure 10.22. The data show a decrease in the vortex radius as the strength of the ambient turbulence is increased. Both experiments with a turbulent ambient have a relatively low Richardson number with the three-dimensional turbulence showing the largest decrease in the radius. For the low and high I^* regimes we see the same qualitative behaviour as in figure 10.22 with the vortex radius increasing over time, but with a reduced magnitude in the presence of turbulence. The general effect of the turbulence on the vortex radius in these regimes can be seen in the velocity profiles in figures 10.19 and 10.21.

Figure 10.23 plots the estimated change in the vortex radius R_e across all of the I^* regimes versus the turbulent Richardson number. As with previous flow properties, the change in the vortex radius is calculated as the value for a turbulent ambient minus the value for a quiescent ambient. The data in figure 10.23 show an interesting trend, with a decrease in the vortex radius at small Ri gradually changing to an increase in the radius as the value of Ri is increased. This is the same trend as seen for the current width in section 10.2.1.2, but the correlation is stronger. The structure of the turbulence also appears to have an effect on the change seen in the vortex radius, with the largest reductions occuring for three-dimensional and transitional turbulence, whilst the largest increases are seen for turbulence that has a

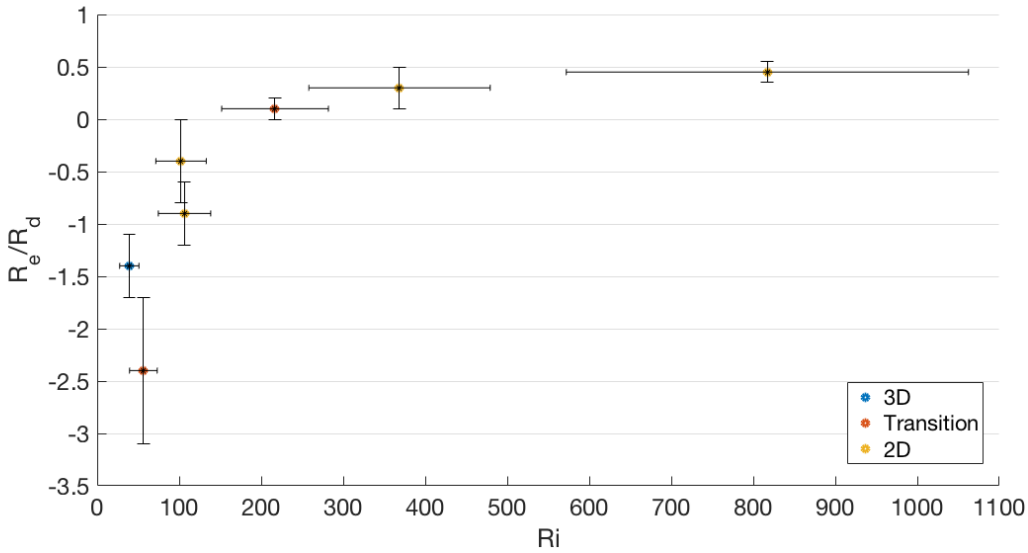

Figure 10.23 The estimated change in the vortex radius R_e versus turbulent Richardson number Ri.

quasi-two-dimensional structure.

10.2.2.4 Discussion

The effects of a turbulent ambient on the vortex properties shows both similarities and differences to the effects seen on the current properties in section 10.2.1. The similarities occur with the effect of the turbulence on the vortex radius, where a decrease is seen for small Ri and three-dimensional turbulence and an increase occurs for larger Ri and turbulence that is quasi-two-dimensional in nature. This is the same behaviour that occurred with the current width where the turbulence was also acting on a horizontal density interface. In the 3D regime the turbulence acts to disrupt the formation of the outflow vortex preventing it from expanding at its normal rate seen in a quiescent ambient by strengthening the interface. For turbulence in the 2D regime we see the occurrence of cyclonic eddies at the surface that act to entrain fluid across the horizontal interface which increases the vortex size.

The vortex depth decreases with the introduction of turbulence into the ambient, which is in contrast to the increase seen for the current depth, despite both features occurring at a vertical density interface. The increase in the vortex depth represents what is perhaps the expected behaviour with a scouring of the interface from below by the turbulence causing it to retreat upwards. This behaviour also adds strength to the hypothesis that the increase seen

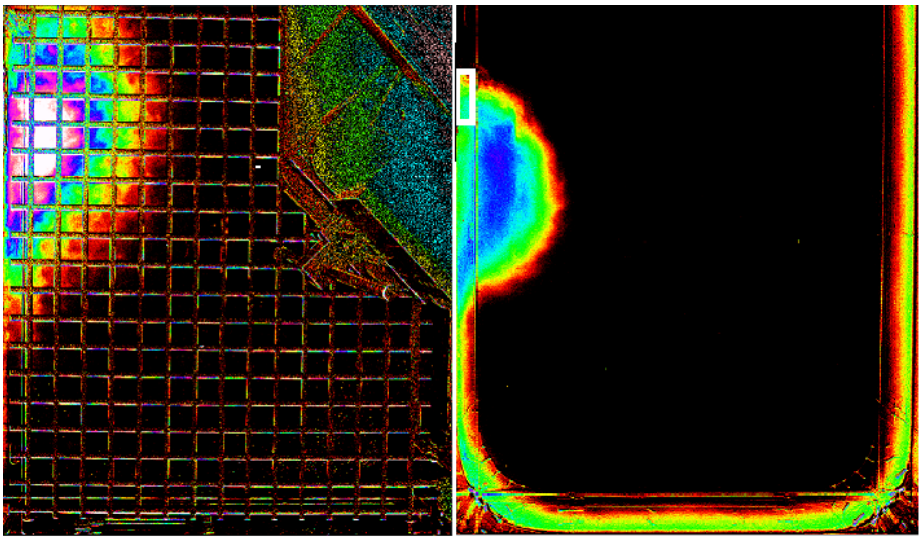

Figure 10.24 A plan view of two experiments in the intermediate I^* regime for an outflow with the same parameters, with (left-hand image) and without (right-hand image) turbulence in the ambient. The depth of the freshwater is indicated by the colour scale with white the deepest and red the shallowest. The scale is the same for both images. The location of the source is indicated by a white box and is also the same for both images.

in the current depth is likely caused by the mean flow along the tank boundary.

10.2.3 Stopping the current

At sufficiently high levels of turbulence the propagation of the boundary current is halted entirely as the freshwater leaves the source and is immediately and vigorously mixed into the saltwater ambient. In extreme cases at small Richardson number and low volume flux, the freshwater is seen to move to the left of the source. The combination of the strong turbulence and low volume flux provides a possible explanation for the observations in the simulations of Lacroix et al. (2004), where river water from the Rhine was identified at the French-Belgian coastal border, which lies to the left of the Rhine outflow. An example image of an experiment where the current was stopped for a grid depth of 4 cm is shown in figure 10.24. A plan view taken from an experiment with the same parameter values, but a non-turbulent ambient is also shown for comparison in the right-hand image. The freshwater outflow is pushed to the left of the source (indicated by the white box) and deepens significantly compared to the case of a quiescent ambient.

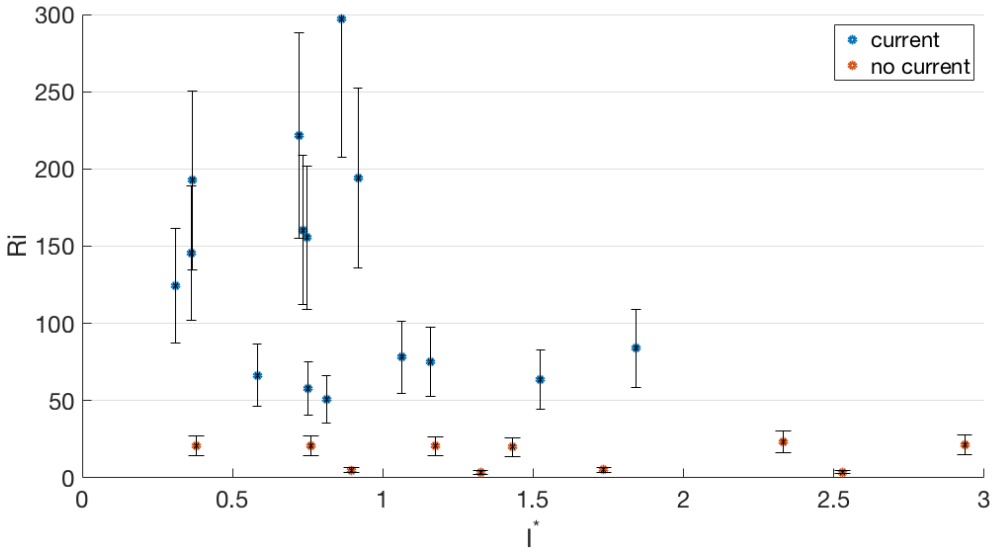

Figure 10.25 The turbulent Richardson number versus I^* for the experiments with a turbulent ambient. The experiments are divided into two groups according to whether or not the grid-generated turbulence was able to stop the propagation of the boundary current.

Experiments were conducted across a large range of parameters to determine a critical parameter value at which the turbulence was able to stop the propagation of the boundary current. The parameter ranges are as follows: $0.25 \leq f \leq 1.5$ s^{-1}, $16.5 \leq Q \leq 40$ cm^3 s^{-1} and $1.5 \leq g' \leq 64.6$ cm s^{-2}, with the grid depth ranging from $z = 4 - 16$ cm. The experiments cover the three I^* regimes with $0.31 \leq I^* \leq 2.94$. The turbulent Richardson number is plotted versus I^* in figure 10.25, with the legend identifying whether or not the current was stopped by the turbulence. The Ri values are calculated at the surface of the flow and therefore represent the maximum value, which will decrease with depth. The data show a clear trend with the lowest values of the Richardson number able to stop the current progression. For low Ri the intensity of the turbulence is strong enough to mix the freshwater as it leaves the outflow and prevent the formation of the boundary current. As the value of Ri is increased the current is able to form and propagates around the perimeter of the tank. The data suggest a critical Ri value of $25 \lesssim Ri_c \lesssim 50$.

10.3 Discussion

Experiments were conducted where the freshwater outflow entered into a rotating non-quiescent saltwater ambient where a mixing grid was used to generate turbulence. The struc-

ture of the turbulence was controlled via the mixing grid depth, with shallow depths resulting in three-dimensional turbulence and larger grid depths producing quasi-two-dimensional turbulence. The strength of the turbulence was quantified via a turbulent Richardson number. The effect of the turbulent ambient on the flow properties was investigated in the low, intermediate and high I^* parameter regimes.

A cyclonic mean flow was found to occur along the tank boundary for rotating turbulence, which acted to oppose the propagation of the current. The effect of the mean flow could be seen in the current velocity measurements with a general reduction in the peak velocity for a turbulent ambient compared to the quiescent case. Evidence was also seen of other possible mechanisms at work, with the current velocity decreasing by up to three times the magnitude of the mean flow at small Ri, which suggests a possible role of mixing in slowing the progression of the current. The maximum current depth was found to increase in the presence of a turbulent ambient which is perhaps the opposite of the expected behaviour based on observations in the literature. It was hypothesized that the mean flow was likely the cause of the depth increase, which was supported by the measurements of the vortex depth which decreased in the presence of turbulence. This followed the expected pattern of behaviour with the turbulence scouring the density interface from below causing it to retreat upwards.

The structure of the turbulence appeared to play a key role in the effect that it had on the current width. For three-dimensional turbulence the current width was reduced, most likely due to a strenghtening of the horizontal interface, while for quasi-two-dimensional turbulence the current width increased, possibly via entrainment from cyclonic eddies at the surface of the flow. The same effects were seen for the vortex radius, with 3D turbulence reducing the radius and 2D turbulence causing it to increase.

Overall, the effect of a turbulent ambient on the flow properties appears to be dependent on the structure of the turbulence. For three-dimensional turbulence we see a strengthening of density interfaces causing a decrease in the vortex depth, vortex radius and the current width. For river outflows into shallow seas we would therefore expect observational measurements to demonstrate a smaller river plume than is predicted by the theory. As the turbulence transitions to quasi-two-dimensional the effect of the turbulence on horizontal interfaces appears to change, with possible entrainment by the cyclonic eddies causing the interface to expand into the turbulent region. This leads to an increase in the vortex radius and current

width. In the coastal currents of Norway and California, for example, the observational measurements are therefore likely to suggest a larger current than is predicted by the theory.

The results obtained in this chapter are very interesting and leave several unanswered questions that provide possible avenues for future study. One possible example would be to remove the mean flow from the tank to allow the effect of the turbulence on the current depth and the current velocity to be analysed in more detail. It would be particularly interesting to see whether the current depth still increased due to the turbulence and the possible method of vortex stretching or whether it decreased as seen in the vortex depth via a scouring of the interface.

Chapter 11

Summary

At the beginning of this thesis, three unanswered questions were presented that we believed were critical to improving our understanding of the dynamics of a buoyant outflow entering into a rotating environment. These questions served as the motivation for this work and here we outline the key findings of this study in relation to the original questions.

First, what is the effect of the finite potential vorticity of the outflow on the properties of the outflow vortex and the boundary current? Laboratory experiments were conducted where the freshwater outflow was discharged horizontally and with a finite value of potential vorticity to provide a better representation of the natural environment. In chapter 3 we presented a steady state model for the boundary current formed from an outflow of finite PV which was compared to the zero PV model of Thomas and Linden (2007). The current depth remained unchanged by the addition of finite PV, while the current width was seen to increase and the current velocity to decrease for an increasing value of PV. The model was then compared with experimental data in chapter 4 and the effect of the finite value of PV shown to only be important below a critical parameter value. The zero PV model of Thomas and Linden (2007) was able to capture the key flow dynamics above a critical value of $Ro/Fr_c = 1/\sqrt{2}$, which is equal to the constant value predicted by the zero PV model. In chapter 5 the vortex growth model of GL was extended to the case of a finite PV outflow. The vortex radius increased and the vortex maximum depth decreased as the value of PV was increased. The presence of the boundary wall alongside the source was incorporated into the new model by assuming a semi-circular vortex shape, with the loss of mass to the boundary current accounted for by the reduction in the vortex volume. This model and the vortex growth model of NP were compared with experimental results in chapter 6. The time-dependent growth rates

of the vortex maximum depth and radius showed good agreement with the theoretical models.

Second, what role does the presence of the outflow vortex play in determining the behaviour of the current? Analysis of the vortex velocity profiles in chapter 6 revealed that the vorticity ratio decreased with time. This led to the introduction of a time-dependent vorticity model in chapter 7 which demonstrated two key roles played by the outflow vortex. The model showed that the vorticity ratio must decrease over time, while the vortex depth increases, in order to conserve PV. Once the vorticity ratio reaches zero corresponding to a limiting vortex depth, the excess fluid entering into the vortex is then absorbed by the radius which continues to grow at a constant rate. This is of vital importance to ensure that PV is conserved and it enables the current to continue to propagate by supplying it with a non-zero velocity which is fixed by the vortex velocity field via a Bernoulli condition. The time-dependent model was compared with experimental results in chapter 8 and promising qualitative agreement was seen between the model and the data.

Third, what is the effect of background turbulence on the flow properties? An oscillating grid was added to the experimental setup to produce a turbulent ambient and thus a more realistic simulation of the natural environment in the laboratory. In chapter 9 the properties of the grid-generated turbulence were shown to be similar to those seen in previous studies both with and without rotation. In chapter 10 the effect of a turbulent ambient on the flow properties was shown to be dependent on the structure of the turbulence. For three-dimensional turbulence we saw the expected behaviour with a strengthening of density interfaces causing a decrease in the vortex depth, vortex radius and the current width. For river outflows into shallow seas we would therefore expect observational measurements to demonstrate a smaller river plume than is predicted by the theory. As the turbulence transitioned to quasi-two-dimensional the effect of the turbulence on horizontal interfaces appeared to change, with possible entrainment by cyclonic eddies causing the interface to expand into the turbulent region, leading to an increase in the vortex radius and current width. This means that in the coastal currents of Norway and California for example, where large surface eddies are observed, the field measurements are likely to suggest a larger current than is predicted by the theory.

Having improved our understanding of the fundamental processes at work in outflow regions, we now apply the mathematical models derived in this thesis to the real-world environments of the Rhine outflow and the Norwegian coastal current to demonstrate their

robustness. The Rhine has a mean discharge of 2000 $m^3\ s^{-1}$ which enters into the southern North Sea and turns to the right under the Coriolis force to flow along the Dutch coast. It is located in water of depth $10-20$ m and exhibits a salinity deficit $\Delta S \sim 4$ near to the coast. It extends ~ 20 km from the coast and more than 200 km in the along coast direction (Simpson and Sharples, 2012). The mouth of the Rhine has a width of $1500-4000$ m and a depth of $10-20$ m. We estimate the reduced gravity to be $g' \sim 0.04$ m s^{-2} and the Coriolis parameter $f \sim 1\times10^{-4}\ s^{-1}$. Using these values the theory predicts a current depth of $\sim 5-10$ m, a current width of $\sim 10-20$ km and a current velocity of $\sim 0.25-0.5$ m s^{-1}. These values show agreement with the observations of Simpson (1997). Fisher et al. (2002) record a peak negative value in the alongshore velocity of the current on the order of -0.5 m s^{-1}. This means that the tidal flow is moving against the current which provides a possible explanation for the movement of water from the Rhine to the left of the outflow as seen in the simulations of Lacroix et al. (2004). Similar behaviour was also seen in our experiments with strong ambient turbulence in section 10.2.3.

The Norwegian coastal current transports up to 3 Sv of brackish water from the Baltic Sea along the Norwegian coast for ~ 1000 km. The current is ~ 75 km wide and flows over the deep Norwegian trench (> 200 m) meaning that it is unaffected by frictional stresses at the seabed (Simpson and Sharples, 2012). Measurements by Rodhe (1987) estimate the depth of the current to be ~ 100 m. Satellite imagery (Mork, 1981) shows the occurrence of large eddies with a scale of ~ 80 km which tend to broaden the current. The source of the current is the Skagerrak which has an average depth of ~ 200 m and a width of $\sim 80-140$ km. The salinity deficit between the current and the ocean gives $g' \sim 0.05$ m s^{-2}, with the Coriolis force $f \sim 1\times10^{-4}\ s^{-1}$. The theory predicts a current depth of ~ 100 m, a current width of ~ 50 km and a current velocity of ~ 1 m s^{-1}, which are all in agreement with observations. Johannessen et al. (1989) measured the Rossby number of cyclonic eddies along the Norwegian coast and found the range $0.16 \leq Ro \leq 0.25$. This is very similar to the values acheived in our experiments conducted in chapter 10 for quasi-two-dimensional turbulence with $0.16 \leq Ro \leq 0.19$. In our experiments we saw an increase in the current width for 2D turbulence, possibly due to entrainment by the surface eddies. This behaviour is in agreement with the observed current width of ~ 75 km for the Norwegian coastal current which is larger than the the theoretically predicted value of ~ 50 km.

Despite having successfully addressed three previously unanswered questions in the field, we have uncovered many new questions that will require further investigation in future

studies. We will outline the key areas that have been identified for possible future work beginning with modifications to the current experimental setup used in this study. Two possible modifications were identified in this thesis in sections 4.3.2 and 10.2.1. Firstly, more accurate measurements of the source vorticity field are required in order to provide initial values which can be fed into the theoretical models. Here, the vorticity field was measured outside of the source opening (at a distance of $\sim 0.1 - 0.2$ cm from the source) due to experimental limitations, however, with the new setup described in section 4.3.2 measurements will be able to be made inside the source structure which will provide much better insight into the flow conditions at the source. Secondly, the mean flow generated by the rotating turbulence setup may be removed in future experiments using the setup described in section 10.2.1 which will enable the effects of the rotating background turbulence on the current depth and current velocity to more accurately be identified. In particular, by removing the mean flow we would be able to investigate whether the increase in the current depth still occurred in the presence of turbulence and thus identify the mechanism by which the turbulence is acting on the interface. For exmaple, were the depth still to increase, it would suggest possible vortex stretching due to the two-dimensional nature of the rotating turbulence, whilst a decrease in the current depth would suggest a scouring of the interface from three-dimensional turbulence.

The later sections of work presented in this thesis in chapters $7 - 10$ provide two possible avenues for further investigation. The time-dependent model introduced in chapter 7 was compared with the experimental data in chapter 8 to assess the capability of the model to capture the first-order physics of the flow. The analysis of the model performance was carried out qualitatively as we were concentrating on a proof-of-principle style comparison between the model and the data as a preliminary for futrue work. The next stage of the study would be to conduct a full statistical analysis of the capability of the time-dependent model to capture the flow behaviour and ultimately refine the model further. Possible refinements include investigation of a non-circular vortex shape guided by the experimental results of section 8.2.4 where the radius in the direction perpendicular to the boundary was seen to be approximately half of the parallel radius. Furthermore, the results presented in section 8.2.5.2 seemed to suggest that a different choice of finite wall velocity is required in the time-dependent model to accurately capture the change in the current width over time. A constant fraction of the predicted current velocity is one possible alternative that may provide improved agreement between the model and the data.

Finally, in chapters 9 – 10 experimental results are presented where background turbulence is introduced to the saltwater ambient. These experiments are preliminary as the setup had not previously been investigated and thus there are several open questions that remain. Further experiments using the setup that explore a greater range of experimental parameters, alongside the develpment of a theoretical model to incorporate the effects of turbulence on the flow features would provide a plethora of further research questions that could be explored in future studies. For example, the change in the effect that the turbulence was seen to have on the current width depending on whether its structure was two or three-dimensional is of particular interest, with 2D turbulence leading to an increase in width and 3D a decrease. Identifying the critical point at which the switch in behaviour occurs and also obtaining more information about the mechanism by which the current width is increased by possible entrainment from cyclonic eddies would be worthwhile endeavours.

Overall, this work has furthered the understanding of the dynamics of the spread of buoyant water into a rotating environment by investigating three previously unanswered questions in the field. We have extended several mathematical models to new flow configurations and constructed a new model that provides improved insight into the role of a key feature of the flow in the form of the outflow vortex. The models replicate well the results seen in laboratory experiments and can be applied to real-world environments to give results that agree with observations. Many questions remain unanswered, however, and hopefully the results presented here will encourage further research in this area as we strive to improve our scientific understanding of the world around us.

References

Avicola, G. and Huq, P. (2002). Scaling analysis for the interaction between a buoyant coastal current and the continental shelf: Experiments and observations. *Journal of Physical Oceanography*, 32(11):3233–3248.

Avicola, G. and Huq, P. (2003a). The characteristics of the recirculating bulge region in coastal buoyant outflows. *Journal of Marine Research*, 61(4):435–463.

Avicola, G. and Huq, P. (2003b). The role of outflow geometry in the formation of the recirculating bulge region in coastal buoyant outflows. *Journal of Marine Research*, 61(4):411–434.

Batchelor, G. K. (2000). *An introduction to fluid dynamics*. Cambridge University Press.

Bowman, M. J. and Iverson, R. L. (1978). Estuarine and plume fronts. In *Oceanic fronts in coastal processes*, pages 87–104. Springer.

Brink, K., Beardsley, R., Niiler, P. P., Abbott, M. R., Huyer, A., Ramp, S., Stanton, T., and Stuart, D. (1991). Statistical properties of near surface currents in the California coastal transition zone. *Journal of Geophysical Research*, 96(C8):14693–14706.

Cenedese, C. and Dalziel, S. (1998). Concentration and depth fields determined by the light transmitted through a dyed solution. In *Proceedings of the 8th International Symposium on Flow Visualization*, volume 8.

Conley, D. J., Björck, S., Bonsdorff, E., Carstensen, J., Destouni, G., Gustafsson, B. G., Hietanen, S., Kortekaas, M., Kuosa, H., Markus Meier, H., et al. (2009). Hypoxia-related processes in the Baltic Sea. *Environmental Science & Technology*, 43(10):3412–3420.

Conley, D. J., Carstensen, J., Aigars, J., Axe, P., Bonsdorff, E., Eremina, T., Haahti, B.-M., Humborg, C., Jonsson, P., Kotta, J., et al. (2011). Hypoxia is increasing in the coastal zone of the Baltic Sea. *Environmental Science & Technology*, 45(16):6777–6783.

Dalziel, S. (2006). Digiflow user guide. *DL Research Partners, Version*, 1.

Davies, P., Jacobs, P., and Mofor, L. (1993). A laboratory study of buoyant fresh-water boundary currents in tidal cross-flows. *Oceanologica Acta*, 16(5-6):489–503.

De Boer, G. J., Pietrzak, J. D., and Winterwerp, J. C. (2008). Using the potential energy anomaly equation to investigate tidal straining and advection of stratification in a region of freshwater influence. *Ocean Modelling*, 22(1):1–11.

d'Hières, G. C., Didelle, H., and Obaton, D. (1991). A laboratory study of surface boundary currents: Application to the Algerian Current. *Journal of Geophysical Research: Oceans*, 96(C7):12539–12548.

Fernando, H. J. (1991). Turbulent mixing in stratified fluids. *Annual Review of Fluid Mechanics*, 23(1):455–493.

Fisher, N., Simpson, J., and Howarth, M. (2002). Turbulent dissipation in the Rhine ROFI forced by tidal flow and wind stress. *Journal of Sea Research*, 48(4):249–258.

Fleury, M., Mory, M., Hopfinger, E., and Auchere, D. (1991). Effects of rotation on turbulent mixing across a density interface. *Journal of Fluid Mechanics*, 223:165–191.

Fong, D. A. and Geyer, W. R. (2002). The alongshore transport of freshwater in a surface-trapped river plume. *Journal of Physical Oceanography*, 32(3):957–972.

Gill, A., Green, J., and Simmons, A. (1974). Energy partition in the large-scale ocean circulation and the production of mid-ocean eddies. In *Deep Sea Research and Oceanographic Abstracts*, volume 21, pages 499–528. Elsevier.

Gill, A., Smith, J., Cleaver, R., Hide, R., and Jonas, P. (1979). The vortex created by mass transfer between layers of a rotating fluid. *Geophysical & Astrophysical Fluid Dynamics*, 12(1):195–220.

Gill, A. E. (1982). *Atmosphere-Ocean Dynamics*, volume 30. Academic Press.

Griffiths, R. (1986). Gravity currents in rotating systems. *Annual Review of Fluid Mechanics*, 18(1):59–89.

Griffiths, R. and Hopfinger, E. (1983). Gravity currents moving along a lateral boundary in a rotating fluid. *Journal of Fluid Mechanics*, 134:357–399.

Griffiths, R. and Linden, P. (1981). The stability of vortices in a rotating, stratified fluid. *Journal of Fluid Mechanics*, 105:283–316.

Hacker, J. and Linden, P. (2002). Gravity currents in rotating channels. Part 1. Steady-state theory. *Journal of Fluid Mechanics*, 457:295–324.

Hickey, B., Pietrafesa, L. J., Jay, D. A., and Boicourt, W. C. (1998). The Columbia River plume study: Subtidal variability in the velocity and salinity fields. *Journal of Geophysical Research*, 103(C5):10339–10368.

Hopfinger, E., Griffiths, R., and Mory, M. (1983). The structure of turbulence in homogeneous and stratified rotating fluids. *Journal de Mécanique Théorique et Appliquée*, pages 21–44.

Hopfinger, E. and Toly, J.-A. (1976). Spatially decaying turbulence and its relation to mixing across density interfaces. *Journal of Fluid Mechanics*, 78(01):155–175.

Horner, A., Fong, D., Koseff, J., Maxworthy, T., and Monismith, S. (2000). The control of coastal current transport. In *Fifth International Symposium on Stratified Flows*, volume 2, pages 865–870.

Horner-Devine, A. R. (2004). *The dynamics of buoyant, rotational river plumes*. PhD thesis, Stanford University.

Horner-Devine, A. R., Fong, D. A., Monismith, S. G., and Maxworthy, T. (2006). Laboratory experiments simulating a coastal river inflow. *Journal of Fluid Mechanics*, 555:203–232.

Horner-Devine, A. R., Hetland, R. D., and MacDonald, D. G. (2015). Mixing and transport in coastal river plumes. *Annual Review of Fluid Mechanics*, 47:569–594.

Jacobs, W. (2004). *Modelling the Rhine river plume*. PhD thesis, TU Delft, Delft University of Technology.

Johannessen, J. A., Sandven, S., Lygre, K., Svendsen, E., and Johannessen, O. (1989). Three-dimensional structure of mesoscale eddies in the Norwegian coastal current. *Journal of Physical Oceanography*, 19(1):3–19.

Kawasaki, Y. and Sugimoto, T. (1984). *Experimental studies on the formation and degeneration processes of the Tsugaru warm gyre*, volume 39. Elsevier Oceanographic Series.

Lacroix, G., Ruddick, K., Ozer, J., and Lancelot, C. (2004). Modelling the impact of the Scheldt and Rhine/Meuse plumes on the salinity distribution in Belgian waters (southern North Sea). *Journal of Sea Research*, 52(3):149–163.

Lentz, S. J. and Helfrich, K. R. (2002). Buoyant gravity currents along a sloping bottom in a rotating fluid. *Journal of Fluid Mechanics*, 464:251–278.

Linden, P. F. (1979). Mixing in stratified fluids. *Geophysical & Astrophysical Fluid Dynamics*, 13(1):3–23.

Linden, P. F. and Simpson, J. E. (1988). Modulated mixing and frontogenesis in shallow seas and estuaries. *Continental Shelf Research*, 8(10):1107–1127.

Martin, J. and Lane-Serff, G. (2005). Rotating gravity currents. Part 1. Energy loss theory. *Journal of Fluid Mechanics*, 522:35–62.

Martin, J., Smeed, D., and Lane-Serff, G. (2005). Rotating gravity currents. Part 2. Potential vorticity theory. *Journal of Fluid Mechanics*, 522:63–89.

Mcdougall, T. J. (1979). Measurements of turbulence in a zero-mean-shear mixed layer. *Journal of Fluid Mechanics*, 94(03):409–431.

Mork, M. (1981). Circulation phenomena and frontal dynamics of the Norwegian coastal current. *Philosophical Transactions of the Royal Society of London A: Mathematical, Physical and Engineering Sciences*, 302(1472):635–647.

Münchow, A. and Garvine, R. W. (1993a). Buoyancy and wind forcing of a coastal current. *Journal of Marine Research*, 51(2):293–322.

Münchow, A. and Garvine, R. W. (1993b). Dynamical properties of a buoyancy-driven coastal current. *Journal of Geophysical Research: Oceans*, 98(C11):20063–20077.

NERC (1987). *The North Sea Project*. British Oceanographic Data Centre.

Nof, D. and Pichevin, T. (1999). The establishment of the Tsugaru and the Alboran gyres. *Journal of Physical Oceanography*, 29(1):39–54.

Nof, D. and Pichevin, T. (2001). The ballooning of outflows. *Journal of Physical Oceanography*, 31(10):3045–3058.

Nof, D., Pichevin, T., and Sprintall, J. (2002). "Teddies" and the origin of the Leeuwin Current. *Journal of Physical Oceanography*, 32(9):2571–2588.

Nof, D., Van Gorder, S., and Pichevin, T. (2004). A different outflow length scale? *Journal of Physical Oceanography*, 34(4):793–804.

Nokes, R. (1988). On the entrainment rate across a density interface. *Journal of Fluid Mechanics*, 188:185–204.

Oey, L.-Y. and Chen, P. (1992). A nested-grid ocean model: With application to the simulation of meanders and eddies in the Norwegian coastal current. *Journal of Geophysical Research: Oceans*, 97(C12):20063–20086.

OSPAR (2010). *OSPAR Quality Status Report 2010*. OSPAR Comission. London.

Otto, L., Zimmerman, J., Furnes, G., Mork, M., Saetre, R., and Becker, G. (1990). Review of the physical oceanography of the North Sea. *Netherlands Journal of Sea Research*, 26(2):161–238.

Pichevin, T. and Nof, D. (1997). The momentum imbalance paradox. *Tellus A*, 49(2):298–319.

Rennie, S., Largier, J., and Lentz, S. (1999). Observations of low-salinity coastal pulses downstream of Chesapeake Bay. *J. Geophys. Res*, 104(18):227–18.

Rodhe, J. (1987). The large-scale circulation in the Skagerrak; interpretation of some observations. *Tellus A*, 39(3):245–253.

Simpson, J. (1997). Physical processes in the ROFI regime. *Journal of Marine Systems*, 12(1):3–15.

Simpson, J., Sharples, J., and Rippeth, T. (1991). A prescriptive model of stratification induced by freshwater runoff. *Estuarine, Coastal and Shelf Science*, 33(1):23–35.

Simpson, J. H., Crawford, W. R., Rippeth, T. P., Campbell, A. R., and Cheok, J. V. (1996). The vertical structure of turbulent dissipation in shelf seas. *Journal of Physical Oceanography*, 26(8):1579–1590.

Simpson, J. H. and Sharples, J. (2012). *Introduction to the physical and biological oceanography of shelf seas*. Cambridge University Press.

Stern, M. E., Whitehead, J. A., and Hua, B.-L. (1982). The intrusion of a density current along the coast of a rotating fluid. *Journal of Fluid Mechanics*, 123:237–265.

Sturges, W. (1994). The frequency of ring separations from the Loop Current. *Journal of Physical Oceanography*, 24(7):1647–1651.

Thomas, P. and Linden, P. (1998). A bi-modal structure imposed on gravity driven boundary currents in rotating systems by effects of the bottom topography. *Experiments in Fluids*, 25(5-6):388–391.

Thomas, P. J. and Linden, P. (2007). Rotating gravity currents: small-scale and large-scale laboratory experiments and a geostrophic model. *Journal of Fluid Mechanics*, 578:35–65.

Thompson, S. and Turner, J. (1975). Mixing across an interface due to turbulence generated by an oscillating grid. *Journal of Fluid Mechanics*, 67(02):349–368.

Turner, J. (1968). The influence of molecular diffusivity on turbulent entrainment across a density interface. *Journal of Fluid Mechanics*, 33(04):639–656.

van der Voet, E., Kleijn, R., and de Haes, H. A. U. (1996). Nitrogen pollution in the European Union–origins and proposed solutions. *Environmental Conservation*, 23(02):120–132.

Whitehead, J. A. and Chapman, D. C. (1986). Laboratory observations of a gravity current on a sloping bottom: the generation of shelf waves. *Journal of Fluid Mechanics*, 172:373–399.